Impacts of Nonsteady Load Responses on Utility Scale Wind Turbine Main Bearings by the Passage of Daytime Atmospheric Turbulence Eddies

Jarred Kenworthy

Wind and Marine Energy Systems and Structures
Electronic and Electrical Engineering
University of Strathclyde, Glasgow

A thesis presented for the degree of
Doctor of Philosophy

This thesis is the result of the author's original research. It has been composed by the author and has not been previously submitted for examination which has led to the award of a degree.

Signed: Jarred Kenworthy

Date: 04/06/2025

Abstract

Main bearings (MB) in wind turbines are prematurely failing, sometimes before 6 years in service, yet the exact damage mechanisms are still debated. This research hypothesises premature main bearing failures may be linked to repetitive force changes driven by the passage of energy-dominant atmospheric turbulence eddies through the wind turbine rotor in the atmospheric boundary layer. A high-resolution large-eddy simulation (LES) of a daytime atmospheric boundary layer was developed using the AMR-Wind finite volume code, and validated against the existing literature. The [Brasseur and Wei, 2010] framework was employed to improve the accuracy in the surface layer, where LES typically struggles. The overshoot in the prediction of the normalised mean velocity gradient was minimised, though not be fully removed, likely due to the contributions from numerical dissipation in the AMR-Wind code. Moderately convective boundary layers (MCBL) were simulated for several eddy-turnover times until quasi-stationarity was achieved. A novel methodology was developed to quantify the eddy passage time of the MCBL, showing good agreement with the literature. A sensitivity analysis parametrised a state-of-the art actuator line model (ALM). The sensitivity analysis showed low sensitivity with a blade sweep ratio (BSR) less than 1.0, though a possible connection between the maximum BSR and the non dimensional parameter ϵ/Δ is discussed. The classical ALM shows low sensitivity with a smoothing-ratio of 0.85 or greater. However, this is increased to 300 actuator points for ALM with the addition of the filtered-lifting line correction (FLLC). The FLLC significantly improved the accuracy compared to the classical ALM in both fixed and chord-varying ϵ configurations. The latter could achieve similar accuracy, but grid refinement limitations,

due to computational cost, were mitigated by using the FLLC. A static force balance model was used to explore mechanisms driving time variations in the MB force vector. The analysis showed the modified out-of-plane bending moment vector drives the time variations in the MB force vector, due to the contribution from the hub forces being 1-3 order of magnitude smaller in comparison. Furthermore, rotor weight contributes only to the average MB force vector and not to the time variations, in a rigid rotor configuration. It is demonstrated that asymmetry in the velocity field over the rotor disk drives variations in the MB force. Comparing the out-of-plane bending moment generated by ABL turbulence against a steady shear inflow, atmospheric turbulence generates high levels of fluctuations at the low and high frequency content and modulates the time variations in the 3P frequency content. Leading to the classification of three distinct frequency ranges (low, 3P, high). Specific periods of high-frequency and 3P activity were identified and found to qualitatively align with low-frequency peaks in MB force. However, limited overlap between peak "bursting" events across frequencies suggests distinct underlying mechanisms. A novel blade asymmetry vector was introduced, revealing that blade asymmetry is the dominant driver of MB force variability across all frequency bands. But there are subtle differences in the way asymmetry drives the time variations over the three frequency ranges. Using a novel methodology high-frequency fluctuations were shown to cause sub-second force jumps comparable in magnitude to rotor weight, posing a risk for edge loading, flange impact, and reduced lubrication film thickness. These extreme transients may be contributing to surface-initiated failure mechanisms. Further analysis demonstrated that LSS contribute more to rotor asymmetry and large force jumps than HSR, likely due to their higher coherence and internal velocity gradients. Finally, the influence of blade flexibility was assessed by re-running simulations with deformable blades. A less than 10% change between the calculations indicated that the core findings from the rigid rotor analysis remain valid. High-frequency loading events persist, suggesting that ABL turbulence, particularly in the form of coherent eddies like LSS, plays a key role in triggering dynamic load variations that may initiate MB failure.

Contents

List of Figures

List of Tables

Nomenclature

Acronyms

ABL Atmospheric Boundary Layer

ADM Actuator Disk Method

ALM Actuator Line Model

AMR Adaptive-Mesh Refinement

AoA Angle of Attack

AR Aspect Ratio

BE Blade Element

BEMT Blade-Element Momentum Theory

BPF Band Pass Filter

BSR Blade Sweep Ratio

CC Correlation Coefficient

CDF Cumulative Distribution Function

CFD Computational Fluid Dynamics

CFL Courant–Friedrichs–Lewy

CRB Cylindrical Roller Bearing

CWF Cyber Wind Facility

DEL Damage Equivalent Load

DLC Design Load Case

DNS Direct Numerical Simulation

DRB Double-row Roller Bearing

FE Finite Element

FFT Fast-Fourier Transform

FLLC Filtered-Lifting Line Correlation

HAZ High Accuracy Zone

HPF High Pass Filter

HSR High-Speed Region

IC Initial Capital

IEC International Electrotechnical Commission

Int Intermediate-speed region

ISO International Standards Organisation

LCOE Levelised Cost Of Energy

LES Large-Eddy Simulation

LOTW Law Of The Wall

LPF Low Pass Filter

LSS Low-Speed Streak

MB Main Bearing

MCBL Moderately Convective Boundary Layer

N-S Navier-Stokes

NBL Neutral Boundary Layer

NCAR National Center for Atmospheric Research

NREL National Renewable Energy Laboratory

O&M Operation and Maintenance

OOPBM Out-Of-Plane Bending Moment

PDF Probability Distribution Function

PLM Piecewise Linear Method

PPM Piecewise Parabolic Method

PSD Power Spectral Density

RCF Rolling Contact Fatigue

SCADA Supervisory Control And Data Acquisition

SFS Sub-Filter Scale

SRB Spherical Roller Bearing

SST Shear Stress Transport

TKE Turbulent Kinetic Energy

TRB Tapered Roller Bearing

TST Tip Speed Ratio

URANS Unstready Reynolds Averaged Navier-Stokes

WT Wind Turbine

Greek Letters

α Angle of attack

α_c	Contact angle
α_s	Shear exponent
α_{eff}	Effective angle of attack
α_{geo}	Geometric angle of attack
α_i	Induced angle of attack
$\boldsymbol{\tau}_0^{tot}$	Total shear stress vector
$\boldsymbol{\tau}_u^{SFS}$	Momentum sub-filter scale stress tensor
ΔR	Actuator point spacing
δ	Height of boundary layer attached to the blade
Δ_f	Filter width
Δ_{Blade}	Time for the blade tip to traverse one grid cell
ϵ	Body force characteristic length scale
ϵ_{comp}	Body force characteristic length scale applied to the calculation
ϵ_{mod}	Corrected body force characteristic length scale by FLLC algorithm
η_ϵ	Body force projection function
Γ	Circulation
κ	von Kármán constant
μ	Mass density of a blade segment
μ_i	Statistical moments
ν	Kinematic viscosity of air
ν_1	Reference kinematic viscosity
ν_t	Momentum turbulent viscosity

ν_θ	Potential temperature turbulent viscosity
Ω	Wind turbine blade angular velocity
Ω_E	Earth's angular velocity
ϕ	Inflow angle
ϕ_c	Coriolis twist angle
ϕ_m	Normalised mean velocity gradient
ρ	Density
ρ_0	Reference density
σ	Standard deviation
$\tau_{\theta_3}^{tot}$	Total surface temperature flux
τ_u	Eddy turnover time characterising surface shear
τ_w	Eddy turnover time characterising buoyancy
τ_θ^{SFS}	Sub-filter scale Potential temperature flux
Θ	Potential temperature
θ	Azimuth angle
θ_B	Blade twist angle
θ_L	Latitude

Latin Letters

$\mathbf{f}_N$	Actuator force vector
$\mathbf{f}_\epsilon$	Actuator body force vector
$\mathbf{I}$	Asymmetry vector
$\mathbf{I}_B$	Blade asymmetry vector

$\mathbf{R}$	Sub-filter stress tensor
$\mathbf{r}^{CR}$	Position vector from the hub centre of mass to an actuator point on a blade
$\mathbf{r}^{QC}$	Position vector from the apex of coning angle to the hub centre of mass
$\mathbf{S}$	Strain-rate tensor
$\widetilde{u}$	Lubrication entrainment speed
A	Area
a	Acceleration
a_c, b_c	Contact patch length and width
a_1, a_{ISO}	Bearing life modification factors
c	Airfoil chord length
c^*	Fictitious elliptic planform
C_D	Drag model constant in total stress stress vector
C_d	Coefficient of drag
c_D	Basic dynamic load rating
C_l	Coefficient of lift
c_p	Specific heat capacity
C_s	Smagorinsky constant
C_t	One-equation model constant
C_u	Bearing fatigue load limit
C_θ	Drag model constant in surface temperature flux
e	Sub-filter scale turbulent kinetic energy. $\sqrt{e} = u_t$
e_C	Contamination factor

e_D	Dynamic load ratio
F	Force
f	Coriolis Parameter
F_a	Axial bearing force
F_D	Drag force
F_L	Lift force
F_r	Radial bearing force
F_z, F_n	Airfoil force perpendicular to the direction of rotation
F_θ, F_t	Airfoil force in the direction of rotation
g	Gravitational constant
I_A	Asymmetry parameter
k	Wavenumber
k_{filter}	Filter Wavenumber
k_{peak}	Peak Wavenumber
L	Obukhov length scale
l	length of the largest eddies in the ABL
L_1	Distance between hub and main bearing
L_2	Distance between main bearing and gearbox
L_{10m}	Modified life rating
L_{10}	Basic life rating
$l_{\nu\,LES}$	LES viscous length scale
M	Moment

m^H	Mass of the hub
M_{pitch}	Pitching moment
N_δ	Vertical grid resolution
P	Power generation per year
p	Pressure
p^*	Effective pressure
p_0	Reference pressure
p_e	Load life exponent
P_r	Damage equivalent load
P_{eq}	Equivalent applied bearing load
Q_0	Surface temperature flux constant
r, R	Radial distance
R_a	Gas constant of air
Re_l	ABL Reynolds number
Re_{LES}	LES Reynolds number
s_0^*	Dimensionless chord location
T	Temperature
t	Time
T_0	Reference temperature
T_B	Total time of bursting periods for a signal
t_B	Time bursting periods between two signals overlap
t_c	Bearing lubrication advection time scale

T_R Fluctuating resolved velocity components and the shear component of the mean SFS stress tensor

T_S Sub-filter stress velocity components and shear stress component

$T_{surface}$ Initial surface temperature

u', v', w' Fluctuating velocity components

U, V, W Average velocity components

u, v, w Velocity components

u_* Friction velocity

U_g Geostrophic wind

U_∞ Incoming wind speed

U_{rel} Relative velocity in the frame of reference of the rotating airfoil section

V_x Axial velocity

W Actuator element width

w_* Characteristic velocity in the mixed layer

W_R Rotor weight

x', y', z' Coordinates aligned with mean velocity

x, y, z Global coordinates

X_D, Y_D Dynamic load factors

X_{max} Statistical mode

z_0 Roughness length scale

z_i Capping inversion height

z_r Reference height above the ground

Other symbols

ℓ	One-equation model length scale
$\mathfrak{R}$	Ratio of resolved to modelled averaged shear stress

Subscripts and Superscripts

$'$	Fluctuation about the mean value (e.g. $u' = u - U$)
0	Base state or reference condition, Surface of the domain
1	First grid cell in the domain
$\perp$	Out-of-plane
$\sim$	Tilde indicates the aerodynamic contribution
$\widehat{H}$	Hub coordinate system rotating with blade 1
A	Area
a	Airfoil coordinate system
B	Main Bearing
b	Blade coordinate system
c, t, r	chord, thickness, radial
E	Deformable
H	Non-rotating hub coordinate system
h	Horizontal components
i	Actuator point number
j	Blade number j=1,2,3
mod	Modified
n, t	normal, tangential

R	Rigid
r	Effectively filtered/resolved scales
$s1$	Grid resolved sub-filter scales
$s2$	Grid unresolved scales
s	Sub-filter scales
x', y', z'	Stream aligned coordinates
x, y, z	Global coordinates

Acknowledgements

I would like to acknowledge the people who have put in so much to make sure this project is successful. Dr. James (Jim) Brasseur of University Colorado Boulder for his support throughout the project, especially while I was living in Colorado, and for the opportunity to learn so much from someone with so much experience. Dr. Edward Hart of Strathclyde University for giving me the opportunity to work on the project, and for the support whenever I needed it. Dr. Jon Keller (NREL) for lending his expertise to the project. Dr. Matthew (Matt) Churchfield (NREL) was a secondary mentor who provided a great deal of help and expertise, especially on the use of AMR-Wind for simulation of the atmospheric boundary layer. Dr. Luiz (Tony) Martinez (NREL) was an invaluable source of expertise in the application of the "filtered-lifting-line correction" to the actuator line model of the wind turbine blades. I also received much help from Dr. Jason Jonkman (NREL), Dr. Ganesh Vijayakumar (NREL), Dr. Michael Brazell (NREL) and Dr. Geogios Deskos (NREL), which is greatly appreciated. Dr. Patrick Moriarty for allowing the use of computational resources.

The research was performed using the computational resources sponsored by the AWAKEN: The American WAKE experimeNt, and the Department of Energy's Office of Energy Efficiency and Renewable Energy, located at the National Renewable Energy Laboratory.

Chapter 1

Introduction

1.1 Motivations

In response to the climate change emergency, Europe installed 18.3 GW of new wind capacity in 2023, 14.5 GW onshore and 3.8 GW installed offshore. To further combat and reduce emissions over the next six years (2024 - 2030), it is expected that 33 GW a year of new wind capacity will need to be installed [WindEurope, 2024]. To ensure the continued expansion of wind energy capacity, a key factor is to continue reductions in the levelised cost of energy (LCOE). A simplified LCOE is the ratio of the initial capital cost of constructing (IC) the wind farm plus the yearly operation, and maintenance costs ($O\&M$), to the wind farm power generation per year (P) (Eq. 1.1). Research has been undertaken which investigates routes to reducing LCOE, with a key areas of research being maximising power production, reduction in operations and maintenance costs, and reduction of component failures [Veers et al., 2023] [Stehly and Duffy, 2023].

$$LCOE = \frac{IC + O\&M}{P} \tag{1.1}$$

The WT drive train (Figure 1-1) is a critical sub-assembly as it is responsible for

supporting the transfer of mechanical power from the rotor to the generator to deliver the electrical power to the grid. Furthermore, as there is no redundancy in the drive train if a failure occurs the turbine is shut down. Resulting in significant losses to the operator until repairs are made and the WT is functional again, which can be costly and complex since large and expensive cranes are required to remove the rotor assembly to access the drive train components such as the main bearing (MB) [Pulikollu et al., 2024]. There are several single points of failure along the drive train, such as the gearbox, the drive shafts, the generator, and, of primary interest to this PhD thesis, the MB. Higher than acceptable MB failures are documented in the literature, MBs have been recorded failing on or before 6 years in service and failure rates as high as 30% are documented across wind farms [Sethuraman et al., 2015] [Chovan, 2018] [Chovan, 2019] [Hart et al., 2019] [Hart et al., 2023]. This is a serious issue as the bearings are designed for a minimum of 20 years of service as per ISO BS EN IEC 61400-1 [International Electrotechnical Commission, 2019].

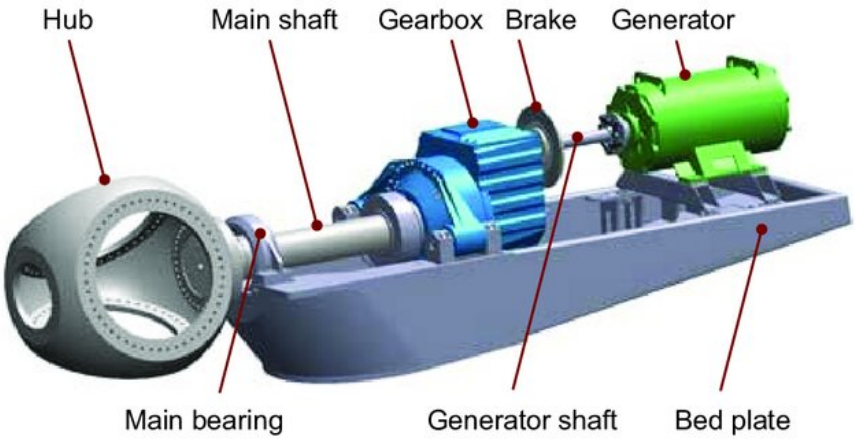

Figure 1-1: Typical Drive train assembly. Acknowledgement: [Sheng et al., 2011].

There are several damage mechanisms that can occur in MBs, rolling contact fatigue, wear and corrosion (discussed in more detail in section 2.4.5). However, there is no current consensus in the literature concerning the damage mechanisms that underlie the premature failures of WT MBs [Nejad et al., 2022] [Guo et al., 2021] [Kenworthy

et al., 2024] [Hart et al., 2020]. Therefore, there is a recognised need to identify the principle drivers of MB failures.

Utility scale WTs typically operate within the highly turbulent atmospheric boundary layer (ABL), the 1-2 km region of the troposphere adjacent to the earth's surface. The structure of the daytime ABL is driven by strong mean shear-rate close to the surface and a buoyancy dominated region which systematically varies with the stability state of the ABL. During the day energy dominant, highly coherent turbulent eddy structures are transported within the ABL driven by strong convection and mean shear. These energy-dominant eddies interact with the rotating WT blades and directly impact the nonsteady time variations in the rotor hub loads, which has been shown to lead to fluctuations on the order of 40-50% [Vijayakumar et al., 2016], with a wide range of time scales. The most recognised nonsteady time variations being the characteristic 3P variations, the longest being on the order of 20 s - 60 s (eddy passage time), and the shortest of these is below 1 second [Nandi et al., 2017] (see Figure 1-2). The term nonsteady is used to describe time variations in time series and implies the flow is turbulent. As the eddies interact with the rotating WT blades, the high temporal variabilities in the aerodynamic loads pass from the rotor hub to the main shaft in the form of torque, out-of-plane bending moment (OOPBM), out-of-plane force and thrust which force to time response of the MB.

The proposed research (see Section 1.2), centres on the hypothesis that premature MB failures may result from specific repetitive changes in the forces and moments that underlie changes in the load zone on the MB. Which is in response to specific temporal changes in the turbulent velocity flow over the rotor disk, that result from the continual passage of the energy-dominant atmospheric turbulence eddies through the WT rotor plane. Since the ABL turbulence structure varies with atmospheric stability the loading characteristics at the MB changes during the day and among the seasons, as well as with topography.

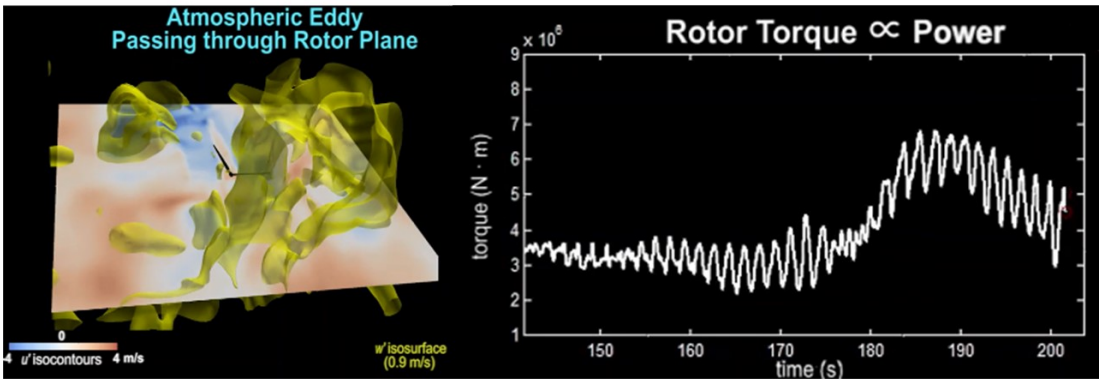

Figure 1-2: Wind turbine response to the passage of daytime atmospheric eddies. Left Atmospheric eddy passing through rotor disk. Right Rotor torque time series. Acknowledgement: Lavely, Vijayakumar, Brasseur, et al.

During the design of utility scale WTs several design load cases, which cover different situations a WT may experience during its lifetime (power production, start-up, emergency stop, etc), are simulated using an aeroelastic dynamic model (Bladed, FAST, HAWK2) [International Electrotechnical Commission, 2019]. The wind conditions used in the simulations are modelled using a kinematic turbulence model with a mean shear profile and specified turbulence intensity. Parameters to define the inflow conditions are typically calculated from 10 minute time averages from a measurement campaign. Several studies have investigated MB loads with respect to time averaged wind field characteristics such as wind speed, shear exponent and veer gradient [Hart et al., 2019], [Hart et al., 2022c]. Time variations in MB force have been shown to be highly sensitive to these time averaged wind field characteristics notably veer gradient [Hart et al., 2022c]. Several of the above studies use synthetically generated turbulence, however, kinematic turbulence is not representative of real turbulence and the structure of the ABL, as it is unable to model the interactions between buoyancy from surface heating and shear which creates spatial correlated eddy structures. Therefore, we must also question how important is it to represent the structure of the true ABL to capture the time response of WTs, in the case of this thesis the time response of the MB.

1.2 Aims and Objectives

The overall aim of this research program is to characterise and quantify the impacts of energetic atmospheric turbulence eddies on the time variations in the loads on wind turbine MBs using high-fidelity computer models and simulations. The specific objectives of my research program include:

1. Develop a high resolution large-eddy simulation (LES) of the daytime atmospheric boundary layer (ABL).

2. Develop a state-of-the-art simulation of a utility scale wind turbine, embedded within the atmospheric boundary layer, using an advanced actuator line model, with deformable turbine rotor blades, to contrast rigid and elastic blade response.

3. Develop computational experiments to investigate the effects of ABL turbulence-generated nonsteady loadings on main bearing and wind turbine function.

4. To the extent possible, characterise potential damage modes on the main bearing, due to the nonsteady ABL turbulence-generated loadings.

The above objectives were developed to answer the key research questions:

R1: what is the role of the energetic daytime atmospheric turbulence eddies, that pass through the wind turbine rotor, in the generation of the time variations in the loads on wind turbine main bearings?

R2: what are the characteristics of the main bearing response as wind turbine blades interact with spatially and temporally varying coherent structures within the daytime atmospheric boundary layer turbulence?

R3: to what extent does blade elasticity and deformation influence the time variations in main bearing loads induced by ABL turbulence?

1.3 Thesis Organisation

This thesis covers several themes, to ensure the reader has the necessary background information, technical details are laid out in Chapter 2. Section 2.1 explains relevant details of the atmospheric boundary layer and cites related works. Section 2.2 describes the basic actuator line method and addresses the modelling approaches cited in the literature. Section 2.3 gives an overview of the field of unsteady aeroelastics as it pertains to WTs and following this the work relevant to the impact of atmospheric turbulence on the response of WT it presented, as it is the foundation this thesis is built upon. Section 2.4 describes the architecture, typical operation of MBs, failure mechanisms/modes and examines statistical analyses of WT MBs. Chapter 3 provides the technical details of the state-of-the-art simulation tools developed and analyses to justify the choices made, along with description of the different boundary layers used in subsequent analyses. Chapter 4 describes the methodology used to parametrise the actuator line model and analyses the sensitivity of varying the ALM parameters, resulting in the final actuator line model which is implemented in the simulation of the atmospheric boundary layer and used to simulate the response of the NREL 5 MW WT to the passage of atmospheric eddies. Chapter 5 and 6 describe the advances in our knowledge of the time variation in the MB force vector and the interactions between daytime atmospheric turbulence eddies. Chapter 7 investigates the impact of blade deformations to the time variations in the MB force, to answer the question to what extent are the conclusions drawn from Chapters 5 and 6 applicable for a deformable rotor. Finally, the key results are summarised in Section 8.1, and potential future work is discussed to extend the work done in this thesis is proposed in Section 8.2.

Chapter 2

Background and Literature Review

In this thesis several tools were used to calculate the time varying response of a utility scale wind turbine (WT) to the passage of atmospheric turbulence eddies in the atmospheric boundary layer. Each tool has its own physics, different levels of approximations and literature surrounding the subject matter.

Atmospheric turbulence eddies in the atmospheric boundary layer is simulated using large-eddy simulation using the open source code AMR-Wind. Section 2.1 provides an introduction into the atmospheric boundary layer (ABL), turbulence and large-eddy simulations (LES) of the ABL, details the structure of the ABL and the impact of stability state on the structure. Section 2.1.1 provides a technical depiction of modelling ABLs using large-eddy simulation, including describing the models and boundary conditions required to numerically solve the conservation equations. Section 2.1.4 discusses well-known issues with modelling the ABL and the work done to improve the accuracy.

The interaction between the atmospheric turbulence and the response of the WT is modelled using actuator line method. Section 2.2 describes the basic Actuator Line

Method (ALM), discusses the numerical nuances associated with the ALM, address the modelling approaches developed in the literature for the actuator force and body force projection function and outline the relationships detailed in the literature between the characteristic length scale of the body force projection, actuator grid spacing and computational grid spacing. Furthermore, this section aims to compare the ALM with the actuator-disc method (ADM), blade-element-momentum theory (BEMT) and full blade-resolved simulations.

The WT response to the passage of atmospheric eddies is modelled using the multi-body aeroelastic code OpenFAST v3.4.1, several options for physics models are implemented in OpenFAST to model the aerodynamic response and structural response. Section 2.3 gives an overview of the field of unsteady aeroelastics as it pertains to WTs. This requires an in-depth examination of unsteady aerodynamics of airfoils and WTs, followed by a comprehensive review of the structural modelling of WTs. Following, an outline of the work done to understand the aeroelastic response of WTs to the passage of atmospheric turbulence is presented.

2.1 Atmospheric Boundary Layer

The ABL is a wall bounded, high Reynolds number, turbulent flow adjacent to the earth's surface. The ABL, located in the lower troposphere, has an exceptionally wide range of length and time scales due to the high Reynolds number. A Reynolds number in the ABL can be defined as: $Re_l = ul/\nu$, where u - characteristic velocity of the ABL, l - length of the largest eddies in the ABL and ν - kinematic viscosity of air. The current research program addresses the impacts of turbulence in the daytime ABL. The daytime ABL is capped by a local inversion layer typically 1000 m - 2000 m from the surface, above which resides the free troposphere where most the weather systems are located. The entire troposphere is approximately 10 km - 20 km in depth. Meteorologists refer to the motions above the ABL in the free troposphere as "mesoscale", while the ABL

motions are "microscale". From the point of view of the ABL the mesoscale flow above imposes largely horizontal quasi-mean flow onto the ABL (see Figure 2-1 left), due to the order of magnitude differences in scales of mesoscale eddies in the free troposphere compared to the microscale turbulence eddies in the ABL.

The separation between the ABL and the upper troposphere is demarcated by the "capping inversion", a stably stratified layer that confines turbulence eddies in the convective mixed layer of the daytime ABL. The capping inversion height denoted z_i, has historically been defined as the level of minimum vertical heat flux $\overline{w'\Theta'}$ [Lilly, 1968], [Deardorff, 1979], [Fedorovich and Mironov, 1995] (see Figure 2-1 right), where w' is vertical fluctuating velocity, Θ' is fluctuating potential temperature (see below for description) and the over-bar represents an ensemble average. In principle, the ABL over land is non-stationary, and changes with the diurnal cycle (discussed below) and commonly varies statistically in the horizontal (i.e, inhomogeneous in the horizontal). However, if the time-scale changes are much larger than the eddy turnover times, ($\tau_u = z_i/u_*$, $\tau_w = z_i/w_*$) in the ABL, then the ABL can be approximated as quasi-stationary, where u_* is the friction velocity. This is typically the case in the early afternoon after the sun has reached its apogee to an hour or so before sunset. Similarly, if the spatial scales of statistical variations in the horizontal are much smaller than spatial variations at the mesoscale, then the ABL may be approximated as statistically homogeneous in the horizontal [Wyngaard, 2010].

Furthermore, as Figure 2-1 illustrates the daytime ABL can be split into three sub-regions each with separate characteristics. The "surface layer" is roughly the lowest 15-20% of the ABL adjacent to the surface, the region where turbulence eddies are directly modified by the impermeable surface. In the ABL the surface layer is also characterized by the highest vertical gradients in horizontal mean velocity and temperature. Above the surface layer is the "mixed layer", characterized by strong mixing due largely to turbulence transported by convection and generated by buoyancy from solar heating.

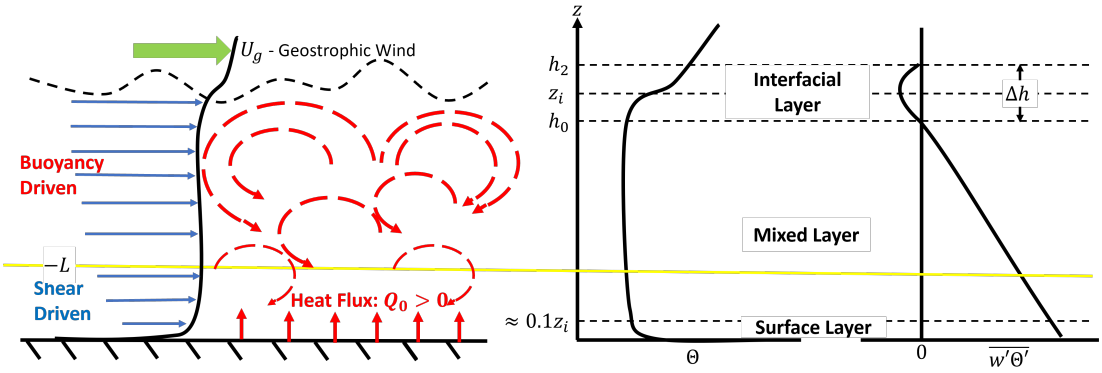

Figure 2-1: Qualitative illustrations of the structure of the moderately convective daytime ABL. Left - Turbulence structure and mean velocity profile, Center - Potential temperature vs height, Right - Heat flux $\overline{w'\Theta'}$ vs height.

Potential temperature Θ is defined as the temperature an air parcel would have if it were expanded or compressed adiabatically from its existing pressure p and temperature T to a reference pressure p_0, typically 1000 mbar. Hydrostatic variations in pressure cause changes to temperature and density. A commonly used approach is to split the pressure p, temperature T and density ρ into an adiabatic motionless "base state" (p_0, T_0, ρ_0) and a deviation from this "base state" $(\Delta p, \Delta T, \Delta \rho)$:

$$p_0 = p - \Delta p; \quad T_0 = T - \Delta T; \quad \rho_0 = \rho - \Delta \rho. \tag{2.1}$$

Mathematically potential temperature can be derived to be:

$$\Theta = T \left(\frac{p_0}{p} \right)^{\frac{R_a}{c_p}}, \tag{2.2}$$

where T is the current temperature of the fluid parcel, R_a is gas constant of air and c_p is the specific heat capacity heat at constant pressure [Nappo, 2012].

The ABL goes through a diurnal cycle (Figure 2-2), where at sunrise the solar heating of the earth's surface creates an increasing surface temperature that peaks roughly when the sun is at its highest apogee. The absorbed solar radiation is re-emitted as heat

flux from the ground leading to buoyancy driven turbulence and unstable stratification and creating a convective mixed layer between the surface and inversion layers. As the mixed layer extends vertically so does the height of the capping inversion. After the sun reaches its apogee, a quasi-equilibrium ABL can be produced under steady mesoscale winds until the sun has descended towards sunset. Following sunset, the nighttime ABL develops, which has major differences from the daytime ABL. In the typical nighttime ABL, the earth's surface (land) is cooler than its surroundings, and heat flux is into the ground, leading to stable stratification which suppresses turbulence and turbulent mixing.

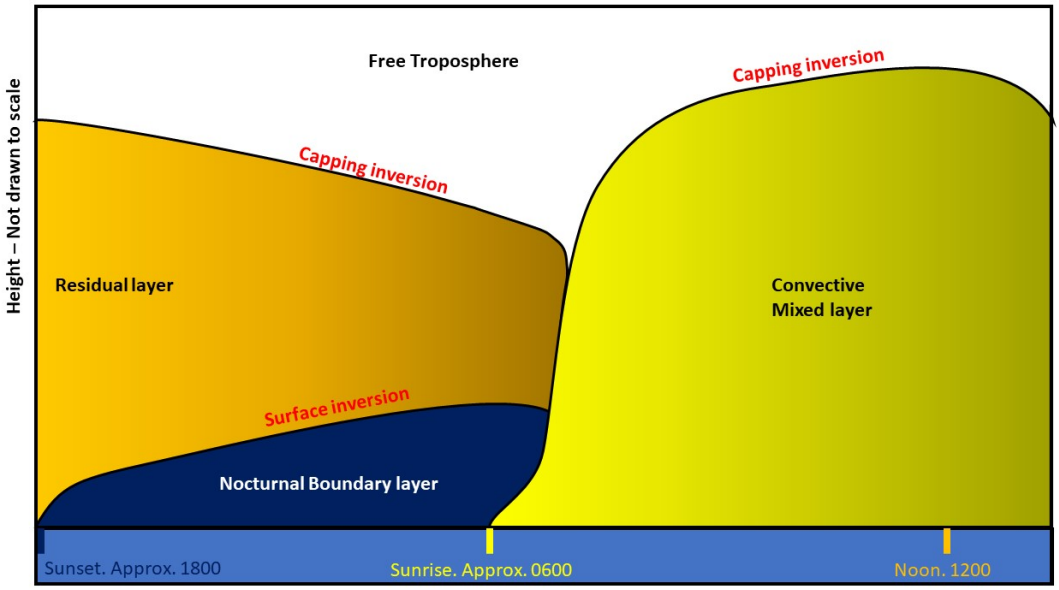

Figure 2-2: Qualitative illustration of the overall structure of the atmospheric boundary layer over the diurnal cycle.

The ABL stability state can be quantified with the non-dimensional scale ratio $-z_i/L$, where L is the Obukhov length scale is derived from scaling the statistical rates of shear and buoyancy production

$$L = \frac{-u_*^3}{\kappa \frac{g}{T_0} Q_0}, \tag{2.3}$$

where u_* is friction velocity, κ is the von Kármán constant typically taken to be 0.40, g is the gravitational constant, T_0 is the base state surface temperature, Q_0 is the base state surface temperature flux. Note that L is defined to be negative in the unstable daytime ABL and is positive in the stable nighttime ABL. In the daytime (unstable) ABL the stability parameter, $-z_i/L > 0$, is used in numerous papers to characterize the extent to which the daytime ABL is globally unstable [Deardorff, 1972], [Jayaraman and Brasseur, 2021], [Salesky et al., 2017], [Khanna and Brasseur, 1998], [Lemone, 1973]. The Obukhov length scale is the approximate height from the surface where turbulence production due to shear and turbulence production due to buoyancy are approximately equal within an order of magnitude. Friction velocity $u_*[m/s]$ is the characteristic velocity at the surface layer and $w_* = \left(\kappa \frac{g}{T_0} Q_0 z_i\right)^{1/3}$ is the characteristic velocity in a buoyancy-dominated flow. Thus, $z_i/L = (u_*/w_*)^3$ and $-L$ characterizes, within an order of magnitude, the height above which buoyancy production is higher than shear production and below which shear production dominates buoyancy.

As previously mentioned, in the daytime ABL, Q_0 is positive and the Obukhov length scale is negative and in the nighttime ABL Q_0 is negative and $L > 0$. Therefore, $-z_i/L$ characterizes the proportions of the ABL dominated by either shear-rate or buoyancy production. When $-z_i/L >> 1$ the ABL is globally fully convective driven ("convective boundary layer") meaning turbulence is fully generated by buoyancy. By contrast, when $-z_i/L << 1$, the ABL is globally shear-driven ("neutral boundary layer"). The daytime ABL typically is "moderately convective" where $-z_i/L \sim 1 - 10$. In the moderately convective boundary layer (MCBL) the ABL has a region which is shear dominated and a region of buoyancy dominated turbulence. The MCBL is the focus of study in this thesis as it is representative of the daytime ABL when turbulence levels are at their highest, so the strongest time changes from turbulent eddies will be during the daytime. In the MCBL, the region of high shear-rate tends to be located between the surface and $-L$ (see Figure 2-1). High shear-rate drives the production of the streamwise component of the turbulent kinetic energy (TKE) u'^2, while in the

buoyancy-dominated region, buoyancy force drives the vertical component of the TKE w'^2.

[Deardorff, 1972] studied a neutral boundary layer, two moderately convective boundary layers and a convective boundary layer, with among the earliest large-eddy simulations. [Deardorff, 1972] found that for the neutral case the streamwise velocity fluctuation u', and passive scalars concentrated within elongated coherent patterns near the surface aligned with the time averaged streamwise velocity. [Moeng and Sullivan, 1994] also found "low" and "high" speed "streaks" in the horizontal fluctuating velocity in the shear dominated ABL, where the streaks alternate between above the average and below the average streamwise velocity. These coherent structures are referred to as high and low speed streaks (see Left - Figure 2-3). These streaks are also observed for the MCBL cases however, [Moeng and Sullivan, 1994] observed that the low-speed streaks decrease in variance with increasing height which implies a reduction in intensity, as it is well established elongated low speed streaks are a ubiquitous characteristic of turbulent shear flows. Contrary to expectations, coherence length of vertical and horizontal motions increase with a small levels of heat flux through the ground [Jayaraman and Brasseur, 2021]. When heat flux is added to a neutral ABL (zero heat flux through the ground), one would expect the addition of buoyancy force to reduce the coherence of shear generated low speed streaks. However, [Jayaraman and Brasseur, 2021] showed the coherence of the horizontal and vertical motions increase with stability state $-z_i/L$ until they reach their critical stability states. At the critical stability state $-z_i/L \sim 0.433$ the streamwise streaks extended horizontally, thickened vertically, and increased in aspect ratio [Jayaraman and Brasseur, 2021]. While concentrations of vertical velocity merge together and extend in the horizontal [Jayaraman and Brasseur, 2021]. It is well known that positive vertical velocity fluctuations ($+w'$) and passive scalars tend to concentrate within the low-speed streaks [Deardorff, 1972] [Moeng and Sullivan, 1994], consequently the vertical velocity is elongated and negatively correlated with the streamwise velocity $-\langle u'w' \rangle$.

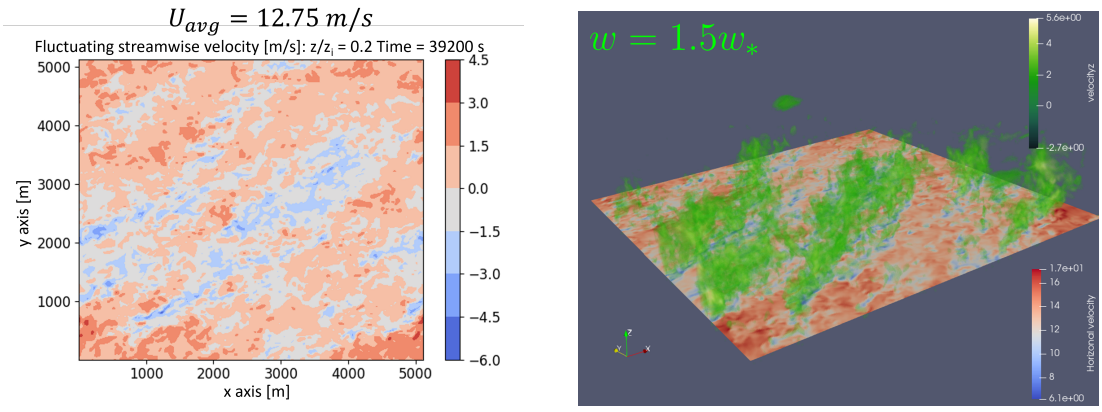

(a) (b)

Figure 2-3: (a) Isocontour streamwise velocity fluctuations at $\sim$ 200 m (surface layer) illustrating low and high speed streaks. (b) Isosurfaces vertical motions ($1.5w^*$) overlaying streamwise fluctuations illustrating spatial correlation between low speed streak and vertical motions.

[Khanna and Brasseur, 1998] and [Jayaraman and Brasseur, 2021] argue that atmospheric thermals within the mixed layer (vertical velocity fluctuations concentrated within updrafts) are generated within the low speed streaks within the surface layer. Because the streaks result from strong shear-rate in the near-surface region, mean shear in the surface layer is central to the global structure of turbulent eddies in the moderately convective daytime ABL. These observations are consistent with studies by [Deardorff, 1972] and [Moeng and Sullivan, 1994] that showed vertical temperature flux to be correlated with the low speed streaks. [Khanna and Brasseur, 1998] and [Jayaraman and Brasseur, 2021] explain that in the MCBL temperature fluctuations tend to concentrate in the low speed streaks, creating the near-surface buoyancy force that drive thermals vertically from the low speed streaks (Figure 2-3 - right).

The buoyancy-induced updrafts, local to the low speed streaks, grow in the vertical with distance from the ground as they merge with other thermals to create the observed updraft turbulence structure in the mixed layer. In the buoyancy-dominated mixed layer the updrafts form coherent sheets. The updrafts combine with horizontal turbulence fluctuations to create helical motions at the boundary layer scale. At

the capping inversion the sheets of upward-moving fluid are forced to turn and form the downward legs of horizontal roll vortices [Khanna and Brasseur, 1998] that fill the ABL and modulate the near-surface region. The surface layer streaks, mixed-layer updrafts, and large-scale atmospheric rolls all interact with WTs within the wind farms to generate the non-steady loading that underlie this current research program.

While this thesis does not directly study the impact of turbulence of stable boundary layers it is useful to have an understanding of the differences between unstable and stable boundary layers. As stated above, at night the earths surface is cooler than its surroundings, and heat flux is into the ground leading to a stable stratification leading to the development of the nocturnal boundary layer. Turbulence in the stable boundary layer is a result of mean shear and buoyancy, however whereas, in the unstable boundary layer buoyancy generates turbulence, in the stable boundary layer buoyancy removes turbulence. This leads to intermittent turbulence regions where at times the turbulence generated by shear is too little to support turbulence and the flow is no longer fully turbulent [Stull, 2012].

The stable boundary layer also has particular characteristics such as low level jets, thin stream of fluid with speeds close to and sometimes surpassing the geostrophic wind, located 100 m - 300 m above the ground [Stull, 2012]. Stable boundary layers can also support buoyancy (gravity waves) The effect of these characteristic structures on WTs has been extensively researched (Low level jets [Gutierrez et al., 2016] [Gutierrez et al., 2017] [Gadde and Stevens, 2021]), (Gravity waves [Allaerts and Meyers, 2018] [Smith, 2010]).

2.1.1 Large-Eddy Simulation of the Atmospheric Boundary Layer

[Moeng, 1984] pioneered a large-eddy simulation (LES) algorithm for the ABL, the basis of which is still used today in modern day LES ABL codes. Taking advantage of the numerically fast application of the fast Fourier-Transform (FFT), the pseudo-

spectral algorithm underlying LES ABL codes used by researchers at the National Center for Atmospheric Research (NCAR), uses pseudo spectral in the horizontal and second-order finite difference in the vertical on a staggered grid. In pseudo-spectral methods, the fluctuating variables are explicitly filtered to an "effective grid" that is at least 50% coarser than the "geometric grid" to remove aliasing error [Patterson Jr and Orszag, 1971]. Boundary conditions are required for the total temperature flux and total surface shear stress vector under each cell at the surface, where "total" implies that space-time variations in both mean and fluctuations must be provided. The general LES ABL algorithm given in [Moeng, 1984] has been used in many ABL LES studies [Moeng and Sullivan, 1994], [Khanna and Brasseur, 1998], [Vijayakumar et al., 2016] and [Sullivan and Patton, 2008] to name a few.

Due to mixed pseudo-spectra with finite difference LES scheme's being limited to uniform grids, therefore the addition of complex geometries, such as wind turbines, into the pseudo-spectral calculation is impractical. Thus, there is a demand in the geophysics and engineering communities for highly paralyzable finite-volume schemes suitable for LES ABL codes that can incorporate complex geometries into the simulation [Giacomini and Giometto, 2021]. However, finite-volume codes have their own drawbacks such as high dissipation relative to pseudo-spectral LES codes, and truncation error [Ghosal, 1996], [Kravchenko and Moin, 1997]. Regardless, finite-volume schemes have been applied to ABL LES codes and often include wind turbines within the calculation such as, [Churchfield et al., 2010], [Churchfield et al., 2017] and the AMR-Wind code used in this current study.

The LES method centres on the prediction of variables effectively filtered by the geometric grid and added dissipative elements in the algorithm and sub-models. The LES framework decomposes all fluctuating variables (velocity, pressure, temperature) into a grid-resolved effectively filtered part, where a superscript r or tilde over the variable implies variables on the effective grid, where "effective" includes additional

filtering from dissipative elements in the algorithm and sub-models, which is explicitly calculated, and a sub-filter scale part (denoted by a superscript s):

$$\mathbf{u} = \mathbf{u}^r + \mathbf{u}^s,\ p = p^r + p^s,\ \Theta = \Theta^r + \Theta^s. \tag{2.4}$$

This is done with two effective filtering levels: the grid filter only allows fluctuations with scales larger than the effective grid scale to be carried forward in the calculation, and a dealiasing filter to reduce the aliasing error. Aliasing error is due to subgrid scale motions, from the calculation of the nonlinear terms in the equation of motion [Kravchenko and Moin, 1997], being placed into the resolved scales as there is nowhere else they can exist because there is no grid support for subgrid scale motions.

In physical space LES codes, numerical dissipation effectively filters the nonlinear term to reduce aliasing error. Effective filtering is accomplished implicitly through numerical dissipation and from the dissipative nature of the sub-filter scale (SFS) stress model. Therefore, fine tuning of these dissipative elements is key to accuracy in LES in practice. Figure 2-4 illustrates the two levels of filtering (grid and dealiasing filters) create three ranges of scales in LES: the resolved scales (u^r), the grid-resolved sub-filter scales (u^{s1}), and the grid-unresolved scales (u^{s2}).

Theoretically the LES momentum equation for a Newtonian fluid is obtained by filtering the Navier-Stokes equation:

$$\frac{\partial \mathbf{u}}{\partial t} + \nabla \cdot (\mathbf{u}\mathbf{u}) = -\frac{1}{\rho}\nabla p + \nu \nabla^2 \mathbf{u}, \tag{2.5}$$

where $\mathbf{u}$ is the velocity vector, p is pressure and ν is kinematic viscosity.

A filtered variable ϕ is formally given by:

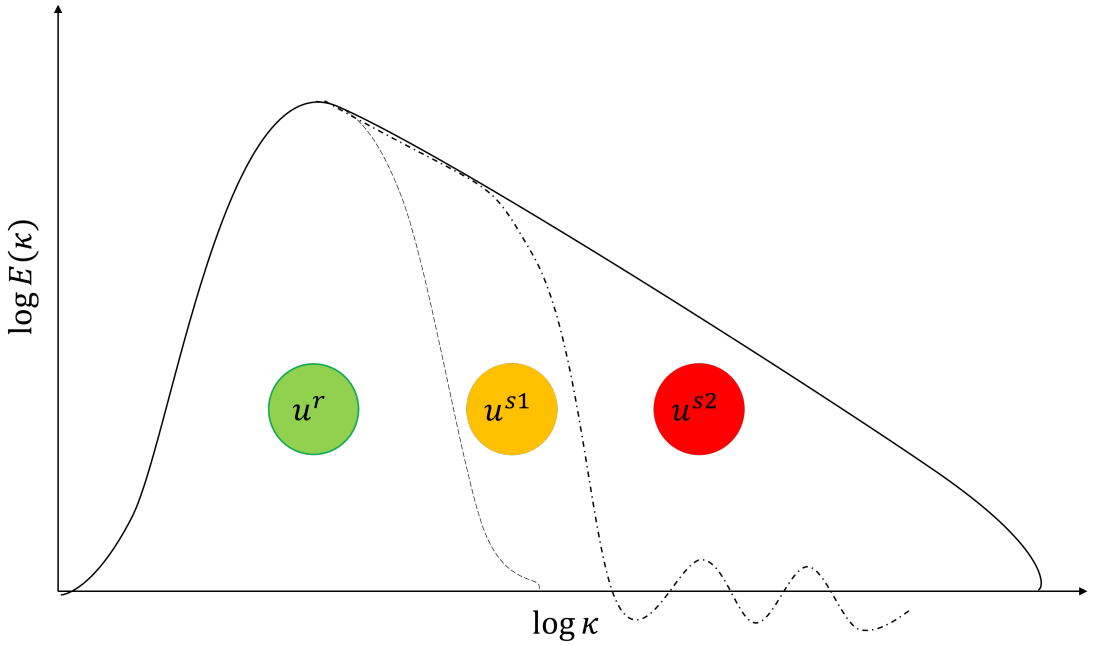

Figure 2-4: Energy Spectrum illustrating effective filter and grid filter. Where the solid line is the energy spectrum, the dashed dotted line is the grid filter, and the dashed line is the effective filter.

$$\phi^r(\overrightarrow{x}) = \int g\left(\overrightarrow{x} - \overrightarrow{\xi}\right) \phi\left(\overrightarrow{\xi}\right) dV(\overrightarrow{\xi}), \tag{2.6}$$

where $g\left(\overrightarrow{x} - \overrightarrow{\xi}\right)$ is the effective filter, localised within the domain at the scale of the effective grid, that includes the grid and dealiasing filters. To predict atmospheric boundary layers, the following dynamical system must be solved with appropriate boundary and initial conditions:

$$\text{Continuity: } \nabla \cdot \mathbf{u}^r = 0, \tag{2.7}$$

$$\text{Momentum: } \frac{\partial \mathbf{u}^r}{\partial t} + \nabla \cdot (\mathbf{u}^r \mathbf{u}^r)^r = -\frac{1}{\rho_0} \nabla p^* + \nabla \cdot \boldsymbol{\tau}_u^{SFS} + \frac{\mathbf{g}}{\Theta_0} (\Theta^r - \Theta_0) + \mathbf{f} \times (\mathbf{U_g} - \mathbf{u}^r), \tag{2.8}$$

$$\text{Potential temperature: } \frac{\partial \Theta^r}{\partial t} + \nabla \cdot (\Theta^r \mathbf{u}^r)^r = -\nabla \cdot \boldsymbol{\tau}_\theta^{SFS}. \tag{2.9}$$

The LES model approximates as locally incompressible with varying potential temperature $\Theta(\mathbf{x}, t)$, density $\rho(\mathbf{x}, t)$ and buoyancy. This is the Boussinesq approximation and is valid in the lower troposphere, but degrades above. In the above equations $\mathbf{u}^r$ is the filtered velocity vector, p^* is effective pressure (explained below), $\boldsymbol{\tau}_u^{SFS}$ is the momentum SFS stress tensor (described below), $\boldsymbol{\tau}_\theta^{SFS}$ is the SFS potential temperature flux vector, $\mathbf{g}$ is the acceleration due to gravity, Θ_0 is reference potential temperature, Θ^r is filtered potential temperature, $\mathbf{f}$ is the Coriolis parameter (described below) and $\mathbf{U_g}$ is geostrophic wind. The viscous term from the Navier-Stokes equation (Eq. 2.5) is left off, which is typical for LES ABL calculations [Moeng, 1984] [Churchfield et al., 2012a], because the viscous term is negligible [Wyngaard, 2010], due to the high Reynolds numbers in the ABL. The superscript r outside the brackets of the filtered advective derivatives indicates that the dissipation-centred dealiasing implicit filter (physical space code see Section 3.3) or truncation (pseudo-spectral codes) has been applied.

After applying the LES decomposition to the non-linear term in the Navier-Stokes equation the non-linear term is separated into the effectively filtered non-linear term $(\mathbf{u}^r \mathbf{u}^r)^r$ and:

$$\mathbf{R} = \left(\mathbf{u}^r \mathbf{u}^s + \mathbf{u}^s \mathbf{u}^r + \mathbf{u}^s \mathbf{u}^s\right)^r, \tag{2.10}$$

commonly known as the SFS stress tensor denoted $\mathbf{R}$ and must be modelled.

Eddy viscosity models are by far the most common approach to modelling the SFS stress tensor $\mathbf{R}$. The eddy viscosity model approach is analogous of the stress-strain-rate relationship for a Newtonian fluid. The SFS stress tensor is set proportional to the filtered strain-rate tensor which is explicitly calculated. The constant of proportionality

is $2\nu_t$, where ν_t is commonly referred to as the turbulent, or eddy viscosity which requires modelling (section 2.1.2). However, mathematically the SFS stress tensor $\mathbf{R}$ (in its current form) cannot be set proportional to the strain-rate tensor, as the strain-rate tensor is symmetric and traceless. To make $\mathbf{R}$ symmetric and traceless, 1/3 of the trace of $\mathbf{R}$ is subtracted from $\mathbf{R}$ and is added to the pressure force term in the Navier-Stokes equation (Eq. 2.5). Mathematically:

$$\boldsymbol{\tau}_u^{SFS} = \mathbf{R} - \frac{1}{3} Tr\{\mathbf{R}\}\mathbf{I}, \tag{2.11}$$

$$p^* = p' + \frac{\rho_0}{3} Tr\{\mathbf{R}\}, \tag{2.12}$$

where $\boldsymbol{\tau}_u^{SFS}$ is the deviatoric part of the momentum SFS stress tensor, p^* is effective pressure, by taking the divergence of the momentum equation, which yields a Poisson equation, the effective pressure p^* can solved for. Lastly, $p' = (p - P)$ is fluctuating pressure, where we use the Reynolds decomposition,

$$\phi' = \phi - \Phi, \tag{2.13}$$

where the ensemble average is commonly denoted by capitalization of the letter or symbol and the fluctuating variable is commonly denoted with a prime.

Similarly, after applying the LES decomposition to the non-linear term in the potential temperature equation, the nonlinear term can be separated into the effectively filtered nonlinear term $(\Theta^r \mathbf{u}^r)^r$ and SFS potential temperature flux vector:

$$\boldsymbol{\tau}_\theta^{SFS} = \left(\mathbf{u}^r \Theta^s + \mathbf{u}^s \Theta^r + \mathbf{u}^s \Theta^s\right)^r . \tag{2.14}$$

Models are required for the SFS tensor $\boldsymbol{\tau}_u^{SFS}$ and vector $\boldsymbol{\tau}_\theta^{SFS}$. These are described in section 2.1.2.

To account for buoyancy forces in the ABL, the buoyancy body force is modelled, $\frac{\mathbf{g}}{\Theta_0}(\Theta^r - \Theta_0)$, using the Boussinesq approximation for locally incompressible flows with varying potential temperature $\Theta(\mathbf{x}, t)$ and density $\rho(\mathbf{x}, t)$. This approximation is applicable to low Mach number flows with variable density and temperature. To account for the rotation of the earth and non-inertial rotating frame of reference, the Coriolis acceleration, $\mathbf{f} \times \mathbf{u}^r$, is added to the filtered Navier-Stokes equation, where $\mathbf{f}$ is the "Coriolis parameter". The Coriolis parameter is the earth's angular velocity Ω_E, projected onto the plane at any latitude θ_L of the surface of the earth. Where in engineering flows the Coriolis parameter is defined as: $\mathbf{f} \equiv [0,\, 2\Omega_E \cos\theta_L,\, 2\Omega_E \sin\theta_L]$, however, in the atmospheric community only the vertical (z) component is used [Wyngaard, 2010]. The mesoscale flow above the capping inversion of the ABL imposes horizontal variations at scales much larger than ABL turbulence scale and are modelled locally with the geostrophic wind vector $\mathbf{U_g}$, defined to characterise the mean pressure gradient, $-\nabla P \equiv -\rho \mathbf{f} \times \mathbf{U_g}$.

2.1.2 Sub-filter Stress and Flux Models

As mentioned previously eddy viscosity models are a typical approach to modelling the deviatoric part of the SFS stress tensor $\boldsymbol{\tau}_u^{SFS}$ and the SFS potential temperature flux vector. The mathematical forms are:

$$\boldsymbol{\tau}_u^{SFS} = 2\nu_t \mathbf{S}^r, \tag{2.15}$$

$$\boldsymbol{\tau}_\theta^{SFS} = -\nu_\theta \nabla \Theta^r, \tag{2.16}$$

where the filtered strain-rate tensor and filtered potential temperature gradient are

explicitly calculated and the turbulent viscosities ν_t and ν_θ, require modelling.

A common eddy viscosity model is the one-equation model and is the eddy viscosity model used in the LES simulations of the ABL conducted in this research, using the LES code AMR-Wind:

$$\nu_t\left(\mathbf{x},t\right) = C_t u_t\left(\mathbf{x},t\right)\ell, \tag{2.17}$$

$$\nu_\theta\left(\mathbf{x},t\right) = \left[1+\left(2\ell/\Delta s\right)\right]\nu_t\left(\mathbf{x},t\right). \tag{2.18}$$

Through the one-equation model constant C_t, is taken to be proportional to the filter width $\Delta s = \sqrt{\Delta_x \Delta_y \Delta_z}$. The turbulent viscosity for momentum is calculated using a characteristic velocity and length scale:

$$\ell = \min\left[0.76 u_t \left(\frac{g}{\Theta_0}\frac{\partial \Theta^r}{\partial z}\right)^{-1/2}, \Delta s\right]. \tag{2.19}$$

The characteristic length scale ℓ takes into account the local stratification [Deardorff, 1980]. The characteristic velocity scale is modelled as the square root of the SFS turbulent kinetic energy $\sqrt{e}$, which is modelled using the transport equation for turbulent kinetic energy (TKE), where $e = 1/2Tr\{\mathbf{R}\}$. The SFS turbulence energy e is modelled using the equations below [Moeng, 1984],

$$\frac{\partial e}{\partial t} = -\nabla\cdot\left(\mathbf{u}^r e\right)^r - \nabla\cdot\left(\mathbf{u}^s e\right)^r - \frac{1}{\rho_0}\nabla\cdot\left(\mathbf{u}^s p^s\right)^r - \left(\mathbf{u}^s\mathbf{u}^s\right)^r : \nabla\mathbf{u}^r + \frac{g}{\Theta_0}\left(w^s\left(\Theta-\Theta_0\right)^s\right)^r - \epsilon. \tag{2.20}$$

The first three terms of the right hand side (RHS) are the transport terms, the fourth term on the RHS represents the exchange of energy between the resolved kinetic energy

and subgrid kinetic energy, as the same term appears in the dynamical equation for resolved kinetic energy with the opposite sign. The fifth term is the buoyancy production (through the Boussinesq approximation) term and finally, the sixth term ϵ is the rate of dissipation. All the resolved non-linear SFS terms: $\left(w^s\left(\Theta-\Theta_0\right)^s\right)^r$, $\left(\mathbf{u}^s e\right)^r$, $\left(\mathbf{u}^s p^s\right)^r$ and the dissipation rate ϵ must be modelled, details can be found in papers such as: [Deardorff, 1980], [Moeng, 1984] and [Khanna, 1995].

2.1.3 Boundary Conditions

To be able to numerically solve the continuity, momentum and potential temperature equations given in section 2.1.1, boundary conditions on velocity and temperature must be supplied on all the boundaries. The ABL is approximated as statistically homogeneous in the horizontal, thus it is appropriate to set the boundaries at the sides (x, y) as periodic. The boundary conditions on the top and bottom of the domain are in line with those used in [Moeng, 1984]. However, the boundary condition on the lower surface is a special case, due to the inclusion of the SFS stresses, (Eq. 2.11 and Eq. 2.14), the total shear stress vector and temperature flux perpendicular to the surface under each grid cell, must be provided as boundary conditions:

$$\text{Total shear stress vector: } \boldsymbol{\tau}_0^{tot} = C_D S_1 \mathbf{u}_{h_1}^r, \tag{2.21}$$

$$\text{Surface temperature flux: } \tau_{\theta_3}^{tot} = C_\theta S_1 \left(\theta_1^r - \theta_0\right). \tag{2.22}$$

Where subscript 1 implies the first grid level, $S_1 = |\mathbf{u}_{h_1}^r|$ is the magnitude of the horizontal resolve velocity components at the first grid level, where h implies horizontal components only, and C_D and C_θ are model constants that must be modelled.

To model C_D, the approach is to take the ensemble average then the absolute value of Eq. 2.21 producing, $|\langle\boldsymbol{\tau}_0^{tot}\rangle| = u_*^2$ so that,

$$C_D = \frac{u_*^2}{|\langle S_1 \mathbf{u}_{h_1}^r \rangle|}, \tag{2.23}$$

the numerator is area averaged mean surface stress magnitude (drag), and requires a model, that importantly incorporates the impacts of surface roughness. This so-called "drag model" typically uses an empirical form centred on Monin-Obukhov similarity theory [Moeng, 1984]. Similarly C_θ is derived by taking the ensemble average of Eq. 2.22 but not the absolute value since $\tau_{\theta_3}^{tot}$ is a scalar:

$$C_\theta = \frac{Q_0}{\langle S_1 \theta^r \rangle - \langle S_1 \theta_0 \rangle}, \tag{2.24}$$

where the surface temperate flux Q_0 is specified as a driving boundary condition, along with specification of the geostrophic wind.

2.1.4 Issues with Modelling the Atmospheric Boundary Layer

It is well known that LES generally does not predict law of the wall (LOTW) in the inertial surface layer in the rough surface ABL. LOTW is a scaling phenomenology based on the assumption that, in the equilibrium boundary layer at sufficiently high Reynolds numbers, only one characteristic length and velocity scale are relevant to scale the vertical average velocity gradient, where the average is over horizontal planes and in time, in the inertial surface layer adjacent to a hydro-dynamically rough surface. Under LOTW, the only length and velocity scale necessary to scale $\partial U/dz$ in the inertial surface layer are z and u_*, where U is average streamwise velocity, z is distance from the surface and u_* is the friction velocity, so that:

$$\phi_m(z) = \frac{\kappa z}{u_*} \frac{\partial U}{\partial z}. \tag{2.25}$$

Friction velocity is defined such that ρu_*^2 is the average of the surface shear stress.

LOTW implies that $\phi_m(z)$ should be constant in z through the inertial surface layer, and the von Kármán constant κ is found empirically to make $\phi_m = 1$. However, as initially pointed out in [Mason and Thomson, 1992], and many papers since, LES typically produces a well defined peak, or "overshoot", in the LOTW normalized average velocity gradient near the surface. A consequence of the overshoot is an over-prediction in the streamwise component kinetic energy and Reynolds shear stress, since the average velocity gradient enters the evolution equations for both as a source term. Furthermore, although the overshoot is associated with mean shear-rate in the neutral and moderately convective ABL, convection drive the errors vertically to change the entire ABL structure [Khanna and Brasseur, 1998].

By analysing a turbulent rough surface ABL and comparing to a smooth surface ABL [Brasseur and Wei, 2010] showed in a stationary, fully developed, high Reynolds number ABL, both in the smooth surface and rough surface an overshoot near the surface existed. In a smooth surface ABL the real overshoot is due to the real viscous length scale changing the LOTW scaling in the viscous layer. However, [Brasseur and Wei, 2010] discovered that a non-physical overshoot in LES of the rough surface ABL is in part due to the frictional content in the SFS stress model dominating the resolved turbulent stress at the first few grid levels, thus introducing a false viscous length scale denoted $l_{\nu\,LES}[m]$ interfering with the LOTW scaling. After comparing the total stress, which is a summation between the resolved turbulent stress and sub-filter-scale SFS stress,

$$\frac{\partial P}{\partial x} = \frac{\partial T_R(z)}{\partial z} + \frac{\partial T_S(z)}{\partial z}, \tag{2.26}$$

where $T_R(z) = \langle u^{r'} w^{r'} \rangle$ is the fluctuating resolved velocity components and the shear component of the mean SFS stress tensor Eq. 2.11 and $T_S(z) = \langle \tau_{13}^{SFS} \rangle$ is the SFS velocity components and shear stress component calculated from Eq. 2.20. When the

normalized SFS stress is dominating the resolved turbulence stress at the first few grid cells a false overshoot appears.

Using a pseudo-spectral LES ABL code [Brasseur and Wei, 2010] (BW10) designed a framework to systematically remove the spurious overshoot and satisfy the LOTW requirement $\phi_m \sim$ constant in the surface layer. A consequence of the BW10 theory, the aspect ratio of the grid and the model constant of the SFS stress model are adjusted to move the simulation into a particular supercritical region of the "$\mathfrak{R} - Re_{LES}$ parameter space". This parameter space is formed by representing each simulation as a point on a plot formed by three parameters: $\mathfrak{R} = [T_R/T_S]_1$, $Re_{LES} = z_i/l_{\nu\,LES}$ and N_δ/Δ_z. The first parameter $\mathfrak{R}$ is the ratio of resolved to modelled averaged shear stress (see section 2.1.2), The relative modelled contributions to vertical momentum flux, at the first grid level. The "LES Reynolds number" Re_{LES}, is the ratio of the boundary layer scale to a non-physical viscous scale resulting from the modelled LES viscosity in the eddy viscosity closure for the SFS stress tensor (see BW10). N_δ is the number of (uniformly spaced) grid points from the surface to the capping inversion, effectively the resolution of the grid in the surface layer. To capture LOTW, BW10 show that $\mathfrak{R}$, Re_{LES} and N_δ must exceed critical values, $\mathfrak{R}^* \sim O(1)$, $N_\delta^* \sim 50 - 60$ and Re_{LES}^* was estimated to be $\sim 300 - 400$. The aim is to systematically adjust the LES to place the simulation just into the supercritical region of the $\mathfrak{R} - Re_{LES}$ parameter space. BW10 further showed that, for eddy viscosity models, $Re_{LES} \sim N_\delta/D_t$ and $\mathfrak{R} \sim 1/D_t$, where $D_t = (AR)C_t^b$ for Smagorinsky and one-equation models, where C_t is the model constant and AR is the grid aspect ratio. Thus, by systematically adjusting the grid resolution and aspect ratio, and the model constant, it is possible to reduce or suppress deviations from LOTW and increase accuracy of wall-bounded boundary layers such as the ABL.

This framework was employed by BW10, [Vijayakumar, 2015] and [Jayaraman and Brasseur, 2021], and showed that LES could be systematically driven into the super-

critical $\mathfrak{R} - Re_{LES}$ region, with N_δ fixed, by systematically adjusting the grid aspect ratio primarily and, secondarily the SFS stress model constant. [Vijayakumar, 2015] and [Jayaraman and Brasseur, 2021] successfully applied the approach in a pseudo-spectral LES of the neutral and moderately convective ABL. [Vijayakumar, 2015] also repeated the same experiments with a 2nd order central differencing finite volume LES ABL code and consistently produced lower $\mathfrak{R}$ and Re_{LES} compared to the pseudo-spectral code, due to numerical dissipation and dispersion. However, the details by which numerical dissipation and dispersion interact with model dissipation (BW10), to the authors knowledge, have not been systematically studied and not well understood.

2.2 Actuator Line Method

The actuator line method (ALM), developed for modelling helicopter rotors, is applied to wind turbines in [Sorensen and Shen, 2002]. The ALM represents wings/blades as lines with discrete numbers of actuator points along the line. The ALM is two-way coupled with the computational flow computation. That is to say the forces calculated at the actuator points are projected onto the fluid flow and the fluid flow reacts to the actuator force. The velocity field from the computational domain is used to determine the aerodynamic force at the actuator points.

The flow field in the computational domain is solved using the Navier-Stokes (N-S) equations with appropriate boundary conditions and initial conditions. The influence of WT blades on the flow field is represented as a body force per unit volume, $\mathbf{f}_\epsilon$, in a localized volume surrounding each actuator point with characteristic length ϵ

$$\rho\frac{D\mathbf{u}}{Dt} = -\frac{1}{\rho}\nabla p + \mathbf{g} + \nu\nabla^2\mathbf{u} + \frac{1}{\rho}\mathbf{f}_\epsilon, \tag{2.27}$$

where $\mathbf{u}$ and p are local velocity and pressure and ρ, μ are fluid density and viscosity in incompressible flow.

The above is the N-S equation with the body force added as a momentum source term. The current research applied the filtered N-S equation for large-eddy-simulation coupled with the ALM. ALM has been implemented with direct numerical simulation (DNS) and unsteady Reynolds-averaged Navier-Stokes (URANS) as well.

The actuator force per unit volume spread over a volume $\sim \epsilon^3$ surrounding each actuator point, $\mathbf{f}_N$, is calculated using blade element (BE) theory. The BE approach splits a blade into discrete 2D airfoil sections with the actuator force per unit volume vector calculated using:

$$\mathbf{f}_N = \frac{1}{2}\rho U_{rel}^2 cW \left(C_l \hat{e_l} + C_d \hat{e_d}\right), \tag{2.28}$$

where U_{rel} is the relative velocity of the incoming flow in the frame of reference of the rotating airfoil section (see Figure 2-5), c is the chord length of the airfoil section, W is actuator element width, (C_l, C_d) are coefficients of lift and drag respectively with $\hat{e}_l$ and $\hat{e}_d$ denoting the unit vectors in the direction of lift and drag respectively. Defining z and θ as per Figure 2-5, the components of $\mathbf{f}_N$ are given by:

$$f_z = \frac{1}{2}\rho U_{rel}^2 cW \left(C_l \cos\phi + C_d \sin\phi\right), \tag{2.29}$$

$$f_\theta = \frac{1}{2}\rho U_{rel}^2 cW \left(C_l \sin\phi - C_d \cos\phi\right), \tag{2.30}$$

where ϕ is inflow angle (see Figure 2-5). C_l and C_d are obtained empirically using wind tunnel data from 2D airfoils as a function of angle-of-attack (AoA) α. In Figure 2-5 and using BE theory, U_∞ is incoming wind speed, Ω is angular velocity of the rotating blade sections, and θ_B is blade twist angle.

To project the singular actuator element forces on the 3D CFD mesh as a body force,

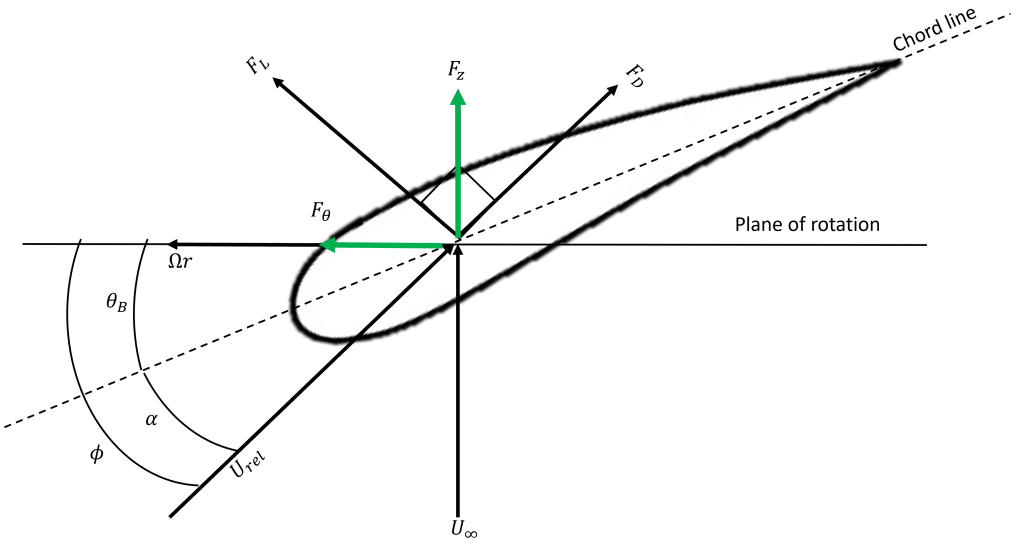

Figure 2-5: 2D airfoil Blade Element representation of the loads, velocity components and airfoil angles.

[Sorensen and Shen, 2002] introduced a function which, for this study will be referred to as the "body force projection function" η_ϵ:

$$\eta_\epsilon = \frac{1}{\epsilon^3 \pi^{\frac{3}{2}}} exp\left(-\left(\frac{\overrightarrow{x} - \overrightarrow{x_m}}{\epsilon}\right)^2\right), \tag{2.31}$$

where ϵ is the characteristic length scale of the body force projection function and $\overrightarrow{x} - \overrightarrow{x_m}$, $m = 1, ..., N$, is the vectoral distance between the point at which the body force projection function is applied (actuator element point) and the measured point on the CFD grid (see figure (2-6)). The purpose of the body force distribution function is to smoothly distribute the actuator element force across multiple CFD mesh points (see figure (2-6)) and avoid singularities in the body force [Sorensen and Shen, 2002], which could occur if the actuator element forces were to be directly applied to CFD cells as the actuator line is rotated through the CFD grid.

The body force projection function and the modelling approaches will be discussed in

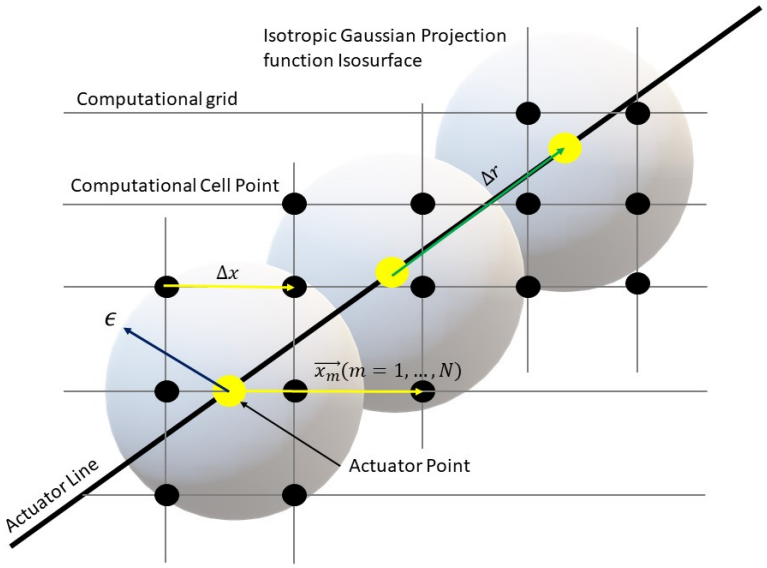

Figure 2-6: Projection of the Actuator element forces with isotropic Gaussian projection function onto computational mesh.

more detail later. The body force projection function given in Eq. (2.31) is an isotropic 3D Gaussian profile. After applying the isotropic Gaussian body force projection function around each actuator point, the net body force at each CFD grid point is the summation of all distributed actuator element forces that cross that grid point:

$$\mathbf{f}_\epsilon = \sum_{m=1}^{N} \mathbf{f}_N \, \eta_{\epsilon,\, N}. \tag{2.32}$$

The body force projection function spreads the actuator element force so that adjacent distributed actuator element forces can overlap one another, and multiple actuator point forces can contribute to the body force at a single CFD cell. [Churchfield et al., 2017] showed that the isotropic Gaussian projection function spread within spheres surrounding individual actuator points results in an effective cylindrical volume over which the body forces are spread surrounding the actuator line.

2.2.1 Blade Element Theory

The actuator force is a model of the force at an actuator along the blade. In the following section, the modelling assumptions, the implications of the assumptions will be discussed.

The actuator element force is modelled using a blade-element (BE) approach. From Eq. (2.29) and (2.30) the BE model requires six inputs: density of air (typically measured at a site or chosen from literature), relative velocity, lift and drag coefficients, inflow angle and angle-of-attack (AoA), α. The lift and drag coefficients for each 2D airfoil section at each of the actuator nodes are determined through the use of lookup tables (airfoil $C_l(\alpha)$, $C_d(\alpha)$ curves). The $C_l(\alpha)$, $C_d(\alpha)$ curves are calculated from steady uniform inflow wind tunnel tests. There are three approximations implicit with the BE model: the flow local to the airfoil section is quasi two-dimensional, steady and uniform and the inflow angle/AoA is well-defined. However, these approximations become questionable at some radial locations along the WT blade.

The relative velocity at each actuator point is computed from the computational domain typically using an interpolation scheme and the AoA is defined as the angle between the relative velocity vector at the actuator point and chord line (Figure 2-5). [Shives and Crawford, 2013] showed that there is an increase in the error of the computed angle of attack when there is insufficient grid resolution. Alternative velocity sampling methods have been proposed in the literature, [Churchfield et al., 2017] proposed an integral sampling method, and [Xie, 2021] proposed a Lagrangian average velocity sampling method.

2.2.2 Lifting Line Theory

Prandtl's lifting line theory is important to understand how it relates to the ALM. This section will briefly cover the key concepts in lifting line theory and show how it can be applied to the ALM to interpret results.

Lifting line theory assumes incompressible, inviscid 2D flows. The problem will be formulated for a finite wing which has been collapsed onto a straight line which could easily describe a WT blade. The flow is described a semi-infinite vortex sheet made of vortex filaments along the span [Chattot and Hafez, 2015] that is commonly denoted the bound vortex, which turns 90° and go to infinity in the positive x-direction.

The infinite array of vortex filaments with different circulation, form the bound vortex and trailing vortex sheet, the Kutta-Joukowski lift theorem tell us the bound vortex generates a lift/circulation distribution along the span of the blade.

$$F_L(y) = \rho U_\infty \Gamma(y), \tag{2.33}$$

where the cross product of the free-stream velocity U and the circulation at span y times the density of the fluid (air) ρ, is the lift per unit span [Wu, 2018]. In addition, the trailing vortex sheet induces a downwash a velocity component that is in the negative z-direction at the lifting line/bound vortex locations [Wu, 2018]. The downwash reduces the geometric angle of attack α_{geo}, so the effective angle of attack is:

$$\alpha_{eff} = \alpha_{geo} + \theta_B + \alpha_i, \tag{2.34}$$

where θ_B is any angle or twist of the wing and α_i is the induced angle of attack due to the downwash [Chattot and Hafez, 2015]. Skipping over some of the details, when the effect of the trailing vortices is integrated for a single point along the span y we yield the integro-differential equation of Prandtl [Wu, 2018]

$$\Gamma(y) = \pi U_\infty c(y) \left[\alpha_{geo}(y) + \theta_B(y) - \frac{1}{4\pi U_\infty} \int_{-\frac{b}{2}}^{\frac{b}{2}} \frac{\Gamma'(\eta)}{y-\eta} d\eta \right], \tag{2.35}$$

where the integro-differential is the induced angle of attack due to the trailing vortices

modifying the incoming velocity U_∞.

[Martínez-Tossas and Meneveau, 2019] reformulated the classical lifting line equations for ALM and showed the downwash calculated for a spanwise location depends on the characteristic length of the body force projection function ϵ. If the downwash is under-predicted the effective angle of attack and subsequently the circulation and thus lift force will be over-predicted. This can be clearly observed in [Martinez et al., 2012] where the power is over-predicted for larger ϵ. When the lifting line equations are reformulated for ALM it can be shown that the bound and trailing vortices have finite core sizes which scale on ϵ. If ϵ is too large this leads to the calculated trailing vortices to be "too weak" [Martínez-Tossas and Meneveau, 2019]. Consequently, the downwash is under-predicted and lift is over-predicted.

To accurately predict the forces along the span an ϵ needs to be chosen to ensure the trailing vortices have realistic core sizes, and thus effective angle of attack. Section 2.2.3 discusses the optimal size for ϵ.

2.2.3 The Body Force Projection Function

The body force projection function is a model of the force distribution surrounding the blades. In the following section, the modelling assumptions, the implications of the assumptions, and the choices of parameter selections, will be discussed. The body force projection function spreads the actuator element force per unit volume, over multiple CFD mesh points. In this study only the Gaussian function was employed.

[Sorensen and Shen, 2002] show that there are three key parameters that affect the actuator line method: the characteristic length scale of the Gaussian ϵ, computational grid spacing Δx and the actuator point spacing Δr (see figure 2-6). [Troldborg, 2009] studied the influence of ϵ with respect to the computational grid spacing Δx and found that larger $\epsilon/\Delta x$ smooths out oscillations in velocity along the blade. Their results suggested that $\epsilon/\Delta x \geq 2$ is necessary to avoid oscillations in velocity. However, studies

by [Jha et al., 2013] that applied the [Troldborg, 2009] rule of thumb found that optimal $\epsilon/\Delta x$ is dependent on the numerical scheme. Furthermore, it was noted that deviations from the expected results in the aerodynamic coefficients and AoA were most apparent at the blade tips and roots, where the two-dimensional BE approximation is strongly violated due to strong radial velocities. [Martinez et al., 2012] performed a sensitivity analysis on the parameters that affect the ALM. The sensitivity analysis showed that, as the computational grid is refined or as ϵ is increased, predicted power increases.

[Martinez et al., 2012] compared the axial velocity and AoA for different ϵ and grid refinements. Their results indicate larger ϵ and smaller Δx causes less axial induction along the span of the blade, increasing angle of attack and lift and drag coefficients. Thus, predicting an increase in the force on the blades and increased power output.

[Shives and Crawford, 2013] theorized that ϵ should be proportional to the local airfoil chord length c. Employing tests with simple analytical solutions (infinite span wing, finite span wing with constant and elliptical spanwise circulation distributions), the ALM solution and the analytical solutions were compared. The results showed that the error in the computed AoA depends significantly on the computational grid resolution. To maintain an error of less than 0.5° $\epsilon/\Delta x \geq 4$ was recommended. Furthermore, specifying $\epsilon/c = \text{constant}$, the ALM solution converged to the exact analytical solution as ϵ/c decreased. The ALM matched the analytical solution most closely for $\epsilon/c = 1/4$, while the root and tip continued to display a sharp spike in the downwash.

A sharp spike at the blade tip in the radially distributed loads has been observed in several papers, many papers have tried to improve the behaviour at the tip to what is believed to be correct. [Martínez-Tossas et al., 2016] showed using an optimized ALM ($\epsilon_c/c = 0.4$ and $\epsilon_t/c = 0.4$) (see section 2.2.3 for details), the behaviour at the tip is improved and the spike is removed. [Shen et al., 2005] and [Jha et al., 2014] have applied tip loss correction models to the ALM to correct the behaviour at the tip, which was shown to agree well with experimental data and removes the spike at

the tip. However, [Martínez-Tossas et al., 2016] argues a tip loss correction for the ALM is unnecessary if the optimized ALM is used. This is believed to be due to the tip vortices being highly resolved and the forces applied do not extend past the blade tips [Martínez-Tossas et al., 2016]. In addition, the experimental data used to compare against appears to not include a data point at the tip, therefore, it cannot be concluded that the behaviour predicted by the models is completely correct.

Several analytical approaches have been proposed to improve the accuracy of the Actuator Line Model (ALM). [Martínez-Tossas et al., 2017] compared the velocity field from a Gaussian force projection to the potential flow around a Joukowski airfoil. By minimizing the error between fields, optimal dimensionless parameters for the Gaussian width ($\epsilon^* = \epsilon/c$) and chordwise force location ($s_0^* = s_0/c$) were identified. These were found to be largely independent of angle of attack (AoA), with only weak sensitivity to airfoil camber and thickness.

[Jha et al., 2013] and [Jha et al., 2014] introduced an alternative method to define ϵ using a fictitious elliptic planform (c^*) and user-specified bounds. Their method, validated using the NREL Phase VI rotor, showed improved predictions—especially at blade tips and roots—compared to constant $\epsilon/\Delta x$ or ϵ/c formulations.

Recent studies have focused on using non-isotropic Gaussian functions with separate chordwise (ϵ_x) and thickness-wise (ϵ_y) length scales. [Martínez-Tossas et al., 2017] and [Martínez-Tossas et al., 2016] demonstrated that such elliptical distributions enhance accuracy, with optimal values of $\epsilon_c/c = 0.4$, $\epsilon_t/c = 0.2$, and grid resolution $\Delta x/c = 0.1$. These distributions better capture tip effects and flow features.

[Churchfield et al., 2017] extended this approach to include a third scale in the radial direction ($\epsilon_r = a_r \Delta R$), further improving agreement with experiments. Their non-isotropic Gaussian projections closely matched real blade-induced flow, including 3D effects like downwash. However, due to computational constraints, these methods were not employed in the present AMR-Wind simulations.

2.2.4 Improvements to the Classical Actuator Line Method

The literature is in fairly good agreement that $\epsilon/c = 0.25$ is the optimal choice for scaling the body force. Most recently, [Martínez-Tossas et al., 2017] showed $\epsilon/c = 0.25$ minimizes the error between the flow field calculated for a Joukowski airfoil using the ALM algorithm and the potential flow solution over a Joukowski airfoil. However, due to constraints on grid resolution and time step, practically $\epsilon/c = 0.25$ is not feasible for production runs that require long time periods (multiple eddy turnovers).

In a recent development [Martínez-Tossas and Meneveau, 2019] derives a sub-filter velocity correction method, implements in a LES code and tests over several finite wings with uniform, non-turbulent inflow. The method is denoted filtered lifting line correction (FLLC). The basis of the FLLC is to correct the velocity at each actuator point with $\epsilon = \epsilon_{comp}$, so the velocity at each actuator point matches that of a pre-selected $\epsilon = \epsilon_{mod}$; where typically $\epsilon_{mod} < \epsilon_{comp}$. The benefit to using a larger ϵ in the calculation allows for coarser grid refinements and larger time steps saving computational cost.

The formulation for the FLLC is derived from lifting line theory, which Section 2.2.2 explains, the downwash predicted depends on the size of ϵ. The correction step is:

$$\widehat{\mathbf{u}}\left(\mathbf{x}_i\right) = \widetilde{\mathbf{u}}\left(\mathbf{x}_i\right) + \left[u_y\left(z_i;\epsilon_{mod}\right) - u_y\left(z_i;\epsilon_{calc}\right)\right]\mathbf{j}, \tag{2.36}$$

which says the difference between the predicted induced velocities for the optimal epsilon and calculated epsilon ($\Delta u_y = u_y\left(z_i;\epsilon_{mod}\right) - u_y\left(z_i;\epsilon_{comp}\right)$), corrects the velocity at actuator point $\widetilde{\mathbf{u}}\left(\mathbf{x}_i\right)$ giving the velocity that ϵ_{mod} would give at the actuator point $\widehat{\mathbf{u}}\left(\mathbf{x}_i\right)$. Where x is in the direction of the incoming velocity, z is in spanwise direction along the length of the wing/blade and y satisfies the right hand rule.

The algorithm to calculate Δu_y is based on the reformulation of lifting line theory for

the actuator line method and is fully explained in [Martínez-Tossas and Meneveau, 2019].

For a fixed wing in a uniform inflow, [Martínez-Tossas and Meneveau, 2019] shows that for $\epsilon_{comp}/c = 0.25$ to $\epsilon_{comp}/c = 4$ with very fine grid resolutions, to avoid any numerical sensitivities, when the FLLC is applied the lift and drag integrated along the blade is independent of the choice of ϵ_{comp}/c, which is the desired outcome. The FLLC is a recent development and is compared with a classical ALM approach in Section 4.3 and then used in the simulations of the response of utility scale wind turbines to atmospheric turbulence.

2.2.5 Comparison of Actuator Line Method with alternative methods

In this section the actuator line method (ALM) is compared with the actuator disc method, blade element momentum theory and blade-resolved simulations.

Blade element momentum (BEM) theory, introduced in section 2.2.1, is a lower order method compared to ALM because it is only one-way coupled. One-way coupling means the aerodynamic rotor forces do not modify the flow field. Blade-resolved simulations, on the other hand, are a higher order fidelity method. Blade-resolved simulations model the boundary layer scales on a WT blade, this can be achieved in different ways. [Vijayakumar and Brasseur, 2019] developed a new hybrid URANS/LES turbulence model that works over an extraordinary range of length and time scales. An issue with turbulence models with WTs is the range of length and time scales that are required to be resolved (see Table(2.1)). In [Vijayakumar and Brasseur, 2019] multiple turbulence models were selected to work optimally at the different length scales and blended together.

[Lavely, 2017] studied the ability of BEM theory and ALM to capture the unsteady load response of WTs due to the passage of eddies in an ABL, compared to the blade-resolved model developed in [Vijayakumar and Brasseur, 2019]. The ALM and BEM

Table 2.1: Length and time scales in a blade-resolved atmospheric boundary layer simulation [Vijayakumar and Brasseur, 2019]. c - chord length. δ - height of the boundary layer attached to the blade.

	Time Scales	Length Scales
Integral eddies in the ABL	$\sim \mathcal{O}$ [minutes]	$\sim \mathcal{O}$ [10 m - 1000 m]
Tip vortex	$\sim \mathcal{O}\ (c/u_{rel})$ [seconds]	$\sim \mathcal{O}\ (c)$ [1 m - 5 m]
Boundary layer on blade	$\sim \mathcal{O}\ (\delta/u_{rel})$ [milliseconds]	$\sim \mathcal{O}\ (\delta)$ [0.1 mm - 1 mm]

theory capture the general trends of the aerodynamic forces and the integrated torque, however, both the ALM and BEMT lead the blade-resolved model in time and the variation of forces and integrated torque are larger. The time variations predicted by the ALM are in better agreement with the blade-resolved simulation compared with BEM theory, also indicated when the sectional blade forces (forces at different span locations) are examined. However, both ALM and BEM theory deviate further and further from the blade-resolved simulation as one moves inboard along the blade span. This is due to 3D effects becoming more prevalent at the inboard sections and ALM and BEM theory cannot accurately predict these highly unsteady effects.

The actuator disc method (ADM) is conceptually similar to ALM, but the difference is the rotor is modelled as a permeable disc, divided into elements, which applies a surface force onto the flow. A difference between ALM and ADM, ADM fails to capture the vortical structures due to the individual turbine blades [Martinez et al., 2012]. A further effect of ADM not being able to generate tip-vortices is an over-prediction of the power production. Predominately, the distributed loads along the blades are more accurately predicted using ALM compared to ADM [Tzimas and Prospathopoulos, 2016]. However, ALM is more computationally costly compared to ADM, as the ALM time-step is severely restricted. To maintain numerical stability the tip (fastest moving part of the blade) should not pass through more than a single computational grid cell each time-step [Martinez et al., 2012], thus, ALM is restricted by the rotor tip speed. Because the actuator disc does not rotate, typically the time-step is most often much less restrictive compared to the ALM.

2.3 Unsteady Aeroelastic Response of Wind Turbines

2.3.1 Unsteady aerodynamic response of wind turbines

There are several contributing factors that provoke an unsteady aerodynamic and unsteady elastic response on WTs. [Leishman, 2002] reviews the challenges in modelling the unsteady aerodynamics of WTs, amongst those were wake modelling, dynamic stall and tower shadow. The study of the unsteady response of airfoils has been motivated to reduce undesirable effects such as dynamic stall which leads to hysteresis in the aerodynamic lift and drag (Figure 2-7). Dynamic stall events result in stall delay on airfoils undergoing oscillatory or unsteady motion. Delay in stall, during increasing pitch, followed by strong stall produces much higher lift and large hysteresis in the loads likely reducing the fatigue life.

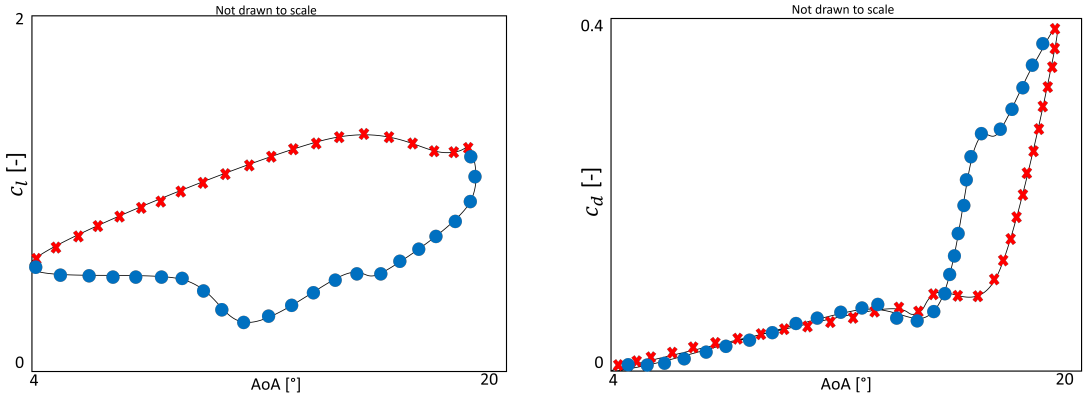

(a) (b)

Figure 2-7: Dynamic stall experimental data of aerodynamic coefficient predictions with AoA for $\alpha(t) = 120 + 80\sin(\omega t)$, $\kappa = 0.1$. Red crosses-upstroke, Blue circles-down stroke. Reconstructed from [Nandi et al., 2016].

A significant part of modelling the nonsteady loadings on WTs is predicting aerodynamic performance. [Simms et al., 2001] is a well cited report that compared results of a blind test, where experts submitted results predicting the behaviour of an extensively instrumented NREL WT rotor, which was operated under strict conditions in a wind tunnel. The results of the blind comparison showed significant scatter between the WT

modelling predictions, even under the supposedly "easy to predict" turbine operating conditions. The intent of the report was to help identify uncertainties associated with WT model predictions. [Simms et al., 2001] highlighted uncertainties in the predictions such as aerodynamic coefficients and root flap bending moment. However, these predictions are limited to the conditions in the wind tunnel and may not be representative of the conditions WTs actually face. An aim of [Simms et al., 2001] was to stimulate advancements in WT aerodynamic modelling.

[Muñoz-Simón et al., 2020] compared traditional BEM methods with vortex methods for WT flow. The accuracy of BEM was shown to be equivalent to the vortex methods under simple inflow conditions. However, under unsteady conditions such as the turbine yawed out of the direction of the average wind, the vortex methods surpassed BEM, in terms of being able to capture key flow physics and being able to estimate of the location of maximum and minimum loads during a blade rotation. Using the Beddoes-Leishman unsteady aerodynamics model incorporated into the AeroDyn [Moriarty and Hansen, 2005] subroutines, [Pierce, 1996] made comparisons between aerodynamic force coefficients for Reynolds numbers, Mach numbers and reduced frequencies appropriate to utility scale WTs and data obtained from the the Combined Experiment Rotor (CER). The load coefficients predicted by the Beddoes-Leishman model were found to be in good agreement with the experimental data over a range of reduced frequencies and angles of attack typical of WTs.

Advanced numerical models for computing unsteady aerodynamics of airfoils and WT rotors, using computational fluid dynamics (CFD) models have begun replacing BEM and other such methods discussed above, due to the lack of empirical inputs required [Hansen et al., 2006]. CFD methods routinely apply the Reynolds-averaged Navier-Stokes (RANS) equations and turbulence models such as $(k-\epsilon,\ k-\omega)$, to study nonsteady loadings on WT rotors. Due to the nature of RANS modelling it is unable to fully resolve the boundary layer at the airfoil surface, thus there are some discrepancies

between the standard turbulence models and experimental observations [Ekaterinaris and Menter, 1994] [Wang et al., 2010].

[Langtry et al., 2006] developed a correlation based transition model to more accurately predict the onset of transition from laminar to turbulent along an airfoil surface. The $\gamma - Re_\theta$ transition model was validated using the NREL Phase VI WT rotor. [Langtry et al., 2006] compared the $\gamma - Re_\theta$ transitional flow model against the SST turbulence model and experimental data. The transitional flow model was in good agreement with the experimental results and shows a significant improvement over the SST turbulence model especially at higher wind speeds. [Laursen et al., 2007] performed also compared the $\gamma - Re_\theta$ transition model with a fully turbulent setup. The results of the study are unable to conclusively show that the transitional flow model was more accurate than the fully turbulent model.

[Nandi et al., 2016] assessed the ability of a URANS based $k - \omega$ SST turbulence model and the $\gamma - Re_\theta$ transition model, to predict the boundary layer dynamics for a static and oscillating aerofoil dynamic stall regimes, likely to be experienced by WT blade sections, by comparing to data from wind tunnel experiments at the University of Glasgow [Sheng et al., 2006]. Results from [Nandi et al., 2016] indicate that the $\gamma - Re_\theta$ transition model is in better agreement with the static lift curve from the Glasgow experiments, notably near stall, compared to the fully turbulent SST model. However, delayed stall predictions were observed accompanied by over-prediction of lift in the $\gamma - Re_\theta$ transition model. For deep stall, the transition model predicts boundary layer events observed in the experiment more accurately than the SST turbulence model.

There is a strong focus on predicting aerodynamic quantities such as coefficients of lift and drag, and in particular during dynamic stall events, which has been highlighted as a deficiency in the current unsteady aerodynamic models. The consensus from the literature around the inclusion of dynamic stall model, transition model or turbulence models to capture unsteady aerodynamics of WTs is undecided. There is not enough

evidence to suggest empirically based models such as the Beddoes-Leishmann dynamic stall model will improve the accuracy of the WT calculation within the large-eddy simulation. The high-fidelity large-eddy simulation, two way coupled to the turbine calculation, should be sufficient to capture the non-steady response.

2.3.2 Unsteady Structural Response of Wind Turbines

To be able to determine the deformations, velocities and accelerations of WT components a structural model capable of computing the dynamic structural response of the entire WT is required. The time-varying loads calculated using aerodynamic models are discussed in section 2.3.1, and are prerequisites in the formulations of dynamic structural models. Fully 3D Finite-Element (FE) methods are considered the higher fidelity modelling tool for calculating WT structural responses and are useful for examining the internal stress distributions [Zhang and Huang, 2011] [Wang et al., 2016]. However, due to the computational expense fully 3D FE methods are not widely used in industrial applications [Zhang and Huang, 2011] [Wang et al., 2016].

In place of computationally expensive FE models 1D equivalent beam models have been developed. In 1D equivalent beam theory WT blades and the tower are represented as 1D lines in the direction of the largest dimension (along the length of the blade), with multiple nodes along the length. Linear beam models such as Euler-Bernoulli (classical beam model) and the Timoshenko beam model [Oñate, 2013] can be applied to the 1D beam to calculate the dynamic structural response. In order to discretize the blade into a series of 1D beam elements, three types of discretization methods are often used: modal approach, multi-body dynamics model and 1D FE method [Wang et al., 2016]. An overview description of the discretization models can be found in section 3.2 of [Wang et al., 2016].

Linear beam models carry the assumption of small deformations which is considered fair for WT blades, which are often treated as rigid. Rotors are often treated as rigid

to simplify the problem and address rotor aerodynamic response to complex inflow conditions. While this is a useful approach, as it removes aerodynamic effects due to the elastic deformations, WT blades are elastic deforming structures. [Dose et al., 2018] highlights some of the differences between rigid and elastically deforming blades on aerodynamic parameters such as power, thrust and sectional blade forces for a uniform inflow, at rated conditions without blade cone and rotor tilt and neglecting gravity. In the steady-state, (wake has developed far enough downstream and global quantities have sufficiently converged), the integrated quantities power and thrust were negligibly different due to the lack of periodic excitation's caused by gravity and non-uniform inflow [Dose et al., 2018]. This result was later replicated in [Trigaux et al., 2022] using an actuator line representation for the blades.

When the effect of gravity was investigated the simulation predicted almost identical values for power and thrust, averaged over one full rotor revolution, compared with the results without gravity. The main role of gravity loading is variations of the blade deformations over one revolution [Dose et al., 2018]. The effect of computing structural deformations along the blades were shown to result in deviations in the distributed blade loads, where the deviations increase with span location [Dose et al., 2018]. Similar results were obtained by [Trigaux et al., 2022] using an ABL precursor inflow condition in the turbine simulation. Additionally, [Trigaux et al., 2022] observed a significant phase shift is observed in the power and thrust with regard to the blades azimuthal position when comparing rigid and flexible blades.

There is a strong argument for modelling the structural deformations of WT rotors to accurately capture the time variations in the aerodynamic quantities. However, understanding the various contributions to the aerodynamic responses are only made more complex when structural deformations are included. Therefore, it is necessary to remove effects due to structural deformations to isolate effects due to the specified inflow.

Many structural codes have incorporated non-linear beam models (E.g. BeamDyn - OpenFAST) and there is a significant body of literature which investigates the effects of including large blade deflections in aeroelastic calculations, comparing linear and non-linear approaches. [Larsen et al., 2004] quantified the effects of large deflections. The results showed the flap and edgewise deflections displayed no significant difference between the linear and non-linear models, but the torsional rotation of the tip displayed a large difference between the linear and non-linear model. [Larsen et al., 2004] concludes the effects of large deflections cannot be completely neglected, however, regarding fatigue loads only minor differences appeared. [Larsen et al., 2004] normalises all variables to hide the distinguishing features of the WT, so it is unclear what size mega-watt turbine was used. As WTs have continued to grow the structures have become more flexible, which may require non-linear beam models to be employed to accurately predict the structural response.

[Panteli et al., 2022] analysed the DTU 10 MW rotor (radius 89.2 m) in isolation under a uniform flow (at rated wind speed 11.4 m/s), including gravity and tower shadow effect, comparing a linear and two non-linear beam models. Comparing blade root torsional moment at the blade tip, the linear model considerably under predicts the amplitudes of the variations of both the moment and the angle [Panteli et al., 2022]. While differences in the amplitudes of the variations of the blade root flap-wise moment, between the linear and two non-linear models, are not as severe, there are still significant differences displayed [Panteli et al., 2022]. Furthermore, the time series demonstrate that the linear model significantly over-predicts the moment amplitudes due to stall vibrations, while the two non-linear models predict very similar load response. [Panteli et al., 2022] suggests that there is a place for linear models, however, when instabilities do exist, the linear model is conservative as it omits the non-linear couplings that tend to suppress instabilities. For example: near rated conditions bending-torsion couple effects the pitching moment and linear models predict smaller loads [Panteli et al., 2022].

[Wang et al., 2014] discuss whether the small deflections assumption in linear beam theory is still applicable to modern day WTs, and believes it is no longer valid due to the highly flexible blade design. [Wang et al., 2014] investigates a novel non-linear aeroelastic model combining BEM theory and mixed-form formulation of GEBT (geometrically exact beam theory). The results showed good agreement with experimental data. Furthermore, comparing the tip deflection between the linear aeroelastic code in FAST [Jonkman et al., 2005], and the non-linear model used in [Wang et al., 2014], the non-linear code displays a significant reduction in the tip deflection. The applicability of linear beam theory due to the small deflection assumption must be carefully examined, due to the increasing size of WT rotor.

[Mo et al., 2015] performed a time domain aeroelastic analysis of the response of the NREL 5 MW WT, the results indicated that, vibrations on the blades modify the angle of attack, and has a significant effect on the aerodynamic loads, in agreement with the literature [Hansen et al., 2006] [Zhang and Huang, 2011]. Damping is required to suppress the onset of vibrations generated by the unsteady aerodynamic loads [Hansen et al., 2006]. However, from the literature it is understood there is an edgewise instability present in many pitch regulated WTs, due to a small and even negative aerodynamic damping for edgewise modes [Zhang and Huang, 2011] [Hansen et al., 2006]. It is generally accepted that due to non-linear effects the flapwise blade deflections cause the edgewise blade mode to couple to the torsional blade mode affecting the aerodynamic loads through the changes in the angle of attack [Kallesøe, 2011] [Mo et al., 2015] [Chaviaropoulos, 2001] [Kallesøe and Hansen, 2009]. [Kallesøe, 2011] investigates the importance of including the effects of non-linear geometric coupling in the aeroelastic response of WT. Using a second order non-linear beam model the damping of the first edgewise mode decreased by approximately $14m/s$. [Kallesøe, 2011] explained this was due to the flapwise deflection shifting sign, thereby the coupling between the edgewise and torsional motion also shifts, and thus, changing the non-linear geometric couplings effect on the aeroelastic damping contribution. This is

in agreement with work done by [Lindenburg and Snel, 2003].

An aero-servo-elastic test was undertaken comparing the response of the NREL 5 MW WT with ElastoDyn and BeamDyn, for a average wind speed of 12 m/s with turbulence. [Wang et al., 2017] showed excellent agreement in the root reaction forces and moments calculated by BeamDyn and ElastoDyn. However, noticeable differences in the tip-displacement time histories were present. [Wang et al., 2017] goes onto explain due to the simplifying features of the NREL 5 MW WT blade there is not much benefit to moving to the much more computationally expensive BeamDyn.

In summary, there are some differences in the non-linear models not captured by the linear beam methods. In the case of the NREL 5 MW WT the linear beam model ElastoDyn is a suitable model to calculate the structural response, while studying the time variations in the rotor aerodynamics to the effects of atmospheric turbulence. However, larger and more flexible turbines where torsional coupling is a major part of the response, non-linear models may be required.

2.3.3 Response of Wind Turbines due to the Passage of Large Eddies in the Atmospheric Boundary Layer

The former "cyber wind facility" (CWF) programme at Penn State University lead to the development of an OpenFOAM-based code with which a large-eddy simulation (LES) of the atmospheric boundary layer (ABL) is coupled to a hybrid URANS-LES OpenFOAM code that predicts ABL-induced flow around rotating wind-turbine blades while resolving the turbulent boundary layers over the blade surfaces. Using the LES, ABL modules of the CWF code, [Vijayakumar, 2015] quantified the nonsteady response of a WT in a moderately convective day time atmospheric boundary layer. [Vijayakumar, 2015] performed an analysis on a single rotating blade, the integrated moments (torque and out-of-plane bending moment) display ramp like structures. These rapid reductions and increases are in the range of 40-50% of the average, and [Vijayakumar,

2015] suggested these ramp like events are due to the internal variations in the atmospheric turbulence eddies. This is supported qualitatively when plots of the blade passing through these eddy structures at times at and around these ramps are examined.

[Churchfield et al., 2012b] performed a large-eddy atmospheric boundary layer simulation, similar to [Vijayakumar, 2015], but using the actuator line method to couple the fluid dynamics to NRELs FAST model, which was used to calculate the response of the WT. Periods of high frequency response in the rotor moments were qualitatively examined. In one of the cases examined, the inflow velocity contour plot shows the turbine rotor is partially covered by a low speed region and partially covered by a high speed region. As blades rotate through these high and low speed regions, the out-of-plane bending, and yaw moment display sudden increases similarly to the ramp like events in [Vijayakumar, 2015]. Additionally, [Churchfield et al., 2012b] observed the most significant loading event occurs when a very low-speed streaky structure interacted with the outer half of the rotor disk. The asymmetry of the velocity field at the rotor plane appears to be driving some of the high frequency content in the rotor moments.

[Churchfield et al., 2012b] also, explored the effects of atmospheric stability and surface roughness on wind turbine dynamics. Overall, the root-mean-squared out-of-plane bending hub moment, yaw moment at the hub and torque increase when surface roughness increases. [Churchfield et al., 2012b] also noted the streaky structures become more pronounced with higher roughness. Furthermore, the moments were also found to increase when atmospheric stability changed from globally neutral to unstable, although the increase is not as great as the increase when the roughness was changed. This indicates the the state of the atmosphere and the topographical features (such as surface roughness) change the response of the WT to the passage of atmospheric eddies.

[Nandi et al., 2017] analysed a $128s$ time series taken from a field experiment of a GE 1.5 MW WT in northwestern Germany. The data analyse were for a 2-3 hour

period in the early afternoon of the daytime ABL after the sun had reached its apogee. Furthermore, the data were selected from periods where the turbine was operating with constant rotor speed, fixed pitch and fixed yaw to avoid contaminating the data with turbine-induced variations. The relative velocity (see Figure 2-8a) and spanwise angle exhibit strong once-per-revolution (1P) periodicity, this is also the most dominant time scale/frequency present in the spectral plots. The dominant 1P frequency is reflected by a very sharp peak in the relative velocity (see Figure 2-8b) and spanwise angle spectra. This is in agreement with [Vijayakumar, 2015]. Furthermore, a larger time scale depicted in the envelope surrounding the peak to peak variations can be seen in the relative velocity (see Figure 2-8a) and spanwise angle time series which is registered in the spectral plots as a wide peak in the low frequency content. Lastly, a shorter time scale can be seen during every 1P cycle, which doesn't result in a distinct peak in the spectra. [Nandi et al., 2017] characterises four characteristic time scales from the analysis of the velocity components and angles. The eddy passage frequency, blade rotation frequency (1P), in between these two is a range of frequencies with depleted energy and sub-1P high frequency fluctuations. [Churchfield et al., 2012b] plotted the spectra for the rotor moments and found the turbine responds to a wide range of frequencies with the dominant being the 3P frequency and then higher harmonics of the 3P frequency, however, the eddy passage frequency is barely visible compared to the results seen in [Nandi et al., 2017].

[Vijayakumar, 2015] performed a spatial correlation between the local flow angle and the streamwise velocity fluctuations (refer to [Vijayakumar, 2015]). They found that the local flow and correlates extremely well with the streamwise velocity fluctuations, which is in agreement with [Nandi et al., 2017]. This suggests that the streamwise velocity fluctuations are causing most the fluctuations in the local flow angle along the blade, leading one to theorize that the streamwise velocity fluctuations are also causing most of the temporal load fluctuations. A coordinated analysis of WT response to day time atmospheric turbulence using BEM theory was undertaken by [Vijayaku-

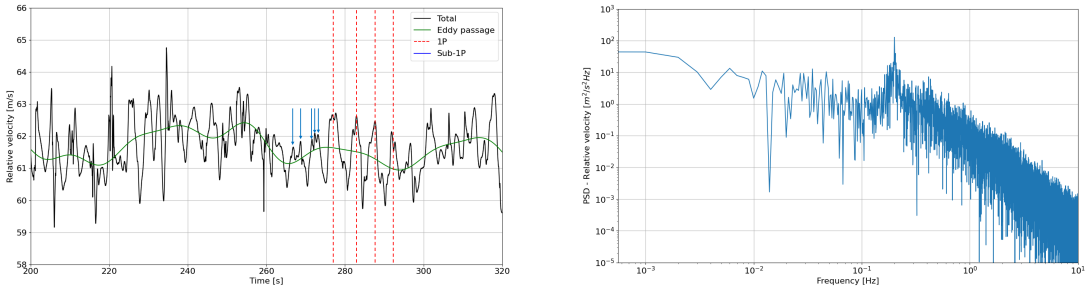

(a) (b)

Figure 2-8: Velocity magnitude from the 75% span location along a blade of the NREL 5 MW wind turbine from the LES ALM simulation (see Chapter 3.) (a) 120 s period highlighting the three characteristic time scales [Nandi et al., 2017]. (b) Spectra calculated from 1000 s period.

mar, 2015] and [Lavely, 2017]. The LES ABL modules in the CWF code were used to generate a precursor simulation, then planes of data from the LES ABL were used as inflow conditions to a BEM based code. Using the modelled horizontal homogeneity of the simulated ABL, 196 turbines were placed within in the domain, and time averaged once converged statistics were obtained. Using a threshold criterion, defined in [Vijayakumar, 2015], the loads on the WT were conditioned on the streamwise and vertical fluctuations and filtered into high, low, and "near average". The results showed that the WT responds to the streamwise velocity fluctuations more strongly than to the vertical velocity fluctuations. In addition, the average torque per unit span at the 75% span location, the average AoA, and the velocity magnitude were conditioned and filtered using the threshold criteria. The results indicate that the WT responds to the energy-containing eddies through the changes AoA and not the magnitude of the velocity vectors relative to the rotating blade.

The literature implies that fluctuations in the loads are correlated to fluctuations in the AoA. [Vijayakumar, 2015] investigated the correlation between the torque per unit span, plotted along the span of the blade, with surrogate AoA, velocity magnitude and boundary layer separation point. The correlation coefficient between surrogate AoA and torque, in the outer 70% of the blade, was calculated as approximately 0.9. In a

further analysis, [Vijayakumar, 2015] found the sectional load fluctuations compared well with surrogate AoA in the outer 32% of the blade. This is likely because the inboard 50% of the airfoil sections primary role is to provide structural support and not support the aerodynamic lift. Furthermore, it was found that the inner 50% of the blade experiences larger fluctuations in AoA compared to the outer sections. This was attributed to unsteady aerodynamic effects [Vijayakumar, 2015] [Nandi et al., 2017].

Using the actuator line model for the NREL 5 MW wind turbine in a canonical daytime ABL, [Lavely, 2017] developed a measure to quantify the "level" of asymmetry in the streamwise velocity over the rotor disk:

$$\delta U_{xT} = max\left(|u_{x'}\left(r,\theta\right) - u_{x'}\left(r,\theta+\frac{2\pi}{3}\right)|,\, |u_{x'}\left(r,\theta-\frac{2\pi}{3}\right)|\right) \tag{2.37}$$

$$I_A = \iint_A r\left(y,z\right)\delta U_{xT} dA. \tag{2.38}$$

The "asymmetry parameter" (Eq. 2.38) was used to show that out-of-plane bending moments on the low speed shaft caused off-design motions of the gearbox, due to velocity asymmetry across the rotor plane. Denoted the "asymmetry parameter" the maximum velocity difference of three points $+/-120°$ from a point at some radial and azimuthal location on the rotor disk is calculated using Eq. 2.37 and then is integrated over the rotor disk area (Eq. 2.38). The time changes in the asymmetry parameter was found to be extremely well correlated with the time changes in the out-of-plane bending moment on the low speed shaft, indicating the temporal characteristics in nonsteady out-of-plane bending moment variations are driven by the characteristics of the time variations in asymmetry in the rotor-normal velocity over the rotor disk. [Lavely, 2017] also showed the rotor-average wind speed is exceptionally well correlated to the torque and thrust, while being extremely poorly correlated with out-of-plane bending moment and asymmetry.

[Churchfield et al., 2012b] hypothesised that the blade root moments are correlated with the inflow velocity. A two point correlation between the blade root out-of-plane bending moment, yaw moment, torque and the streamwise velocity component was performed in [Churchfield et al., 2012b]. The blade root out-of-plane bending moment and torque was discovered to be well correlated with the inflow velocity, but the yaw moment was poorly correlated. It was reasoned that the yaw moment responds to asymmetry in the flow field at the rotor plane. Whereas, results presented in [Churchfield et al., 2012b] appear at odds with [Lavely, 2017], [Churchfield et al., 2012b] correlates individual blade root forces and moments, while [Lavely, 2017] correlates hub forces and moment. Which indicates the mechanisms driving the rotor forces and moments, which are the combination of the time variations from all three blades, are fundamentally different to the mechanisms driving the time variations on the individual blades.

In summary research using the codes developed within the CWF showed WTs respond strongly to three characteristic time scales present in the day time turbulent ABL; the time scale associated with the passage of eddies, rotor passing frequency and sub 1P frequencies. WTs have been shown to respond most strongly with streamwise velocity fluctuations, more than the vertical, and the load variations are shown to be largely due to the variations in the AoA. In the outer 50% of the blade, where 3D effects are not strong, average wind speed at the rotor plane can be used as a predictor for torque and thrust. Lastly, asymmetry created by the passage of coherent eddy structures is shown to be well correlated with the out-of-plane bending moments. There is evidence to suggest that specific repetitive time variations in the loads due to the passage of highly energetic turbulence eddies in the atmospheric boundary layer, may be responsible for potential damage modes on WT drive trains in particular WT MBs.

2.4 Wind Turbine Main Bearing Function and Failures

The aim for this section is to give a general description of WT MBs, WT MB design and WT MB operation as described in the literature. Next, potential failure mechanisms/modes as pertaining to rolling element bearings are reviewed. Following, statistical studies relevant to WT component failures are examined to argue whether there is an increase in WT MB failures. Primarily, the aim of this section is to discuss potential drivers of MB failures/damage in the literature.

2.4.1 Wind Turbine Main Bearings

Rolling element bearings are simple in construction, and seemingly simple in design. Bearing assemblies include an outer-ring, cage, rolling elements, inner-ring (see Figure 2-9) and placed in a housing. The primary function of a rolling element bearings is to support a rotating shaft, restrict the number of degrees of freedom of the shaft to rotation along its primary axis and potentially allow some translation in the direction of the primary axis.

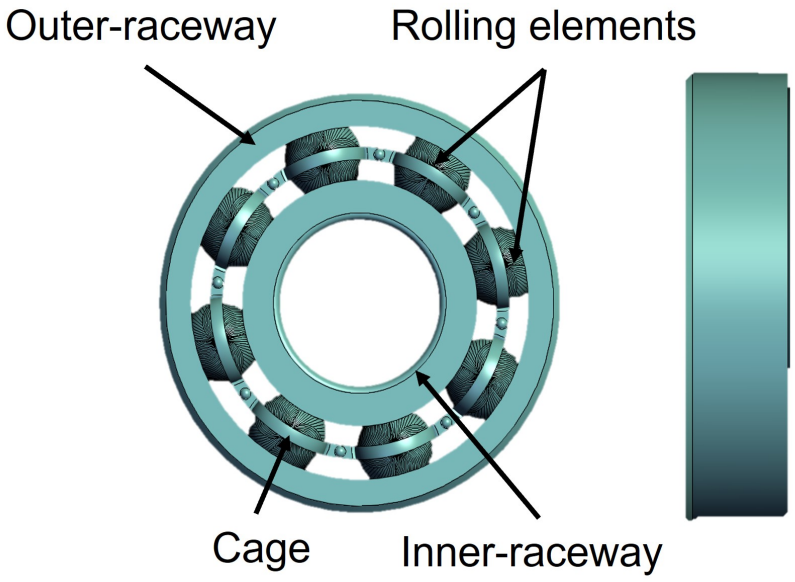

Figure 2-9: Generic bearing diagram.

Rolling element bearings are simple in construction, however, there are variations in the design, which includes the type of rolling element used such as: spherical roller bearings (SRBs), tapered roller bearings (TRBs) and cylindrical roller bearings (CRBs) (see Figure 2-10), also two rows of rolling elements can be installed in a bearing (double-row). Furthermore, WT drive trains can have different configurations: three-points/single MB (MB), four point suspension/double MB layouts. Different bearings have different load carrying capabilities; therefore, it is common to see a combination of bearings being installed. WTs with gearboxes typically typically will use a locating DSRB for the rotor-side bearing, and a SRB, CRM or DTRB as the generator-side bearing [Hart et al., 2020].

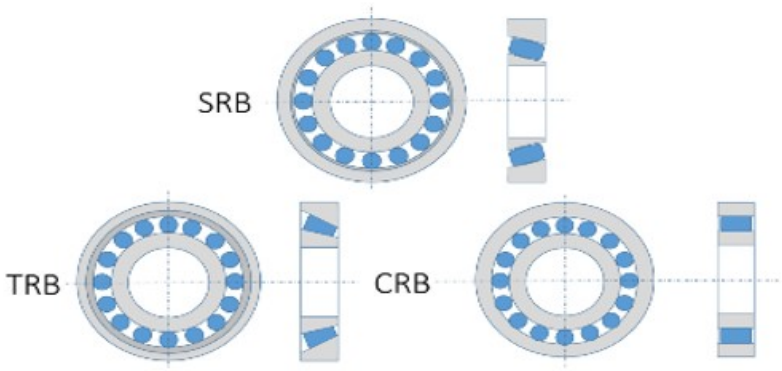

Figure 2-10: Bearing rolling element types. A single row is only shown for each. [Hart et al., 2020].

Rolling element bearing operation is seemingly simple, however, WT MBs operate in a wider envelope than what might be typical for bearings. Modern day utility scale WT MBs operate under variable speed, ramping up and down, from stationary to rated rotational speed of the turbine. Furthermore, WT rotors experience complex 3-dimensional time varying loading, which is passed down the main shaft and reacted by the MB. One of the primary loads at the main shaft is the rotor weight, the MB supports the overhung weight moment primarily in the radial direction, but can include some axial component dependent on the drive train tilt angle.

[Hart et al., 2019] investigated the relationship between WT MB loads and deterministic characteristics of the incident wind field for a 2 MW WT. Hub loads were extracted from a fully aeroelastic multi-body simulation, where the turbulent wind field was modelled using the Kaimal spectrum. MB reaction loads were calculated using a static load balance model, from the extracted hub loads. Time averaged axial and radial loads were analysed for 10 m/s, 12 m/s, 16 m/s and 20 m/s hub height wind speeds, at low, medium and high turbulence intensity ([International Electrotechnical Commission, 2019]), 0.2 and 0.6 shear exponent.

Interestingly, the time averaged radial load did not respond strongly to changes in hub height average wind speed compared to the time averaged axial load which was found to be most sensitive to changes in the hub height average wind speed. The time averaged radial loads were found to be most sensitive to shear, but opposed to what one expects, the lower shear exponent resulted in higher time averaged and peak radial loads. Higher shear was found to have a lifting effect on the rotor, thus, in a time averaged sense the MB experiences a reduction in the radial load. This lifting effect was also observed in [Kenworthy et al., 2024]. The results of [Hart et al., 2019] showed there are strong links between MB loads and deterministic characteristics of the incident wind field, however, the synthetic turbulence modelled using the Kaimal spectrum may not fully represent the loads atmospheric turbulence would produce. Therefore, some of the effects due to true atmospheric turbulence eddies are not captured in this study.

[Hart, 2020] studied time varying loads experienced by WT MBs, using a similar framework presented in [Hart et al., 2019]. 10 minute MB radial load time histories of a 1.5 MW WT were analysed, and repeating looping patterns were discovered to exist in the time histories of the radial load trajectories. To assess the relative importance and potential impacts of these identified structures on bearing rollers, an internal load model for double-row spherical roller bearings is also developed. The identified looped structures are shown to be only 2.4 seconds, the MB experiences either full or partial

load loops 40 - 50% of its operational time and the loop area appears to give an indication of the size of the roller load fluctuation. This discovery showed MBs experience highly fluctuating radial loads in both magnitude and direction, which could contribute to surface fatigue of WT MBs.

Modern day utility scale WTs use a variable speed, collective pitch control strategy. The function of a WT controller is to maximise power, which is achieved by varying the rotor speed below the rated wind speed, minimise operational loads, through pitching the blades to shed load and maintaining a relatively constant rated power at above rated wind speed, and minimise actuator activity [Burton et al., 2011]. The influence of the controller has been shown to strongly impact the response of structural components including the MB [Hart et al., 2022c].

Rolling element bearings commonly use a lubricant to maintain separation and reduce contact pressure between the rolling elements and the inner and outer raceways, dissipate heat which isn't of the most importance in WTs which operate at relatively low rotational speeds [Hart et al., 2020] and corrosion protection. The lubricant is forced between the roller and the raceway during rolling or sliding which creates a hydrodynamic pressure and a lubricant film to separate the contact surfaces and reduce the contact pressure [Halme and Andersson, 2010]. The ratio between the oil film thickness and the surface roughness during contact is used to categorize the degree of separation between the contacting surfaces [Halme and Andersson, 2010]. The degree of separation/lubrication mechanism has a strong impact on the bearing life and damage mechanism which is reducing the bearing's operational life [Hart et al., 2020] [Kenworthy et al., 2024] (see sections 2.4.3 and 2.4.5).

SCADA (Supervisory Control and Data Acquisition) is placed on WTs to monitor the condition of various components such as the MB to more accurately predict when maintenance or a full replacement is required. This aims to avoid catastrophic failures and reduce downtime, therefore, contributing to a lower cost of energy. Common

condition monitoring devices/techniques include accelerometers for vibration analysis, temperature probes on the housing and testing the lubricant periodically for contaminants. [de Mello et al., 2021] gives a good example of how MB temperature can be used effectively to anticipate MB damage and predict failure, if the natural variations that contributed to an increase in temperature, such as changes in rotor speed, power and wind speed are delineated [de Mello et al., 2021].

In the analysis of vibration signals commonly, a set of so-called characteristic features such as signal root-mean-squared value, frequency component amplitudes or statistical moments are extracted which are then used to relate the signal to previous operating data or known fault cases [Hart et al., 2020]. This is well shown in [de Mello et al., 2021], the damaged bearing shows additional peaks in the energy spectra corresponding to the first three harmonics of the ball-pass-frequency on the outer raceway [de Mello et al., 2021]. However, WT MBs are components which operate at low speeds and high loads. [Hart et al., 2020] explains this has the effect of making them less sensitive to vibrations. Hence, making analysis of vibration signals less reliable than in high-speed and moderately loaded cases.

Condition monitoring techniques are continuing to develop and with the aid of machine learning will become more and more reliable in detecting the onset of bearing wear and fatigue. However, condition monitoring currently does not provide a way forward to determine the root cause of these premature WT MB failures.

2.4.2 Wind Turbine Main Bearing Design

WT MBs operational life can be estimated through the rating life assessment as presented in [International Electrotechnical Commission, 2019] and [International Organization for Standardization, 2007]. [International Organization for Standardization, 2007] specifies methods of calculating the “basic dynamic load rating”, “basic rating life” and “modified rating life” for bearings with commonly used high quality material,

good manufacturing quality and with conventional operating conditions. The life of an individual rolling bearing is the operational duration (given in units of time or number of revolutions), before the first evidence of fatigue develops in the material [International Organization for Standardization, 2007]. The "basic life rating" for a population of bearings is the value for the "life" which 90% of the population are expected to attain. [International Organization for Standardization, 2007] defines the "modified rating life" similarly but accounting for non-conventional operating conditions, including bearing fatigue load, lubrication and contamination. However, there are studies which employ different approaches to the rating life assessment to estimate MB fatigue life [Zheng et al., 2020] [Liang et al., 2013] [Loriemi et al., 2021].

The basic life rating developed by Arvid Palmgren takes the form:

$$L_{10} = \left(\frac{c_D}{P_{eq}}\right)^{p_e}, \tag{2.39}$$

where L_{10} is the basic life rating given in millions of revolutions, p_e is the load life exponent; this is a result of fitting pre-1940's bearing failure data to Palmgren and Lundberg bearing life model [Harris, 2001]. $P_{eq} = XF_r + YF_a$ is the equivalent applied bearing load. Constant load under which a rolling bearing would have the same life as it would attain under the actual load conditions [International Organization for Standardization, 2007]. Where the coefficient values (X and Y) depended on the type of bearing, its nominal contact area and the ratio F_a/F_r. F_a is axial load and F_r is radial load. c_D is the "basic dynamic load rating", constant load at which a rolling bearing can theoretically endure for a basic rating life of one million revolutions [International Organization for Standardization, 2007] (i.e. $L_{10} = 1$). The basic dynamic load rating can be calculated from [International Organization for Standardization, 2007] or is more typically provided by the bearing manufacturer.

The "modified life rating" is given by:

$$Lnm = a_1 a_{ISO} L_{10}, \tag{2.40}$$

where the "modified life rating" L_{nm} can consider the rating life corresponding to different levels of survivability through the modification factor a_1. Formulae presented in [International Organization for Standardization, 2007] allows one to calculate the modification factor a_1 to change the proportion of the population expected to survive, by considering a Weibull distribution other levels of survivability can be obtained [Kenworthy et al., 2024]. The modification factor a_{ISO} seeks to account for effects such as lubrication, contamination levels and bearing load limit, and is given by:

$$a_{ISO} = f\left(\frac{e_C C_u}{P_{eq}}, \frac{\nu}{\nu_1}\right), \tag{2.41}$$

where C_u is the bearing's fatigue load limit and can be thought as the load below which the bearing will not fatigue. A bearing's fatigue load limit is typically supplied by the bearing manufacturer or, alternatively calculated from semi-empirical formulae given in [International Organization for Standardization, 2007]. e_C is the contamination factor, there are five levels of contamination specified in [International Organization for Standardization, 2007] ranging from "high cleanliness" to "very severe contamination". Equations for e_C given in [International Organization for Standardization, 2007] all have the same form but the coefficients changes with the level of contamination. ν is the kinematic viscosity of the bearing lubricant, which is specified via a lookup table as a function of operating temperature. ν_1 is a reference kinematic viscosity, below which the rating life is reduced and above which the rating life is extended [Kenworthy et al., 2024]. Formulae are given for the reference kinematic viscosity in [International Organization for Standardization, 2007].

[Kenworthy et al., 2024] provides a detailed summary and discussion on the rolling element bearing life assessment presented in [International Organization for Standard-

ization, 2007] and [International Electrotechnical Commission, 2019]. [Kenworthy et al., 2024] recognizes there are significant uncertainties/short comings in the applicability of the ISO standards to rolling element bearings of the size used in utility scale WTs. In the review of [International Organization for Standardization, 2007], [Kenworthy et al., 2024] suggests the inclusion of the fatigue load limit in the a_{ISO} modification factor may lead to over-predictions of the rating lives, because results from fatigue experiments for through-hardened AISI 52100 bearing steel does not support the existence of a fatigue limit for through-hardened AISI 52100 bearing steel [Zaretsky, 2013] [Shimizu, 2009]. Other issues [Kenworthy et al., 2024] highlights are the validity of the load life exponent, the influence of inclusions and effect of the level of lubrication. For a complete account of the rolling bearing rating life assessment review see [Kenworthy et al., 2024] Section 2.

[International Electrotechnical Commission, 2019] requires wind energy generation systems to a equal or exceed a design life of 20+ years, this includes the bearing modified rating life of 90% survivability. In context with [International Organization for Standardization, 2007] an equivalent bearing load (P_{eq}) representative of the loads over those 20 years needs to be computed. [International Electrotechnical Commission, 2019] provides a set of design load cases (DLCs), where load time histories are generated for each of these cases. For analysing fatigue of the MB the most relevant DLC is 1.2, wherein normal power production simulations are undertaken across the wind speeds between turbine cut-in and cut-out [Kenworthy et al., 2024]. The design methodology [International Electrotechnical Commission, 2019] requires that an aeroelastic code is used for the specific design calculations that includes a WT controller. The wind field must include a constant average wind (cut in - cut out) with turbulence, represented by the Kaimal model or other model specified in [International Electrotechnical Commission, 2019]. The resultant time load histories need to be combined in some manner to produce a single equivalent load. Neither [International Electrotechnical Commission, 2019] nor [International Organization for Standardization, 2007] specify how to

combine the time histories into a single equivalent load. However, the linear damage rule (Palmgren-Miners rule) is a commonly used approach to accommodate variable operating conditions [Kenworthy et al., 2024] [Zaretsky, 2013] [Harris, 2001]:

$$\sum_{i=1}^{i=n} \frac{N_i}{L_i} = 1, \tag{2.42}$$

refers to the proportion of the bearing life that has been consumed under condition i, damage is assumed cumulative under the Palmgren-Miners rule and failure occurs when the summation reaches unity or more specifically when the summation reaches unity 10% of a population of bearings have failed. The are limitations and uncertainties associated with the generation of the time load histories and particularly the linear damage rule. These include the use of medium fidelity modelling and kinematic turbulence in the aeroelastic simulations. Kinematic turbulence is representative of "real" turbulence up to second order statistics but does not contain true turbulent-eddy structures [Kenworthy et al., 2024]. Also, linear damage accumulation is a significant assumption and the validity of which is likely to change depending on the conditions experienced and the levels/nature of the variability [Kenworthy et al., 2024]. For a detailed explanation on the implementation of the linear damage rule in the bearing life assessment see [Kenworthy et al., 2024].

2.4.3 Wind Turbine Main Bearing Failure Mechanisms/Modes

There are several damage mechanisms/modes relevant to WT MBs, failure modes can be interactive and overlapping. The damage mechanisms most relevant to MBs are **rolling contact fatigue** (RCF) which is separated into subsurface and surface initiated and **wear** which is separated into abrasive wear and adhesive wear [Hart et al., 2020]. Abrasive wear is closely coupled to surface-initiated fatigue and is recognized as a major mode of failure for bearings [Ai, 2001]. Particles can get pulled under the rollers causing surface indentation. These surface indents act as local stress raisers during

post-indentation over-rolling [Ai, 2001], which is discussed below. Adhesive wear is the transfer of material from a surface that is accelerating or skidding to another surface.

RCF in a MB can be summarised as the generation of stress and plastic deformation as a result of the rollers loading and unloading the inner and outer raceways, eventually leading to the formation of cracks and progressively worse spalling. Which are cavities formed on a rolling surface.

Failures due to RCF can be due to sub-surface-initiated mechanisms, or surface initiated mechanisms such as dents, surface roughness, inclusions and insufficient lubrication [El Laithy et al., 2019]. Under optimal operating conditions: properly lubricated, no misalignment, lubricate free of contaminates, moisture, and corrosives, and loaded within the design specification - RCF is then considered to be the most likely damage mechanism [Harris, 2001]. Friction and therefore lubrication regime is known to determine the position of the maximum shear stress [El Laithy et al., 2019] [El-Thalji and Jantunen, 2014], this is important because during events that generate high friction, such as under slip/sliding, the location of maximum shear stress moves towards the surface and this is thought to increase the probability of surface-initiated cracks [El Laithy et al., 2019]. However, under rolling with acceptable lubrication, the maximum shear stress moves away from the surface due to lower friction [El Laithy et al., 2019], increasing the probability of sub-surface-initiated cracks.

In the literature the process of surface-initiated RCF is generally broken down into 5 stages.

Stage 1: running in - surface roughness from manufacturing breaks off/gets smoothed out as the rollers roll between the inner and outer raceways. Therefore, the residual stresses are induced with increase in material strengthening and micro yield stress [El-Thalji and Jantunen, 2014] [El Laithy et al., 2019]. However, [Halme and Andersson, 2010] states the running in process can be restarted by changes in operational conditions. [Halme and Andersson, 2010] suggests under unfavourable conditions, the time

to failure is accelerated with abrasive wear being the primary failure mechanism which leads to early failure.

Stage 2: steady-state - considered the healthy stage in the lifetime of the bearing [El Laithy et al., 2019], it is expected that the vibrations due to rolling are at their lowest [Halme and Andersson, 2010], and it is believed that surface-initiated fatigue accumulation during the steady-state stage is negligible, since the surfaces are deformed elastically by the rollers [El-Thalji and Jantunen, 2014]. It is understood that the operating conditions will determine the length of the steady-state stage and the transition to stage 3 [El-Thalji and Jantunen, 2014] [El Laithy et al., 2019] [Halme and Andersson, 2010].

Stage 3: defect initialization - there are three main indentation mechanisms that may lead to wear or surface-initiated RCF becoming the primary damage mechanism: contamination particles, lubrication disturbances and impact events [El-Thalji and Jantunen, 2014]. Different contamination particles have been shown to cause different damage mechanisms, brittle particles break up and cause abrasive wear, whereas, ductile particles larger than the lubricant film thickness indent the surface leading to surface-initiated RCF [Dwyer-Joyce, 1993] [Ne´ lias and Ville, 2000]. The evidence shows that indentation geometry is impacted by the particles size, material type, fracture toughness, hardness level and lubrication film thickness [Dwyer-Joyce, 1993] [Ai, 2001] [Ne´ lias and Ville, 2000].

Stage 4: crack initiation - the indentations formed due to contamination particles, lubrication disturbances and impact events form leading edge and trailing edge asperities. These asperities act as stress raisers and the crack initiation process will have the sufficient stress intensity factor to start the process [El-Thalji and Jantunen, 2014]. Over-rolling, adhesive and abrasive wear have been shown to alter the asperities (well-known as “smoothening” phenomenon [El-Thalji and Jantunen, 2014] [Gao et al., 1999]) and potentially extend the surface-initiated fatigue life but could lead to

increased wear, because of abrasive wear occurring at the leading edge asperity, due to the collapse of the local lubrication film thickness around the indentations [El-Thalji and Jantunen, 2014] [Gao et al., 1999].

Stage 5: Crack propagation - there are three well-known mechanisms that drive crack propagation: shear stresses, fluid pressurisation and fluid entrapment which refers to fluid becoming trapped in the crack and as the rollers seal the crack the fluid pressure results in a significant increase in stress at the crack tip [El-Thalji and Jantunen, 2014].

2.4.4 Statistical Examination of Wind Turbine Main Bearing Failures and Replacements

Very few papers provide statistical data on the failure rates of MBs due to wind farm operators being reluctant to provide their proprietary data. [Sethuraman et al., 2015] was one of the only papers to provide data on MB failures. The data suggests the WT MB failure rate is at a level that is unacceptable to wind farm operators, a substantial number do not reach their design lives of 20 years and some failing in less than 6 years [Sethuraman et al., 2015].

To the authors knowledge, [Hart et al., 2023] and [Pulikollu et al., 2024] are the only other papers which has analysed failure data on WT MBs. The data obtained is from wind farm operators includes 167 wind power plants (7,707 WTs), or 15.3 GW of capacity [Hart et al., 2023] and 60 GW of capacity including 40 operators, 526 wind farms and 27831 turbines [Pulikollu et al., 2024].

[Hart et al., 2023] plots the wind plant age against the total number of MB replacements as a ratio of number of turbines in the wind plant. The data shows many wind plants are replacing 10% of the turbines MBs on or before 20-years, and a wind farm reached the 10% replacement level at approximately 7 years. 10% replacement at 20-years is an important milestone, as bearing designers typically design WT MBs so that 10% or less of a bearing population should fail/be replaced due to rolling contact fatigue

within 20-years of operation (see Section 2.4.2).

[Hart et al., 2023] plotted survivability of the population of MBs against time and [Pulikollu et al., 2024] plotted failure probability against time, both can estimate the time for a proportion of the bearing population to be replaced in that time, or the time taken for a proportion of the bearing population to be replaced. The curves predicted the time for 10% of the bearing population to be replaced is 10.5 years which is almost half the desired 20 years [Hart et al., 2023] [Pulikollu et al., 2024]. Furthermore, the proportion failed/replaced at 20 years, the curves predicted 20 - 25%.

2.4.5 Potential Drivers of Main Bearing Failures

The data available would lead one to conclude a significant proportion of MBs in WTs are failing well before their 20 year design life. However, it is unclear where research efforts should be directed to identify the root cause(s) of premature failures in WT MBs.

Damage reports collected from wind farm operators, which categorises the damage type and location of damage on the MB reported spalling to be the most prominent damage type, which is closely linked to surface- and subsurface-initiated rolling contact fatigue [Hart et al., 2023] [Pulikollu et al., 2024]. Which suggests that rolling contact fatigue may be contributing in part to the MB failures. However, the results presented in [Kenworthy et al., 2024], which went through a case study to calculate the modified rating life, showed in most conditions the estimated MB modified rating life was significantly above the 20 year design life. Which suggests rolling contact fatigue is not a dominant driver in premature MB failures, however, it is equally likely that the rating life assessment methods are unable to provide realistic rating life predictions meaning rolling contact fatigue is still a possible failure mechanism. [Hart et al., 2023] reached a similar conclusion from the failure data.

In [Kenworthy et al., 2024], [Yucesan and Viana, 2019] which studied the impact of

operating conditions; these included: bearing temperature, wind field characteristics, lubricant viscosity and contamination levels on the modified rating life. [Kenworthy et al., 2024] [Yucesan and Viana, 2019] showed temperature, which affects the viscosity of the bearing lubricant (see Section 2.4.2), and contamination are key sensitivities to the modified rating life. While [Kenworthy et al., 2024] showed shear and turbulence levels in the wind field did not strongly influence the modified rating life. Maintaining sufficient lubrication film thickness is essential for the health of rolling element bearings. Insufficient lubrication leads to surface damage which can lead to surface-initiated rolling contact fatigue [Hart et al., 2023] [Pulikollu et al., 2024] [Wu et al., 2023].

To maintain adequate separation between surfaces the minimum film thickness should be a minimum of three times greater than the combined (root-mean-square) roughness of the contacting surfaces [Hart et al., 2022a] (i.e. operate in the elasto-hydrodynamic regime). However, under starved conditions, where there is not an adequate supply of lubricant hence, the film thickness decreases increasing the likelihood of surface damage. Decreasing the regreasing interval is suggested to improve the service life [Pulikollu et al., 2024] [Yucesan and Viana, 2019], however, decreasing the regreasing interval may only mitigate the damage rather than addressing the root cause.

The minimum film thickness can also be affected when there are rapid changes in the loads causing an increase or decrease in entrainment speed (velocity of the lubricant). During a rapid loading or unloading the contact patch of the roller rapidly increases or decreases respectively resulting in an augmented entrainment speed [Hart et al., 2022a] [Venner and Wijnant, 2005] increasing or decreasing the minimum film thickness respectively. The important distinction that must be made is rapid changes in the loads, only become important when the changes in the load occur at times faster than the time it takes a particle of lubricant to pass through the contact area is $dF/dt \leq t_c$. Another, threshold used in the literature is when the ratio between the expansion or contraction of the load zone and the entrainment speed is greater than or equal to 25% non-steady

effects can be considered important [Hart et al., 2022a] [Hooke, 2003] [Venner and Wijnant, 2005].

$$\frac{|db_c/dt|}{\tilde{u}}(\times 100\%) \leq 25\%. \tag{2.43}$$

However, [Hart et al., 2022b] found for loads obtained from an aeroelastic simulation, the ratio of the rate of change of the contact patch in the rolling direction to the entrainment velocity (Eq. 2.43) were an order of magnitude smaller than the critical percentage. However, for the rate of change in transverse direction da_c/dt there is a significant number of operating points where the critical percentage was exceeded.

Failure data suggests wind plant age, and infant mortality are not playing a major role in the failure rates observed [Hart et al., 2023] [Pulikollu et al., 2024]. Suggesting instead site conditions, maintenance practices and technological changes are the more likely candidates. Site conditions typically are described by the average wind speed, shear exponent and turbulence intensity. [Hart et al., 2022c] showed that load fluctuations at the MB rollers were small at $U = 4$ m/s average wind speed and shear exponent $\alpha_s = 0.1$ and increased as wind speed and the shear exponent increased. Veer, defined as a change in the wind direction in the clockwise rotation with height, was observed significantly increasing the load fluctuation magnitudes, while the average load levels remained relatively unchanged [Hart et al., 2022c]. [Kenworthy et al., 2024] showed predicted rating life is only slightly affected by changes in turbulence level, with a slight reduction under higher turbulence and a slight increase for lower turbulence. Suggesting that the principal driver of predicted rating life under [International Organization for Standardization, 2007] is the average load experienced by the MB. This is consistent with the low sensitivity observed between rating life and turbulence level, since kinematic turbulence mostly influences fluctuations rather than the average value.

With the current trend of WTs being designed with larger and larger rated powers, hub heights and rotor diameters, there are several challenges that have been highlighted in the literature that could limit progress such as: social, logistical, economic and technical challenges [McKenna et al., 2016]. [Veers et al., 2023] points to a lack of understanding of the interactions between the atmospheric flow and the WTs being a critical area of research which requires further research. Furthermore, [Pulikollu et al., 2024] found an an increase in the failure rate when comparing 1.5 - 2 MW WTs with 2 - 6 MW rated WTs. The increase in the failure rate could be for a myriad of issues, such as design and manufacturing issues, however, the root cause could be related to increased levels of fluctuations related to an increase in the rotor diameter and the interactions between the WT blades and the atmospheric turbulence. [Hart et al., 2022c] investigated the influences of the deterministic wind field characteristics on the MB load patterns for scaled 5 MW, 7.5 MW, and 10 MW reference WT models. Similar relationships between the average loads, load fluctuations and the deterministic wind field characteristics were observed for the three WTs. However, average loads and load fluctuations increased approximately cubically with the turbine rotor radius [Hart et al., 2022c].

[Cardaun et al., 2019] hypothesised WT yaw misalignment, a strategy to "steer" WT wakes to increase average power production of downwind WTs, may increase load variation, thus increasing damage accumulation on the drive train. The effect of damage accumulation, due to "wake-steering", was studied by extracting loads at the MB, using a similar multi-body simulation model used in [Hart, 2020] and [Hart et al., 2022c], for yaw misalignment's of $-10°$ to $+10°$. To quantify the damage accumulation at the MB, [Cardaun et al., 2019] first calculates load time series as per [International Electrotechnical Commission, 2019] then calculates the damage equivalent load (DEL) according to DIN 50100 for each yaw misalignment. Using DEL to quantify damage accumulation appears to be a sensible approach, however, [Kenworthy et al., 2024] discuss the use of linear damage accumulation and express concerns whether linear damage accumulation is valid for MBs.

[Cardaun et al., 2019] shows the damage equivalent loads associated with the out-of-plane bending moments M_y, M_z and the in-plane force F_y are sensitive to yaw misalignment. Furthermore, it was found that the change of load due to yaw misalignment's is not symmetrical [Cardaun et al., 2019]. [Hart et al., 2022c] found that yaw angles primarily change the average load levels, and fluctuations are significantly less affected. Which may indicate DEL are largely affected by the average load compared to the fluctuations, which is in agreement with [Kenworthy et al., 2024].

The literature supports the need for study which characterises and quantifies the effects of turbulence, and the nonsteady loadings which create time changes at the MB, which could underlie the premature failures (see Section 1.2 for specific objectives of the research program).

Chapter 3

Methodology

In this chapter a neutral boundary layer is developed, and our choice of grid resolution, advective scheme and one-equation model constant, on the accuracy of the LES of the neutral ABL, is investigated using the framework developed in [Brasseur and Wei, 2010]. The results of the investigation are used to inform the design of a precursor moderately convective boundary layer (MCBL). The MBCL is characterised and verified against existing literature. Lastly, aeroelastic calculations of a utility scale wind turbine within the precursor MCBL are described and choices justified.

3.1 Development of a Large-Eddy Simulation of a Neutral Atmospheric Boundary Layer

The code used in the development of high fidelity large-eddy simulations of the ABL is the open-source code AMR-Wind, where AMR stands for adaptive mesh refinement. AMR-Wind is a finite-volume based algorithm second order in space and time. The code is massively parallel, uses a block-structured adaptive-mesh, and is an incompressible flow solver for WT and wind farm simulations. The solver is built on the AMReX library that provides the mesh data structures, mesh adaptivity, and the solvers used

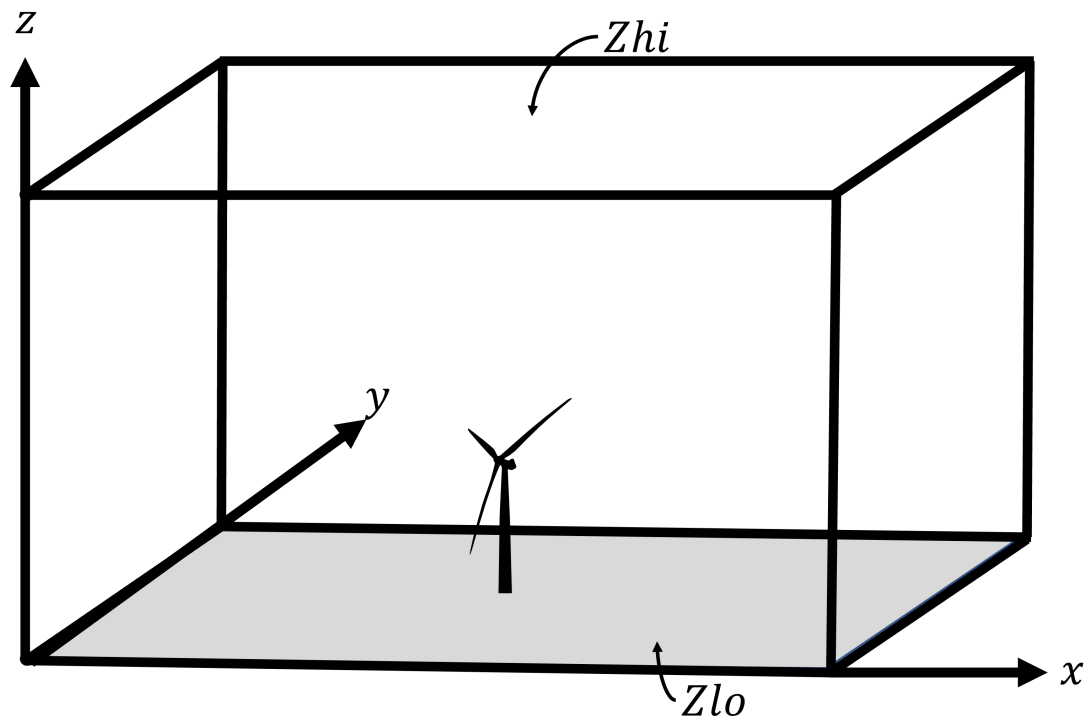

Figure 3-1: LES ABL computational domain with wind turbine. Where *Zhi* refers to the top boundary, and *Zlo* refers to the bottom boundary of the domain.

for solving the governing equations [ExaWind Project, 2025]. AMR-Wind discretizes and numerically solves the incompressible filtered Navier-Stokes equation and filtered potential temperature equation in section 2.1.1. The numerical scheme that advances the solution in time is a type of Godunov predictor-corrector scheme. Details of the algorithm are described in [Almgren et al., 1998].

Several options for advective schemes have been implemented within AMR-Wind: piecewise linear method (PLM), piecewise parabolic method (PPM) with limiters, PPM-nolim (without limiters), weno-js and weno-Z (weno-weighted essentially non-oscillatory). The models for the sub-filter scale (SFS) stress tensor in the filtered momentum equation available in AMR-Wind are the Smagorinsky model and one-equation model. Details of sub-filter scale stress models can be found in section 2.1.2. The one-equation model was applied throughout the simulations performed during the studies,

as this model has been commonly used in LES studies of the ABL and is designed for nonequilibrium dynamics.

AMR-Wind uses the maximum in the mean potential temperature gradient, $\partial\Theta/\partial z$, to define the height of the capping inversion, where the mean is estimated as an averaged over horizontal planes. The initial mean potential temperature profile is set by the user in the initial conditions. In the initial conditions, solenoidal fluctuating velocity components and potential temperature with prescribed variances are applied over the first few grid cells from the surface. The predicted fluctuations evolve to fill the domain through the capping inversion and to the upper domain, at which point the solution evolves towards a stationary turbulent ABL. In the stationary state, the mean potential temperature decreases linearly from the surface to a minimum at the capping inversion. This minimum is often used as a measure of the capping inversion. Therefore, as the simulation evolves from the initial condition, we can track the minimum potential temperature flux height relative to the peak in the mean velocity gradient. When the heights are approximately coincident, the ABL can be considered to be fully formed. The minimum potential temperature flux height, as a measure of the capping inversion height, is only applicable for an ABL with non-zero surface heat flux.

The ABL is simulated for 20000 s or approximately 10.5 eddy turnovers (see Figure 3-3). Figure 3-3 shows the evolution of τ_u for the case using the weno_z algorithm and aspect ratio (AR) = 0.8. There are two eddy turnover times associated with ABLs: $\tau_u = z_i/u_*$ characterises surface shear and $\tau_w = z_i/w_*$ characterises buoyancy. Since there is zero surface heat flux in a neutral ABL, turbulence production due to buoyancy is zero. Thus, τ_u characterises the eddy turnover time in a neutral ABL. The evolution of a neutral boundary layer is illustrated in Figure 3-2, and shows the initial condition (Figure 3-2a) to the final time step (Figure 3-2f) where the calculation is fully developed neutral atmospheric boundary layer. In the neutral ABL calculations the surface temperature flux is set to zero, which can be verified as the temperature

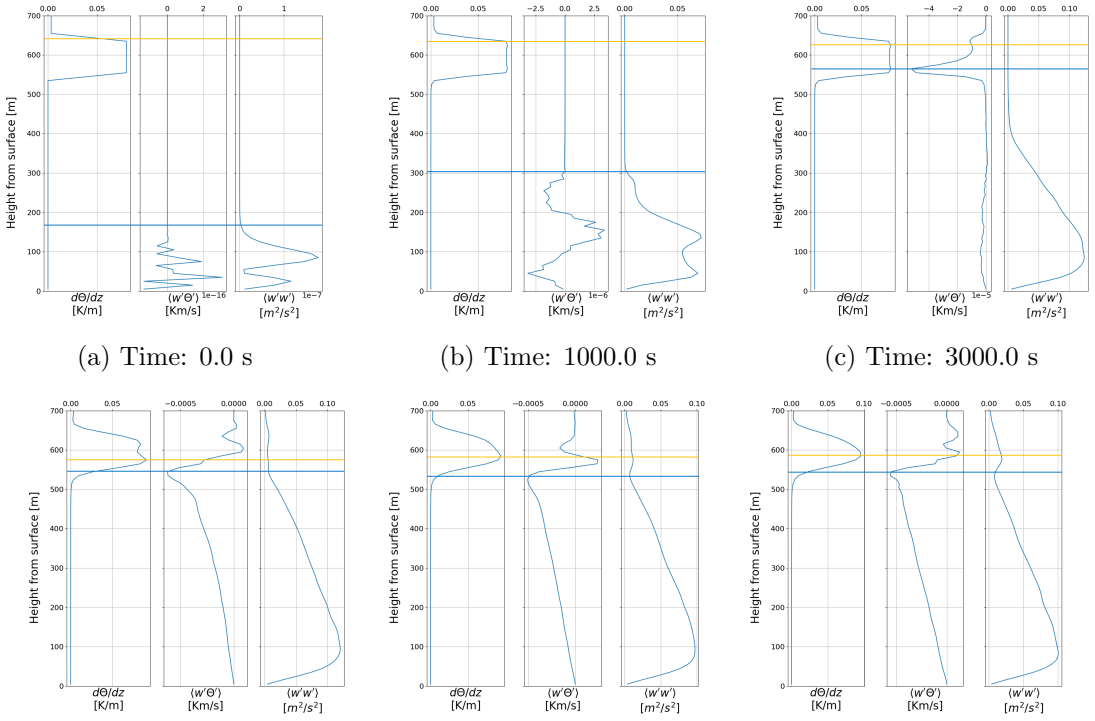

(a) Time: 0.0 s (b) Time: 1000.0 s (c) Time: 3000.0 s

(d) Time: 9000.0 s (e) Time: 15000.0 s (f) Time: 20000.0 s

Figure 3-2: Development of a neutral atmospheric boundary layer from time = 0.0 s to 20000 s. From left to right in each sub-figure: average potential temperature gradient, ensemble averaged vertical temperature flux and average fluctuating vertical velocity variance. Horizontal orange line is the peak in potential temperature gradient (capping inversion). Horizontal blue line is the vertical development of vertical velocity variance.

flux profiles (middle plots) in Figure 3-2 show the temperature flux at the surface is zero. The profile of the temperature flux is shown evolving in time, however, the y-axis indicates the changes in the temperature flux profile over time are very small. Figure 3-3 indicates quasi-stationarity is reached after approximately 15000 s or 7.5 eddy turnovers. Global quantities such as z_i, $-L$ and u_* are time averaged over the final 5000 s or 2.5 eddy turnover times of the simulation. Quasi-stationarity was confirmed by quantifying the growth of the boundary layer, rate of change of the friction velocity (characteristic surface layer velocity scale driven by mean shear-rate) and rate of change of the eddy turnover time associated with the friction velocity τ_u.

Table 3.1 describes the geometric and inflow input parameters used in the development

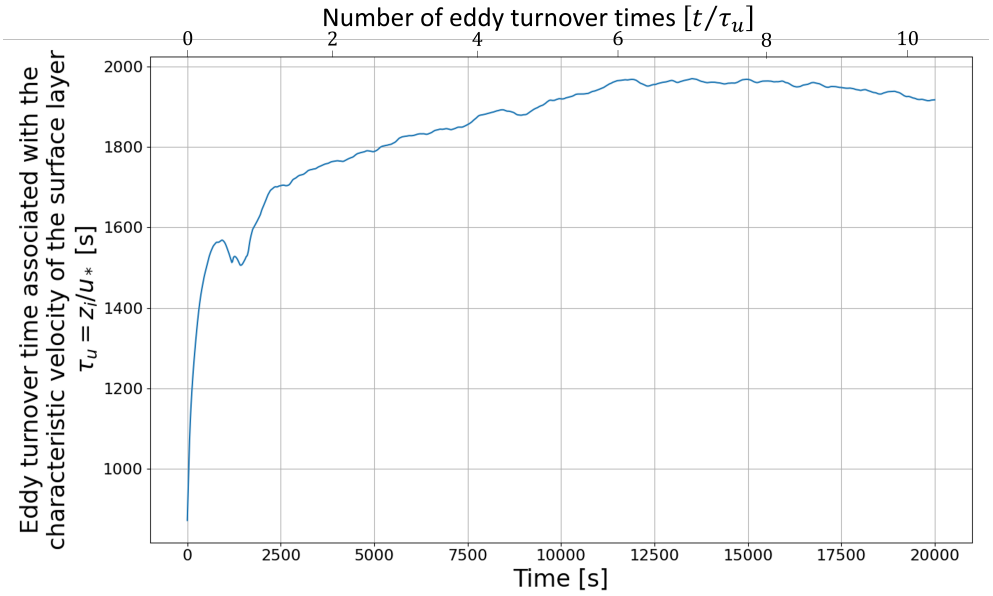

Figure 3-3: Evolution of the eddy turnover time associated with the characteristic velocity of the surface layer $\tau_u = z_i/u_*$, from a simulation using: weno_z, AR = 1.0, neutral boundary layer (NBL).

of high fidelity large-eddy simulations of the atmospheric boundary layer. The domain had to be chosen to satisfy the blocking factor of 8 used by the AMRex library; i.e., the domain must be exactly divisible by the blocking factor. A CFL number of 0.95 was chosen firstly, because it ensures efficient time stepping to reduce the computational cost of each simulation, and secondly the CFL could be chosen on the larger side because the Godunov scheme is capable of maintaining stability with large CFL numbers.

Table 3.1: Description of neutral LES ABL geometric and inflow input parameters.

Domain $[m]$	$5120 \times 5120 \times 1920$
CFL number	0.95
Uniform inflow velocity $[m/s]$	$[10.0, 0.0, 0.0]$
Geostrophic wind velocity $[m/s]$	$[10.0, 0.0, 0.0]$

In developing an optimised computational framework for high resolution LES's of the ABL, several neutral boundary layers were compared using the configuration given in Table 3.1. As discussed above the temperature profile must be supplied to initialize the calculation as well as several other parameters given in Table 3.2. Furthermore, velocity

fluctuations, defined in Table 3.2, are added to initialize the calculation. In AMR-Wind velocity fluctuations in the horizontal are added to the calculation as sinusoidal waves with period x and fluctuation amplitude y up to a reference height z, where perturbations decay above this height.

Table 3.3 summarizes the boundary conditions applied to the boundaries depicted in Figure 3-1. The boundary conditions used follow those used in the literature [Brasseur and Wei, 2010] [Khanna, 1995] [Moeng, 1984].

Table 3.2: Description of neutral LES ABL initial conditions.

Reference temperature $[K]$	300.0			
Height z [m]	0.0	550.0	650	1920.0
Temperature [K]	300.0	300.0	308.0	312.05
Surface Temperature flux [Km/s]	0.0			
Velocity Fluctuations				
Number of sinusoidal waves in x-direction	20			
Number of sinusoidal waves in y-direction	20			
Amplitude of fluctuations in x-direction [m/s]	1.0			
Amplitude of fluctuations in y-direction [m/s]	1.0			
Reference height for velocity perturbations [m/s]	50.0			

Table 3.3: Description of neutral LES ABL boundary conditions.

x	Velocity Temperature	Periodic
y	Velocity Temperature	Periodic
Zhi	Velocity	Slip wall
	Temperature	Fixed gradient = 0.0032 [K/m]
Zlo	Velocity	Wall model (See section 2.1.3)
	Temperature	Fixed gradient = 0.0 [K/m]
	Turbulent kinetic energy	Fixed gradient = 0.0 [m/s^2]

The coordinate system used by AMR-Wind will be referred to as the "global coordinate system" denoted by a subscript x and is illustrated in Figure 3-1. The "global" velocity vector components are defined in the global coordinate system illustrated in Figure 3-1. However, because of Coriolis acceleration, the mean velocity vector (projected on a horizontal plane) is not aligned with the x direction of the global coordinates. As

illustrated in Figure 3.1, the angle between the mean velocity vector and x is $\phi(z)$ that changes with height (see Figure 3-12e). The new coordinate system, denoted "stream-aligned coordinate system", is define such that x' is aligned with the mean velocity, $z' = z$ and y' completes the right-hand-rule. The mean velocity vector is derived from the following expression

$$\mathbf{u}_{x'}(z) = \mathbf{u}_x(z) \begin{bmatrix} cos\phi_c(z) & -sin\phi_c(z) & 0 \\ sin\phi_c(z) & cos\phi_c(z) & 0 \\ 0 & 0 & 1 \end{bmatrix}, \tag{3.1}$$

where the mean velocity vector $\mathbf{u}_{x'}$ is denoted by the subscript x' and the streamwise velocity refers to the components of the mean velocity vector in the x' direction.

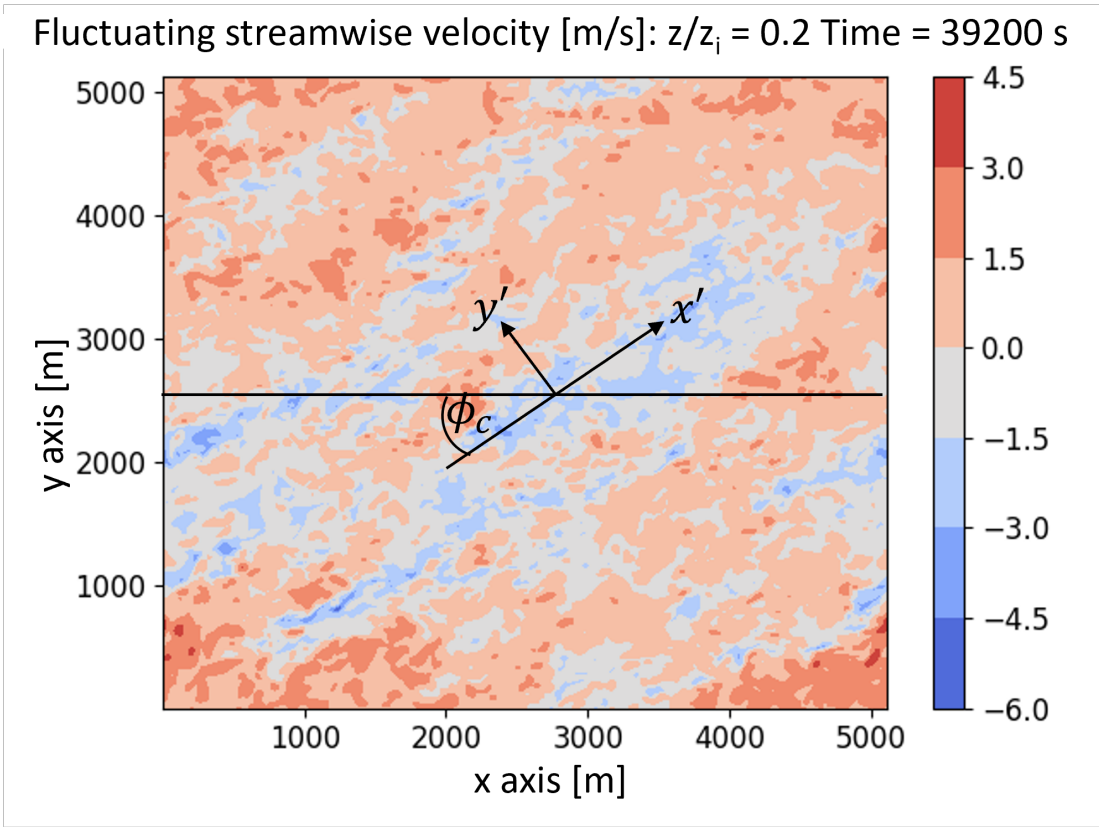

Figure 3-4: Isocontour of a horizontal $x-y$ plane illustrating the global coordinate and $x'-y'$ mean velocity vector components.

3.2 Effect of Aspect Ratio and Numerical Dissipation on Deviations from the Law of the Wall in Large-Eddy Simulations of Neutral Atmospheric Boundary Layers

In developing a highly resolved and accurate LES of an ABL, we must take into account well-known inaccuracies in LES predictions of the surface layer, the lower 20% of the ABL, typically 200 m - 400 m from the surface, where utility scale wind turbines operate. The difficulty of LES predictions, in the surface layer, is towards the surface the resolution of the effective grid deteriorates due to under-resolution of integral-scale eddies as they decrease in scale towards the surface, together with increasing relative levels of model and numerical friction. Using the framework developed in [Brasseur and Wei, 2010], several cases were run to study the effect of systematically reducing the aspect ratio, by increasing the resolution only in the horizontal, on the deviation from LOTW, while the resolution in the vertical and the one-equation model constant were held constant. A further study was undertaken to investigate the effects of numerical friction, arising from the choice of the advective scheme and one-equation model constant.

The atmospheric boundary layers were simulated using the configuration described in Section 3.1. In this section the neutral ABL is analysed because the inaccuracy due to the overshoot is strongest with neutral stability, and has typically been studied in neutral boundary layers [Brasseur and Wei, 2010] [Vijayakumar, 2015]. While buoyancy is a prominent turbulence generation mechanism, the moderately convective ABL is somewhat less susceptible to the overshoot than the fully shear-dominated neutral ABL. Therefore, any results established for the neutral boundary layer are directly applicable to moderately convective boundary layers. However, buoyancy strongly enhances turbulence transport in the vertical, transport that can advect the errors due to the overshoot vertically and potential impact the entire ABL structure [Khanna and

Brasseur, 1998].

In the following studies a similar framework to [Brasseur and Wei, 2010] was employed to optimise the grid structure. The grid aspect ratio was systemically reduced, and in accordance with [Brasseur and Wei, 2010] the simulation is plotted on the "$\mathfrak{R} - Re_{LES}$ parameter space", where $\mathfrak{R}$ is the ratio of the resolved stress to SFS stress, and Re_{LES} is an effective "LES" Reynolds number given by the ratio of boundary layer depth to an "LES length scale" (see section 2.1.4). Four aspect ratios, two advective schemes and two one-equation model constants were used. The global parameters of the eight cases, using the advective schemes weno_z and ppm_nolim, are given in Table 3.4 and Table 3.5.

Table 3.4: Global parameters of weno_z cases.

	weno_z			
Grid cell Aspect ratio	1.0	0.8	0.66	0.6
Grid resolution	512×512×192	640×640×192	512×512×128	1000×1000×192
z_i [m]	595.4	594.8	600	594.0
$-L$ [m]	inf	inf	inf	inf
u_* [m/s]	0.31	0.31	0.31	0.31
w_* [m/s]	0.0	0.0	0.0	0.0
Q_0 [Km/s]	0.0	0.0	0.0	0.0

Table 3.5: Global parameters of ppm_nolim cases.

	ppm_nolim			
Grid cell Aspect ratio	1.0	0.8	0.66	0.6
Grid resolution	512×512×192	640×640×192	512×512×128	1000×1000×192
z_i [m]	587.6	587.2	592	586.3
$-L$ [m]	inf	inf	inf	inf
u_* [m/s]	0.31	0.31	0.31	0.31
w_* [m/s]	0.0	0.0	0.0	0.0
Q_0 [Km/s]	0.0	0.0	0.0	0.0

Figure 3-5a shows the $\mathfrak{R} - Re_{LES}$ parameter space for cases using the advective scheme weno_z, where the horizontal and vertical dashed lines at $\mathfrak{R} = 0.9$ and $Re_{LES} = 400$ are rough estimates of where the simulation transitions to inertia dominated, and the

simulation enters the high-accuracy zone (HAZ) [Brasseur and Wei, 2010]. Figure 3-5a shows two trajectories relating to different effects. As the aspect ratio was systematically reduced, by refining the resolution in the horizontal holding the vertical resolution constant, the solution moves towards the upper-right of the $\mathfrak{R}-Re_{LES}$ parameter space, towards where the "high accuracy zone" (HAZ) is expected to be, following a shallow trajectory. Reducing the vertical resolution from 192 points to 128 pushed the solution towards the upper-right region following a steeper trajectory. The difference in the trajectories may be due to having too much resolution in the vertical, as [Brasseur and Wei, 2010] showed using too many grid points in the vertical negatively affects the LOTW scaling. Figure 3-5a shows the simulations are all not near the HAZ, and therefore unable to largely reduce the overshoot as seen in [Brasseur and Wei, 2010] and [Vijayakumar, 2015].

Figure 3-5b shows the overshoot in the normalized average velocity gradients as a function of height for cases using weno_z, where the overshoots are confined to the lower half of the surface layer, indicating the overshoots are not so severe. Figure 3-5b tells us the changes which move the solution towards the HAZ region translates to only minor reductions to the overshoot in the normalized average velocity gradient. [Brasseur and Wei, 2010] showed significant reductions (almost completely removing it) for similar aspect ratios, however, [Brasseur and Wei, 2010] used a pseudo-spectral LES code which was pseudo-spectral in the horizontal and finite difference in the vertical. Therefore, the differences may be attributed to the level of numerical dissipation in the code.

To examine the influence of the numerical schemes on the deviations from LOTW (i.e, the overshoot), two numerical schemes, weno_z and ppm_nolim, were compared. Figure 3-6a and Figure 3-6b suggests the levels of numerical dissipation in ppm_nolim and weno_z are similar. However, at lower aspect ratios ppm_nolim could be leading to numerical instabilities, as oscillations are observed in the normalized average velocity gradient.

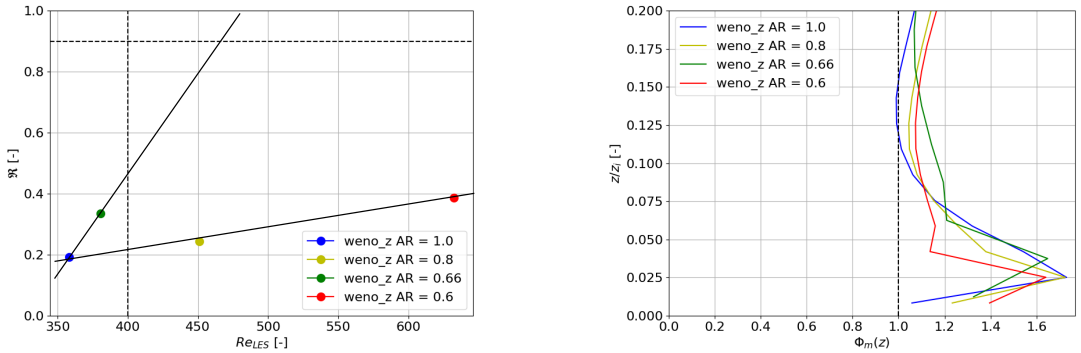

(a) (b)

Figure 3-5: The simulations carried out for this study given in Table 3.4 shown on (a) $\mathfrak{R} - Re_{LES}$ and (b) showing the overshoot in the normalized average velocity gradient $\Phi_m = \frac{\kappa z}{u_*}\frac{\partial U}{\partial z}$.

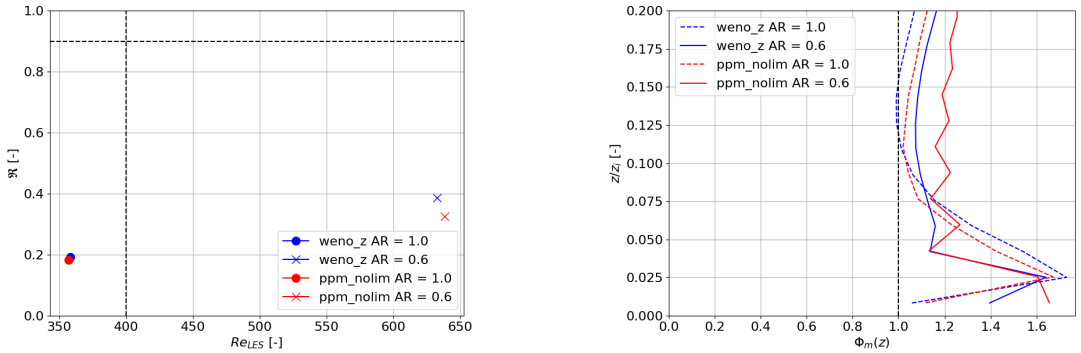

(a) (b)

Figure 3-6: The simulations carried out for this study are: weno_z (blue) and ppm_nolim (red) with AR = 1.0 (○) and 0.6 (×) shown on (a) $\mathfrak{R} - Re_{LES}$ and (b) showing the overshoot in the normalized average velocity gradient $\Phi_m = \frac{\kappa z}{u_*}\frac{\partial U}{\partial z}$.

To further investigate the differences in numerical dissipation in ppm_nolim and weno_z, 2D power spectral density (PSD) spectra of the x component of the velocity covariance was computed from 2-dimensional horizontal plane to compare the energy contents. Figure 3-7a is the x covariance spectra calculated at $z/z_i = 0.025$, closest to the peak at the surface in $\langle u'u' \rangle (z)$ (see Figure 3-7b).

The percentage difference in the total energy content (summation under the curve) between weno_z and ppm_nolim, in the horizontal, calculated from the 2D PSD spectra,

is 9.24% suggesting the overshoot is smaller for ppm_nolim at AR = 1.0. There is also a percentage change of 13.0% in the total energy content between AR = 1.0 and 0.6 due to the increase in the horizontal resolution. The decrease in energy content between AR = 1.0 and AR = 0.6 is due to increased resolution in the horizontal (compared to AR = 1.0), with a corresponding reduction in the numerical friction.

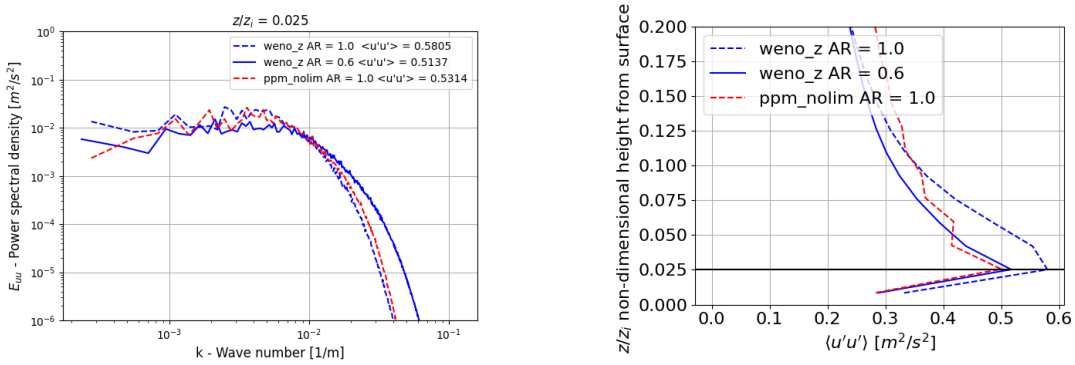

(a) (b)

Figure 3-7: The simulations carried out for this study are: weno_z AR = 1.0 (blue-dashed line) weno_z AR = 0.6 (blue-solid line) and ppm_nolim AR = 1.0 (red-dashed line) (a) $\langle u'u' \rangle$ spectra calculated on a 2D horizontal plane at $z/z_i = 0.025$ and (b) $\langle u'u' \rangle_{T=5000s}$ average vertical profile.

Finally, the effect of reducing the one-equation model constant is investigated, as [Brasseur and Wei, 2010] showed a reduction in the SFS model dissipation, reduces the overshoot. Figure 3-8a shows good agreement with [Brasseur and Wei, 2010], as the one-equation model constant is reduced from 0.1 to 0.07 the solution moves towards the HAZ region and some reduction in the overshoot is observed in Figure 3-8. However, the reduction is not as significant as expected when comparing to [Vijayakumar, 2015].

From the observations in the above analysis, the contributions of numerical dissipation and dispersion, that arises from the algorithms implemented in AMR-Wind, in-addition to model dissipation from the SFS stress model, are not fully understood. However, the results demonstrate that the overshoot has been minimised to the maximum extent possible, within the constraints of the AMR-Wind algorithm. The effects of the

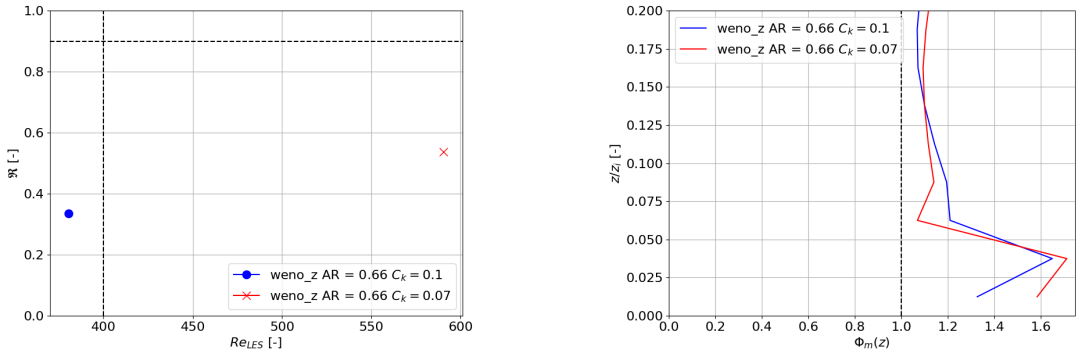

(a) (b)

Figure 3-8: The simulations carried out for this study are: weno_z one-equation model constant $C_k = 0.1$ (blue-circle) and weno_z $C_k = 0.07$ (red-cross) shown on (a) $\Re - Re_{LES}$ and (b) showing the overshoot in the normalized average velocity gradient $\Phi_m = \frac{\kappa z}{u_*}\frac{\partial U}{\partial z}$.

overshoot can be observed in isocontours of the velocity. At many times a thin strip of high speed fluid well above the average can be seen sitting on top of the below average low speed fluid contained within the surface layer, as highlighted in Figure 3-9 of the fluctuating streamwise velocity in the surface layer of the ABL at $t = 226.2s$. Where the fluctuating velocity on a $y' - z'$ plane is obtained by subtracting the mean velocity profile from the total velocity at the corresponding heights. The overshoot is a spurious increase in the average velocity gradient and horizontal variance in the inertia-dominated surface layer, and the layer of high speed fluid can be seen at many times throughout the quasi-stationary period at the approximate height of the overshoot in the ABL calculations. Therefore, the layer of high speed fluid is attributed to the overshoot in the ABL calculation. As Figure 3-9 shows the layer of well above average high speed fluid is mostly being contained to the first few grid cells, affirming the turbulence at the hub height of the turbine (90 m) will be largely unaffected.

Moving forward ABL simulations will use AR = 0.66, with the weno_z advective scheme, and one-equation SFS stress model constant of 0.07, as the results show this combination leads to the largest reduction in the overshoot.

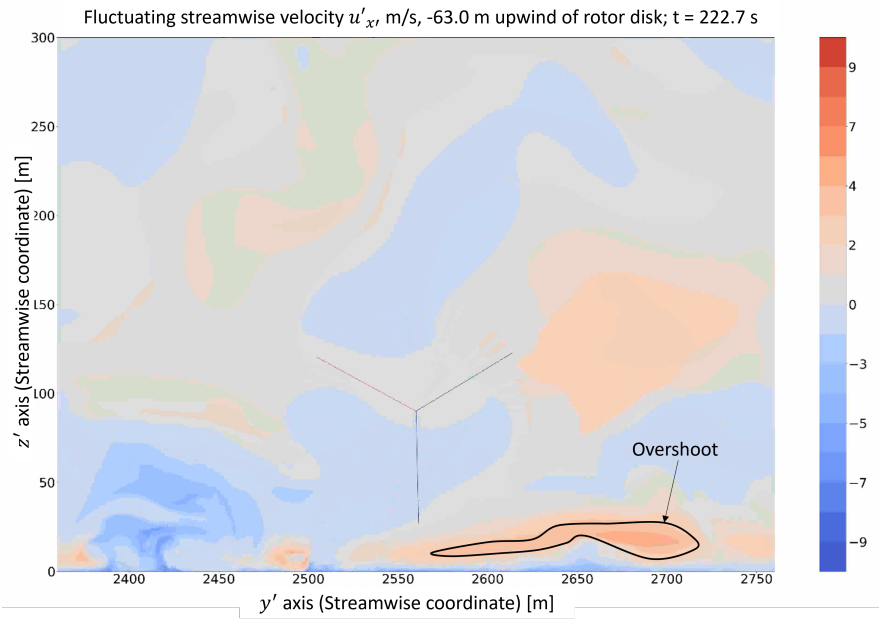

Figure 3-9: Isocontour of the fluctuating streamwise velocity on a $y' - z'$ plane offset -63.0 m from rotor disk at t=222.7 s, Black line encircled region of high speed velocity due to overshoot.

3.3 Development of a Moderately Convective Atmospheric Boundary Layer Precursor Simulation

A precursor moderately convective boundary layer was simulated with a fixed time step of 0.5 s, using the advective scheme weno_z, aspect ratio 0.66, and one-equation model constant 0.07 to limit influence of the overshoot, which could not be completely removed in the boundary layer. A strong but realistic capping inversion strength of 120 K/km [Jayaraman and Brasseur, 2021] was chosen to minimize the growth of the capping inversion (see Table 3.7). A geostrophic wind of 15 m/s (Table 3.6) and surface heat flux of 0.15 Km/s (Table 3.8) were chosen with the purpose of achieving a stability state between 3 and 8 [Khanna and Brasseur, 1998], and an average wind speed at hub height of approximately 11 - 12 m/s, just below rated wind speed (see Table 3.9). Finally, a surface roughness length of 12 cm was chosen, as it represents the north American planes [Lavely et al., 2014].

The MCBL is characteristic of an onshore atmosphere boundary layer, under sunny conditions, particularly in the North American plains. However, it may not be representative of offshore atmospheric boundary layer, where atmospheric turbulence tends to be lower in intensity and more shear-driven [Wyngaard, 2010]. These environmental differences likely manifest in difference in the structure and frequency content of the turbulence interacting with the turbine, and hence, the nature of the load fluctuations on components such as the main bearing.

Table 3.6: Description of moderately convective LES ABL geometric and inflow input parameters.

Domain [m]	$5120 \times 5120 \times 1920$
Grid resolution	512×512×128
Time step [s]	0.5
Uniform inflow velocity [m/s]	$[15.0, 0.0, 0.0]$
Geostrophic wind velocity [m/s]	$[15.0, 0.0, 0.0]$

Table 3.7: Description of moderately convective LES ABL initial conditions.

Reference temperature [K]	300.0			
Height z [m]	0.0	700.0	800	1920.0
Temperature [K]	300.0	300.0	312.0	315.36
Surface temperature heat flux [Km/s]	0.15			
Velocity Perturbations				
Number of sinusoidal waves in x-direction	20			
Number of sinusoidal waves in y-direction	20			
Amplitude of fluctuations in x-direction [m/s]	1.0			
Amplitude of fluctuations in y-direction [m/s]	1.0			
Reference height for velocity perturbations [m]	50.0			

3.3.1 Statistics

The MCBL was simulated for a total of 40000 s or approximately 60 eddy turnovers, where the eddy turnover time is defined as $\tau_w = z_i/w_*$, and calculated as approximately 640 s. Performing spatial averaging over horizontal homogeneous planes at every cell centre, the time variations and mean properties, which describe the MCBL, can be analysed. The time changes in the non-dimensional quantities $\frac{dz_i}{dt}\frac{1}{u_*}$ and $\frac{dz_i}{dt}\frac{1}{w_*}$, $-z_i/L$

Table 3.8: Description of moderately convective LES ABL boundary conditions.

x	Velocity Temperature	Periodic
y	Velocity Temperature	Periodic
Zhi	Velocity	Slip wall
	Temperature	Fixed gradient = 0.0032 [K/m]
Zlo	Velocity	Wall model (See section 2.1.3)
	Temperature	Fixed gradient = 0.0 [K/m]
	Turbulent kinetic energy	Fixed gradient = 0.0 [m/s^2]

Table 3.9: Global parameters of moderately convective boundary layer. Where U_g is the geostrophic wind and initial velocity, Q_0 is the surface temperature flux, z_0 is the roughness length scale, $T_{surface}$ is the initial surface temperature, and $\Delta\Theta$ is the initial temperature change across the interfacial layer of height Δz_i.

U_g [m/s]	15
Q_0 [Km/s]	0.15
z_0 [m]	0.12
$T_{surface}$ [K]	300
$\Delta\Theta$ [K]	12
Δz_i [m]	100
lapse rate [K/m]	0.003
$-z_i/L$	4.4
z_i [m]	1087
$-L$ [m]	244
u_* [m/s]	0.78
w_* [m/s]	1.7

and streamwise velocity $u_{x'}$ at hub-height were used as measures of quasi-stationarity.

There are several periods of time where the ratio of capping inversion growth to: the buoyancy driven mixed layer velocity scale w_* (Figure 3-10b) and the shear driven surface layer velocity scale u_* (Figure 3-10a), are approximately two orders of magnitude smaller than their characteristic velocity scales; indicating the calculation may be quasi-stationary. However, the average streamwise velocity (Figure 3-11b) and stability state (Figure 3-11b) show the calculation is still transient at times before 38000 s. Thus, 38000 s was chosen to begin the ABL-turbine calculations.

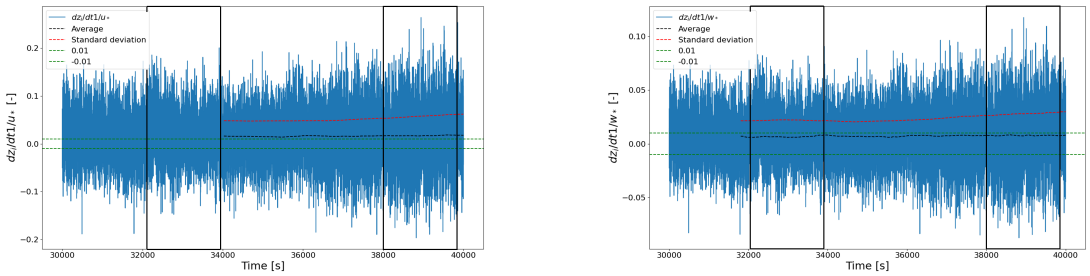

(a) (b)

Figure 3-10: Time evolution of the ratios of the capping-inversion growth to (a) the characteristic velocity scale u_* and (b) the characteristic velocity scale w_*. Solid blue line - average over three eddy turnovers, blue region - one standard deviation above and below the average.

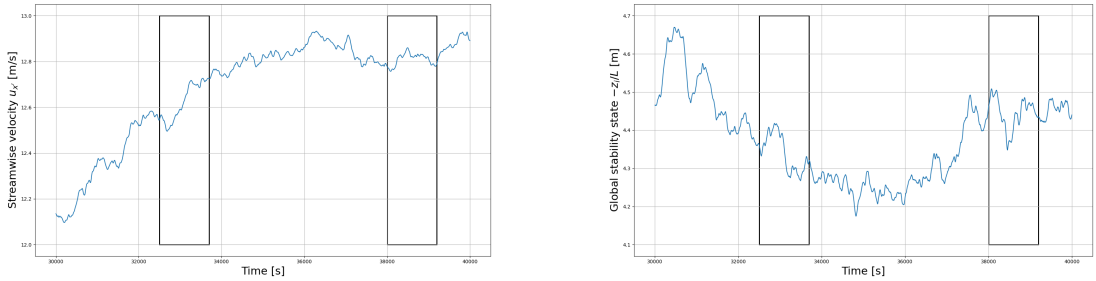

(a) (b)

Figure 3-11: Time evolution of the (a) hub height streamwise velocity and (b) stability state.

Figure 3-12 shows variables, averaged over horizontal planes then time averaged, which describe the MCBL. Figure 3-12a shows the horizontally averaged velocity profile which shows a strong gradient in the surface layer (approx. $0.2z_i$), and a transition across the capping inversion to the geostrophic wind speed in the free troposphere. Figure 3-12b shows the velocity profile up to $0.2z_i$ from the surface, to highlight key average wind characteristics. The hub height average velocity is calculated as 12.75 m/s, the shear exponent calculated, using the power law [International Electrotechnical Commission, 2019], is 0.098, where the velocity gradient is calculated using the velocity at the top and bottom of the rotor disk, and the turbulence intensity is calculated as 10%.

A hub height average wind speed of 12.75 m/s, for the NREL 5 MW wind turbine, places

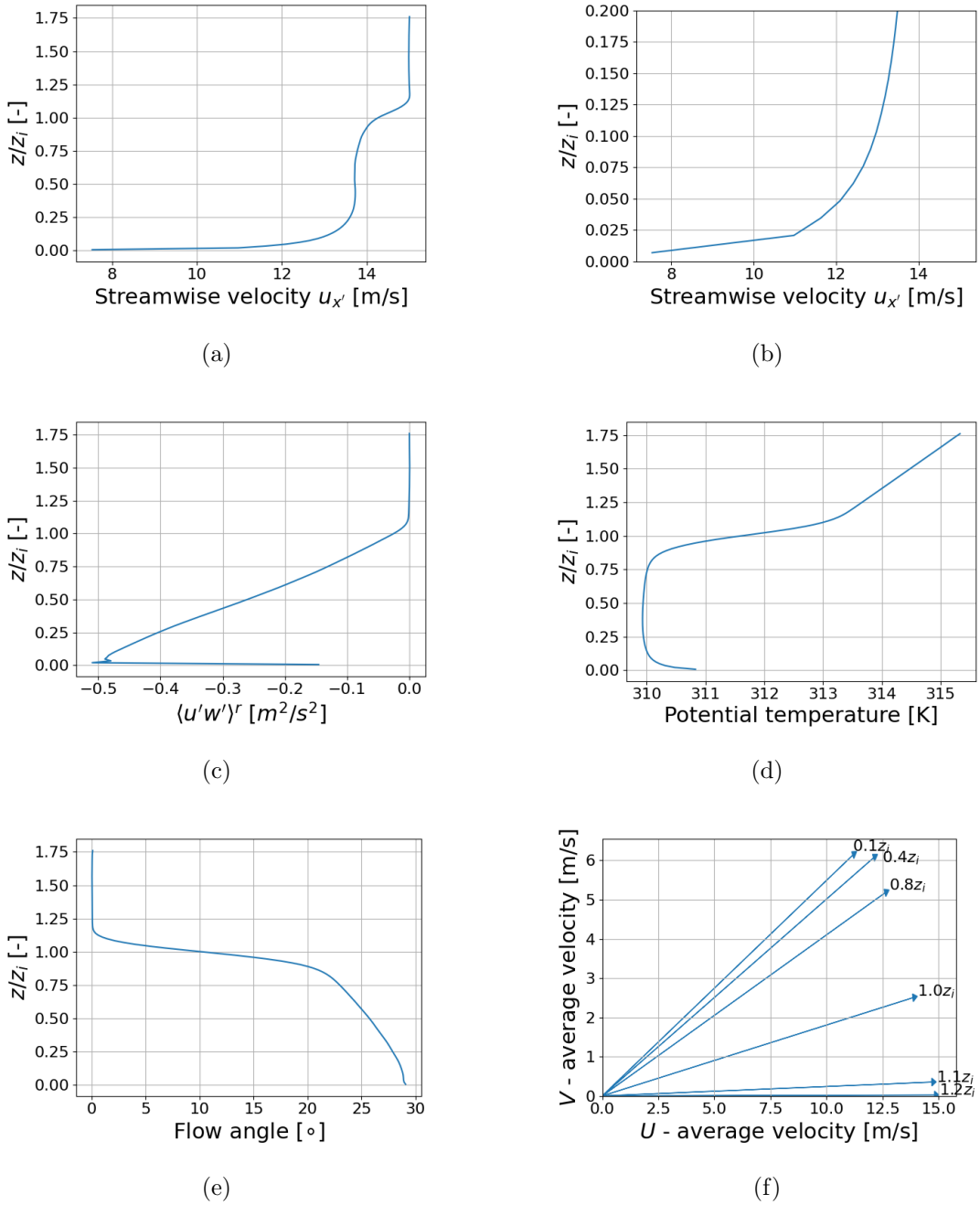

Figure 3-12: MCBL precursor ensemble averaged quantities, averaged over horizontal planes at cell centres and averaged over a 20 minute time period (38000 s - 39200 s) (approx. two eddy turnovers $\tau_w = z_i/w_*$). (a) Streamwise velocity profile. (b) Streamwise velocity profile (0 - 175 m). (c) fluctuating u, w velocity covariance $\langle u'w' \rangle$ profile. (d) potential temperature profile. (e) direction of streamwise velocity profile. (f) hodograph showing average u and v velocity components at different z/z_i locations.

the turbines operating regime in region 3. In this region, the turbine operates at or near rated power characterized by high aerodynamic loads. While this operating points is highly relevant, since turbines spend a considerable fraction of their operational life near or above rated wind speeds, it is not universally representative of all wind turbine operating conditions.

Figure 3-12c show the covariance between fluctuating u and w velocity components $\langle u'w' \rangle$, which shows the strong negative correlation between the horizontal and vertical velocity components, consistent with MCBLs [Moeng, 1984], [Deardorff, 1972]. Figure 3-12d shows the potential temperature profile, is in good agreement with profiles for a MCBL at midday [Moeng, 1984] [Deardorff, 1972] and those from [Jayaraman and Brasseur, 2021] which are not shown in the journal paper but the author has access to. Lastly, Figure 3-12e and Figure 3-12f illustrate the effect of the Coriolis force on the average streamwise velocity. At hub height the mean flow is rotated 29.29°, this decreases across the capping inversion to align with the geostrophic wind, which is aligned with the x direction in the global coordinate system 3-1.

Lastly, Figure 3-17 shows the 2D $u'_{x'}$ and $w'_{x'}$ velocity spectrum averaged over the 1200 s period in the MCBL precursor. Figure 3-17 plots the classical $k^{-5/3}$ highlighting the inertial wavenumbers, in the $u'_{x'}$ and $w'_{x'}$ velocity spectra, do not show a strong $k^{-5/3}$. The $u'_{x'}$ and $w'_{x'}$ velocity spectra displays a strong roll off in the energy content thus, does not show a strong $k^{-5/3}$. This is due to the the contributions of numerical dissipation and dispersion, that arises from the algorithms implemented in AMR-Wind, in-addition to model dissipation from the SFS stress model, discussed in section 3.2.

3.3.2 MCBL structure

Interactions between local generation of turbulence by mean shear close to the surface, where mean shear is strongest, and the non-local generation of turbulence due to buoyancy, results in complex flow patterns [Khanna and Brasseur, 1998]. In this section the

generation of these complex structures due to turbulence interactions are analysed.

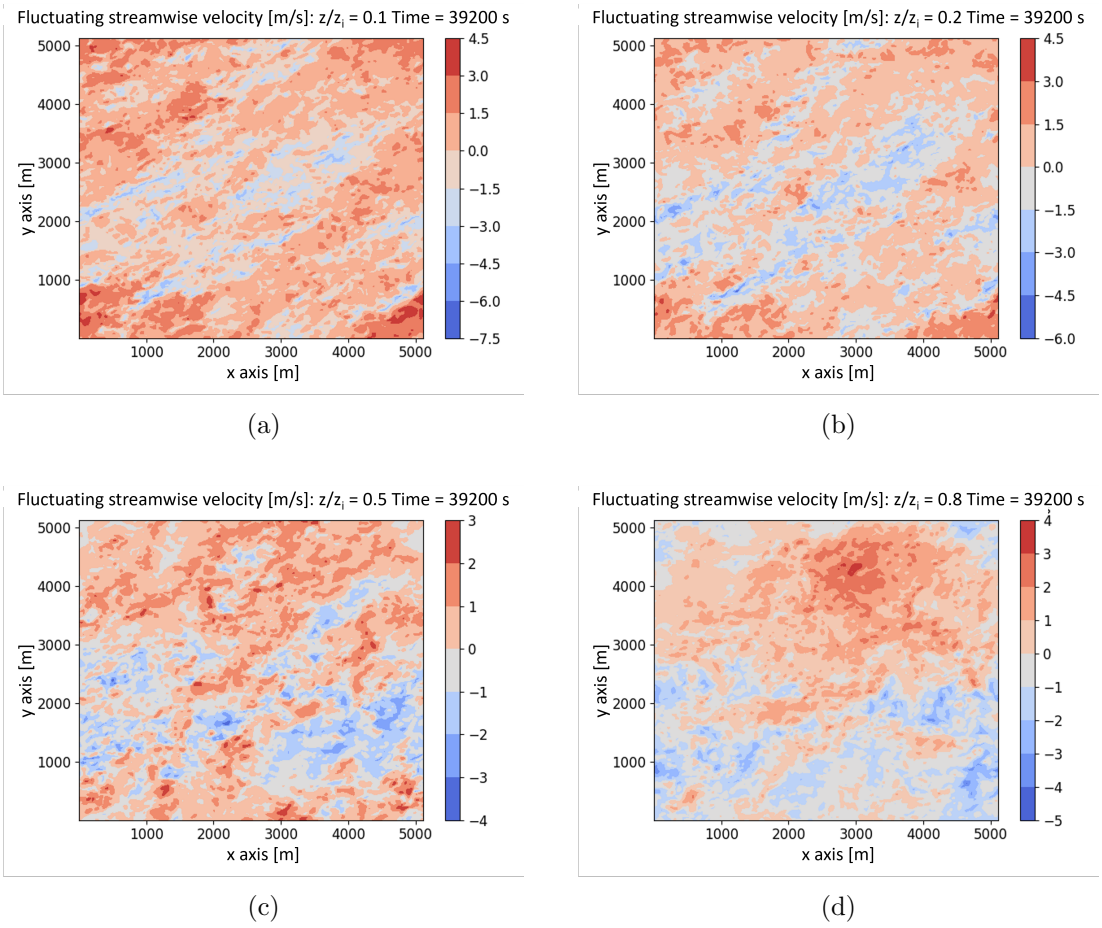

Figure 3-13: Isocontours of the fluctuating streamwise velocity, at time = 39200s, on $x-y$ planes at (a) $z/z_i = 0.1$, (b) $z/z_i = 0.2$, (c) $z/z_i = 0.5$ and (d) $z/z_i = 0.8$. Blue colours indicate (negative values) below average wind speed. Red colours indicate (positive values) above average wind speed.

Isocontours of the x and z components of the fluctuating mean velocity vector, and potential temperature, are plotted to illustrate the flow patterns generated in a typical daytime ABL. Figure 3-13 shows the x component of the fluctuating mean velocity vector on $x-y$ horizontal planes, at 39200s at $z/z_i = 0.1$, 0.2, 0.5, 0.8. Where the fluctuating velocity on each $x-y$ plane is calculated by subtracting the average streamwise wind speed from the total streamwise velocity at the corresponding heights. This is necessary to calculate the fluctuating velocity at different heights due to the vertical in-

homogeneity of the MCBL. Figure 3-13a and Figure 3-13b shows the low speed streaks align with the average wind direction and are surrounded by high speed regions. We see the low speed streaks merging together with increasing height, and the average flow direction align with the geostrophic wind direction, x-direction in the global coordinate system.

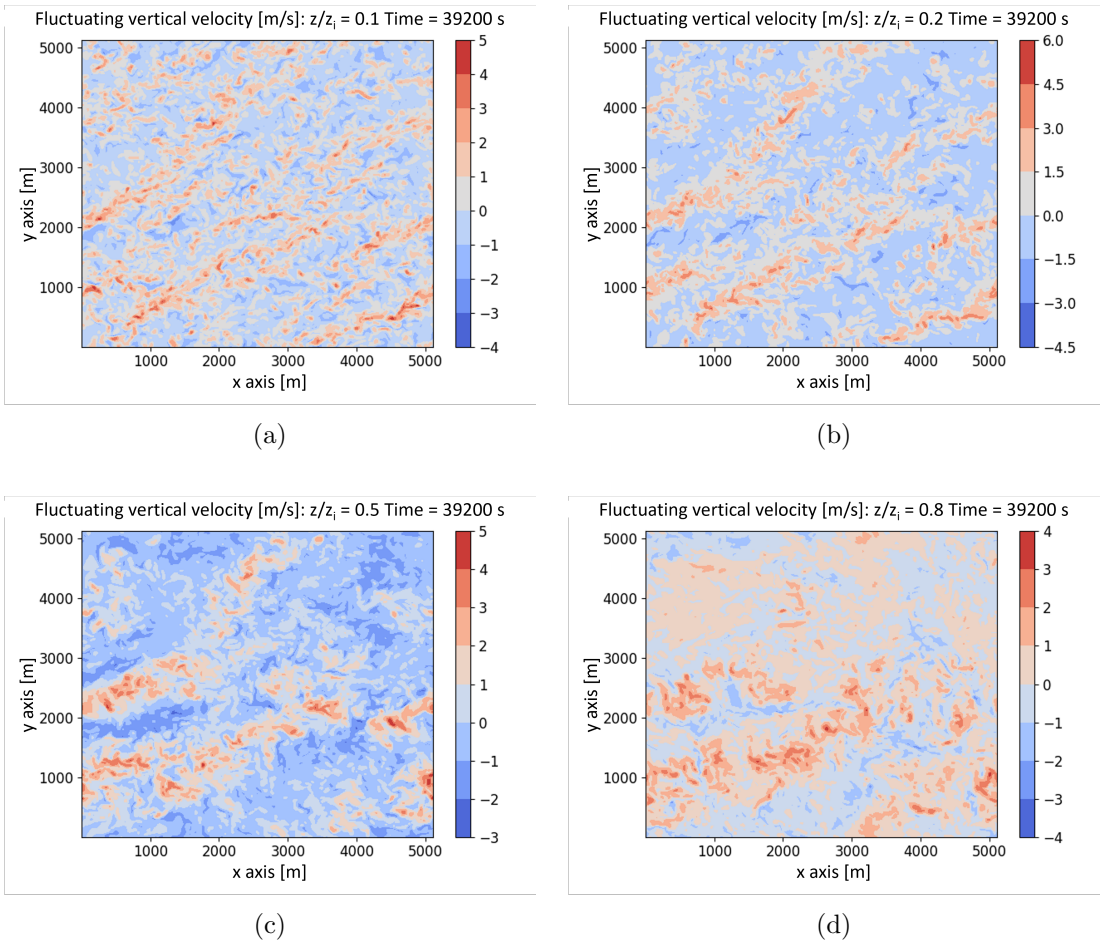

(a) (b)

(c) (d)

Figure 3-14: Isocontours of fluctuating vertical velocity at time 39200 s in the x, y plane at (a) $z/z_i = 0.1$, (b) $z/z_i = 0.2$, (c) $z/z_i = 0.5$ and (d) $z/z_i = 0.8$. Blue colours (negative values) are below average. Red colours (positive values) are above average.

Figure 3-14 shows the vertical fluctuating velocity on $x-y$ horizontal planes at 39200 s at $z/z_i = 0.1$, 0.2, 0.5, 0.8. Figure 3-14a shows that close to the surface updrafts, above-average vertical velocity regions, appear as coherence stream-wise oriented sheet like structures. Figure 3-14a-Figure 3-14d show that these updrafts grow in size with height

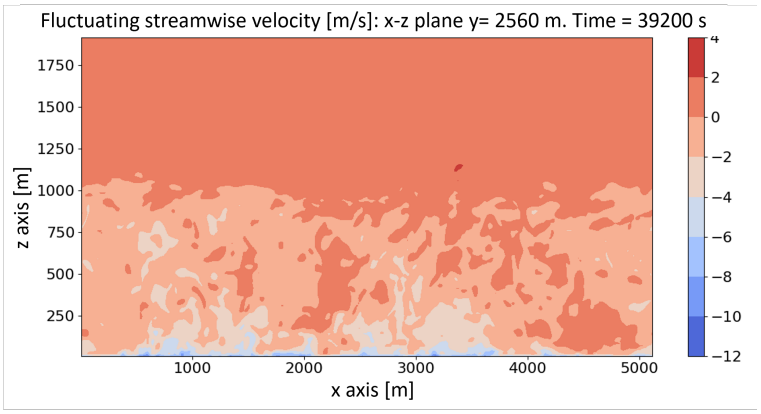

(a)

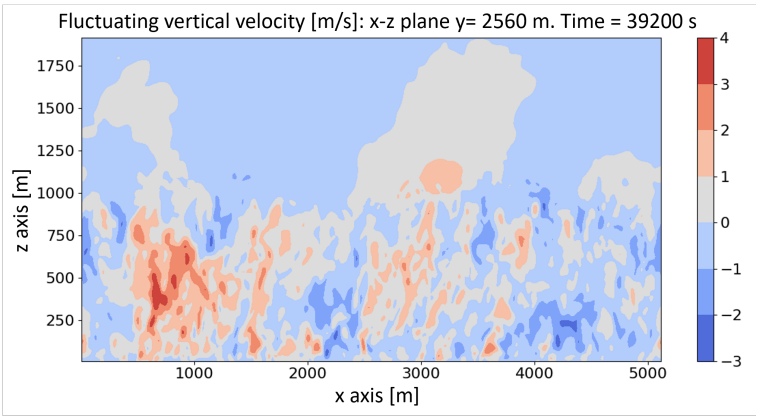

(b)

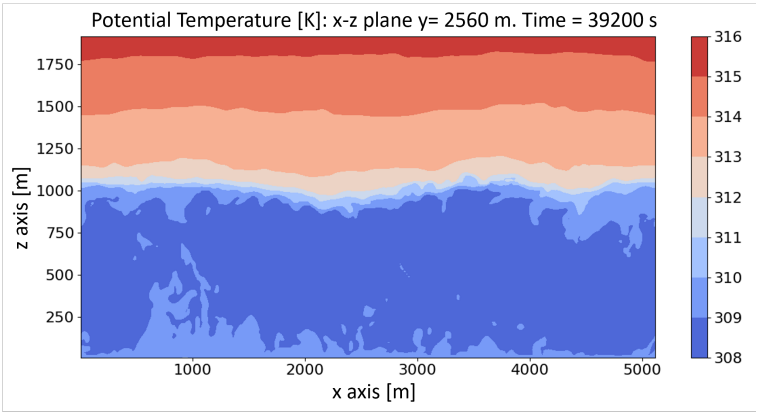

(c)

Figure 3-15: Isocontours at time 39200 s in the $x-z$ plane at $y = 2560$ m (a) fluctuating horizontal velocity, (b) fluctuating vertical velocity and (c) potential temperature.

merging with neighbouring updrafts. Figure 3-15 shows the fluctuating streamwise velocity and vertical fluctuating velocity, and potential temperature on a $x-z$ plane at $y = 2560$ m (centre of the domain) at 39200 s. Figure 3-15b, the updrafts (red regions) are shown to extend vertically up to the capping inversion in strong narrow regions, while broader and less intense downdrafts separate the updrafts.

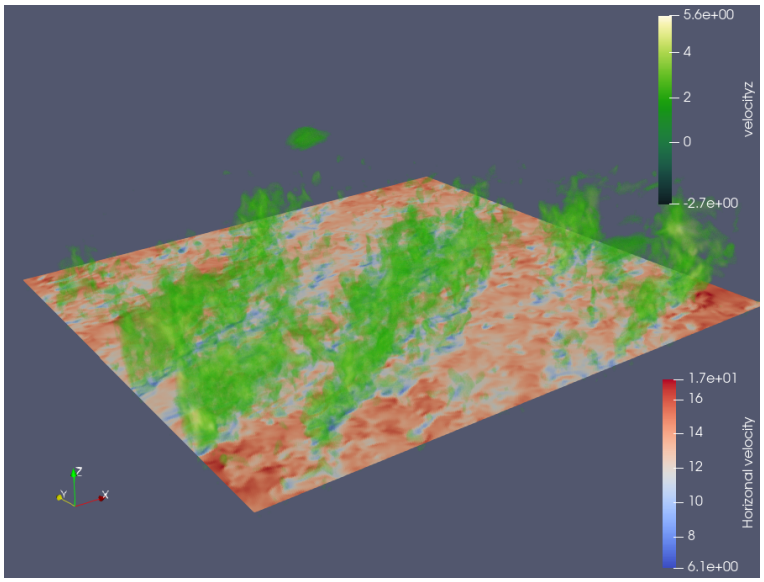

Figure 3-16: Isocontour of total horizontal velocity on a plane at $z/z_i = 0.1$ with isosurface of vertical velocity conditionally sampled $w \geq w_*$ on top of isocontour.

Figure 3-15a shows the low-speed streaks merging with height and qualitatively the low-speeds streaks correlate well with the updrafts in Figure 3-15b which is in agreement with Figure 3-12c and well cited in the literature [Khanna and Brasseur, 1998], [Moeng and Sullivan, 1994]. Figure 3-16 shows an isocontour of the x component of the total velocity at $z/z_i = 0.1$, and an isosurface of total vertical velocity, conditionally sampled at $w \geq +1.5w_*$, which shows the strong spatial correlation between the updrafts and the low speed streaks. Furthermore, a strong positive correlation can be observed between potential temperature and fluctuating vertical velocity Figure 3-15c and Figure 3-15b respectively as to passive scalars tend to concentrated within low speed streaks, in agreement with [Khanna and Brasseur, 1998], [Moeng and Sullivan, 1994].

3.3.3 Characterization of the Eddy Passage Time

The aim of this section is to characterise the eddy passage time for the quasi-stationary period in the precursor MCBL. Frequencies lower than the characteristic peak associated with the 3P frequency are attributed to the passage of atmospheric eddies [Vijayakumar, 2015] [Lavely et al., 2011] [Nandi et al., 2017]. The eddy passage time is defined as the ensemble averaged time associated with the time taken for eddies to advect through a transverse plane. [Vijayakumar, 2015] [Lavely et al., 2011] [Nandi et al., 2017] quantified the eddy passage time through transverse planes at 90 m to be between 20 s - 60 s. Here we quantify the eddy passage time from the current simulation on three horizontal $x-y$ planes at different heights over the rotor disk, (30 m, 90 m, 150 m), to understand the effect of vertical inhomogeneity on the turbine response. Furthermore, the data was further segregated into high-speed regions and low-speed streaks to support in later analyses. By defining the threshold velocities (x component of the fluctuating mean velocity vector) of high-speed regions and low-speed streaks, this will allow one to analyse the response of the WT to the different types of eddies.

To define the threshold velocities of high-speed regions and low-speed streaks, the framework detailed in [Vijayakumar, 2015] was employed. The procedure begins by isolating the integral-scale energy-containing eddies, of the $u'_{x'}$ velocity field (prime over the velocity indicates fluctuating velocity, prime over the x indicates the stream-aligned coordinate system), on horizontal $(x-y)$ planes at each time step, by low-pass filtering at three times the wavenumber of the peak in the time averaged $w'_{x'}$ velocity spectrum from a horizontal $(x-y)$ plane at 90 m (hub height). The wavenumber at the peak on the $w'_{x'}$ velocity spectrum is calculated as $3 \times 10^{-3}\,\mathrm{m}^{-1}$ (see Figure 3-17), therefore the low-pass filter is applied at $(9 \times 10^{-3}\,\mathrm{m}^{-1})$. The cumulative density function (CDF) of the filtered $u'_{x'}$ velocity field over the quasi-stationary period (38000 s - 39200 s), is used to define the threshold of low-speed streaks and high-speed regions. [Vijayakumar, 2015] defines low-speed streaks as the CDF probability < 0.3 and high-speed regions

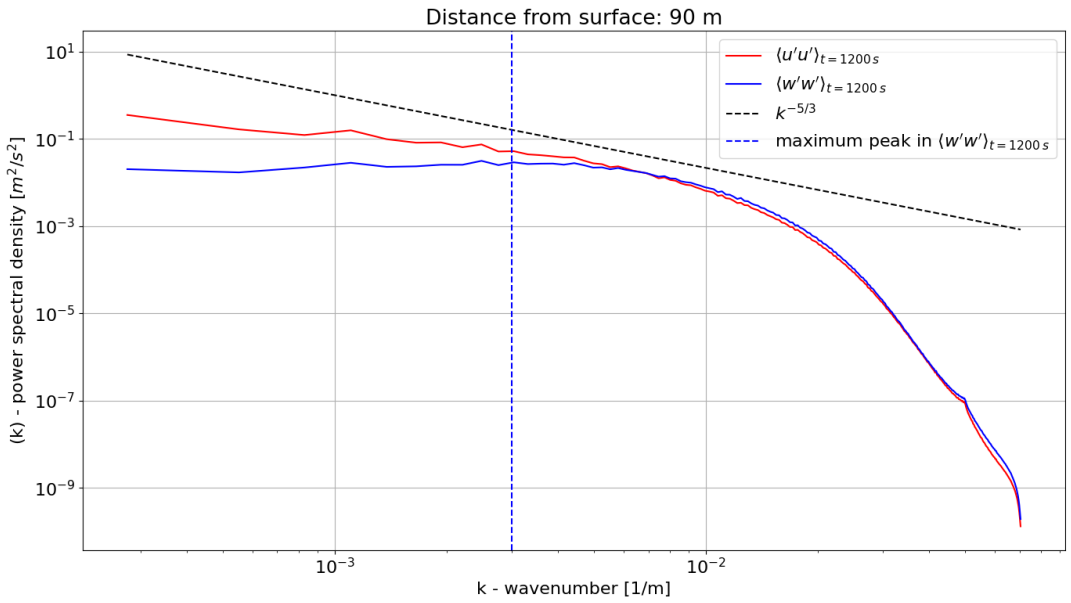

Figure 3-17: 2D PSD spectra of the fluctuating velocity variances $(u'u')$ and $(w'w')$, calculated on 2D $x-y$ planes at 90 m from the surface.

as the CDF probability > 0.7 (Figure 3-18a and Figure 3-18c). Analysis of the MCBL precursor found that the threshold velocity of high-speed regions is $> 0.76\,\mathrm{m/s}$ above the average streamwise velocity and low-speed streaks $< -0.61\,\mathrm{m/s}$ below the average streamwise velocity (Figure 3-18b). Similarly, updrafts and downdrafts can also be classified using the filtered $w'_{x'}$ velocity field. Following the same procedure as the LSS and HSR, the threshold velocity for updrafts is calculated as $> 0.42\,\mathrm{m/s}$ above the average vertical velocity and downdrafts $< -0.48\,\mathrm{m/s}$ below the average vertical velocity (Figure 3-18d).

The methodology to calculate the eddy passage time begins with isolating the integral-scale energy-containing eddies. The $u'_{x'}$ and $u_{x'}$ velocity fields are filtered to remove the small-scale fluctuations, which do not contribute to the energy-containing motions. To investigate the sensitivity of the solution to our choice of filter width $(1/k_{filter})$, five filter widths were used. The filter wavenumber (k_{filter}) is chosen to be multiples of the wavenumber at the peak in the time averaged $w'_{x'}$ velocity spectrum (k_{peak}), from

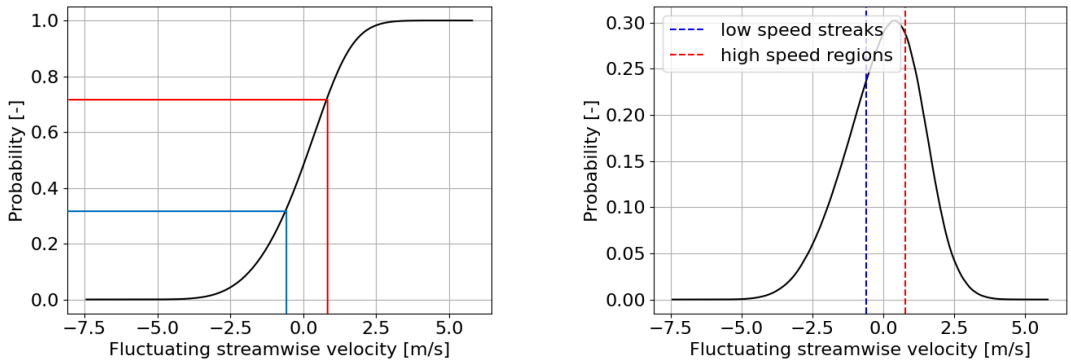

(a) (b)

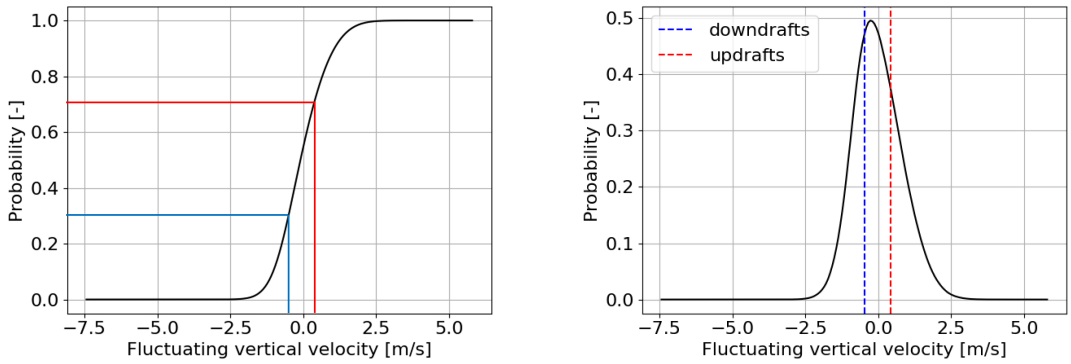

(c) (d)

Figure 3-18: CDF (left) and PDF (right) of the fluctuating streamwise (a,b), vertical velocity (c,d) at hub height (90 m) filtered at $9 \times 10^{-3}\,\mathrm{m}^{-1}$ in the moderately convective precursor simulation.

a horizontal $(x - y)$ plane at 90 m, to calculate the eddy passage time, where:

$$k_{filter} = n k_{peak}. \tag{3.2}$$

Table 3.10 lists the values of n, the corresponding filter wavenumbers k_{filter}, and filter widths defined as $1/k_{filter}$. The actual dimension associated with k_{filter} is more accurately given by π/k_{filter}.

To calculate the eddy passage time, one needs a characteristic speed and eddy length. The eddy length chosen to define the eddy passage time is the length between the

Table 3.10: Low-pass filters k_{filter} and corresponding filter widths used in eddy passage time algorithm.

n	3	2.5	2	1.5	1
$k_{filter} \times 10^{-3}$ [m^{-1}]	9	7.5	6	4.5	3
Filter width $1/k_{filter}$ [m]	111	133	167	222	333
Filter width π/k_{filter} [m]	349	419	524	698	1047

maximum and minimum x stream-aligned coordinate of an eddy. This is easily acquired by using the matplotlib contour function to output the coordinates of all the high-speed and low-speed eddies over horizontal $(x - y)$ planes of the $u'_{x'}$ velocity. The average $u_{x'}$ velocity of the eddy was chosen as the speed to calculate the eddy passage time. The eddy passage time is calculated for all high-speed and low-speed eddies at all time steps in the quasi-stationary period at the three heights.

The mean (time-averaged) and standard deviation of the eddy lengths, average eddy velocities and eddy passage times are plotted as a function of filter width and height from the surface in Figure 3-20. Figure 3-20 shows the average and standard deviation of the eddy length linearly increases as a function of filter width, which is consistent with a systematic increase in the low pass filter width. The segregation between LSS and HSR suggests that low-speed streaks are on average longer than high-speed regions. Since, the data collected was at heights within the surface layer, mean shear is the dominant turbulence production mechanism, which is well-established to generate elongated coherent structures of low-speed fluid. Thus, may explain the longer average and standard deviations of low-speed eddies. Or, another possibility is LSS are much more coherent compared to HSR thus, on average longer low-speed eddies are present in the data. Comparing the average and standard deviation of the eddy lengths as a function of height the plane at 150 m has on average the shortest eddy lengths, then 90 m then the 30 m plane has on average the longest eddy lengths over most the filter widths, which highlights the inhomogeneity as a function of height.

Figure 3-21 shows the average and standard deviation of the eddy speed plotted as a

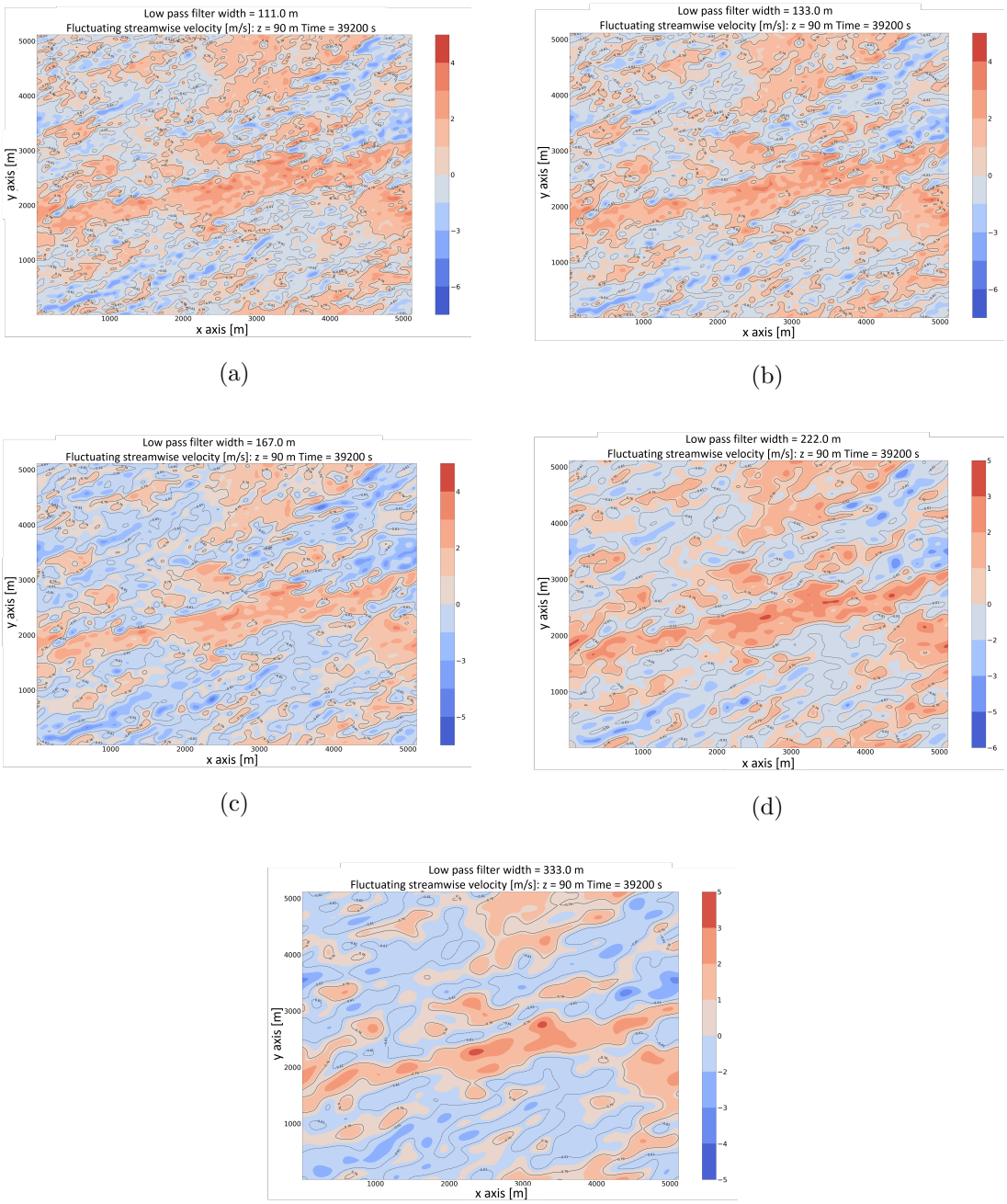

Figure 3-19: Isocontours of the fluctuating streamwise velocity at time 38200 s in the $x-y$ plane at 90 m, low pass filtered at $k_{filter} = nk_{peak}$, where $k_{peak} = 3 \times 10^{-3}\,\mathrm{m}^{-1}$ (a) $n = 3$, (b) $n = 2.5$, (c) $n = 2$, (d) $n = 1.5$ and (e) $n = 1$. $k_{filter} \equiv 1/k_{filter}$. Blue colours, dotted lines are -0.61 m/s below the average (LSS). Red colours solid lines are 0.76 m/s above average (HSR).

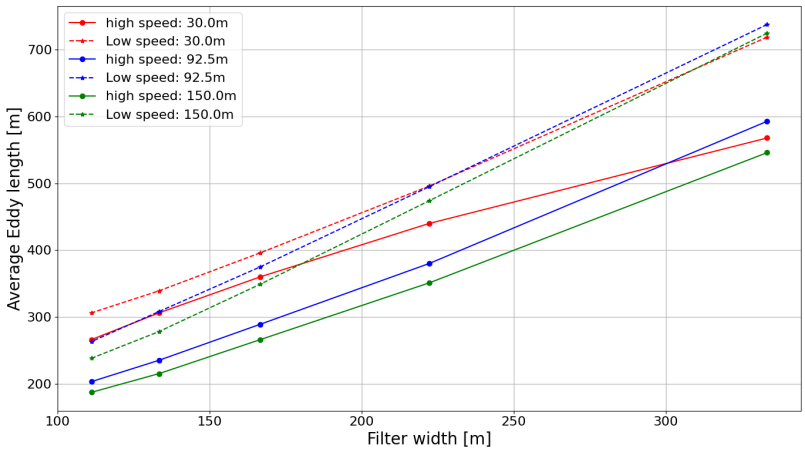

(a)

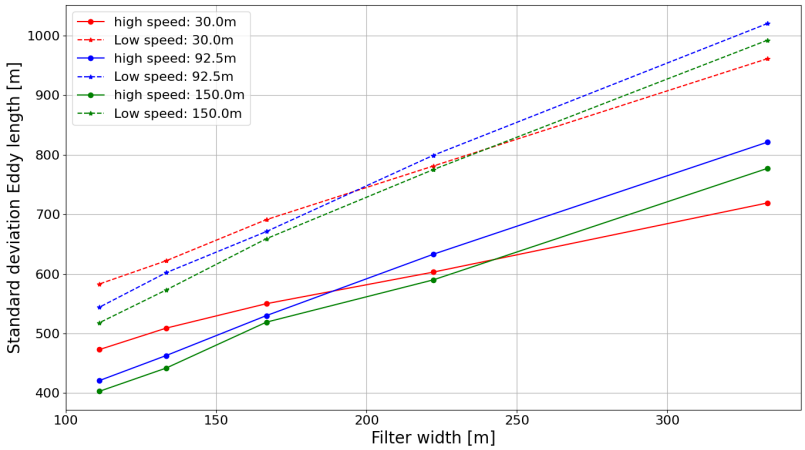

(b)

Figure 3-20: Summary of the (a) average, and (b) standard deviation of eddy length averaged over 1200 s MCBL precursor simulation plotted as a function of filter width, eddy type (LSS/HSR) and distance from the surface.

function of filter width and height from the surface. The average and standard deviation of the average eddy velocity is shown to be insensitive to filter width. The average of the eddy velocities of low-speed streaks and high-speed regions increases with distance from the surface which is consistent with an average velocity shear profile.

Lastly Figure 3-22, the average and standard deviation of the eddy passage time plotted as a function of filter width and distance from the surface, demonstrates similar trends

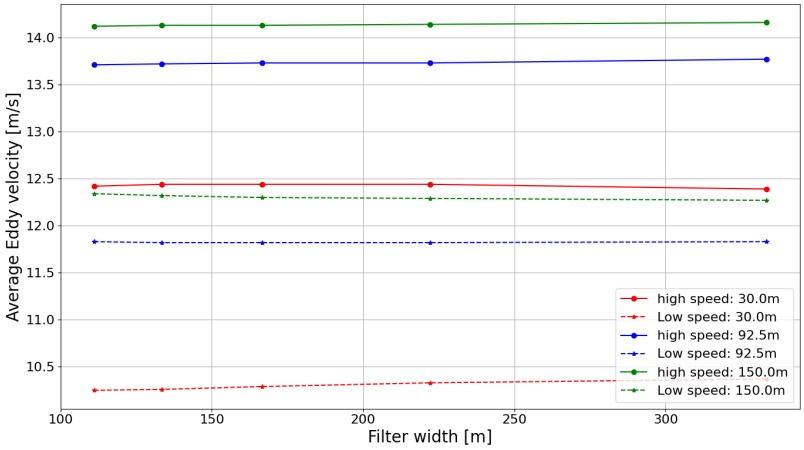

(a)

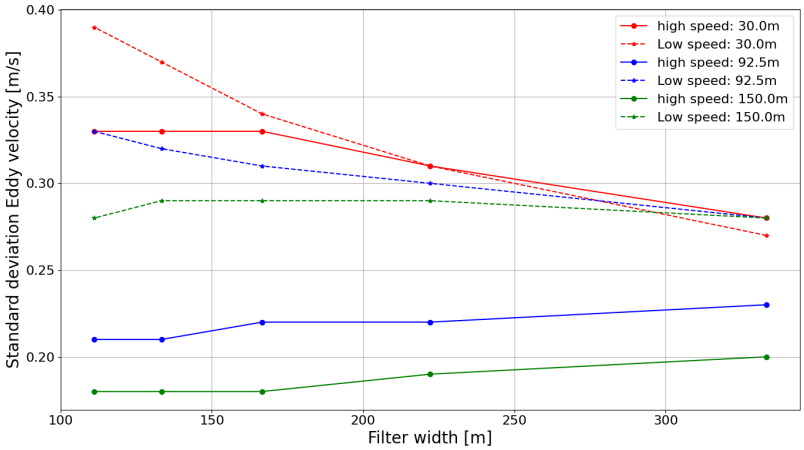

(b)

Figure 3-21: Summary of the (a) average, and (b) standard deviation of eddy velocity averaged over 1200 s MCBL precursor simulation plotted as a function of filter width, eddy type (LSS/HSR) and distance from the surface.

to the average and standard deviation of the eddy lengths because the statistics of eddy velocities are approximately constant with filter width. The eddy passage time is summarized for the filter width of 167 m, as qualitatively a filter width of 167 m filters the small-scale fluctuations without filtering the energy-containing eddies. Figure 3-23 summarizes the mean (blue bar) and the standard deviation (black error bar) of the eddy passage time for a filter width of 167 m (n=2). The mean has a range of 19 s - 40 s and the standard deviation has a range of 35 s - 71 s. Therefore, the eddy passage

time for the current MCBL simulation is on the order of 19 s - 71 s, which is in good agreement with the literature.

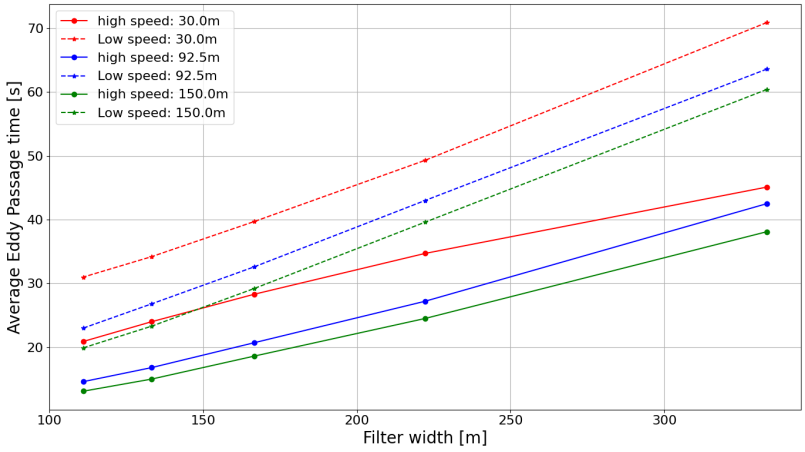

(a)

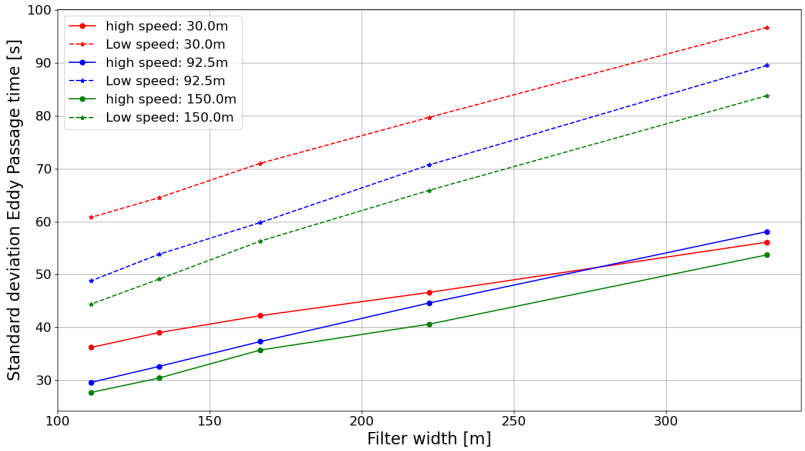

(b)

Figure 3-22: Summary of the (a) average, and (b) standard deviation of eddy passage time averaged over 1200 s MCBL precursor simulation plotted as a function of filter width, eddy type (LSS/HSR) and distance from the surface.

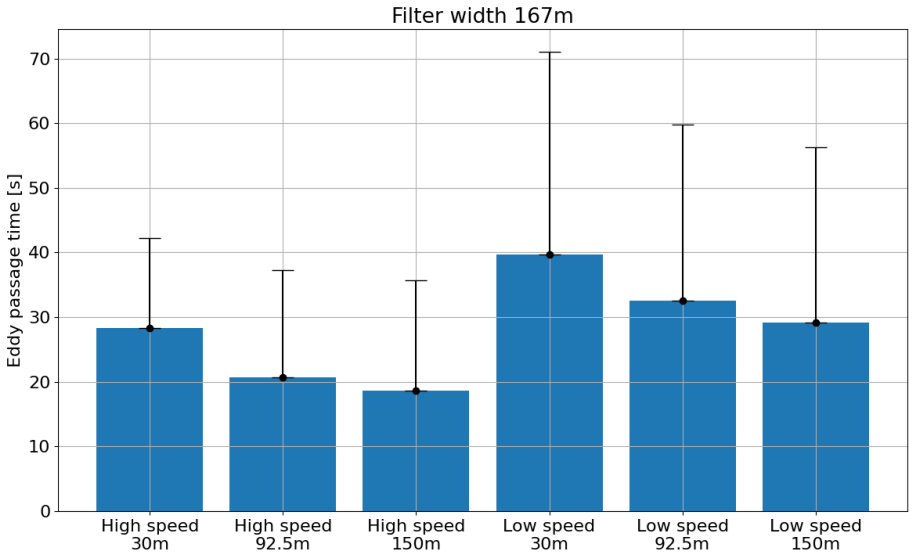

Figure 3-23: Summary of eddy passage mean (bar) and standard deviation (error bars) for filter cutoff of 167 m at 92.5 m.

3.4 Multi-body Aeroelastic Calculation of a Utility Scale Wind Turbine within a Large-Eddy Simulation

To perform ABL-turbine calculations OpenFAST v3.4.1 is two way coupled to AMR-Wind through the actuator line method (see Section 4.1). The NREL 5 MW WT was chosen as the turbine to be simulated in the ABL-turbine calculations, as the NREL 5 MW OpenFAST input files are easily accessible in the OpenFAST Github repository [National Renewable Energy Laboratory, 2023], and has been extensively studied [Dose et al., 2018] [Lee et al., 2017] [Hart et al., 2022c]. Two configurations of the NREL 5 MW WT were used. Firstly a fully rigid case, and secondly a case allowing deformations of the blades (see Table 3.11).

The NREL 5 MW baseline onshore turbine input files were taken from the OpenFAST Github repository to develop the rigid and deformable turbine configurations. In both configurations the main, AeroDyn15, AeroDyn blade, ElastoDyn blade, Tower and

airfoil input files remain the same. In the main input file: the total run time, time step and environmental conditions are set the same as the ABL simulation (or left as default if not applicable), structural dynamics are computed using ElastoDyn only (see Section 2.3.2), the inflow velocity is external from OpenFAST, since it is sampled from the flow solver and the aerodynamic loads are computed from AeroDyn v15.

Within the AeroDyn input file: the wake modification and tower influence are turned off as the wake influence is calculated by AMR-Wind in the flow solve. The tower influence was turned off as these studies aim to focus on the unsteady aerodynamics of the rotor and neglect the influence from the tower. Lastly, the steady blade airfoil aerodynamics model was selected as the high-fidelity CFD approach should be sufficient to capture the non-steady aerodynamics (see Section 2.3.1). The aerodynamic blade properties within the AeroDyn blade input file were interpolated to increase the number of points resolving the blade (see Section 4.2.2).

The differences between the rigid and deforming blade cases arise from the ElastoDyn input file, however, in both cases most the initial conditions are the same. Rotor speed was set constant at 12.1 rpm (rated), to match the rotor speed for a hub height average wind speed of 12.75 m/s, which corresponds to a tip speed ratio (TSR) of 6.26, and the blade pitch angle was set constant at 0.0°. Rotor speed and blade pitch were held constant to isolate the aerodynamic interactions between the wind turbine and the turbulence eddies that pass through the rotor. This enables clear interpretation of load transmission pathways from blade to hub to main bearing. If a different rotor speed, wind speed was chosen, or if the controller was turned on so the rotor speed and blade pitch were allowed to vary, the differences in the operating point would significantly affect the MB response. The implications of operating point, hub height wind speed, rotor speed are discussed in Chapters 5 & 6.

Nacelle-yaw angle was set equal to the Coriolis twist angle at hub height 29.29°, so the rotor disk is normal to the x component of the stream-aligned velocity vector, and

shaft-tilt angle was set to zero. Also, in the rigid case the blade coning angle is set to 0°. Zero coning angle and zero shaft tilt simplifies the analysis of the rigid turbine configuration as the weight of the rotor only contributes to the z component of the hub force. Changing the shaft-tilt from $-5°$ to $0°$ and blade coning angle from $-2.5°$ to $0°$ will have an effect on the solution. However, due to the very small change in the angles, it is very unlikely that the conclusions drawn in the subsequent analyses would change significantly due to the changes in the tilt-angle or coning angle.

A coning angle of $0.0°$ was chosen for the rigid case so the entire blade is approximately in the same plane (rotor plane) normal to the main shaft. Therefore, when analysing isocontours of velocity on planes normal to the rotor disk it is fair to claim the blades will be forced by the velocity seen on the isocontour normal to the rotor plane.

In the rigid cases in the ElastoDyn input file all the degrees of freedom were turned off. In the deforming blade case: the initial blade coning angle is left at $-2.5°$ (default) and the first and second flapwise blade mode and the edgewise blade mode degrees of freedom were turned on to allow only the blades to deform.

Table 3.11: Description of NREL 5 MW setups and parameters.

	Rigid	Deformable
Rotor, Hub Diameter	126 m, 3 m	126 m, 3 m
Hub Height	90 m	90 m
Hub height average wind speed	12.75 m/s	12.75 m/s
Rotor speed	12.1 rpm	12.1 rpm
Tip speed ratio (TSR)	6.26	6.26
Blade pitch angle	0.0°	0.0°
Shaft tilt, Precone	0°, 0.0°	0°, −2.5°
Rotor mass	110,000 kg	110,000 kg
Degrees of Freedom (DOF)	All off	FlapDOF1 FlapDOF2 EdgeDOF

Finally, in AMR-Wind the influences of the nacelle (rotor hub) and tower aerodynamics are excluded. AMR-Wind models the tower and nacelle using the actuator line model, where the nacelle and tower are represented as discrete actuator points. As discussed

above the tower influence was turned off as these studies aim to focus on the unsteady aerodynamics of the rotor and neglect the influence from the tower. In AMR-Wind ALM the nacelle is modelled with an area and drag coefficient. In several studies the importance of the nacelle is primarily attributed to better model near and far wake effects [Churchfield et al., 2015] [Stevens et al., 2018] [Yang and Sotiropoulos, 2018], and the impact of this modelling approach on the blade loads is not well understood. Therefore, a decision was made to exclude the nacelle from the calculation.

3.4.1 OpenFAST Coordinate Systems

The outputs from OpenFAST (see Section 3.4.2) use several different coordinate systems. The following section describes the relevant coordinate systems. Figure 3-24a shows the hub coordinate system, where subscript H indicates the non-rotating hub coordinate system. x_H points along the centreline of the main shaft, z_H points opposite to gravity and y_H completes the right hand rule, in Figure 3-24a y_H points into the page. Subscript $\widehat{H}$ indicates the hub coordinate system is rotating with blade 1. $x_{\widehat{H}} = x_H$, $z_{\widehat{H}}$ points along rigid blade 1 and $y_{\widehat{H}}$ completes the right hand rule.

The blade coordinate system is a coordinate system local to each blade and actuator point along the blade, subscript b indicates the blade coordinate system. Figure 3-24b illustrates the blade coordinate system, the origin is located at the blade pitch axis which is the quarter chord location of each airfoil [Jonkman et al., 2009], thus rotates with the blade. The blade coordinate system is obtained by a rotation about the $y_{\widehat{H},i}$ axis at actuator point i to account for blade coning, then rotating (pitching) around the $z_{\widehat{H},i}$ axis to account for the local pitch and twist angle. Blade pitch angle is set constant to 0.0° and twist angle for the NREL 5 MW is shown in Figure 3-25.

Finally, the airfoil coordinate system (Figure 3-26) is a 2-dimensional coordinate system $x_a - y_a$, where subscript a indicates airfoil coordinate system. Where y_a points along the chord axis and x_a is 90° to y_a, where the origin is at the aerodynamic centre. The

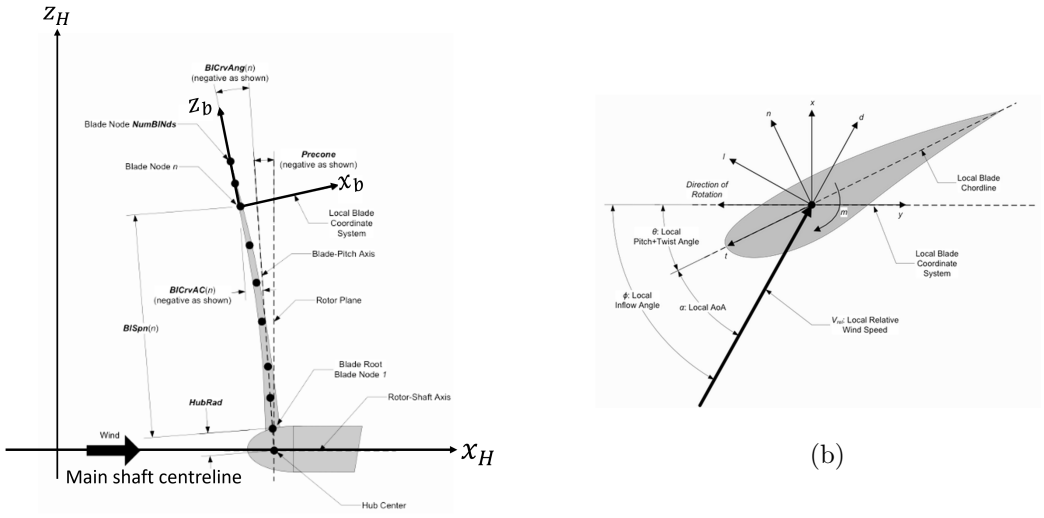

(a) (b)

Figure 3-24: Illustration of the Hub and Blade coordinate systems. Acknowledgment: OpenFAST Github documentation [National Renewable Energy Laboratory, 2023].

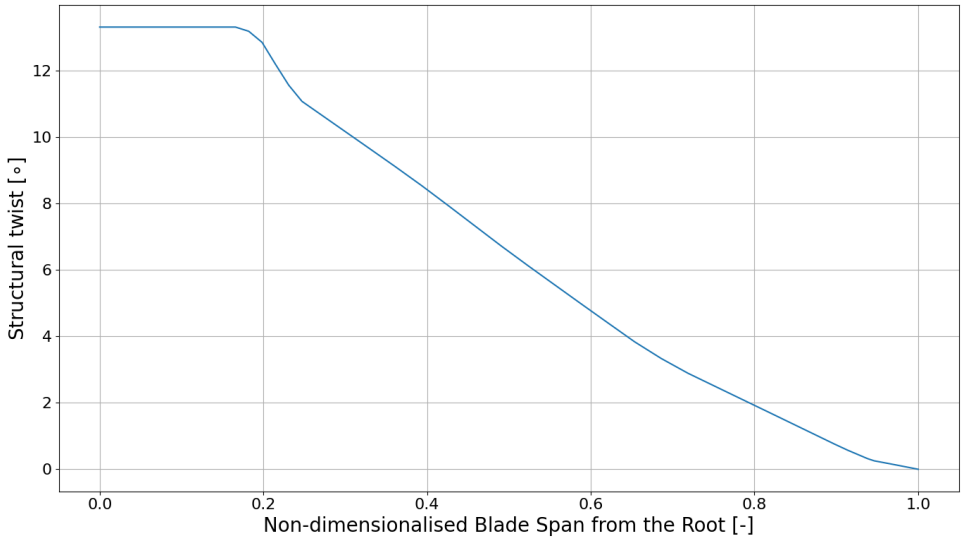

Figure 3-25: NREL 5 MW structural twist along blade span.

aerodynamic centre is not always located at the quarter chord. [Jonkman et al., 2009] provides the fractional distance to the aerodynamic centre from the blade pitch axis as a function of span.

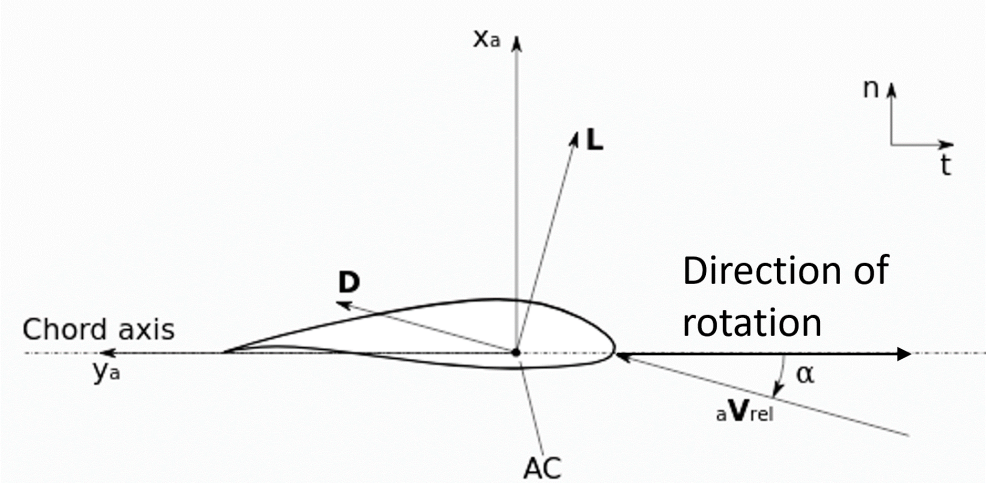

Figure 3-26: Illustration of the airfoil coordinate system. Acknowledgment: OpenFAST Github documentation [National Renewable Energy Laboratory, 2023].

3.4.2 Description of Wind Field Planar Data and Wind Turbine Outputs

Outputs from AeroDyn were: blade 1 azimuth angle, blade 1 pitch angle, net force at the hub from the three blades and hub moment components. Azimuth angle is important to output as the rotor loads are in the rotating hub frame of reference (see section 3.4.1), so the blade azimuth angle is needed to transform the rotor loads into the fixed hub frame of reference. Blade azimuth and pitch angle are also used to confirm the rpm and pitch angle is fixed. The net aerodynamic contribution to the force on the rotor hub is given by

$$\widetilde{\mathbf{F}}_H = \sum_{j=1}^{3} \int_0^R \widetilde{\mathbf{f}}_j (r)\, dr, \tag{3.3}$$

where $\widetilde{\mathbf{f}}_j (r)$ is the force vector per unit span along the blade span and $\widetilde{\mathbf{F}}_H$ is the net force at the hub, where tilde indicates the aerodynamic contribution, and j indicates blade 1-3. Similarly, the aerodynamic contribution to the moment vector acting at the rotor hub is given by

$$\widetilde{\mathbf{M}}_H = \sum_{j=1}^{3} \int_0^R \mathbf{r}^{CR}(r) \times \widetilde{\mathbf{f}}_j(r)\, dr, \tag{3.4}$$

where $\mathbf{r}^{CR}(r)$ is the position vector from the hub centre of mass to an actuator point on the blade. Radially distributed quantities output from AeroDyn include: relative velocity, AoA, lift and drag coefficients, normal and tangential force, local, and axial velocities; which are in the airfoil frame of reference (see section 3.4.1).

Outputs from ElastoDyn are: net force at the hub (Eq. 3.5) and hub moments (Eq. 3.6), which are in the H fixed hub coordinate system. The ElastoDyn outputs differ from the AeroDyn outputs as they include contributions from blade element weight, hub weight and inertial (acceleration) contribution due to blade motion. The acceleration term is zero in the rigid calculation.

$$\mathbf{F}_H = \sum_{j=1}^{3} \left[\int_0^R \widetilde{\mathbf{f}}_j(r) - \mu(r) \left(\mathbf{g}\widehat{e}_z + \mathbf{a}(r) \right) \right] dr - m^H \mathbf{g}\widehat{e}_z \tag{3.5}$$

$$\mathbf{M}_H = \sum_{j=1}^{3} \left[\int_0^R \mathbf{M}_{pitch,j}(r)\, \mathbf{r}^{CR}(r) \times \left(\widetilde{\mathbf{f}}_j(r) - \mu(r) \left(\mathbf{g}\widehat{e}_z + \mathbf{a}(r) \right) \right) dr \right] - m^H \mathbf{r}^{QC} \times \mathbf{g}\widehat{e}_z, \tag{3.6}$$

where $\mathbf{F}_H$ and $\mathbf{M}_H$ are the hub force and hub moment from ElastoDyn in the fixed hub coordinate system, $\mathbf{M}_{pitch,j}$ is the pitching moment due to the moment arm created between the pitch axis and aerodynamic centre, $\mu(r)$ is the distributed mass density (mass/length) of the NREL 5MW blades (see Figure 3-27), $\mathbf{a}(r)$ is the acceleration per unit span, $\mathbf{r}^{QC}$ is the position vector from the apex of coning angle to the hub centre of mass and m^H is the mass of the hub.

To analyse the turbulent velocity field, planar data of the velocity is stored from AMR-Wind every 100 time steps (0.39 s). This is in contrast to the data stored by OpenFAST,

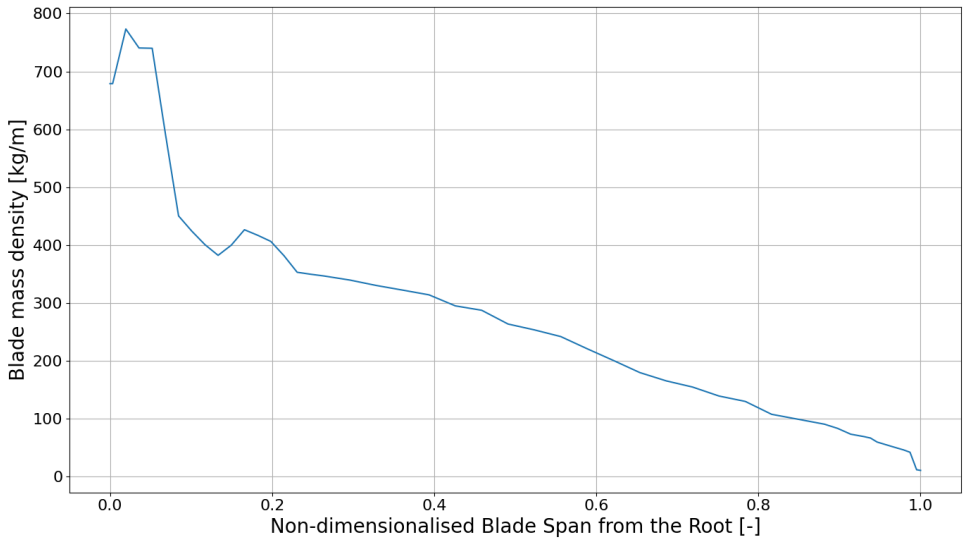

Figure 3-27: Blade mass density of NREL 5MW wind turbine blades.

which saves data every time step (0.0039 s). Planar data is stored every 100 time steps due to practical limitations (storage, increased run time/cost). Five different planes were output from AMR-Wind: 1. Three horizontal (x, y) planes where the origin is at the origin of the CFD domain, with lengths of 5120 m $\times$ 5120 m and 512 $\times$ 512 points, offset 30 m, 92.5 m and 150 m from the surface were output. 2. Two (y', z') planes normal to the x component of the mean velocity vector (rotor disk), centred on the rotor, with lengths of 400 m $\times$ 300 m and 1280 $\times$ 960 points, are output at the rotor disk and 63.0 m in front of the rotor. The number of data points in the horizontal planes is 262144=(512 $\times$ 512), chosen to match the number of cell centred points at level 0 of the grid refinement (see Section 3.5). The number of points in the rotor planes was chosen to match the $\Delta y = 0.3125$ m and $\Delta z = 0.3125$ m at level 5 of the grid refinement.

3.5 Refinement of CFD Grid to Resolve Wind Turbine Blade Forces and Wake

Grid refinement is required to accurately resolve the actuator body forces. Within the design of the computational experiments static refinement using Cartesian boxes aligned with the global coordinate system was used to define the regions of mesh refinement. Where static means the grid refinement is fixed with respect to space and time. The adaptive-mesh refinement (AMR) feature of AMR-Wind was not utilized, because it was deemed unnecessary. Furthermore, a more advanced mesh refinement option, that aligned with the x component of the stream-aligned velocity vector, was explored, but ultimately abandoned when tests showed an increase in the computational cost.

Static refinement increases the mesh refinement in levels, where the mesh resolution is increased by a factor of two at each level. Furthermore, when multiple levels are stacked on top of each other the mesh resolution increases by 2^n where n is the number of levels of refinement. I.e. 3 levels of refinement is an increase in the mesh resolution by a factor of 8. So, with a $\Delta = 10$ m at level 0, 3 levels of refinement results in a $\Delta = 1.25$ m at level 3.

To define the regions of static refinement: two vertices of a Cartesian box are specified in a text file, where the two vertices define the smallest and largest x, y, z coordinates, and the level of the refinement region. It is also advisable to stagger multiple levels of refinement so they all do not start and finish at the same location.

Table 3.12: Mesh refinement 5 levels of refinement.

level	min x [m]	min y [m]	min z [m]	max x [m]	max y [m]	max z [m]
1	2300	2100	0.0	3300	2750	330
2	2400	2300	0.0	3000	2700	300
3	2430	2330	0.0	2700	2680	270
4	2460	2400	0.0	2650	2660	240
5	2500	2480	0.0	2610	2635	210

Table 3.13: Mesh refinement 6 levels of refinement.

level	min x [m]	min y [m]	min z [m]	max x [m]	max y [m]	max z [m]
1	2140	2100	0.0	3310	2770	360
2	2190	2200	0.0	3100	2740	330
3	2240	2300	0.0	2880	2710	300
4	2340	2430	0.0	2780	2690	270
5	2440	2450	0.0	2680	2670	240
6	2540	2470	0.0	2580	2650	210

Table 3.12 lists the coordinates of the two vertices and corresponding level of refinement required to specify the static Cartesian box refinement. The 1st level is specified so the box captures 2 rotor diameters in front and 6 rotor diameters behind the WT, level 3 captures 1 rotor diameter behind the WT, level 5 is made as small as possible, to minimize the computational cost, while still covering the WT and levels 2 and 4 are specified as intermediate levels. A mesh refinement with only 4 levels was also required (see Chapter 4), this was achieved simply by removing level 4 from Table 3.12.

When designing the mesh refinement with 6 levels of refinement the static boxes had to be specified slightly differently to the mesh refinement with 5 levels, to optimize the mesh refinement. Table 3.13 lists the coordinates of the two vertices and corresponding level of refinement required to specify the static Cartesian box refinement. The first level still captures 2 rotor diameters in front and 6 rotor diameters behind the WT, but the second level now captures 1.5 diameters in front and 4 diameters behind the turbine, the fourth level captures 1 rotor diameter behind the WT, the sixth level refines closely around the WT, while the third and fifth levels become the intermediate refinement levels.

Figure 3-28 shows the mesh refinement corresponding to 5 levels of refinement. The mesh is not centred on the WT because the Cartesian box refinement must align with the global axes. So, to completely capture the wake, which is in the direction of the x component of the stream-aligned velocity vector, the mesh had to be designed as such.

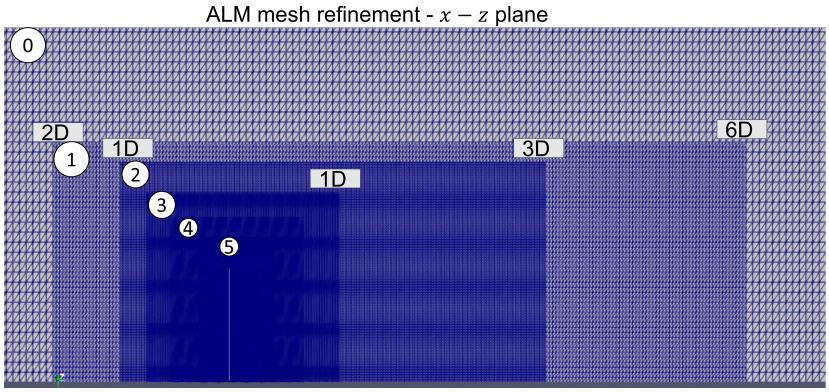

(a)

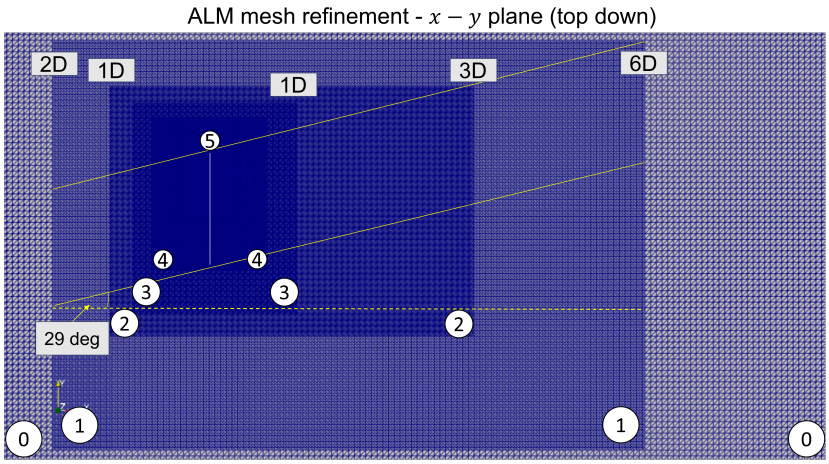

(b)

Figure 3-28: 5 levels of grid refinement white lines illustrating wind turbine tower location, yellow solid lines illustrating path of wind turbine wake direction (a) $x-z$ plane (b) $x-y$ plane.

3.6 Development of the Rotor Asymmetry Vector

The asymmetry vector was developed with the aim to represent the asymmetrical distribution of the rotor-normal velocity over the rotor disk as a vector, correlate well with the out-of-plane bending moment, and correlate well with the "asymmetry parameter" (see section 2.3.3). The asymmetry parameter describes the "level" of asymmetry in the rotor-normal velocity over the rotor disk and was shown to correlate well with the OOPBM magnitude (see Section 2.3.3). To extend our knowledge, of the mechanism

that is asymmetry, a more complex variable is required. The concept of the asymmetry vector is similar to concept of the centre of mass, where the velocity replaces mass. The velocity at a point in the velocity field is multiplied by its distance from the centre of the rotor disk, as this weights the velocity towards the edges of rotor disk, then is integrated over the rotor disk area. This leads to Eq. 3.7, the components of the asymmetry vector are shown in Eq. 3.8 and Eq. 3.9. The asymmetry is calculated around an axis, which is why the velocity is multiplied by the distance in the z or y direction from the axis which it is taken around. I.e. I_y is the asymmetry around the y axis, the same how the y component of a moment is taken around the y axis. Therefore, it is expected the components of the asymmetry vector will correlate well with the OOPBM vector components.

$$\mathbf{I} = (I, \theta_I) = (I_y, I_z) = \iint_A u_{x'} \mathbf{r} dA, \tag{3.7}$$

where $\mathbf{r} = (z\widehat{e}_y,\, y\widehat{e}_z)$ is the distance from the origin (rotor centre) to a point on the rotor disk, $I = |I|$ and $dA = dydz$. The components of $\mathbf{I}$ are

$$I_y = \iint_A u_{x'} z dA, \tag{3.8}$$

$$I_z = \iint_A u_{x'} y dA. \tag{3.9}$$

Figure 3-29 illustrates how the rotor-normal velocity is integrated numerically to calculate the asymmetry vector. The plane normal to the rotor disk is (400 m $\times$ 300 m) with (1280 $\times$ 960) data points, thus $(dy, dz) = (0.3125\,\text{m} \times 0.3125\,\text{m})$. To perform the asymmetry vector calculation a grid is created on top of the planar data so the origin is located at the centre of the rotor disk, so the asymmetry is calculated around the centre of the rotor. The coordinates of the velocity are checked if it is within the rotor

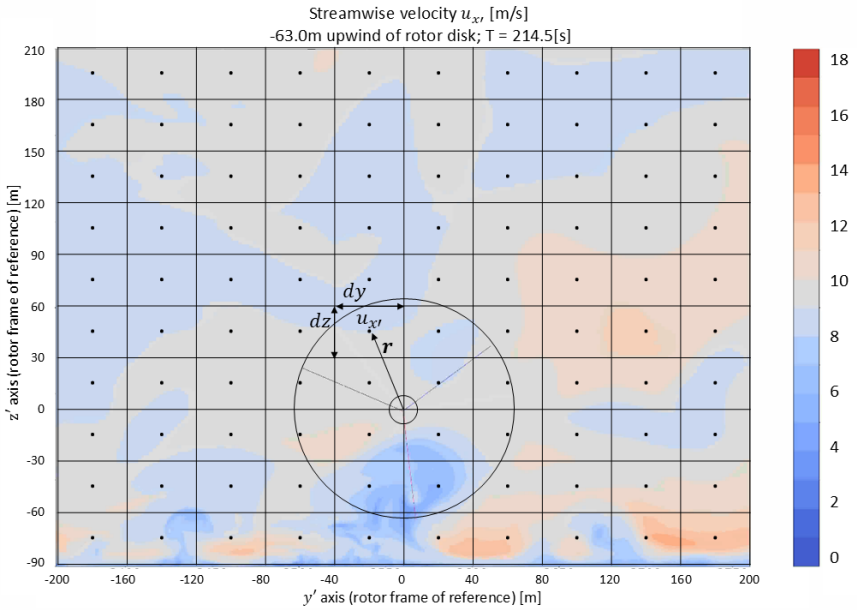

Figure 3-29: Illustration of the numerical estimation of the asymmetry vector (Eq. 3.7) from the rotor-normal velocity defined over continuous space. The grid resolution shown is not to scale.

disk, but also if it is outside the inner annulus. Since the nacelle is not modelled (see section 3.4) a jet of high-speed fluid is generated in the inner annulus with a radius of 1.5 m. Therefore the inner annulus of radius 1.5 m is not included in the integration.

Figure 3-30 shows the asymmetry vector magnitude is in excellent agreement with the asymmetry parameter as it captures the same time variations in the velocity distribution over the rotor disk.

3.7 Development of a Blade Asymmetry Vector

The blade asymmetry was developed due to the need to calculate a measure of asymmetry with a higher range of frequencies compared to the range that can be calculated using the planar data. The blade asymmetry vector represents the asymmetry the blades experience as they rotate through the velocity field. Thus, low-frequency content should correlate well with the asymmetry vector and asymmetry parameter.

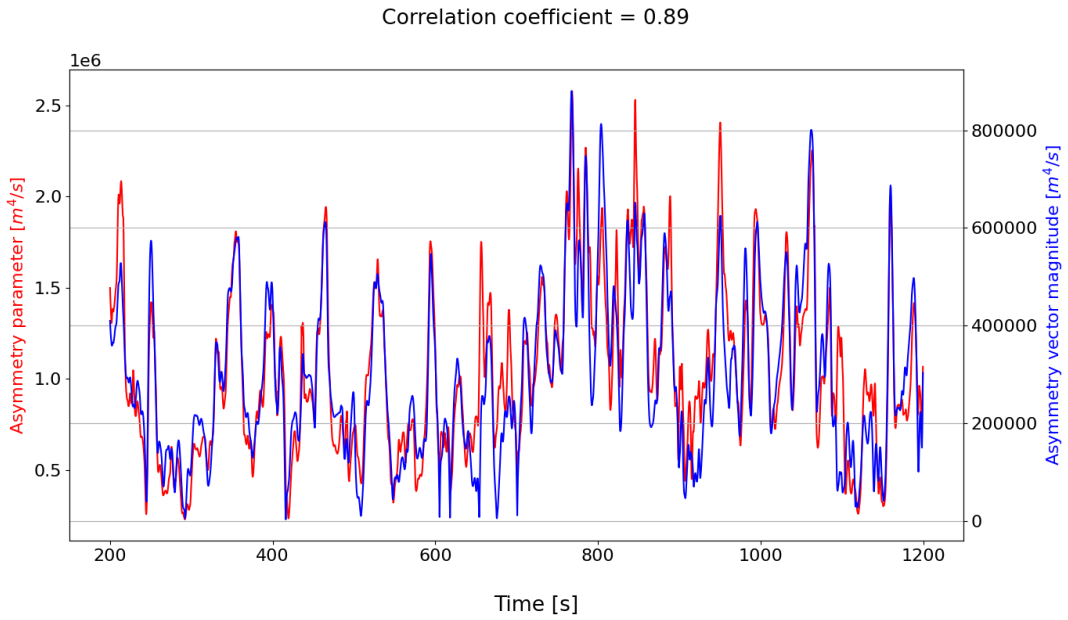

Figure 3-30: Correlation between asymmetry parameter and magnitude of asymmetry vector.

The new asymmetry metric is denoted the blade asymmetry vector and utilises the velocity and coordinates output at each actuator point on the three blades. The blade asymmetry vector has a similar derivation to the asymmetry vector. The asymmetry vector is integrated over every point within the rotor disk, the blade asymmetry is integrated over the blades individually, then summed over the three blades Eq. 3.10

$$\mathbf{I}_B = (I_B, \theta_{I_B}) = (I_{B,y}, I_{B,z}) = \sum_{j=1}^{3} \int_0^R u_{x',j} \mathbf{r}_j dr \tag{3.10}$$

where $I_B = |I_B|$, $\mathbf{r}_j = (z_j \widehat{e}_y, y_j \widehat{e}_z)$ is the distance from the origin (rotor) to an actuator point along the blade, where j indicates the blade. There are 300 actuator points on each blade, thus $dr = 0.21$ m. The components of $\mathbf{I}_B$ are

$$I_{B,y} = \sum_{j=1}^{3} \int_0^R u_{x',j} z_j dr, \tag{3.11}$$

$$I_{B,z} = \sum_{j=1}^{3} \int_0^R u_{x',j} y_j dr. \tag{3.12}$$

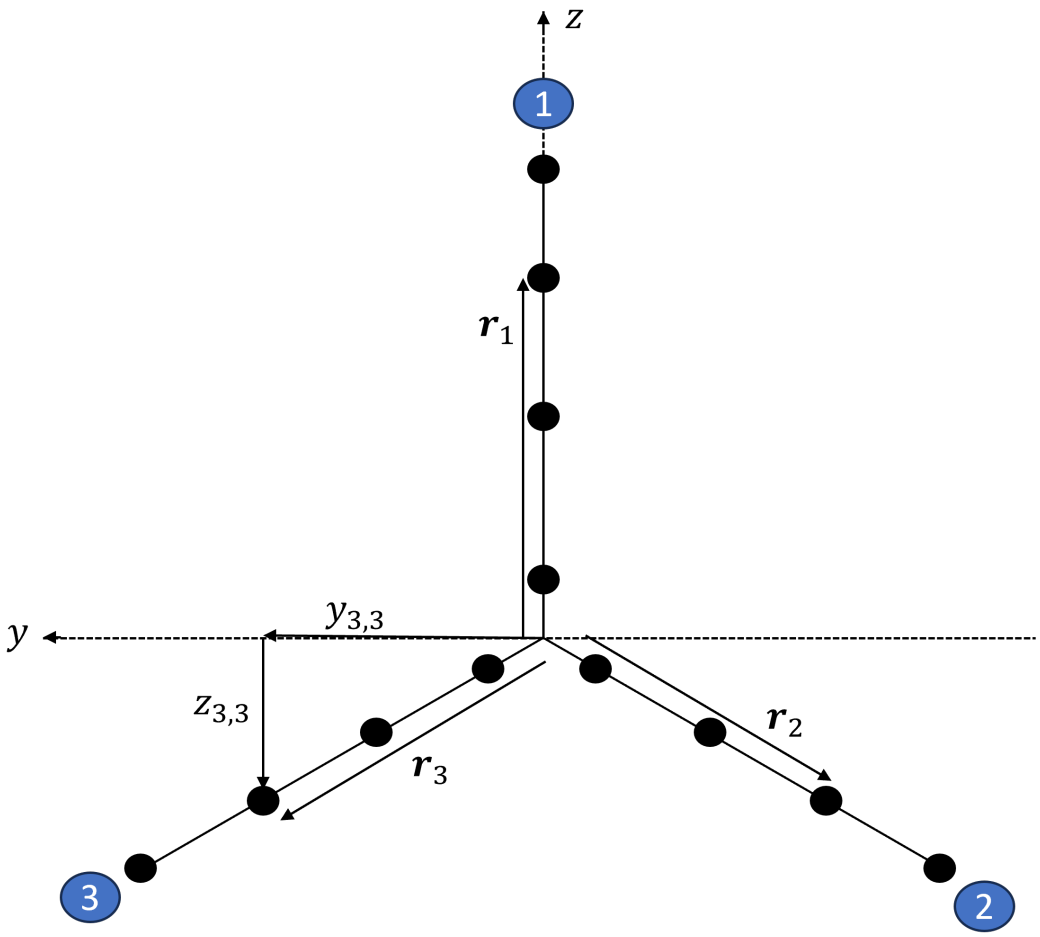

Figure 3-31: Illustration of the algorithm and terms in blade asymmetry vector, using data output at the actuator points.

Figure 3-31 illustrates how the velocity and coordinates output at each actuator point is used to calculate the blade asymmetry vector. To perform the blade asymmetry vector calculation, the coordinates of the actuator points in the (y', z') coordinate system are required, where the origin is shifted so it is located at the centre of the rotor disk and is illustrated in Figure 3-31.

Figure 3-32 shows the low-frequency content of the blade asymmetry vector magnitude

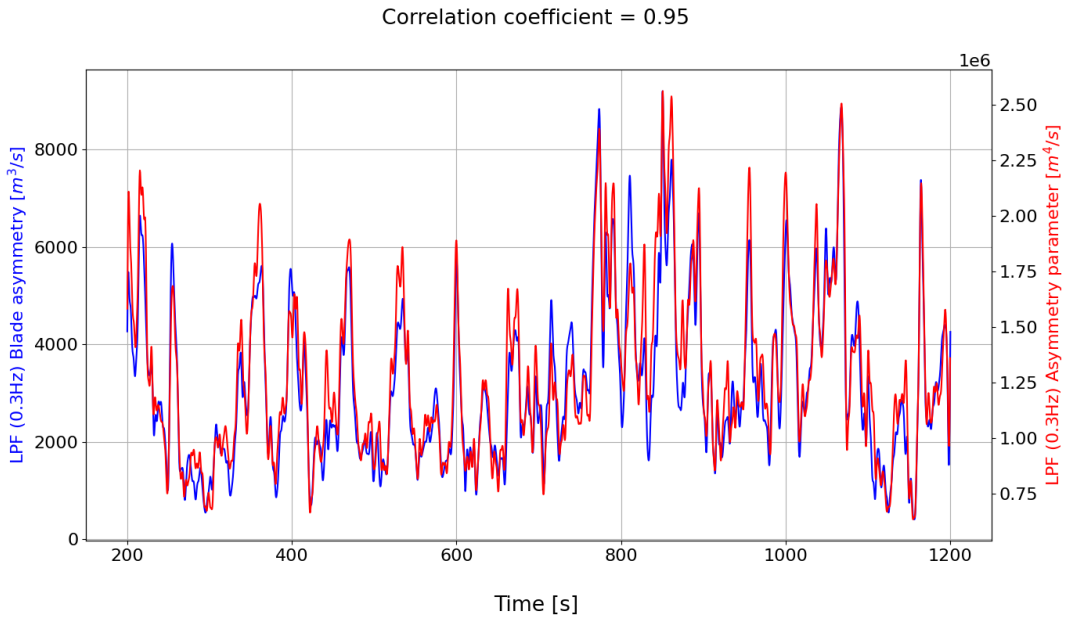

Figure 3-32: Correlation between asymmetry parameter and the low-frequency content (LPF 0.3 Hz) blade asymmetry vector magnitude.

is in excellent agreement with the asymmetry parameter, indicating the blade asymmetry is able to capture the same time variations in the velocity distribution over the rotor disk at the low-frequency time scales.

3.8 Time shift Analysis

Planar data of the rotor-normal velocity field over the rotor disk is offset at 0.0 m and 63.0 m in front of the rotor plane. It was decided that the asymmetry vector and mean rotor-normal velocity over the rotor disk should be calculated from the plane 63.0 m in front of the rotor disk, to ensure the blade wakes are not influencing the velocity field. Often rotor variables output from OpenFAST need to be compared with variables calculated from the velocity field. However, since the velocity field is 63.0 m in front of the rotor the time of the signals are not synchronized in time.

To synchronize the signals in time Taylor's frozen turbulence hypothesis is employed. The turbulence is assumed to be advected entirely by the average flow, thus the signals

are linearly shifted in time. To test the accuracy of applying Taylor's frozen turbulence hypothesis the asymmetry vector magnitude and rotor averaged wind speed calculated at both 0.0 m and 63.0 m in front of the rotor disk are linearly shifted in time, and then correlated and plotted against time shift.

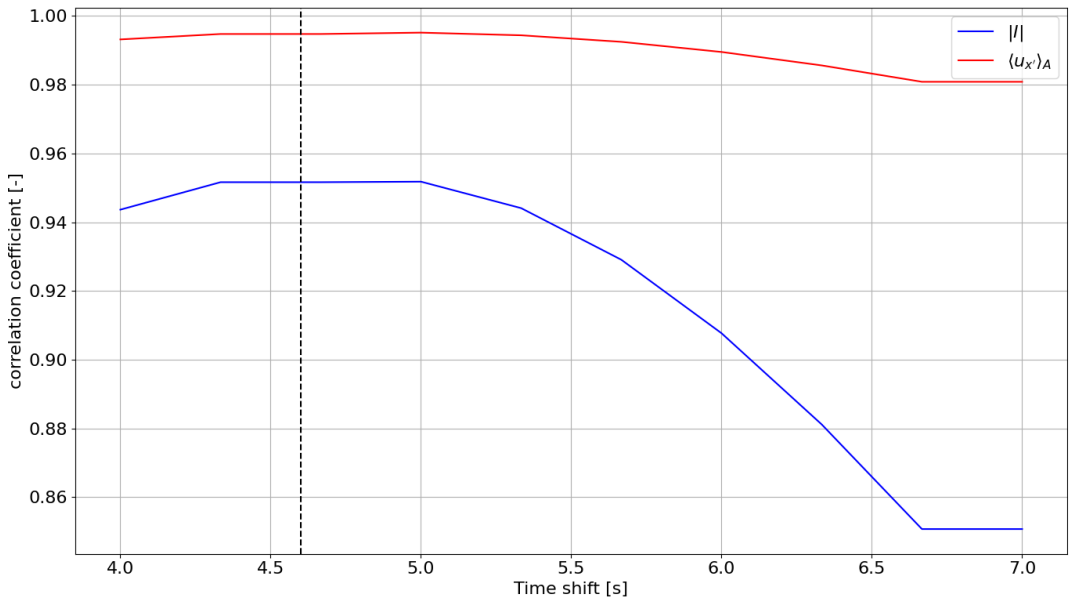

Figure 3-33: Correlation coefficient between time shifted asymmetry vector magnitude calculated from planar data 0.0 m and -63.0 m in front of the rotor disk (blue curve) and time shifted rotor averaged wind speed calculated from planar data 0.0 m and -63.0 m in front of the rotor disk (red curve).

Figure 3-33 shows the the maximum correlation coefficient for both the rotor averaged wind speed and asymmetry vector magnitude, after the time shift has been applied, is 4.6 s. Taylor's frozen turbulence hypothesis is able to be applied reasonably well to the ABL-turbine simulation because the eddy turnover time is orders of magnitude longer than the time shift applied, meaning only the smaller fluctuations in the eddies change during the time the eddy advects 63.0 m into the WT rotor, which is shown does not have a significant effect on the time variations.

3.9 Calculation of Peak-to-Peak Values in a Signal

In Chapter 6 and Chapter 7 the peak-to-peak variations in the OOPBM magnitude and bearing force magnitude are analysed. Here we describe the method used to calculate the magnitudes of the peak-to-peak changes in the force ΔF and the corresponding time over the change Δt. The "derivative method" takes advantage of the fact that the zero crossings of the derivative of a signal give the location in time of the peaks and troughs of the signal.

Figure 3-34a shows the band-pass filtered (0.3 Hz - 0.9 Hz) MB radial force magnitude (blue), the derivative of the signal (black), and shows how the zero crossings of the derivative indicated by the green dots line up vertically with the peaks and troughs of the signal indicated by the red dots. The changes in the magnitude often referred to as "jumps" and the corresponding changes in time are calculated between one peak and the next (see Figure 3-34a).

Figure 3-34b illustrates the derivative method for the high-frequency content (HPF 1.5 Hz - 40 Hz) of the MB radial force magnitude. Comparing the derivative method for the BPF and HPF MB radial force magnitude signals, the method qualitatively works well for both signals, even with the higher frequency content in the HPF signal.

3.10 Filtering

In several of the analyses undertaken in this thesis, the signals analysed over the 1000 s are filtered. To filter the signals a spectral approach is employed. The filtering process is as follows: the signal is fast Fourier transformed (FFT), then the desired Fourier coefficients are zeroed out, depending on the type of filter. The filtered signal in Fourier space is then inverse Fourier transformed (IFFT) back into the time domain. Two types of filters are used: the low-pass filter (LPF) and the band pass filter (BPF). Figure 3-35 demonstrates how the two types of filters are used to filter the main bearing

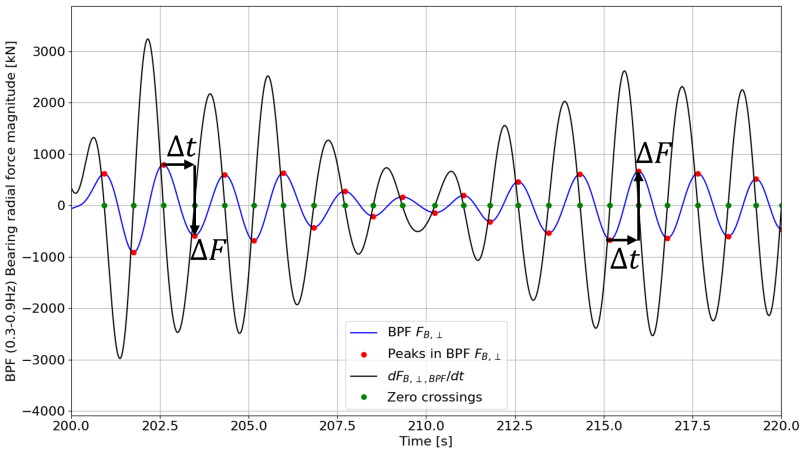

(a)

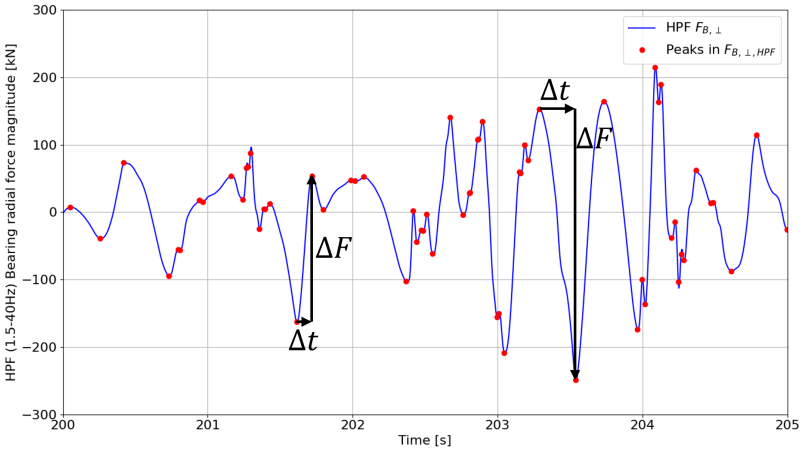

(b)

Figure 3-34: Illustration of the derivative method (a) BPF (0.3 - 0.9 Hz) main bearing radial force magnitude, derivative, zero crossings in derivative and corresponding peaks plotted over a 220 s period (b) HPF (1.5 - 40 Hz) main bearing radial force magnitude and corresponding peaks plotted over a 5 s period.

force magnitude, to generate three different signals which capture the low-frequency content, 3P-frequency content and high-frequency content (see Chapter 6). Because these are sharp filters in Fourier space, over the range of frequencies where the filter value is zero, the Fourier coefficients are zeroed out, the spectra shows the signal drops off to numbers so small they are considered machine error.

The type of filter used is often referred to as hard filters in Fourier space as it zeroes out

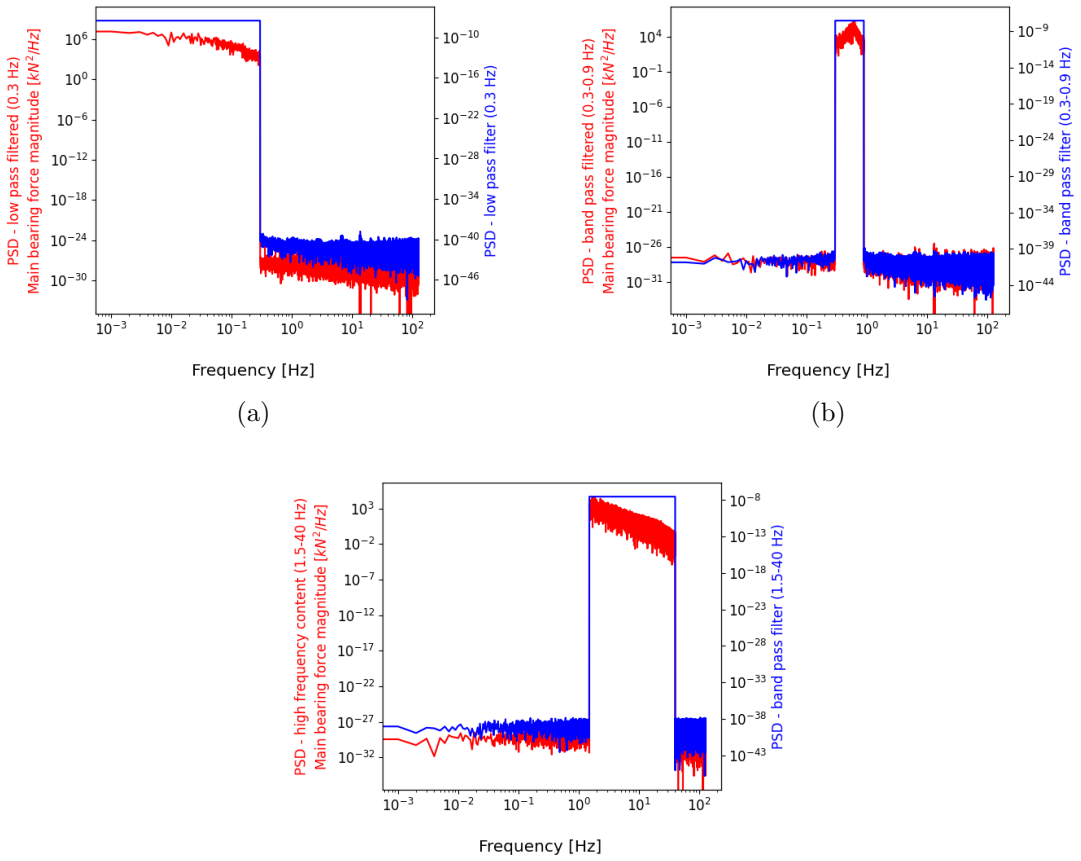

Figure 3-35: Spectra filtered Main bearing force magnitude (left axes) and FFT of respective filter (right axes) (a) Low pass filtered (0.3 Hz). (b) Band pass filtered (0.3 - 0.9 Hz). (c) High frequency content Band pass filter (1.5 - 40 Hz).

the Fourier coefficients above or below a single frequency. Other types of filters exist such as a Gaussian filter which smoothly transitions from 1 to 0 through the cutoff frequency, however, it is more difficult to analyse the behaviour of these types of filters, so the simple hard filter was chosen. Figure 3-35 also shows the corresponding hard filter in frequency space, the filter is shown to sharply cut off at specific frequencies. The hard filter in frequency space results in a sinc function, in the time domain. Figure 3-36 shows the right side of the LPF in time over a 10 s period. The exact solution of the sinc function is known and zero crossings in Figure 3-36 can be checked against the exact solution. The IFFT of a hard LPF filter produces a sinc function where the

signal crosses through zero every $1/2f_0$, where f_0 is the cutoff frequency, in the case of the LPF used in Figure 3-35a $f_0 = 0.3$ Hz, thus the signal should cross zero every 1.6 s. Checking against Figure 3-36 the signal does indeed match the exact solution.

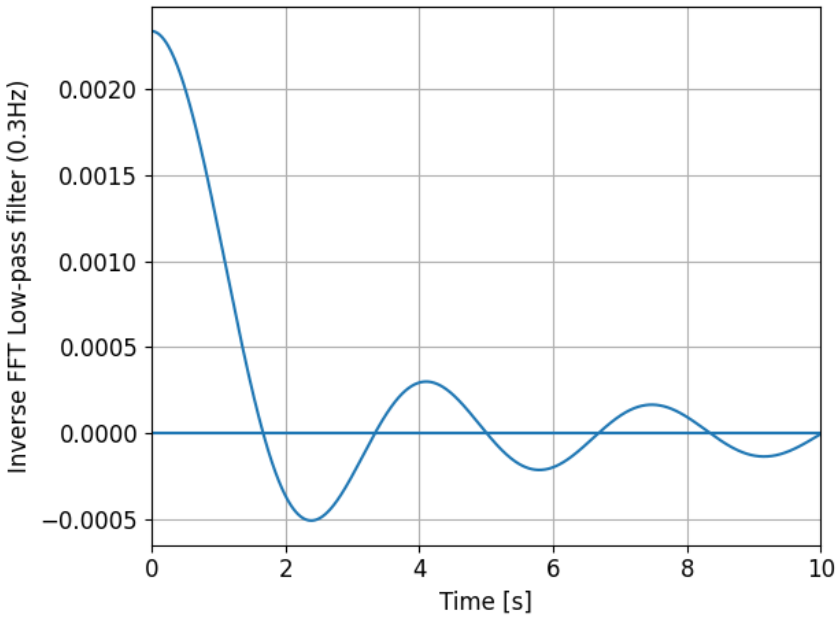

Figure 3-36: One side of the inverse fast Fourier transform of the low-pass filter ($f_0 = 0.3$ Hz) plotted over a 10 s period.

3.11 Summary

This chapter developed and validated a high-resolution large-eddy simulation (LES), of the daytime atmospheric boundary layer, and aeroelastic model of the NREL 5 MW wind turbine that forms the foundation for the analysis in the following chapters. The NREL 5 MW wind turbine is modelled in OpenFAST, and is two-way coupled to AMR-Wind via the Actuator Line Method (ALM). Both rigid and deformable blade configurations are developed to isolate the aerodynamic contribution and blade elasticity on load fluctuations. [Brasseur and Wei, 2010] framework was employed to improve the accuracy in the surface layer, where LES typically struggles. It was established the advective scheme weno_z, aspect ratio 0.66, and one-equation model constant of 0.07

minimised the influence of the overshoot to the maximum extent possible, but could not be completely removed, likely due to the contributions from numerical dissipation in the AMR-Wind code. A novel method is used to characterize eddy passage time, found to be between 19 s - 71 s in good agreement with the literature, and distinguish between low-speed streaks (LSS) and high-speed regions (HSR), $u'_{x'} <$ -0.61 m/s and $u'_{x'} > 0.76$ m/s respectively.

Chapter 4

Sensitivity Analysis of the Actuator Line Method Coupling the LES-ABL Precursor to the Multi-body Aeroelastic Wind Turbine Simulation

This section outlines the actuator line model (ALM), coupling the LES ABL code (AMR-Wind), and the WT multi-body aeroelastic code (OpenFAST). Describes the methodology used to parametrize the actuator line model, and analyses the sensitivity of varying the ALM parameters. The time series of rotor aerodynamic forces and moments, in the rotating frame of reference (see section 3.4.1), are compared for varying ALM parameters. Additionally, the radially distributed variables angle of attack (AoA), coefficient of drag (Cd), coefficient of lift (Cl), normal airfoil force (Fn), tangential airfoil force (Ft) and axial velocity (Vx) in the airfoil coordinate system are

compared for varying ALM parameters. The first 5 seconds of data was removed to remove initial transients from OpenFAST.

The average absolute percentage change between two signals is the primary measure used to quantify the sensitivity. An issue with the average absolute percent change is, for variables that cross zero (Eg. y and z force and moment components), the average absolute percent change is exaggerate due to dividing by very small numbers. Therefore, for variables with zero crossings $1.5\times$ the minimum value is added to the time series to linearly shift the signal above zero, to remove the zero crossings. Radially distributed data is averaged over the last 3 rotor rotations, the same measures of change are used, but the averages are over the span.

4.1 Actuator Line Method Numerical Implementation

AMR-Wind solves for the evolution of the atmospheric boundary layer, restarting from 38000 s into the precursor ABL simulation. The velocity at cell centres from the AMR-Wind domain, within each body force volume is trilinearly interpolated to its respective actuator point. The velocity at the actuator point is passed to OpenFAST which calculates the actuator forces at each actuator point, defined in the AeroDyn blade file. The actuator force per unit volume is passed back to AMR-Wind, where the actuator force is distributed across CFD grid points that are within a body force volume using a Gaussian body force projection function (see section 2.2). The discretized force is added to the right-hand side of the Navier-Stokes equation at the half-time step in the evolution of the ABL algorithm and applied at the location at n+1/2 time step, because the Godunov time stepping scheme discretizes source terms at the half time step [ExaWind Project, 2025].

Correct implementation of the ALM with consideration to the time stepping scheme used to advance the fluid flow (N-S) is imperative to the accuracy of the actuator forces. Incorrect implementation leads to diverging solutions as the time step is reduced, as

the author found out while testing an early version of the ALM implemented in AMR-Wind.

Accurately calculating the actuator forces requires the velocity to be sampled precisely at the locations of the actuator points. This relies on the accuracy of interpolation schemes to interpolate the velocity from the CFD grid points to the actuator points, and sampling the velocity at the actuator points at the beginning of each time step. This ensures the velocity is sampled after the body force has been applied to the fluid flow to ensure the velocity is at the centre of the body force.

4.2 Classical Actuator Line Model Sensitivity Analysis

The classical ALM parameters: body force projection length scale ϵ, CFD grid spacing Δ, since the CFD grid spacing is largest in the z direction Δz is quoted in any results, actuator point spacing ΔR and time step Δt are systematically varied. The "sensitivity" of varying the above parameters is analysed to optimize the parametrization of the ALM. For the following study classical means ϵ is fixed along the span of the blade.

It is most convenient to define non-dimensional parameters to parametrize the ALM. In the literature ϵ/Δ has been well studied and represents how well the body force projection function is being resolved by the CFD grid, and typically values greater than 2 are quoted as being the minimum to avoid under-resolution (see Section 2.2.3). In AMR-Wind ϵ/Δ is varied by changing the number of levels of refinement around the rotor (see section 3.5) or changing the value of ϵ.

The non-dimensional parameter $\epsilon/\Delta R$ was proposed, and is referred to as the "smoothing" parameter, because for fixed ϵ increasing the smoothing parameter by increasing the number of actuator points, thus decreasing ΔR, increases the number of body forces contributing to the force distribution along the span creating a smoother overall force distribution. This can be demonstrated using a simple 1D ALM code, comparing

$\epsilon/\Delta R = 0.65$ (Figure 4-1a) and $\epsilon/\Delta R = 0.85$ (Figure 4-1b) for a fixed ϵ the body forces overlap more and more to a point where the force distribution is smooth along the span. Using the simple 1D ALM code $\epsilon/\Delta R = 0.85$ is the minimum required to achieve a smooth force distribution along the blade. However, a reasonably small value of ϵ is required to accurately capture strong gradients in the force distribution along the span (Figure 4-1). Using the simple 1D ALM code it was determined $\epsilon = 1\,\text{m}$ was sufficiently small to resolve a step change in a force distribution.

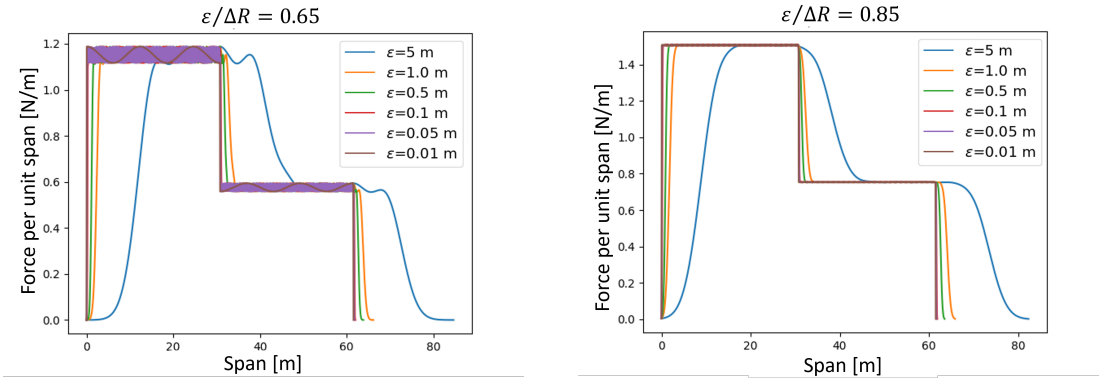

(a) (b)

Figure 4-1: Force per unit span calculated from a 1D actuator line method, for a 63 m span, plotted as a function of ϵ m (a) smoothing ratio $\epsilon/\Delta R = 0.65$, and (b) smoothing ratio $\epsilon/\Delta R = 0.85$.

Finally, the non-dimensional parameter denoted blade sweep ratio (BSR) was introduced, defined as the number of grid cells the blade traverses per time step

$$BSR = \Delta_{Blade}/\Delta t, \tag{4.1}$$

where Δ_{Blade} is defined as the time for the blade tip to traverse 1 grid cell. It is a common conception that the BSR must be less than or equal to 1. This non-dimensional parameter is similar to the CFL number, and the condition that the $BSR \leq 1$ is to maintain stability in the calculation. Going deeper, stability is maintained by ensuring the body force projection distributed from actuator point i at time n is sufficiently

overlapped by the same body force projection but at time n+1. It is argued that $BSR = 1.0$ is not the limit on stability, and the limit is connected to the non-dimensional parameter ϵ/Δ. The limit of the BSR is discussed further in the following section.

4.2.1 Time Step Analysis

Table 4.1 outlines the key parameters and non-dimensional parameters that define the ALM for the time step analysis. The time step is varied which subsequently changes the BSR. BSRs of 2.0, 1.0 and 0.5 are chosen. $\epsilon = 1\,\text{m}$, $\epsilon/\Delta R = 0.85$ were chosen based on the findings from the 1D study, $\epsilon/\Delta z = 2$ was chosen to satisfy the minimum stability criteria from the literature.

Analysing the sensitivity of varying the BSR, the time series and radially distributed data is low pass filtered at 10 Hz, after the first 5 seconds of the data is removed, to remove spurious high frequency content, and ensuring the data is compared over the same range of frequencies. Lastly, the time series data is interpolated so all data has a time step of $\Delta t = 0.0078\,\text{s}$, to ensure the time step is the same for all three cases.

Table 4.1: Description of classical ALM time step sensitivity analysis.

	$\epsilon/\Delta z$	Δz	No. levels of refinement	ϵ	No. actuator points	$\epsilon/\Delta R$	Δt	BSR
1a	2	0.47 m	5	1 m	54	0.85	0.0078 s	2.0
1b	2	0.47 m	5	1 m	54	0.85	0.0039 s	1.0
1c	2	0.47 m	5	1 m	54	0.85	0.00195 s	0.5

Table 4.2 shows the average absolute percent change, for the time series and radially distributed data, converges with decreasing Δt and the average absolute percent change is less than 1%. Figure 4-2 shows the spectra for $\widetilde{F}_{H,x}$, the spectra illustrates as the time step increases the high frequency spurious content shifts to lower frequencies. This could be an issue, as the high frequency spurious content moves to lower frequencies, the spurious content will have a larger contribution to the signal.

Whilst testing the ALM algorithm it was found the ALM algorithm can run using a

Table 4.2: Summary of average absolute percent change comparing 1a to 1b and 1b to 1c.

	Average absolute percent change [%]											
	$\widetilde{F}_{\widehat{H},x}$	$\widetilde{F}_{\widehat{H},y}$	$\widetilde{F}_{\widehat{H},z}$	$\widetilde{M}_{\widehat{H},x}$	$\widetilde{M}_{\widehat{H},y}$	$\widetilde{M}_{\widehat{H},z}$	AoA	Cl	Cd	Fn	Ft	Vx
1a to 1b	0.34	0.54	0.61	0.54	0.71	0.79	0.24	0.12	0.13	0.29	0.52	0.2
1b to 1c	0.15	0.26	0.24	0.3	0.3	0.3	0.34	0.18	0.08	0.11	0.34	0.14

BSR = 2, indicating that the maximum limit of the BSR may not be 1 as suggested in the literature. It is hypothesized the maximum BSR may be connected to ϵ/Δ. From experience the calculation was not able to run with a BSR > 2, suggesting that the BSR may be related to ϵ/Δ. Furthermore, the average absolute percent change between 1a and 1b is not significantly higher than the average absolute percent change between cases 1b and 1c, indicating the calculation may still be behaving correctly. Taking case 1a as an example $\epsilon/\Delta z = 2$. This means in the z direction, ϵ which represents the standard deviation of the Gaussian body force projection, extents $2\Delta z$, and the BSR = 2 means, from time step n to $n+1$ the blade tip, which will move the furthest distance, moves 2 grid cells. Therefore, for case 1a the body force at time n will overlap with the same body force projection at time $n+1$ by $2\Delta z$ or ϵ. There may be a number of other reasons for a calculation with a BSR = 2 remaining stable, such as the ability of the numerical algorithms in AMR-Wind being able to tolerate instabilities. However, there are significant cost savings to being able to increase the size of the time step therefore, it would be worthwhile investigating further in a future study.

To summarize, the sensitivity decreases with decreasing Δt, the average absolute percent change is less than 1%, However, the spectra shows the spurious high frequency content is located at approximately 10 Hz for case 1a and 100 Hz for cases 1b and 1c. Therefore, case 1b $\Delta t = 0.0039\,\mathrm{s}$, BSR = 1.0 is chosen.

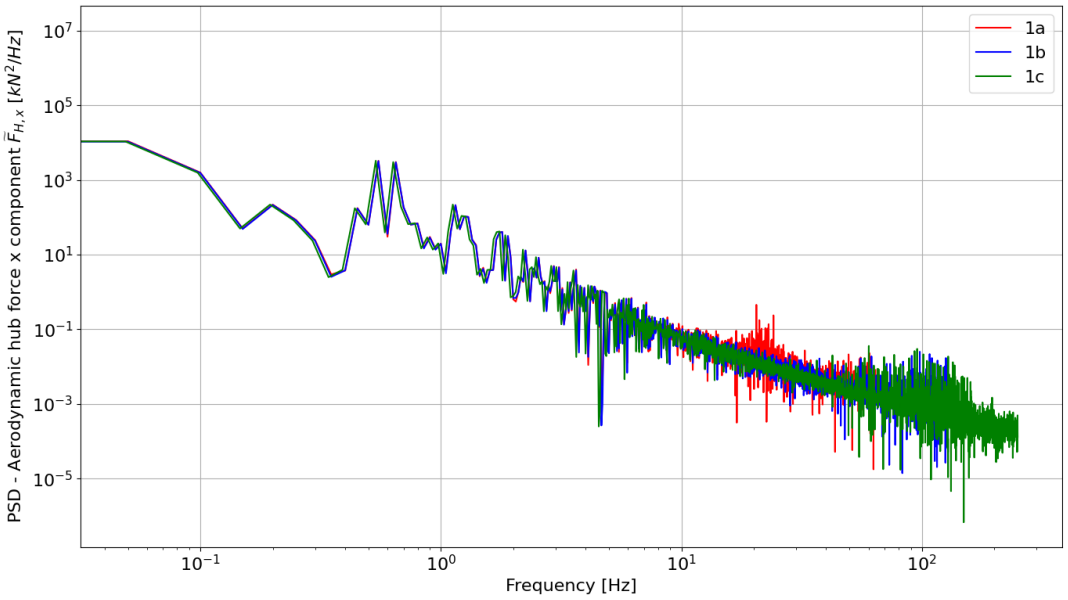

Figure 4-2: Power spectral density (PSD) frequency spectra comparing cases 1a,1b and 1c aerodynamic hub force x component.

4.2.2 Actuator spacing Analysis

Table 4.4 outlines the key parameters and non-dimensional parameters that define the ALM for the actuator spacing study. The actuator spacing is varied by changing the number of actuator points along the span, which subsequently changes the smoothing ratio ($\epsilon/\Delta R$). Smoothing ratios of 0.75, 0.85 and 0.95 are chosen. The time step is fixed from the result of the time step analysis. In order to directly compare radially distributed variables with different numbers of data points, the data is interpolated along the span.

Analysing the sensitivity of varying the smoothing parameter, the time series data and radially distributed data is low pass filtered at 40 Hz to remove the spurious high frequency content. Also, the radially distributed data is interpolated so the number of actuator points is 47 for all cases, so the data can be compared. Also, as a result of changing the number of actuator points, the aerodynamic blade properties within the AeroDyn blade input file were interpolated to ensure the number of actuator points in

OpenFAST matches the number of actuator points in AMR-Wind.

It is important to note when the blade properties are interpolated an airfoil ID needs to be assigned to each actuator point. The airfoil ID identifies a type of airfoil Eg. NACA64 applied to a section of the blade. Figure 4-3 shows the different types of airfoils along the span of the NREL 5 MW blade.

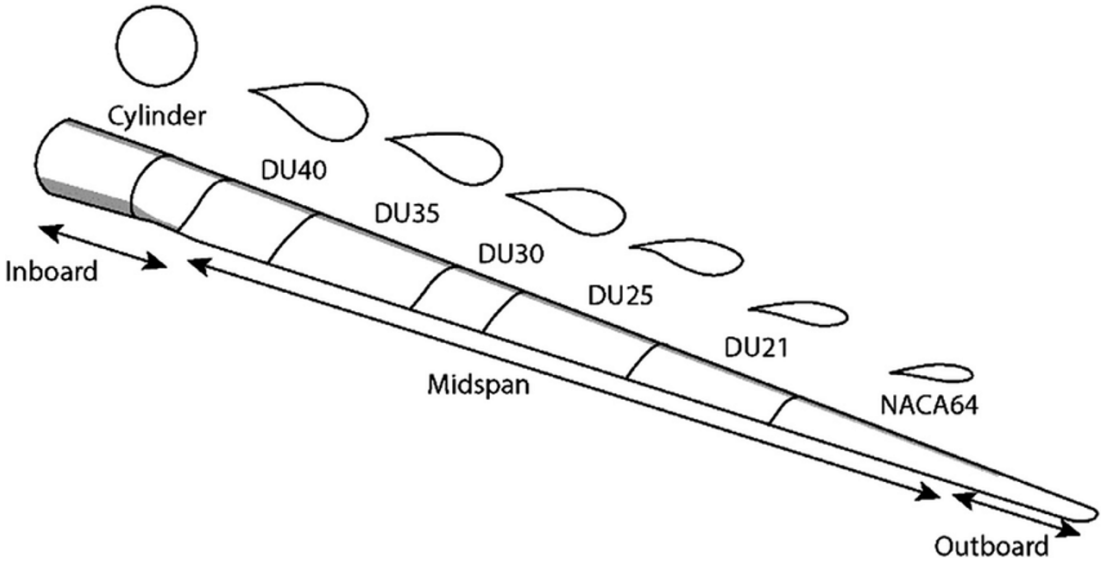

Figure 4-3: Airfoil distribution of NREL 5 MW blade. Acknowledgement: [Joustra et al., 2021].

Spanwise region	Airfoil ID
$R \leq 4.1\,\mathrm{m}$	1
$4.1\,\mathrm{m} < R \leq 10.2\,\mathrm{m}$	2
$10.2\,\mathrm{m} < R \leq 14.35\,\mathrm{m}$	3
$14.35\,\mathrm{m} < R \leq 22.55\,\mathrm{m}$	4
$22.55\,\mathrm{m} < R \leq 26.65\,\mathrm{m}$	5
$26.65\,\mathrm{m} < R \leq 34.85\,\mathrm{m}$	6
$34.85\,\mathrm{m} < R \leq 43.05\,\mathrm{m}$	7
$43.05\,\mathrm{m} < R$	8

Table 4.3: Spanwise airfoil distribution of the NREL 5 MW blade [Jonkman et al., 2009].

Table 4.3 enumerates how the airfoil sections are distributed in the original blade property file found in the NREL 5 MW Baseline OpenFAST model. As a result of the

interpolation the airfoil sections change at slightly different span locations, for different numbers of actuator points, causing spurious spikes in the percentage difference of radially distributed variables (see Figure 4-4). The spurious spikes occur over the transitions between airfoil sections. Therefore, the spurious spikes are removed by omitting the percentage changes at the transitions from the average percent change.

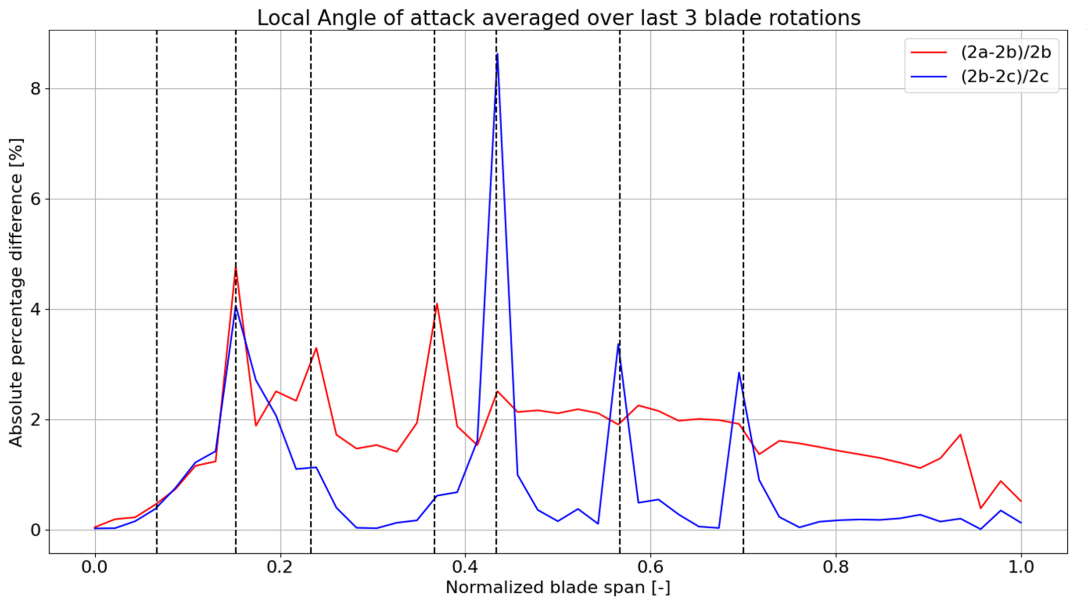

Figure 4-4: Absolute percentage difference plotted against span for local angle of attack illustrating spurious spikes due to transitions between airfoil sections where transitions occur over the vertical dashed lines.

Table 4.4: Description of classical ALM actuator spacing sensitivity analysis.

	$\epsilon/\Delta z$	Δz	No. levels of refinement	ϵ	No. actuator points	$\epsilon/\Delta R$	Δt	BSR
2a	2	0.47 m	5	1 m	47	0.75	0.0039 s	1.0
2b	2	0.47 m	5	1 m	54	0.85	0.0039 s	1.0
2c	2	0.47 m	5	1 m	59	0.95	0.0039 s	1.0

Table 4.5 summarizes the average absolute percent changes, and shows the sensitivity decreases with increasing smoothing ratio. Therefore, $\epsilon/\Delta R = 0.85$ is chosen. Later, in practice, we use 300 actuator points with FLLC, firstly, because more points are needed to maintain the smoothing ratio along the span when a variable ϵ is used, secondly the

literature shows approximately 300 points are required while using FLLC to completely remove the sensitivity at the tip, where the FLLC algorithm modifies the actuator velocity the most and lastly, practically the cost of using 300 actuator points compared to 54 is minimal. Figure 4-5 shows the local normal and tangential airfoil forces per unit length plotted against normalised blade span for the cases given in Table 4.4, where the profiles are in good agreement with the local airfoil forces plotted in [Churchfield et al., 2017]. The dashed lines show the percentage change plotted against normalised blade span comparing 2a to 2b and 2b to 2c. The percentage change between cases 2b and 2c is on average smaller compared with cases 2a and 2b, in agreement with Table 4.5. The percentage change also shows the spurious spikes also observed in Figure 4-4.

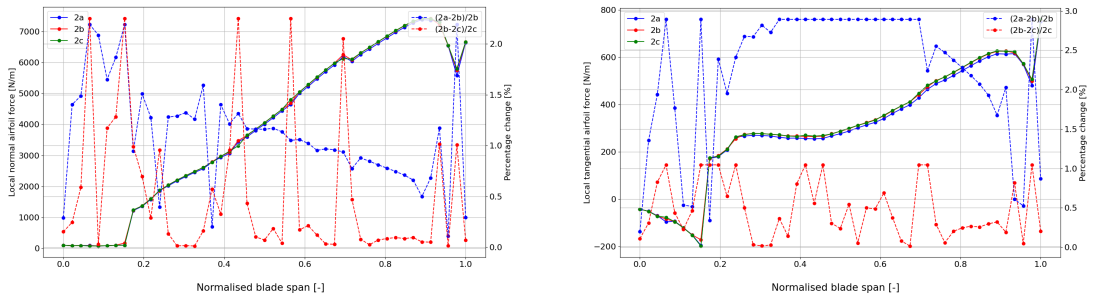

(a) (b)

Figure 4-5: Solid lines show local airfoil force per unit length plotted against normalised blade span for cases given in Table 4.4. Dashed lines show percentage change plotted against normalised blade span comparing 2a to 2b and 2b to 2c. (a) Local normal airfoil force per unit length. (b) Local tangential airfoil force per unit length.

Table 4.5: Summary of the average absolute percent change comparing 2a to 2b and 2b to 2c.

	Average absolute percent change [%]											
	$\widetilde{F}_{\widehat{H},x}$	$\widetilde{F}_{\widehat{H},y}$	$\widetilde{F}_{\widehat{H},z}$	$\widetilde{M}_{\widehat{H},x}$	$\widetilde{M}_{\widehat{H},y}$	$\widetilde{M}_{\widehat{H},z}$	AoA	Cd	Cl	Fn	Ft	Vx
2a to 1b	0.87	0.38	0.37	1.75	0.21	0.18	1.36	0.76	1.13	1.12	2.27	0.84
2b to 2c	0.13	0.08	0.09	0.02	0.05	0.05	0.39	0.2	0.38	0.36	0.61	0.22

4.2.3 Grid resolution Analysis

Table 4.6 outlines the key parameters and non-dimensional parameters that define the ALM for the grid resolution study. The grid resolution is varied by changing the number of refinement levels, which subsequently changes the grid resolution Δ (see Section 3.5) and thus, $(\epsilon/\Delta z)$. $\epsilon/\Delta z = 1$, 2 and 4 are chosen. The time step and smoothing ratio is fixed from the previous analyses.

When designing the grid resolution analysis, it was decided that the time step would be fixed instead of fixing the non-dimensional parameter BSR, because a previous study indicated that the solution is more sensitive to changes in Δt compared to changes in BSR. Due to limited time and resources the sensitivity of Δt compared to BSR could not be fully investigated.

Table 4.6: Description of classical ALM grid resolution sensitivity analysis.

	$\epsilon/\Delta z$	Δz	No. levels of refinement	ϵ	No. actuator points	$\epsilon/\Delta R$	Δt	BSR
3a	1	0.94 m	4	1 m	54	0.75	0.0039 s	0.5
3b	2	0.47 m	5	1 m	54	0.85	0.0039 s	1.0
3c	4	0.23 m	6	1 m	54	0.95	0.0039 s	2.0

Table 4.7 summarizes the average absolute percent change to varying grid resolution and shows the sensitivity decreases with increasing grid resolution for torque, thrust and radially distributed variables. However, $\widetilde{F}_{\widehat{H},y}$, $\widetilde{F}_{\widehat{H},z}$, $\widetilde{M}_{\widehat{H},y}$ and $\widetilde{M}_{\widehat{H},z}$ show increasing sensitivity with increasing grid resolution, which is unexpected.

Figure 4-6 shows the sensitivity increasing for the out-of-plane moments. Qualitatively case 3c tends to predict smaller or larger values at the peaks and troughs of the curve compared to cases 3a and 3b. It is unclear why the sensitivity increased for the out-of-plane moments, so a decision was made based on converging variables and Table 4.7 suggests case 3b is the optimal choice.

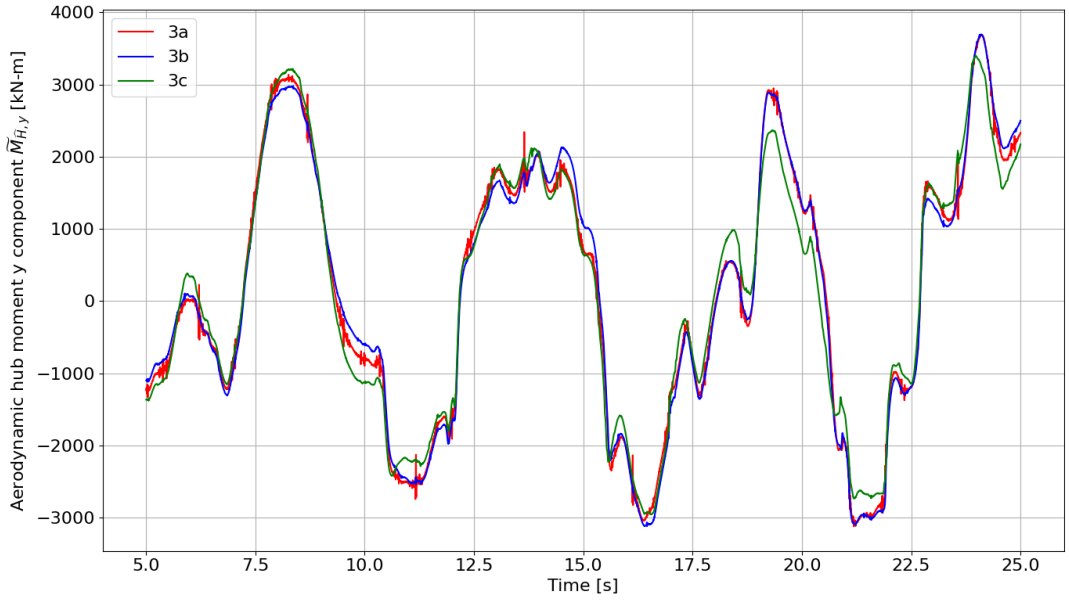

Figure 4-6: Sensitivity to grid resolution time series $\widetilde{M}_{\widehat{H},y}$.

Table 4.7: Summary of average percent change comparing 3a to 3b and 3b to 3c.

	Average absolute percent change [%]											
	$\widetilde{F}_{\widehat{H},x}$	$\widetilde{F}_{\widehat{H},y}$	$\widetilde{F}_{\widehat{H},z}$	$\widetilde{M}_{\widehat{H},x}$	$\widetilde{M}_{\widehat{H},y}$	$\widetilde{M}_{\widehat{H},z}$	AoA	Cd	Cl	Fn	Ft	Vx
3a to 3b	1.26	2.59	2.79	2.85	2.69	2.69	3.00	1.49	2.43	1.7	4.5	1.49
3b to 3c	0.61	6.17	7.15	1.08	6.97	5.74	1.63	0.7	2.4	1.49	2.44	1.04

4.3 Filtered-Lifting Line Correction Actuator Line Model Sensitivity Analysis

In this section the filtered-lifting-line correction (FLLC), implemented in the ALM algorithm in AMR-Wind, is compared against the classical ALM (fixed ϵ), then later parametrized.

4.3.1 Comparing Classical ALM with Filtered-Lifting-Line Correction

The aim of comparing the classical ALM with the FLLC is to observe the differences and investigate the potential increase in accuracy. The FLLC implementation requires additional parameters to be specified compared to the classical ALM: $(\epsilon/c)_{mod}$ and $(\epsilon)_{comp}$. Where mod = model and comp = computational. The FLLC algorithm requires two body force projection lengths to be specified: $(\epsilon)_{comp}$ body force projection that acts on the computational grid and $(\epsilon/c)_{mod}$ body force projection the computational body force is corrected to. The grid refinement ratio ϵ/Δ should be based on ϵ_{comp}, since it "acts" on the computational grid. Additionally, the number of actuator points is increased to 300 points as [Taschner et al., 2024] showed using 300 actuator points with the FLLC completely removes the sensitivity to the number of actuator points, and from experience increasing the number of actuator points does not have a noticeable increase in computation cost. Finally, it was decided to continue using the time step from the classical ALM study (see section 4.2.1), as the inclusion of the FLLC should not affect the stability of the calculation.

Table 4.8: Description of classical ALM case and FLLC cases.

	$(\epsilon/c)_{mod}$	$(\epsilon)_{comp}$	$\epsilon/\Delta z$	Δz	No. levels of refinement
Classical	Fixed ϵ	6.0 m	6.4	0.9375 m	4
FLLC	0.25	6.0 m	6.4	0.9375 m	4
	No. actuator points	$\epsilon/\Delta R$	Δt	BSR	
Classical	300	28.5	0.0039 s	0.5	
FLLC	300	1.74	0.0039 s	0.5	

Table 4.8 describes a classical ALM case and FLLC case, which are compared. To compare the classical ALM with ALM with FLLC, $(\epsilon)_{comp}$ was specified as 6.0 m. A larger $(\epsilon)_{comp}$ was chosen to more easily highlight the differences and be able to draw comparisons between the classical ALM with and without FLLC. $(\epsilon/c)_{mod} = 0.25$ was chosen as the literature suggests this is most optimal [Martínez-Tossas et al., 2016]. 4

levels of refinement was chosen so the grid refinement ratio $\epsilon/\Delta z$ was as high as possible to ensure accuracy, while keeping computational costs low.

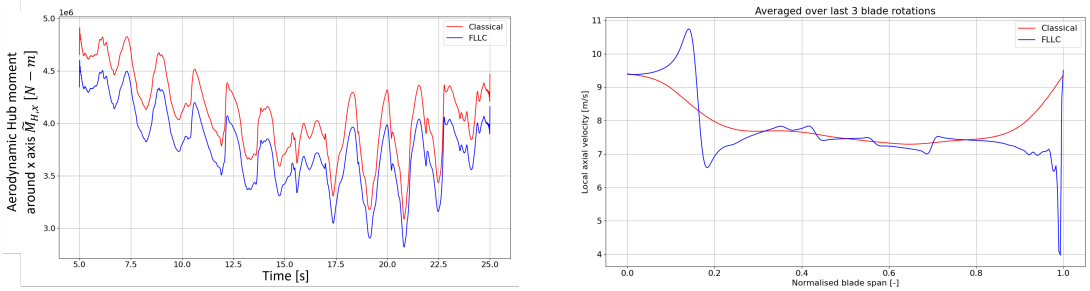

(a) (b)

Figure 4-7: Comparison of the classical ALM against ALM with FLLC. (a) Torque (b) Local axial velocity function of span averaged over last 3 blade rotations.

Figure 4-7b shows effect of the FLLC as it "corrects" the velocity along the blade. Figure 4-7b is in excellent agreement with [Taschner et al., 2024] which also showed there are large differences between the axial velocity along the span of the blade when compared to the classical ALM. Furthermore, the corrections at the root and the tip of the blade are largest [Taschner et al., 2024] [Martínez-Tossas and Meneveau, 2019]. The average absolute percent change in radially distributed variables is between 3-18%, showing the strong influence of the FLLC.

Figure 4-7a shows that FLLC predicts torque having a lower average compared to the classical ALM. The average absolute percent change for hub forces and moments are calculated between 0.5-18%, due to the differences in the radially distributed forces.

In summary, the addition of the FLLC into the classical ALM calculates more representative lift and drag force distributions along the blades compared to the classical ALM. FLLC was shown to make the most difference at the root sections and tip of the blade where classical ALM with fixed ϵ struggles.

4.3.2 Comparing Classical ALM with Chord Varying Epsilon with ALM with FLLC

The aim of comparing the best classical ALM configuration that can be practically achieved, with a comparable FLLC case, is to compare the differences and determine whether it is possible to achieve the same level of accuracy using classical ALM techniques.

Table 4.9: Description of a classical ALM case with a chord varying epsilon, compared with the ALM with FLLC.

	$(\epsilon/c)_{mod}$	$(\epsilon)_{comp}$	$\epsilon/\Delta z$	Δz	No. levels of refinement
Classical	0.5	-	3.0	0.23 m	6
FLLC	0.25	2.0 m	8.5	0.23 m	6
	No. actuator points	$\epsilon/\Delta R$	Δt	BSR	
Classical	74	0.85	0.0039 s	2.0	
FLLC	300	1.74	0.0039 s	2.0	

Figure 4-8 shows there is better agreement between the classical ALM with chord varying ϵ and the FLLC cases, compared to the classical ALM with fixed ϵ. However, the radially distributed variables (Figure 4-8b) continues to show significant differences at the root and tip of the blade. The average absolute percent change for radially distributed variables was calculated between 1.5-7.2%, and 0.4-1.6% average absolute percent change in the hub forces and moments (Figure 4-8a). The average absolute percent changes are smaller compared to the fixed ϵ showing the impact of employing a chord varying ϵ.

However, the differences between the classical ALM with chord varying ϵ compared to ALM with FLLC are due to using a larger ϵ/c. Using a larger ϵ/c for the classical ALM is unavoidable as higher resolution is required to sufficiently resolve the body force at the blade tips. To use an $\epsilon/c = 0.25$ with classical ALM, 7 levels of refinement would be required which is not practical due to computational cost.

In summary, while similar accuracy can be achieved with classical ALM with a chord

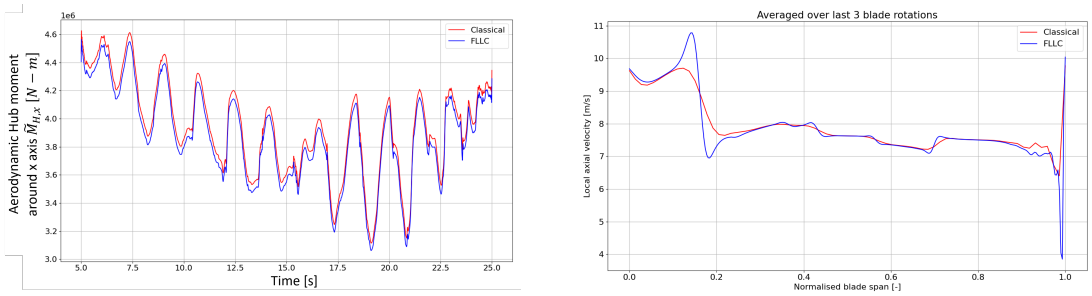

(a) (b)

Figure 4-8: Comparison of classical ALM with chord varying ϵ against ALM with FLLC. (a) Torque (b) Local axial velocity function of span averaged over last 3 blade rotations.

varying ϵ, it is limited by the computational cost. Which is a major advantage of using ALM with the FLLC, as any ϵ/c can be chosen while maintaining the same computational cost.

4.3.3 Computational body force Analysis

The aim of this analysis is to verify the FLLC implementation. [Martínez-Tossas and Meneveau, 2019] showed the FLLC has low sensitivity to changing $(\epsilon)_{comp}$ and as long as $(\epsilon/c)_{mod}$ remains constant this should always be the case as the model is intended to correct from the specified $(\epsilon)_{comp}$ to $(\epsilon/c)_{mod}$.

Table 4.10: Description of the FLLC $(\epsilon)_{comp}$ sensitivity analysis.

	$(\epsilon/c)_{mod}$	$(\epsilon)_{comp}$	$\epsilon/\Delta z$	Δz	No. levels of refinement
4a	0.25	2.0 m	2.1	0.9375 m	4
4b	0.25	6.0 m	6.4	0.9375 m	4
	No. actuator points	$\epsilon/\Delta R$	Δt	BSR	
4a	300	1.74	0.0039 s	0.5	
4b	300	1.74	0.0039 s	0.5	

The results summarized in 4.11 are in good agreement with [Martínez-Tossas and Meneveau, 2019]. Using the FLLC and varying $(\epsilon)_{comp}$ is shown to only have a relatively small effect on the solution. Figure 4-9 shows most the percentage change in the radial distributions appear at the blade tip and root, where the model is know to struggle

due to these being regions of high drag. The integrated variables torque and thrust are shown to be very insensitive to changes in $(\epsilon)_{comp}$ while the out-of-plane bending moment components are slightly more sensitive.

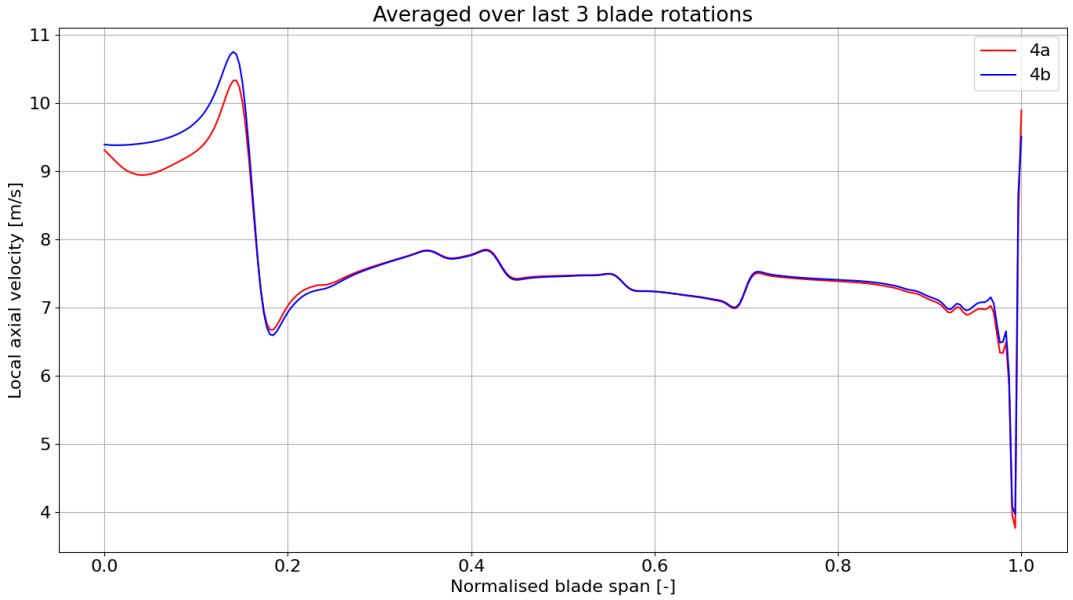

Figure 4-9: Comparing local axial velocity $\epsilon_{comp} = 6.0$ m and $\epsilon_{comp} = 2.0$ m.

Table 4.11: Summary of the average absolute percent change comparing 4a to 4b.

	Average absolute percent change [%]											
	$\widetilde{F}_{\hat{H},x}$	$\widetilde{F}_{\hat{H},y}$	$\widetilde{F}_{\hat{H},z}$	$\widetilde{M}_{\hat{H},x}$	$\widetilde{M}_{\hat{H},y}$	$\widetilde{M}_{\hat{H},z}$	AoA	Cd	Cl	Fn	Ft	Vx
4a to 4b	0.31	1.45	1.39	0.52	1.45	1.4	1.32	0.5	1.55	1.75	2.97	1.03

4.3.4 Filtered-Lifting-Line Correlation Grid Resolution Analysis

In section 4.2.3 the out-of-plane hub forces and moments showed an increase in sensitivity, as the grid resolution was decreased. The grid resolution analysis was repeated using the FLLC, to determine whether the FLLC showed the same increase in sensitivity, in the out-of-plane forces and moments. Table 4.13 shows the same increase in the average absolute percentage change, in the out-of-plane forces and moments, compared with the classical ALM grid resolution analysis (4.2.3).

Table 4.12: Description of the FLLC grid resolution sensitivity analysis.

	$(\epsilon/c)_{mod}$	$(\epsilon)_{comp}$	$\epsilon/\Delta z$	Δz	No. levels of refinement
5a	0.25	2.0 m	2.1	0.94 m	4
5b	0.25	2.0 m	4.2	0.47 m	5
5c	0.25	2.0 m	8.5	0.23 m	6
	No. actuator points	$\epsilon/\Delta R$	Δt	BSR	
5a	300	1.74	0.0039 s	0.5	
5b	300	1.74	0.0039 s	1.0	
5c	300	1.74	0.0039 s	2.0	

Table 4.13: Summary of the average absolute percent change comparing 5a to 5b and 5b to 5c.

	Average percent change [%]											
	$\widetilde{F}_{\widehat{H},x}$	$\widetilde{F}_{\widehat{H},y}$	$\widetilde{F}_{\widehat{H},z}$	$\widetilde{M}_{\widehat{H},x}$	$\widetilde{M}_{\widehat{H},y}$	$\widetilde{M}_{\widehat{H},z}$	AoA	Cd	Cl	Fn	Ft	Vx
5a to 5b	1.48	2.43	2.71	3.17	2.15	2.09	2.97	1.44	2.55	2.1	4.83	1.75
5b to 5c	0.65	6.28	7.24	1.05	7.43	6.02	1.55	0.67	2.17	1.67	2.52	1.06

Therefore, based on the converging variables 5 levels of refinement, $\Delta x, y = 0.31\,\text{m}$ $\Delta z = 0.47\,\text{m}$ is chosen for the grid resolution.

4.4 Summary

In summary, the actuator line method implemented in AMR-Wind showed low sensitivity with a time step of 0.0039 s or lower, blade sweep ratio less than 1.0. Furthermore, the classical ALM shows low sensitivity with a smoothing-ratio of 0.85 or greater. However, this is increased to 300 actuator points for ALM with FLLC. The sensitivity to changing the computational grid size, ϵ/Δ, through changing the number of levels of refinement, was tested with and without FLLC. The thrust and torque, as well as the radially distributed variables, showed low sensitivity with 5 or more levels of grid refinement, however, the out-of-plane forces and moments showed an increase in sensitivity. The final parametrization of the ALM with FLLC is given in 4.14.

Table 4.14: Description of the ALM with FLLC parametrization.

	$(\epsilon/c)_{mod}$	$(\epsilon)_{comp}$	$\epsilon/\Delta z$	Δz	No. levels of refinement
FLLC	0.25	2.0 m	4.2	0.48 m	5
	No. actuator points	$\epsilon/\Delta R$	Δt	BSR	
FLLC	300	1.74	0.0039 s	1.0	

The accuracy of ALM with the FLLC was compared against the classical ALM with fixed ϵ and chord varying ϵ, and in both cases the addition of the FLLC gave a more accurate representation of the blade distributed loads and therefore integrated loads. Classical ALM with chord varying ϵ can achieve similar accuracy, but the major limitation is the maximum grid refinement, limited by computational cost, which is mitigated by using the FLLC. Finally, the functionality of the FLLC within the ALM algorithm was verified by varying $(\epsilon)_{comp}$ and comparing the results with [Martínez-Tossas and Meneveau, 2019].

Chapter 5

Role of the Constituent Terms in the Bearing Force Equation to the Time Variations in the Main Bearing Force Vector

The aim of this section is to provide an understanding of the main bearing (MB) force vector and the role each of the constituent terms play in the time variations in the MB force vector, and understand the primary mechanisms underlying the time variations in the main bearing (MB) force vector, driven by the turbulent velocity field of the ABL in the generation of the non-steady response of the MB force vector.

Figure 5-1 shows the NREL 5 MW 3-point mount drivetrain. Using Figure 5-1, we develop equilibrium force balance equations that relate the moments and forces at the hub to the force acting on the main bearing, at each instant in time. This equation approximates the balance of the MB loads in equilibrium, that is with accelerations neglected i.e. in a quasi-static sense. Further approximations include: neglecting

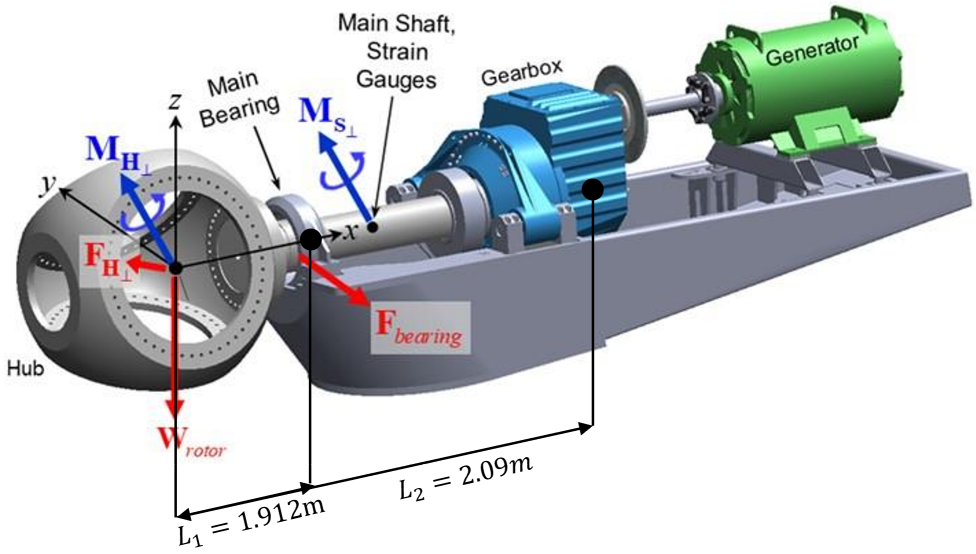

Figure 5-1: Schematic of the hub and 3-point mount drivetrain of NREL 5 MW wind turbine.

frictional forces, neglecting shaft, gearbox and bearing deflection and assuming torque transfer through the MB without loss. [Stirling et al., 2021] compared this simplified analytical model a higher-fidelity 3D finite-element model. Their results indicated reasonable agreement between the analytical model and the 3D FE model.

The first expression below is the force acting on the main bearing, where $F_B = |\mathbf{F}_B|$ is the magnitude of the force acting on the MB. While we want to understand the role of all three components to the time variations in the MB force vector, it is useful to group the y and z components together and separate the x component. The axial force acting on the main bearing is, $F_{B,x} = F_{H,x}$, where $F_{H,x}$ is the force on the rotor hub in the x direction. The second expression below is the result of balancing the loads around the gearbox solving for the force vector acting on the MB in the out-of-plane/radial direction, which points in the plane of the rotor disk (Eq. 5.2).

$$\mathbf{F}_B = (F_B,\, \theta_{F_B}) = (F_{B,x}, F_{B,y}, F_{B,z})\,, \tag{5.1}$$

$$\widetilde{\mathbf{F}}_{B,\perp} = \mathbf{F}_{B,\perp} + \frac{L}{L_2}\mathbf{W}_R = \frac{1}{L_2}\left[\widetilde{\mathbf{M}}_{H,\perp,mod} + L\widetilde{\mathbf{F}}_{H,\perp}\right], \tag{5.2}$$

where:

- Tilde above the variable indicates it is the aerodynamic contribution.
- $\mathbf{F}_{B,\perp} = (F_{B,y}\widehat{e}_y,\, F_{B,z}\widehat{e}_z)$ - main bearing (subscript B) force vector in the out-of-plane (subscript $\perp$) direction, and $F_{B,\perp} = |\mathbf{F}_{B,\perp}|$.
- $\widetilde{\mathbf{M}}_{H,\perp,mod} = \left(-\widetilde{M}_{H,z}\widehat{e}_y,\, \widetilde{M}_{H,y}\widehat{e}_z\right)$ - modified out-of-plane (subscript $\perp$) aerodynamic (tilde) moment vector at the rotor hub (subscript H)
- $\widetilde{\mathbf{F}}_{H,\perp} = \left(\widetilde{F}_{H,y}\widehat{e}_y,\, \widetilde{F}_{H,z}\widehat{e}_z\right)$ - out-of-plane (subscript $\perp$) aerodynamic (tilde) hub force vector
- $L = (L_1 + L_2)$ - distance from the rotor to gearbox (see Figure 5-1)
  - $L_1 = 1.912\,\text{m}$ - distance from the rotor to the main bearing (see Figure 5-1), [Jonkman et al., 2009]
  - $L_2 = 2.09\,\text{m}$ - distance from the main bearing to the gearbox (see Figure 5-1), [Bergua Archeli et al., 2021].
- $\mathbf{W}_R = W_R\widehat{e}_z$ - rotor (subscript R) weight

The lengths L_1 and L_2 are taken from a GE 1.5 MW WT drivetrain [Bergua Archeli et al., 2021]. L_1 is also the same for the 5 MW wind turbine [Jonkman et al., 2009]. Therefore, for convenience L_2 is assumed the same in this work. Although, the distances do naturally affect the magnitude of the MB force, as L_2 is likely undersized for the NREL 5 MW WT simulated in this study, since L_2 appears in all terms in Eq. 5.2 the ratios between all the terms are accurate and also will not affect the frequency response which is of primary interest.

In component form

$$\widetilde{F}_{B,y} = \frac{1}{L_2}\left[-\widetilde{M}_{H,z} + L\widetilde{F}_{H,y}\right] \tag{5.3}$$

$$\widetilde{F}_{B,z} = F_{B,z} + \frac{L}{L_2}W_R = \frac{1}{L_2}\left[\widetilde{M}_{H,y} + L\widetilde{F}_{H,z}\right]. \tag{5.4}$$

The OpenFAST AerodDyn module outputs forces and moments without the weight contributions; the weight contributions are included in the ElastoDyn module. However, due to the turbine configuration used in this analysis - rigid rotor, zero coning angle, zero tilt angle - the force and moment vector components are equivalent with the exception of the z components of the hub force (see section 3.4.2).

To summarize, the main bearing force vector Eq. 5.1 can be separated to analyse the individual contributions to the time variations in the MB force vector. The MB force vector is separated into thrust force ($F_{B,x} = F_{H,x}$) and the MB radial force vector Eq. 5.2, which can be further separated into the modified out-of-plane aerodynamic hub moment (OOPBM) vector ($\widetilde{\mathbf{M}}_{H,\perp,mod}$), out-of-plane (OOP) aerodynamic hub force vector ($\widetilde{\mathbf{F}}_{H,\perp}$) and rotor weight vector ($\mathbf{W}_R$).

The focus of the following analyses is to analyse the contributions of the aerodynamic force and moment vectors acting on the rotor hub, rotor weight vector, and thrust component to the time variations in the main bearing force vector.

5.1 Role of Aerodynamic Loads in the Time Variations in the Main Bearing Force Vector

Eq. 5.2 shows how the aerodynamic out-of-plane (OOP) hub force vector and aerodynamic out-of-plane bending moment (OOPBM) vector contribute to the time variations in the MB radial force vector. To analyse the contributions to the time variations in the MB radial force vector from the aerodynamic load vectors, statistics are calculated

over 1000 s, the first 200 s are removed to allow the wake to fully develop behind the WT and reach a new quasi-stationary state.

Table 5.1: Statistical analysis of main bearing force constituent components (refer to Eq 5.2 - 5.4.

	average [kN]	Standard deviation [kN]	CC with ...
$\lvert\widetilde{\mathbf{F}}_{H,\perp}\rvert\,(L/L_2)$	24.25	14.89	$\widetilde{F}_{B,\perp}$: 0.87
$\lvert\widetilde{\mathbf{M}}_{H,\perp,mod}\rvert\,(1/L_2)$	753.1	467.59	$\widetilde{F}_{B,\perp}$: 1.0
$\theta\left(\widetilde{\mathbf{F}}_{H,\perp}\right)$	-25.13	127.78	$\widetilde{F}_{B,\perp} : -0.26$
$\theta\left(\widetilde{\mathbf{M}}_{H,\perp,mod}\right)$	63.64	88.49	$\widetilde{F}_{B,\perp}$: 0.96
$\widetilde{F}_{B,y}$	-167.36	562.02	$\widetilde{F}_{B,z}$: 0.0
$\widetilde{F}_{B,z}$	425.26	509.34	$\widetilde{F}_{B,y}$: 0.0
$-\frac{1}{L_2}\widetilde{M}_{H,z}$	-154.84	562.1	$\widetilde{F}_{B,y}$: 1.0
$\frac{L}{L_2}\widetilde{F}_{H,y}$	-12.52	17.43	$\widetilde{F}_{B,y}$: 0.01
$\frac{1}{L_2}\widetilde{M}_{H,y}$	429.94	510.9	$\widetilde{F}_{B,z}$: 1.0
$\frac{L}{L_2}\widetilde{F}_{H,z}$	-4.68	18.09	$\widetilde{F}_{B,z}$: -0.07

Table 5.1 summarizes the key statistics over the 1000 s of the aerodynamic MB radial force, aerodynamic OOPBM and aerodynamic OOP hub force vector magnitudes, directions and components. Table 5.1 shows there are strong temporal correlations between the aerodynamic MB radial force magnitude with the aerodynamic OOP force magnitude and aerodynamic OOPBM magnitude, suggesting that the time variations in the MB radial force magnitude may be driven by contributions from both the aerodynamic OOP force and aerodynamic OOPBM. However, the standard deviation of the aerodynamic OOP force magnitude is an order of magnitude smaller than that of the aerodynamic OOPBM magnitude. Thus, although the correlation between the OOP force magnitude and the MB radial force magnitude is strong, the OOP force magnitude does not contribute significantly to the time variations in the MB force. Furthermore, in Figure 5-2 the spectra of the aerodynamic OOP force magnitude is

three orders of magnitude below the aerodynamic OOPBM across the entire frequency range. It is concluded that the aerodynamic OOP force magnitude does not contribute significantly to the time variations in the aerodynamic MB radial force magnitude.

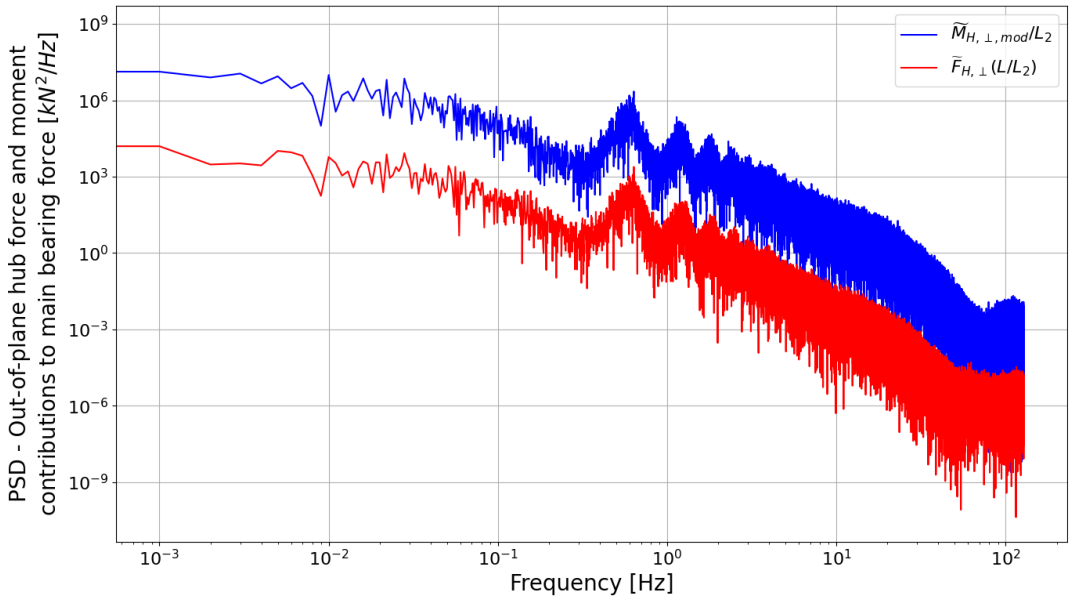

Figure 5-2: Spectra contributions from aerodynamic out-of-plane hub force and aerodynamic out-of-plane bending hub moment to the main bearing force.

Table 5.1 shows that the correlations between the directions (θ) of the aerodynamic MB radial force, the aerodynamic OOP force and aerodynamic OOPBM vectors indicates that the only significant correlation is between the direction of the OOPBM and the aerodynamic MB radial force vectors. The strong correlations between the magnitude and direction of the aerodynamic MB radial force and aerodynamic OOPBM vector, further indicates the aerodynamic MB radial force and aerodynamic OOPBM vectors overall are strongly correlated. Figure 5-3 compares the time "trajectories" for the terms in Eq. 5.2: the aerodynamic MB radial force, the aerodynamic OOPBM divided by L_2, the aerodynamic OOP hub force times L/L_2 and the aerodynamic OOP hub force times $30L/L_2$ vectors, over a 25 s period. The mean and time variations in the aerodynamic OOP hub force contribution $\mathbf{F}_{H,\perp}L/L_2$ to the aerodynamic MB radial force ($F_{B,\perp}$) is so small, compared to the trajectories of the aerodynamic MB radial

force and aerodynamic OOPBM vectors, that the trajectory of $\mathbf{F}_{H,\perp}L/L_2$ had to be multiplied by 30 to be visible. Figure 5-3 shows the trajectories of the MB radial force and hub moment vectors are very similar. It is noted that the trajectory of the OOP aerodynamic hub force vector is rotated by 90°. The above analysis shows the aerodynamic MB force vector is driven nearly entirely by the aerodynamic OOPBM vector. Therefore, contributions from the aerodynamic hub force are neglected when analysing time variations in the MB radial force vector.

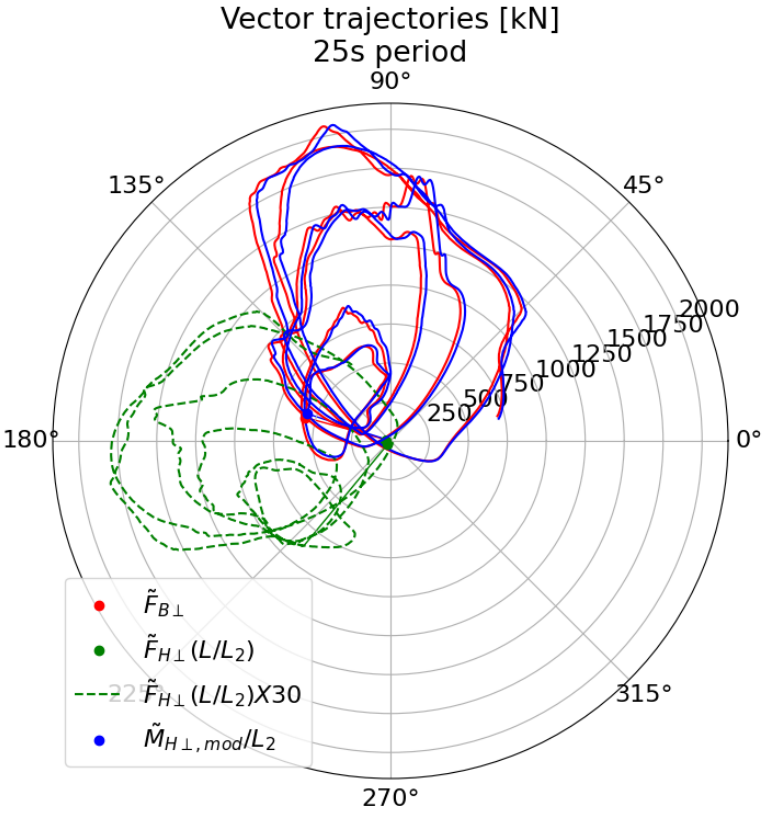

Figure 5-3: Aerodynamic out-of-plane hub force, aerodynamic out-of-plane bending hub moment and aerodynamic main bearing force vector trajectories (refer to terms in Eq. 5.2, over a 25 s period.

Table 5.1 shows that the statistics, with respect to the components of the aerodynamic MB radial force, aerodynamic OOPBM and aerodynamic OOP force, support the same conclusions for the vectors above. Table 5.1 also shows that the correlation coefficient

between the y and z bearing force components is zero. The fact that they are uncorrelated may indicate that the mechanism(s) that drive the time variations in the y component are different to the mechanism(s) that drive the time variations in the z component.

In summary, we conclude from the above that the time variations in the aerodynamic out-of plane main bearing force vector are primarily driven by the out-of-plane aerodynamic hub moments. The aerodynamic OOP force on the rotor hub can be neglected when analysing the time variations in the aerodynamic out-of-plane main bearing force. This leads to the following questions: since the aerodynamic contributions do not include weight, how does rotor weight affect the relationships established? Furthermore, it was discovered that the aerodynamic MB radial force components are uncorrelated, indicating they may be driven by different mechanisms, this issue is analysed in the next section.

5.2 Lack of Correlation between the Out-of-plane Bending Moment Components

Here we analyse the lack of correlation between the y and z components in the aerodynamic MB radial force. The lack of correlation between the y and z components indicates the physics that create the mechanism(s) that drive the y and z components have fundamental differences. Results presented in Section 5.1 shows the aerodynamic OOPBM vector is the primary driver to the time variations in the aerodynamic MB radial force vector. The aerodynamic rotor force is negligible in comparison, and can be neglected. Therefore, in the following analysis the aerodynamic OOPBM is analysed.

It is well understood that the characteristic 3P frequency creates a strong harmonic signal due to the blades interacting with a non-uniform inflow. Furthermore, as the y and z axes are at right angles, i.e. 90°, displaced from each other there will be a

phase shift between the y and z moments, which may underlie the lack of correlation. To investigate this a simple OpenFAST calculation was completed using the same configuration as the NREL 5 MW used in the LES calculation, but using a steady sheared inflow, with a shear exponent of $\alpha = 0.098$ and average hub height wind speed of 12.75 m/s. α_s is calculated using the following expression (power law [International Electrotechnical Commission, 2019])

$$u_{x'}(z) = u_{x'}(z_r)\left(\frac{z}{z_r}\right)^{\alpha_s}, \tag{5.5}$$

where:

$u_{x'}(z)$ - is the wind speed at height z

z - is the height above ground

z_r - is a reference height above the ground used for fitting the profile

α_s - is the wind shear (or power law) exponent.

Where the heights were chosen to be the top and bottom of the rotor disk and the velocities were interpolated at those heights from the average velocity profile from the LES-ABL calculation. The average wind speed used is the mean streamwise velocity at hub height calculated from the precursor calculation time averaged over 38000 s - 39200 s. The power law profile using $\alpha_s = 0.098$ and average wind speed of 12.75 m/s reasonably approximates the LES-ABL mean velocity profile over the rotor disk , but the differences increases as you move away from the centre of the rotor disk (see Figure 5-4). However, perfect correspondence is not necessary for the intended comparison.

Figure 5-5 shows three ~ 1.75 s periods of the normalized out-of-plane bending moment vector trajectory and a 1.75 s period from the steady shear inflow case. All signals were normalized with the maximum value in the aerodynamic OOPBM magnitude from the LES-turbine simulation over the 1000 s. The trajectory of the aerodynamic OOPBM vector from the steady shear case, over the 1.75 s period, is elliptical because of the 90°

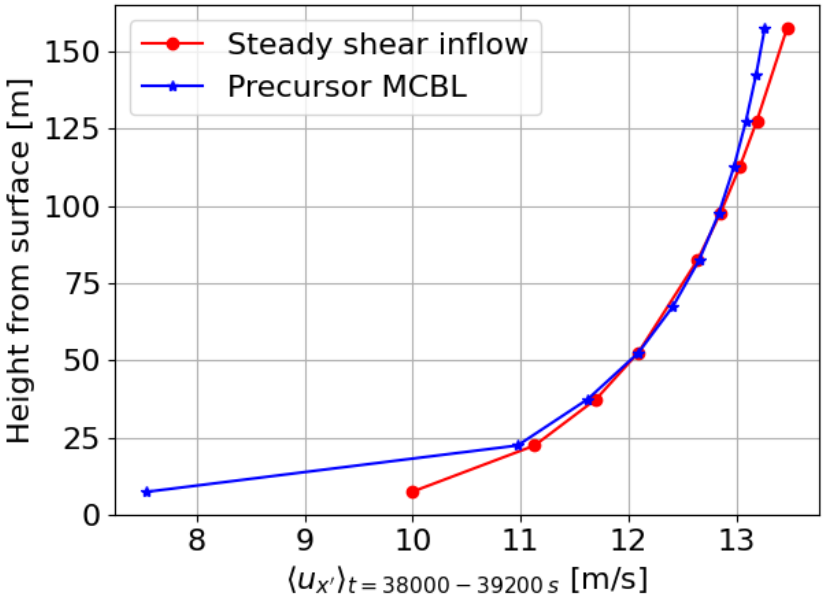

Figure 5-4: Mean streamwise velocity profiles. The red line is the steady shear inflow calculated using the power law (Eq. 5.5). The blue line is calculated from the MCBL precursor streamwise velocity, averaged over horizontal planes then in time between 38000 s - 39200 s (see Section 3.3.1).

phase shift between the y and z out-of-plane bending moment components. Comparing the blue trajectory with the steady shear inflow trajectory highlights the difference between a turbulent inflow compared with a non-turbulent inflow and the impact turbulence has on the fluctuations of the rotor loads; some of the largest fluctuations are many times larger. The impact of turbulence is discussed in more detail in Chapter 6.

Considering the OOPBM components as sinusoidal signals, with an amplitude, phase and period, as these parameters which define the sinusoid vary in time the trajectory of the vector will vary accordingly. The phase shift in the steady shear inflow case is constant with respect to time at 90°, therefore, the trajectory of the steady shear inflow OOPBM vector is consistently elliptical as seen in Figure 5-5. However, in the LES-Turbine calculation the trajectories of the three $\sim 1.75\,\mathrm{s}$ periods are not particularly circular, they are more elliptical and vary in area and position. Indicating as the atmospheric turbulence modifies the steady shear inflow into the structure of the

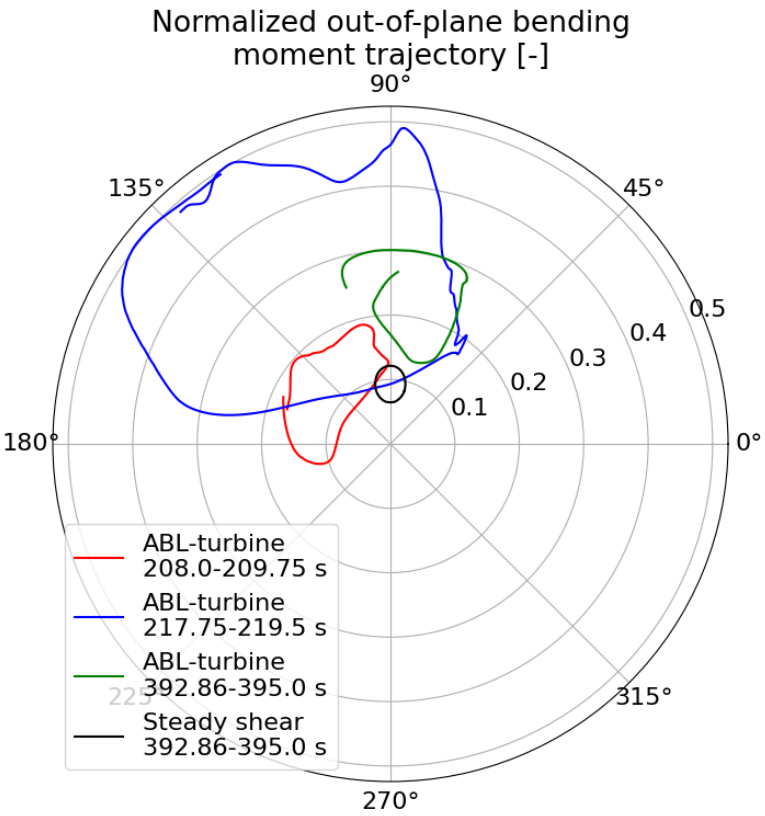

Figure 5-5: Normalized out-of-plane bending moment vector trajectory over individual 3P cycles.

MCBL, discussed in Section 3.3.2, the circular trajectory is modified to reflect the time variations generated by atmospheric turbulence.

[Hart et al., 2022c] showed the MB load response produced similar elliptical load patterns in a turbulent wind field generated using kinematic turbulence. When the trajectory of the full 1000 s is studied, it is clear the trajectory does not always form elliptical patterns. However, due to the strong 3P response the elliptical patterns will be a dominant pattern that appears in the trajectory [Hart et al., 2022c].

Analysis of the steady shear inflow case suggests the elliptical trajectory, due to the lack of correlation of the OOPBM components, is in-part due to three blades rotating through a non-uniform inflow. However, the identified load loops in the OOPBM

response in the MCBL vary significantly from the circular load loops in the steady shear inflow case, due to atmospheric turbulence modifying the harmonic 3P signal, thus modifying the trajectory of the OOPBM vector.

5.3 Role of Rotor Weight to the Time Variations in the Main Bearing Force Vector

So far, we have neglected the rotor weight from Eq. 5.2 to focus on the aerodynamic contributions to the MB force vector. However, rotor weight is always part of the MB force vector, therefore, the following analysis investigates the contribution of weight to the time response of the MB.

The rotor weight vector ($\mathbf{W}_R$) in Eq. 5.2 acts in the z-direction and is 1079 kN. In the rigid rotor configuration, with zero coning, and zero tilt angle (see Section 3.4), one would expect the rotor weight vector to have zero contribution to the time variations in the OOPBM vector thus, MB radial force vector.

To investigate the contribution of weight to the MB radial force vector, vector statistics are calculated (see below) for the MB radial force vector as a function of fraction of rotor weight. Rotor weight is varied by multiplying the actual rotor weight (1079 kN) by a fraction ν between 0 and 1.0, to systematically modify the z-component of the hub rotor force $F_{H,z,mod} = \widetilde{F}_{H,z} - \nu W_R$. The time average of the modified hub force component $F_{H,z,mod}$ decreases linearly with ν, while the fluctuations remain unchanged. Similarly, when the modified hub force is substituted into Eq. 5.4, the mean bearing force component in the z-direction ($F_{B,z}$), will also decrease linearly with ν, crossing zero at approximately $\nu = 0.2$, while the fluctuations remain unchanged.

When collecting statistics of a vector ($\mathbf{A}$) one must distinguish between the average of the magnitude of the vector ($\langle|\mathbf{A}|\rangle$) vs. the magnitude of the average of the vector ($|\langle\mathbf{A}\rangle|$), as these are not the same have different interpretations and one should be

careful choosing which one is the most appropriate for the analysis. In the following analysis the time average of the magnitude of the MB radial force vector ($|\langle \mathbf{F}_{B,\perp} \rangle_t|$), and the variance

$$\sigma^2_{\mathbf{F}_{B,\perp},t} = \langle \left(\mathbf{F}'_{B,\perp} \, \mathbf{F}'_{B,\perp} \right) \rangle_t = \langle \left(\mathbf{F}'_{B,\perp} \right)^2 \rangle_t + \langle \left(\mathbf{F}'_{B,\perp} \right)^2 \rangle_t, \tag{5.6}$$

of the MB radial force vector are calculated as a function of the fraction, ν, of the rotor weight included in the MB force.

Figure 5-6a shows the magnitude of the average MB radial force vector, plotted against the fraction, ν, of the rotor weight included. Initially, $|\langle \mathbf{F}_{B,\perp} \rangle_t|$ decreases linearly, then reaches a minimum at approximately $0.2W_R$ where $|\langle \mathbf{F}_{B,\perp} \rangle_t|$ starts to increase. This is due to $F_{B,z}$ passing through zero at $0.2W_R$, the sign change causes the $\mathbf{F}_{B,\perp}$ to change direction. When no rotor weight is included, $\nu = 0.0$, the bearing force is fully due to the aerodynamic contribution to the mean, the contribution from mean shear-rate in the velocity field over the rotor disk. When the full rotor weight is included $\nu = 1.0$, the mean bearing force, $|\langle \mathbf{F}_{B,\perp} |\rangle$, is a result of a combination of impacts from mean shear-rate in the flow and rotor weight. Finally, at $\nu = 0.2$, when $F_{B,z}$ passes through zero, rotor weight is balanced by the force on the rotor in the z-direction due to the mean flow shear-rate. Figure 5-6b shows that the variance of the MB radial force vector is independent of the rotor weight, suggesting the variability is entirely as result of the nonsteady deviations from the passage of ABL turbulence eddies through the rotor disk. Figure 5-6 suggests the only difference between the MB radial force vector with and without weight is a shift in the average, and the level of variability is independent of rotor weight.

Figure 5-7 shows the trajectories with and without rotor weight over 1000 s, are the same relative to the mean. Thus, as weight increases, the deviations from the average do not change, while the deviations relative to the average decrease.

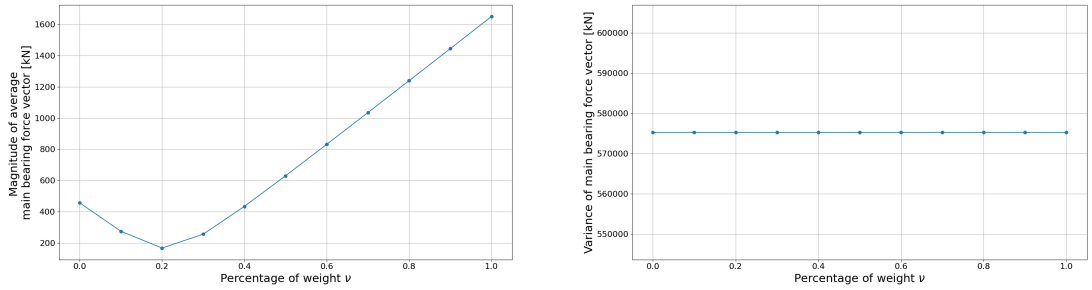

(a) (b)

Figure 5-6: Statistics of the Main bearing radial force vector as a function of the percentage of rotor weight included (ν) (a) Magnitude of the average vector, $|\langle \mathbf{F}_{B,\perp} \rangle_t|$ (b) Variance of the fluctuations of the radial bearing force, $F'_{B,\perp}$.

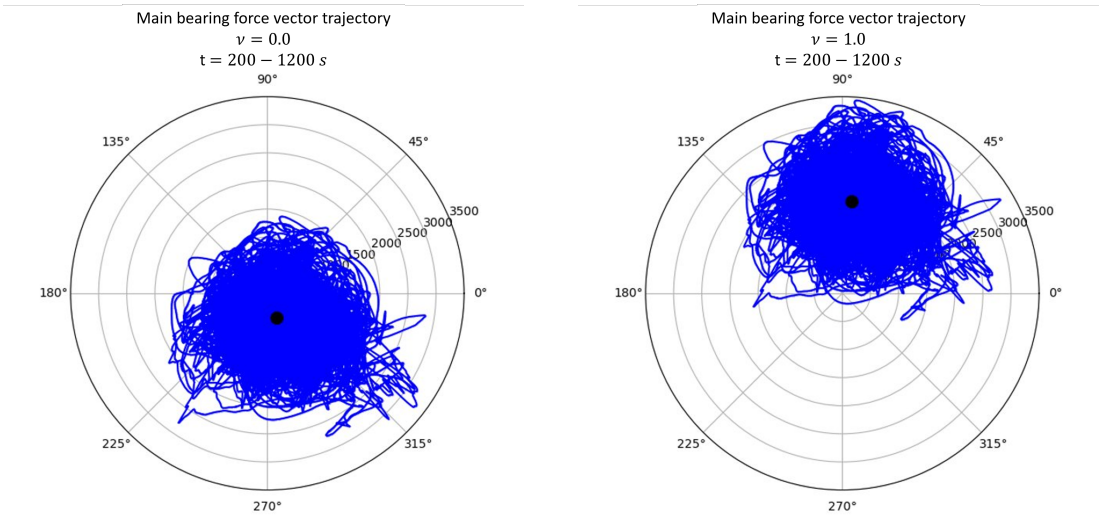

(a) (b)

Figure 5-7: Main Bearing force vector trajectory (blue curves). The black dot is $|\langle \mathbf{F}_{B,\perp} \rangle_t|$, the magnitude of the average main bearing radial force vector. (a) $\nu = 0.0$ (b) $\nu = 1.0$.

5.4 Role of Atmospheric Turbulence in the Creation of the Time Variations in the Hub Moments

In section 5.1 the OOP hub force does not significantly contribute to the time variations in the MB radial force vector, and may be neglected in the evaluation of the main bearing force. Figure 5-8 shows the time variations in the aerodynamic OOPBM

magnitude and torque over 1000 s are poorly correlated. This is visually evident in that overall time variations of the two signals are largely dissimilar. [Brasseur et al., 2024] found a similar lack of correlation between torque and OOPBM, in analysis of the response of the DOE 1.5 MW WT loads to turbulent eddy passages. However, the correlation calculated in [Brasseur et al., 2024] is 0.05, the difference in the correlation may be because the response of the NREL 5 MW, to the passage of turbulence eddies in a MCBL, is analysed for only a single 1000 s dataset.

In addition, Figure 5-8 indicates that the fluctuations of the aerodynamic OOPBM are much larger than those for torque, consistent with results in [Brasseur et al., 2024]. This has significant implications as power production which is proportional to torque has significantly lower fluctuations compared to potentially deleterious drive train loads, which are driven by time variations in the OOPBM.

The lack of correlation between the OOPBM and torque indicates that different mechanisms drive the time variations in torque/power and out-of-plane bending moment. Figure 5-8 shows that rotor-averaged wind speed, $\langle u_{x'} \rangle_A$ (velocity perpendicular to the rotor disk averaged over the rotor disk), is strongly correlated with torque and thrust. The correlations calculated over the 1000 s period are in excellent agreement with [Brasseur et al., 2024] experimental data. [Lavely, 2017] developed a measure which quantified the level of asymmetry in the velocity field over the rotor disk (see Section 2.3.3). Figure 5-8 shows the low-pass filtered (LPF) asymmetry parameter at 0.3 Hz is strongly correlated with the LPF aerodynamic OOPBM vector magnitude.

It should be noted that rotor-averaged wind speed and the asymmetry parameter were calculated from planar data 63 m (1/2 rotor diameter) in front of the WT rotor, output every 0.39 s. Whereas, torque, thrust and OOPBM are output from OpenFAST every 0.0039 s (Section 3.4.2). Therefore, to correlate variables calculated from planar data with variables from OpenFAST, the OpenFAST variables are interpolated in time to match the resolution of the planar data. Next, both the planar variables and the

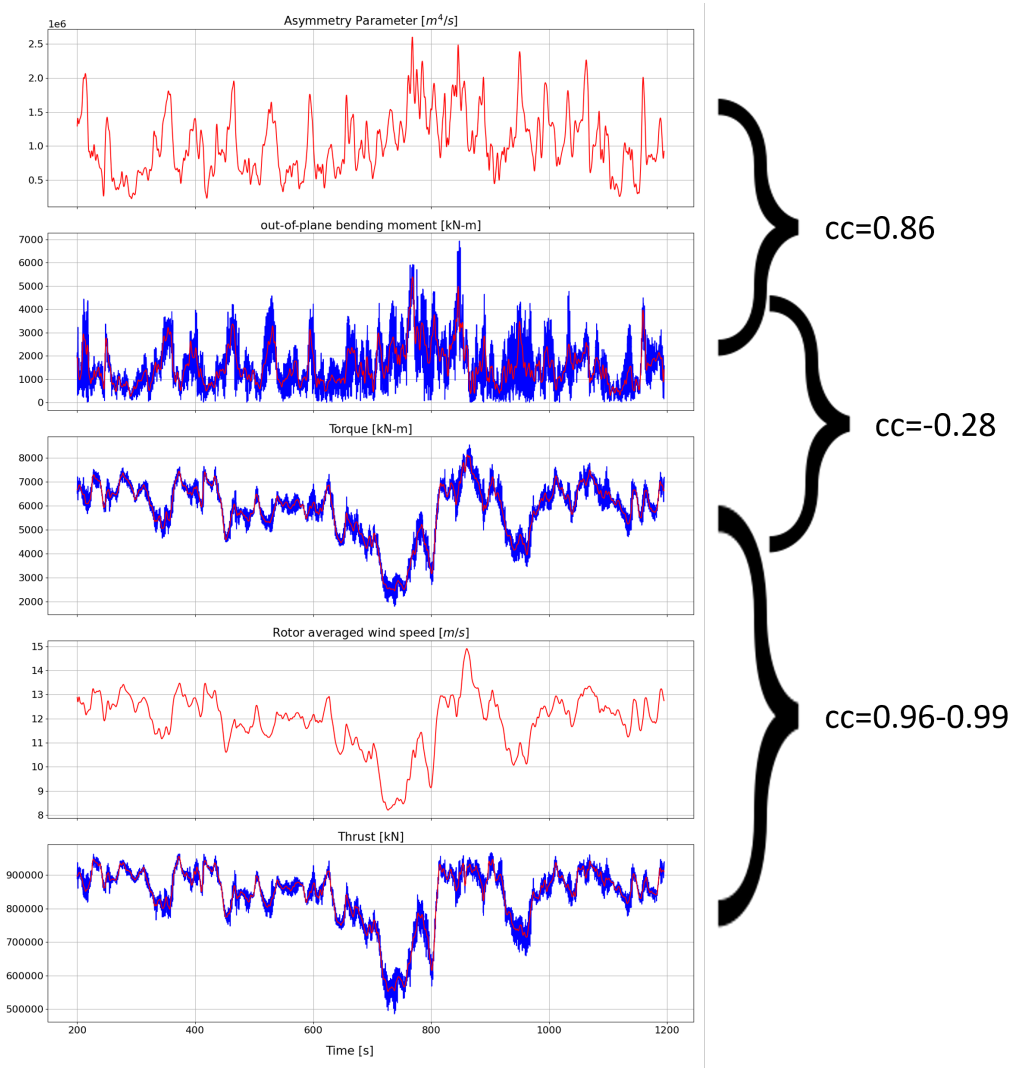

Figure 5-8: Summary of correlation coefficients blue lines show total signal, red lines show low pass filtered signal below 3P (0.3 Hz), curly brackets indicate which variables are being correlated.

OpenFAST variables are low-pass filtered at 0.3 Hz to ensure that they are compared over the same range of frequencies. Lastly, the planar data is linearly shifted in time to account for the advection time from a plane 63 m in front of the rotor disk to the rotor plane. Variables were shifted in time 4.6 s, see Section 3.8 for the procedure used to determine the time shift. The plane 63 m in front of the rotor disk (half the rotor diameter) was chosen to calculate velocity field derived parameters, such as the asymmetry parameter, to remove the influence of the blade wakes which alter the

velocity field in the rotor plane.

It should be noted these correlations correspond to the interactions between daytime atmospheric turbulence and a rigid, constant rotor speed and pitch angle, utility scale wind turbine operating at 12.75 m/s. It is likely these correlations would remain the same if the turbine were interacting with offshore atmospheric turbulence. However, in an offshore environment, with generally lower turbulence intensity [Van Der Tempel et al., 2011], and more intermittent turbulence [Wyngaard, 2010], the aerodynamic OOPBM would likely experience on average lower peak-to-peak fluctuations, but occasionally experience strong fluctuations due to the intermittent turbulence, compared with the aerodynamic OOPBM from an onshore WT. Furthermore, changing the operating point, wind speed or rotor speed, the wind turbine is operating at would not change the conclusions drawn from these correlations, but some of details of the frequency content would likely be affected (see Section 6.4). Chapter 7 explores the impact of blade deformations.

The key results from Figure 5-8 are: the time variations in torque are driven by the time variations in the rotor averaged wind speed, while the mechanism driving the time variations in the OOPBM is shown to be the level of asymmetry in the velocity distribution over the rotor disk. Further analysis is conducted on asymmetry as it is responsible for driving the time variations in the OOPBM which are potentially responsible for deleterious effects on the drive train in particular the MB.

Earlier the OOPBM vector was shown to be well correlated with the MB radial force vector. The "asymmetry parameter" is correlated with the magnitude of the OOPBM. To go beyond what the "asymmetry parameter" can tell us, an asymmetry vector was developed with the aim to correlate the asymmetry vector with the OOPBM vector and compare their trajectories. Whereas the asymmetry parameter is a scalar, the asymmetry vector provides directional information and can be generalised to provide more local information on asymmetry contributions.

As shown by Eq. 3.7 the asymmetry vector is calculated by multiplying the streamwise velocity $u_{x'}$ by the position vector from the origin to the locations of the streamwise velocity on the grid, and integrated over the rotor disk area. Section 3.6 gives a detailed derivation and explanation of the asymmetry vector and shows the asymmetry vector magnitude is in excellent agreement with the asymmetry parameter, as it captures the same time variations in the velocity distribution over the rotor disk.

Figure 5-9 summarises the correlation coefficients between the asymmetry vector and aerodynamic OOPBM vector. The correlation between the asymmetry vector magnitude and aerodynamic OOPBM vector magnitude is in excellent agreement with Figure 5-8, likewise, the components show very strong correlations. However, the correlation between the direction of the asymmetry vector and direction of the aerodynamic OOPBM vector is lower compared with the magnitude.

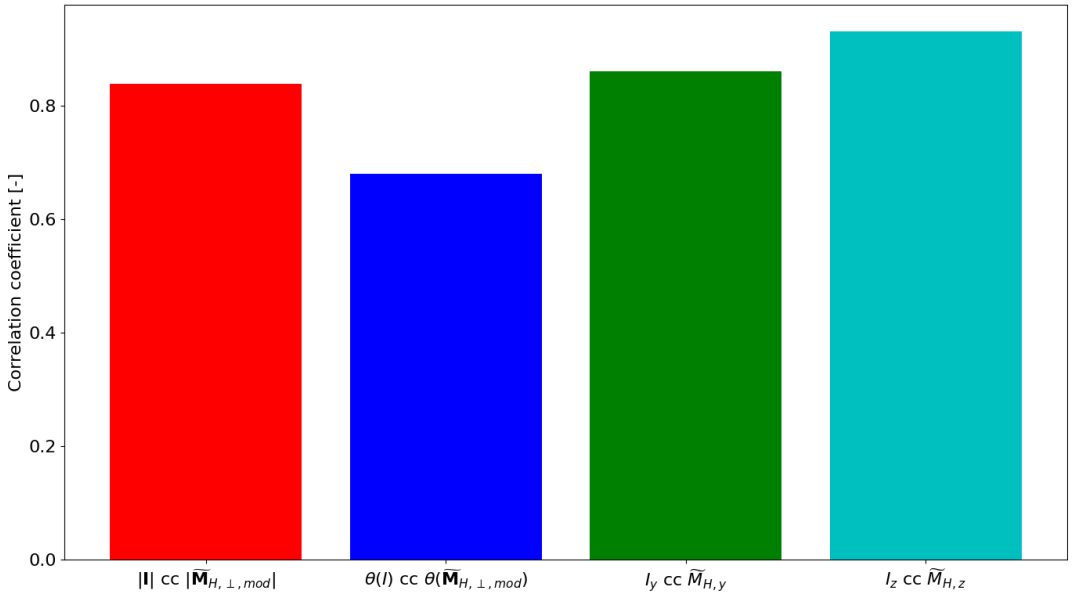

Figure 5-9: Summary of correlation coefficients between the asymmetry vector and out-of-plane bending moment vector.

Using planar data to calculate the asymmetry vector has the issue that the asymmetry vector can only be calculated and analysed for frequencies less than the 3P frequency.

Figure 5-10 compares the spectra of the normalised magnitude of the asymmetry vector and OOPBM vector. Over the frequencies lower than the 3P frequency (<0.3 Hz), the spectra are in excellent agreement. However, after 0.3 Hz the spectra are very different. The spectrum of the asymmetry vector magnitude ends at a much lower frequency than the spectrum of the OOPBM magnitude, due to the much lower sampling rate of the planar data compared to the OpenFAST data. Moreover, the asymmetry vector does not display the characteristic peak at 0.605 Hz, at the 3P frequency, which is to be expected, because the 3P frequency is a feature of the turbine response and cannot be present in the incoming velocity field. The lack of frequency content above 0.3 Hz limits the strong correlation to these frequencies. The conclusion that asymmetry is the primary mechanism driving the time variations in the MB force vector is therefore limited, to frequencies below 0.3 Hz. Section 6.3 extends the asymmetry vector to all frequencies and goes into more detail discussing the mechanisms driving the time variations.

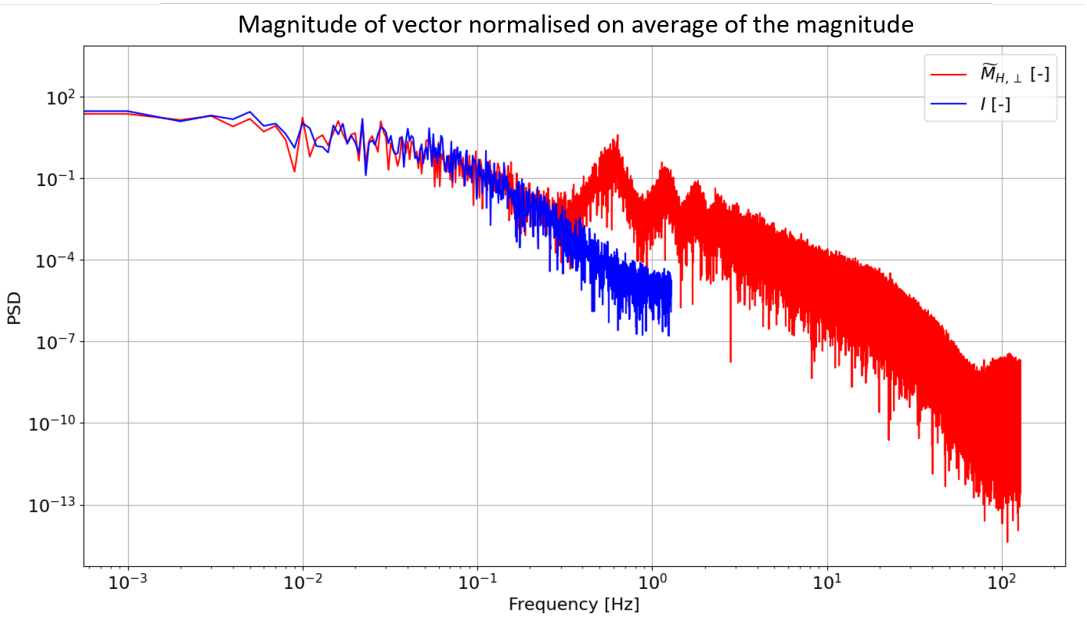

Figure 5-10: Spectra of the asymmetry vector magnitude compared with out-of-plane bending moment vector magnitude normalised on average of the magnitude.

5.5 Analysis of a Second 1000 s Dataset

While there is excellent agreement between most of the correlations in Table 5-8 with experimental data [Brasseur et al., 2024], the difference in the correlation between the aerodynamic OOPBM magnitude and torque is not insignificant. It was suggested the difference may be due to the fact that only one 1000 s period is being used to calculate statistics compared to the experimental data which calculated its statistics from a three month period.

In an attempt to ascertain whether the statistics calculated in the 1000 s period between 38200 s - 39200 s are representative of the WT response to the turbulence in the daytime ABL, a second 1000 s period is used to calculate the same statistics. The period chosen is from 32500 s - 33700 s (removing first 200 s), Figure 3-11 shows this period to be non-stationary, so perfect correspondence should not be anticipated. At the time of running the calculation the period of time 32500 s - 33700 s was the best option to run a second ABL-turbine calculation.

Figure 5-11 summarises the correlation coefficients between the asymmetry vector and aerodynamic OOPBM vector, and is compared with the statistics collected in Figure 5-8. The correlation between the asymmetry parameter magnitude and aerodynamic OOPBM magnitude, and the correlations between thrust, torque and rotor averaged wind speed, are in excellent agreement with the correlations calculated over the first ABL-turbine calculation (38200 s - 39200 s), shown in Figure 5-8. Which suggests that the correlations between these variables are robust, and broadly applicable over stationary and some level of non-stationary flow.

However, the correlation between aerodynamic OOPBM magnitude and torque is $\sim$ 57% smaller, not insignificant. However, both correlations between the aerodynamic OOPBM magnitude and torque, from both 1000 s, show the lack of correlation; in agreement with the literature [Brasseur et al., 2024]. If statistics were calculated for a

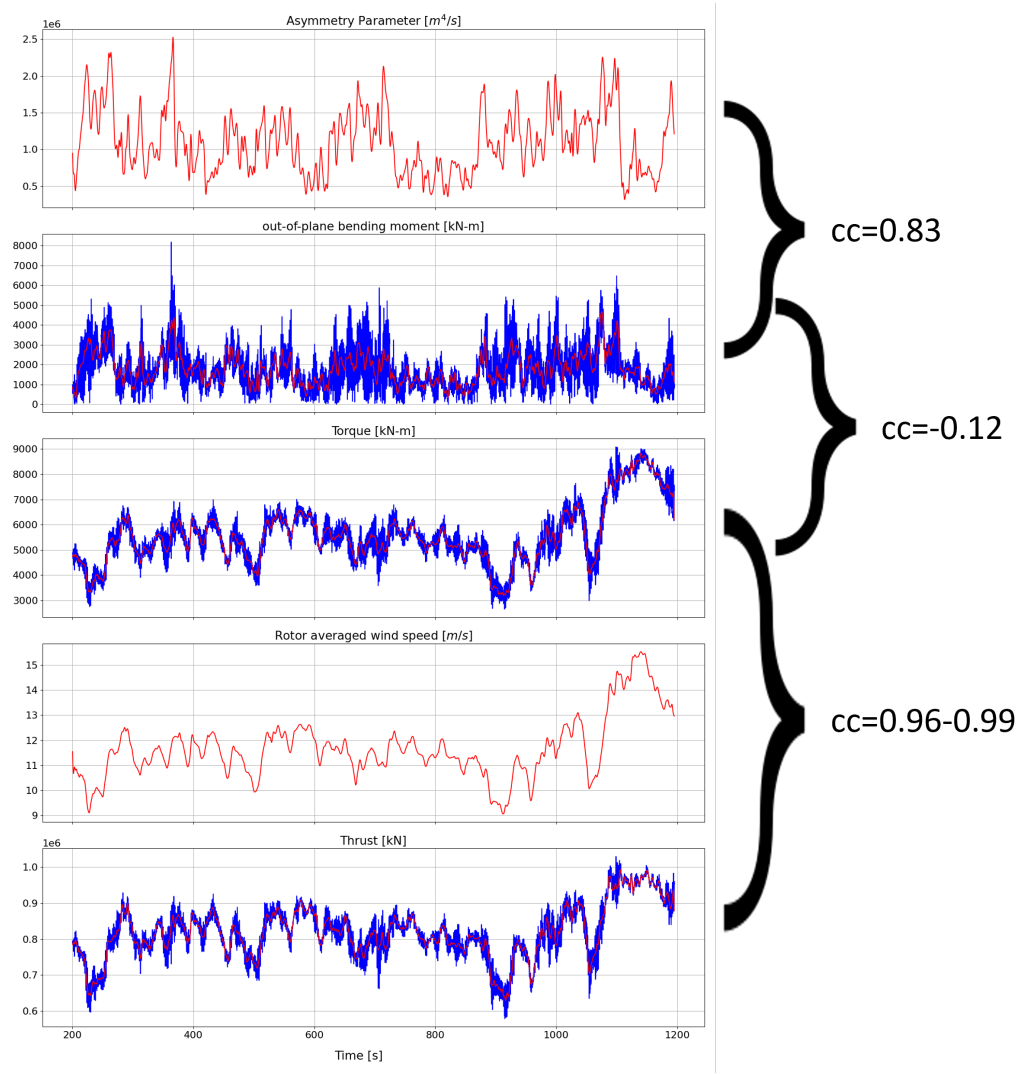

Figure 5-11: Summary of correlation coefficients 32700 s - 33700 s, blue lines show total signal, red lines show low pass filtered signal below 3P (0.3 Hz), curly brackets indicate which variables are being correlated.

much longer period of time it is likely the correlation between aerodynamic OOPBM magnitude and torque would converge on 0.0 based on the statistics calculated from experimental data [Brasseur et al., 2024].

5.6 Role of Rotor Thrust to the Function and Potential Failure Mechanisms of the Main Bearing

In this section we analyse the potential contribution of the axial component of the bearing force to detrimental impacts on the MB. In our setup the turbine has zero main shaft tilt, the x axis is aligned along the main shaft, and the blades are rotor are rigid with zero coning. The force balance in Eq. 5.2 - 5.4 is for an equilibrium state (no inertia) and assumes no deformations (rigid). Thus, rotor thrust is the axial load acting on the MB: $F_{B,x} = F_{H,x}$.

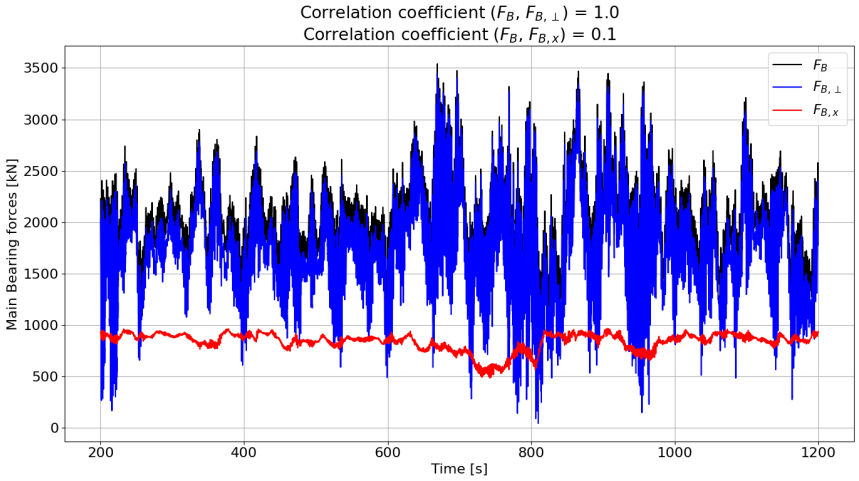

Figure 5-12: Comparison of the time variations between the main bearing force components.

Figure 5-12 shows the time variations in the MB force magnitude are primarily driven by the MB radial force magnitude. The correlation indicates the axial MB force component (thrust) contributes comparatively little to the time variations in the MB force magnitude, compared to the MB radial force magnitude; as the variance of the axial MB force is an order of magnitude smaller than the MB radial force magnitude. However, these results do not account for the internal geometry of the roller bearing, in particular the contact angle of the bearing. As illustrated in Figure 5-13 the contact angle is the angle between the direction of the force vector on the inner and outer race-

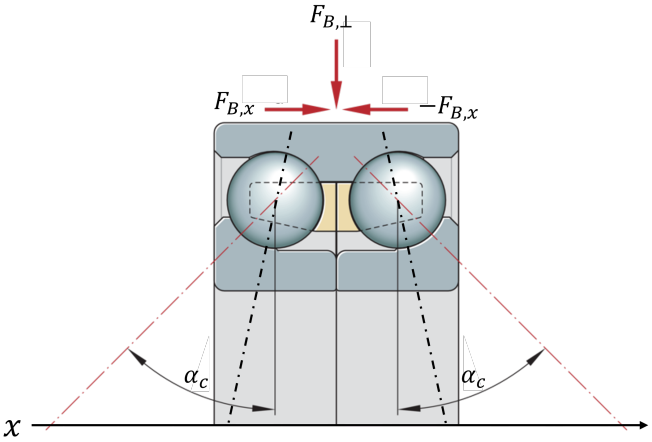

Figure 5-13: Illustration of bearing internal geometry highlighting contact angle.

way of the bearing arising from to the radial and axial bearing force components, and the line perpendicular to the x axis along the main shaft. The contact angle is a result of the internal bearing geometry. If the contact angle is 90° the damage equivalent load (P_r) on the inner and outer raceways will result completely from the axial bearing force component, so $P_r = F_{B,x}$. If the contact angle is 0° the damage equivalent load on the inner and outer raceways will result completely from the radial bearing force magnitude, so $P_r = F_{B,\perp}$. Evidently, bearing designers can optimise the contact angle to achieve desirable outcomes, such as maximizing the rating life.

Methods for estimating the basic rating life for a population of identical rolling bearings are specified in [International Organization for Standardization, 2007], where rating life is defined as number of revolutions before the first evidence of fatigue damage is observed. The rating life, defined as

$$L_{10} = \left(\frac{c_D}{P_r}\right)^{p_e}, \tag{5.7}$$

is the predicted life based on its basic dynamic load rating (c_D). The basic rating life is the value of bearing life where 90% of the MB population is expected to attain or exceed under load P_r. [Kenworthy et al., 2024] provides a detailed case study where

the bearing rating life is calculated using different conditions and the relevant bearing life theory is reviewed.

For a particular radial roller bearing, [International Organization for Standardization, 2007] provides the following expression to calculate the dynamic equivalent radial load:

$$P_r = XF_{B,\perp} + YF_{B,x}, \tag{5.8}$$

where the "dynamic load factors" X and Y depend on the ratio $F_{B,x}/F_{B,\perp}$ and the contact angle as shown in Table 5.2.

Table 5.2: Values of X and Y for radial roller bearings from [International Organization for Standardization, 2007].

Bearing type	$F_{B,x}/F_{B,\perp} \leq e_D$		$F_{B,x}/F_{B,\perp} > e_D$		e_D
	X	Y	X	Y	
Single row	1	0	0.4	$0.4\cot(\alpha_c)$	$1.5\tan(\alpha_c)$
Double row	1	$0.4\cot(\alpha_c)$	0.67	$0.67\cot(\alpha_c)$	$1.5\tan(\alpha_c)$

We chose the following two values for contact angle to calculate the dynamic equivalent radial load: $\alpha_c = 8.34°$ and $\alpha_c = 11.31°$. These are the values for MBs in Vestas and GE turbines, which use 240/750 bearings. Figure 5-14 shows the axial bearing force component and MB radial force magnitude multiplied by their respective dynamic load factors X, Y in Table 5.2. Comparing Figure 5-12 with Figure 5-14, the average and the variance of the axial bearing force contributions have significantly increased relative to the average and variance of the MB radial force magnitude contributions. Furthermore, Figure 5-14 shows that the correlation between the dynamic equivalent radial load and the axial bearing force component is comparable, to the correlation between the dynamic equivalent radial load and MB radial force magnitude.

The results in Figure 5-12 indicate that rotor thrust does not contribute significantly to the time variations in the MB force vector. However, Figure 5-14 suggests, in the context of rolling contact fatigue, when internal bearing geometry is accounted for,

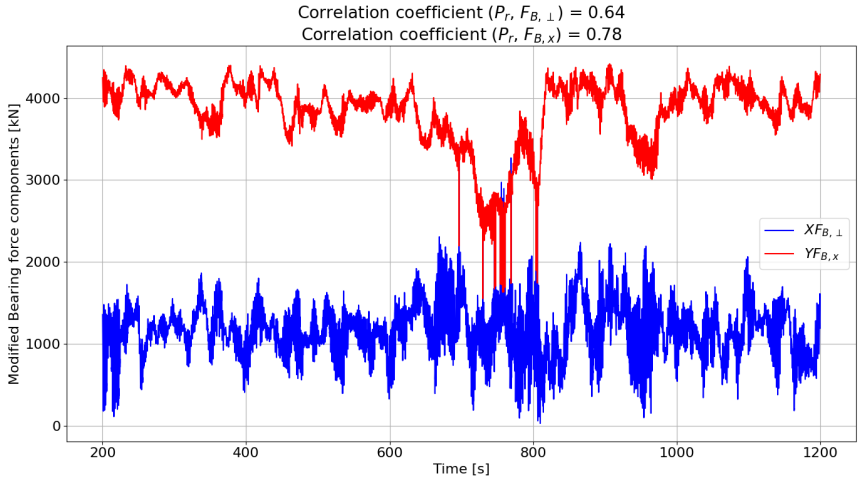

(a)

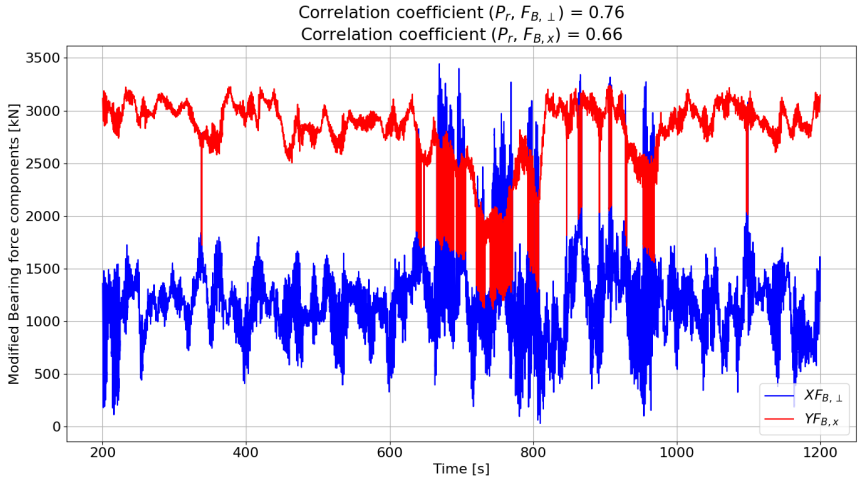

(b)

Figure 5-14: Main bearing radial force magnitude and main bearing axial force component modified as per [International Organization for Standardization, 2007] (a) $\alpha_c = 8.34°$ and (b) $\alpha_c = 11.31°$.

according to the model in [International Organization for Standardization, 2007], the axial bearing force component may plays a significant role in the time variations in the dynamic equivalent radial load. As the time variations in both the MB radial force magnitude and axial main bearing force component, when modified by the dynamic load factors, are comparable.

5.7 Summary

This chapter explored the primary contributors to the time-varying forces experienced by the main bearing (MB) of a utility-scale wind turbine. Through a detailed force decomposition analysis, it was demonstrated that the primary driver of time variations in the MB force is the aerodynamic OOPBM vector, which was shown to be driven by the asymmetrical distribution of the velocity field over the rotor disk. In contrast, the other terms, aerodynamic hub forces and rotor weight, were shown to play secondary or negligible roles in the time variations of the MB force vector. Specifically, rotor weight contributes significantly to the average MB force vector but not to its fluctuations. A second 1000 s dataset confirmed the robustness of the results, as the results were in excellent agreement between the two datasets.

A key finding is the lack of correlation between the components of the OOPBM vector, which lead to differences being identified in the OOPBM vector trajectory between the ABL-turbine and a steady shear inflow. Which demonstrated that atmospheric turbulence plays a significant role in the time variations of the OOPBM vector, and is in-part responsible for the lack of correlation.

The analysis of rotor thrust revealed that fluctuations in thrust do not significantly contribute to the time variations in the MB force vector. However, the variations in radial force significantly impacts the MB force response, likely impacting lubrication film thickness and contact stress distribution. This has important implications for bearing life and potential failure modes, such as surface-initiated damage mechanisms.

Overall, this chapter established that eddy-dominant coherent atmospheric turbulence eddies drive MB force vector fluctuations, with the asymmetry in the velocity field across the rotor disk acting as the key mechanism driving these time variations.

Chapter 6

Frequency Response of the Out-of-plane Bending Moment to the Passage of Atmospheric Turbulence Eddies

In Section 5.2 important differences in the trajectory of the out-of-plane bending moment vector were highlighted, in the response of the NREL 5 MW WT, comparing a steady sheared inflow, to the passage of atmospheric turbulence. The aim of the following sections is to compare the response of the NREL 5 MW WT to a steady sheared inflow, and the passage of atmospheric turbulence eddies. With the objective to understand the role turbulence is playing in the generation of the time variations in the aerodynamic out-of-plane bending moment, which is responsible for driving the time variations in the MB radial force vector (Section 5.1). Furthermore, the mechanisms which create the time variations in the out-of-plane bending moment are explored further, and extended to a wider range of frequencies. As the conclusions drawn from Section 5.4 are limited to frequencies below 0.3 Hz. Lastly, the relative contributions

from the three characteristic frequency ranges, to the time variations in the MB force magnitude are analysed, and the potential of these time variations to contribute to potential failures of MBs is discussed.

6.1 Role of Turbulence in the Atmosphere in the Creation of the Time Changes in Aerodynamic Hub Loads

The simple OpenFAST calculation, analysed in Section 5.2, was simulated with an average wind speed profile, comparable with the MCBL precursor. The 3P peak-to-peak variations in the out-of-plane bending moment magnitude occur every 1.65 s, due to the three blades rotating through the steady shear profile, producing an extremely periodic signal; which is obviously non-turbulent. Due to the highly periodic nature of the OOPBM magnitude, in the steady shear inflow case, the frequency spectra, shown in Figure 6-1, displays a well defined peak at the 3P frequency (0.605 Hz). In contrast, the OOPBM magnitude spectra, calculated from the LES-turbine calculation, shows the response of the WT to the passage of atmospheric turbulence, is spread over a wide range of frequencies.

Figure 6-1 shows the OOPBM frequency spectra from the LES-turbine and steady shear inflow calculations. Three frequency ranges are identified using the OOPBM frequency spectra: frequencies below the 3P frequency <0.3 Hz are defined as the low-frequency content, 3P frequency content is defined to be between 0.3 Hz - 0.9 Hz, and high-frequency content is between 1.5 Hz - 40 Hz. The lower limit of the high-frequency content was chosen as 1.5 Hz to remove the 6P harmonic frequency from the high-frequency response. A low-pass filter (LPF) at 40 Hz is applied to all signals, because at $\sim$ 40 Hz the variability in the spectra starts to increase, indicating the signal past this point is likely noise, thus is removed. While analysing the non-steady WT responses from interactions between energy-dominant daytime atmospheric turbulence eddies, and the rotating blades of a GE 1.5 MW WT [Nandi et al., 2017] identified three

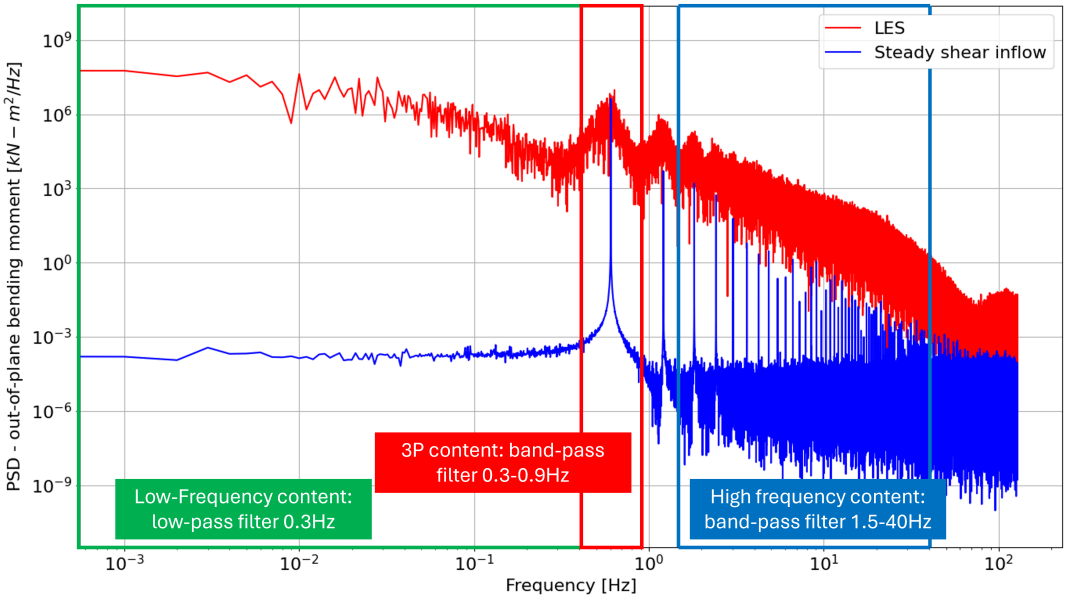

Figure 6-1: PSD spectra of the out-of-plane bending moment magnitude comparing the response from a steady shear inflow to the response from the LES-turbine calculation. Defining the three characteristic frequency ranges.

characteristic frequency responses in the WT response. [Nandi et al., 2017] identified a long frequency response which was attributed to the passage of atmospheric eddies (∼ 25 s - 60 s), the 3P frequency, and a sub-second response from the blades interacting with the internal eddy structure, which are consistent with the three frequency ranges identified in Figure 6-1.

Comparing the frequency spectra of the OOPBM magnitude, from the steady shear inflow, and the LES-ABL inflow, over the three frequency ranges, Figure 6-1 shows the passage of atmospheric turbulence eddies through the wind turbine rotor, adds an enormous amount of variability to the low- and high-frequency content of the OOPBM magnitude. Approximately 9 orders of magnitude separate the lowest frequency, and 1-3 orders of magnitude separate the high frequency content, in the steady shear inflow and the LES-Turbine OOPBM frequency responses. Indicating the time variations in the low- and high-frequency content are primarily generated due to the presence of atmospheric turbulence. Furthermore, the 3P frequency is modified, as the 3P peak in

the LES-turbine is spread over a wide range of frequencies.

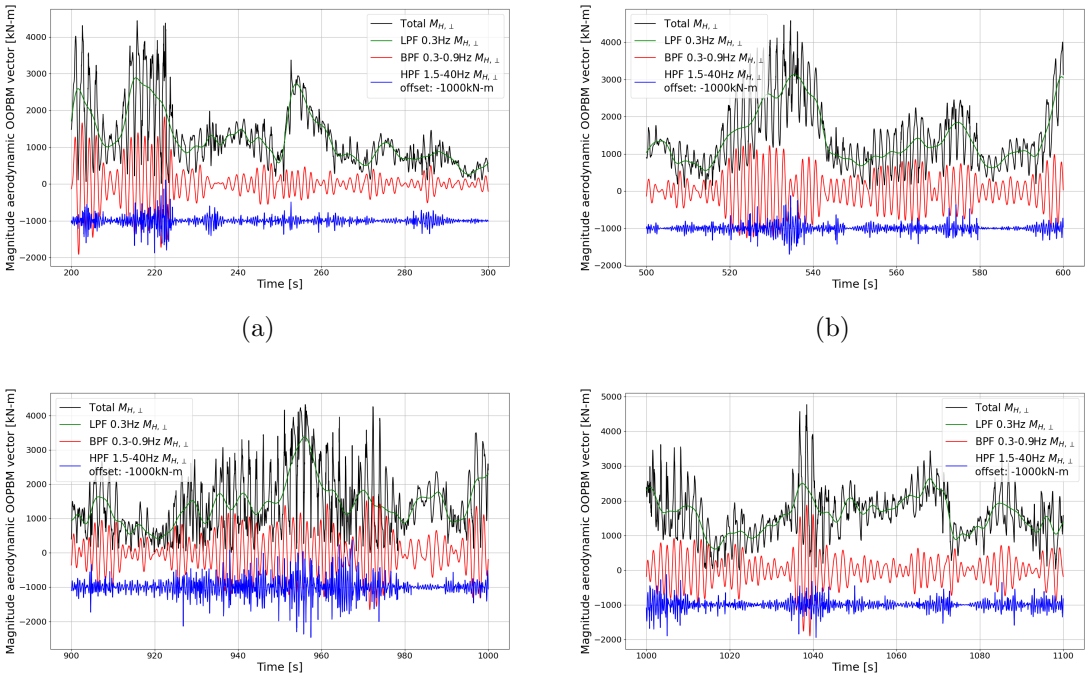

Figure 6-2: Aerodynamic out-of-plane bending moment magnitude over 100 s periods. Where the black curve is the total, the green curve is the low-frequency content (LPF 0.3 Hz), the red curve is the 3P frequency content (BPF 0.3-0.9 Hz), and the blue curve is the high-frequency content of the aerodynamic OOPBM (BPF 1.5-40 Hz) offset by -1000 kN-m. (a) 200-300 s, (b) 500-600 s, (c) 900-1000 s, (d) 1000-1100 s.

Figure 6-2 shows short 100 s periods of the aerodynamic OOPBM magnitude and the aerodynamic OOPBM magnitude filtered over the three frequency ranges. The low-frequency content of the OOPBM is associated with the eddy passage time scale [Nandi et al., 2017], and is an order of magnitude longer than the time scale associated with the 3P frequency 1.65 s. Qualitatively Figure 6-2 indicates the low-frequency content is driving the "trend" in the aerodynamic OOPBM, where the trend is defined as the longest time variations on the order of 20 s - 60 s, on the order of the eddy passage time. Similar to the OOPBM calculated from a steady shear inflow, the 3P frequency content is highly periodic. However, unlike the steady shear inflow, modulation of the 3P frequency content is observed, at a time scale on the order of the eddy passage time;

indicating the 3P frequency content may be modulated by the passage of atmospheric turbulence. The high-frequency content of the aerodynamic OOPBM magnitude is highly chaotic (turbulent), and appears to sit atop the peak-to-peak variations of the periodic 3P frequency. Qualitatively, on average the high-frequency fluctuations increase the peak-to-peak variations of the 3P frequency, which can be observed in the total OOPBM magnitude. Figure 6-1 shows the high-frequency content, on average, has lower variability compared to the 3P frequency content. However, Figure 6-2 indicates the time variations from the high frequency content are at times equal to or larger than those from the 3P frequency. Lastly, groupings of high activity are observed in the 3P and high-frequency signals, and appear to be qualitatively correlated with the modulation of the 3P frequency signal, and the time variations in the low-frequency signal. Suggesting the passage of eddies is modulating all the characteristic frequencies at the eddy passage time scale, and suggests the three characteristic frequencies of the OOPBM magnitude are all related by one key mechanism driving the time variations.

6.2 Passage of Atmospheric Eddies Influencing the Structure of the Three Frequencies

In section 6.1 three characteristic frequency ranges are identified in the OOPBM response to the passage of atmospheric eddies, and qualitative observations led to the hypothesis that, the three characteristic frequency ranges are modulated by the passage of atmospheric eddies. Hence, this section aims to quantify the interrelationships between the unique three frequency ranges. The interrelationships between the three frequencies are quantified by correlating the modulations in the 3P- and high-frequency content of the aerodynamic OOPBM with the low-frequency content of the aerodynamic OOPBM. Furthermore, groupings of high activity in the OOPBM, denoted bursting periods, unique to the 3P frequency and high-frequency content, are observed to qualitatively correlate with the time variations in the low-frequency content in the OOPBM.

Therefore, the level at which these bursting periods overlap, during the 1000 s, is used as another measure to quantify the interrelationships between the three frequencies.

The low-frequency content is associated with the passage of atmospheric eddies [Nandi et al., 2017], however, there is a small distinction that should be made clear. The low-frequency content is associated with the passage of atmospheric eddies "through the WT rotor disk". In section 3.3.3, the eddy passage time scale is calculated as 19 s- 71 s, while peak-to-peak variations in the low-frequency OOPBM shorter than this have been observed. Eddies move in and out of the rotor disk during advection, causing changes to the asymmetry, which subsequently cause changes in the OOPBM at time scales smaller than the eddy passage time.

To capture the modulation of the 3P- and high-frequency content in the OOPBM, to the passage of atmospheric eddies, new signals are generated. Since the 3P-frequency is highly periodic the peaks, on the positive side, of the 3P-frequency content of the aerodynamic OOPBM magnitude are linearly joined together, to create a signal that captures the modulation in the 3P frequency content. Figure 6-3 shows the new signal, denoted the envelope of the 3P frequency of the OOPBM (Env $M_{H,\perp,BPF}$), captures the modulation of the 3P frequency content.

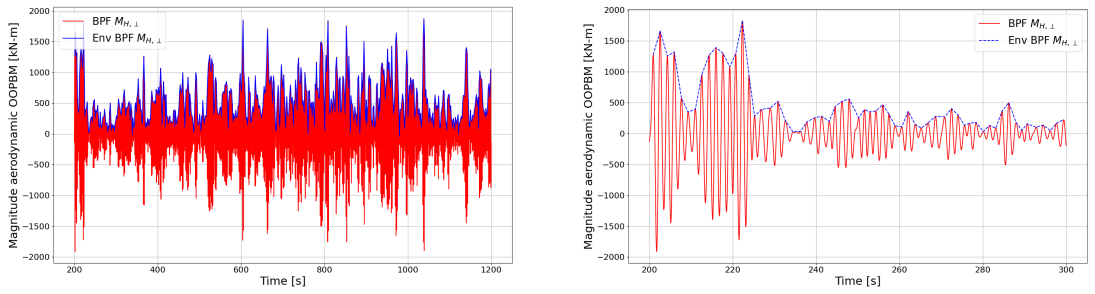

Figure 6-3: Out-of-plane bending moment bandpass filtered at 0.3-0.9 Hz, isolating the 3P frequency content, the red signal is the $M_{H,\perp,BPF}$, and the blue signal is the envelope of the 3P frequency content. (a) 1000 s, (b) 200 - 300 s.

An attempt to apply the same approach to the high-frequency content of the OOPBM

magnitude, to capture the modulations, was unsuccessful due to the signal being extremely chaotic. Therefore, to produce a new signal from the high-frequency content, which captures the modulations, a window of a specific size is slid over the high-frequency signal, and at every time step the window of the high-frequency content of the OOPBM is averaged; filtering the already filtered signal. The new signal is denoted the effectively filtered high-pass filtered signal. To determine the optimal window size the envelope of the 3P-frequency, and the low-frequency content of the OOPBM magnitude, are both correlated with the effectively filtered high-pass filtered signal, and the correlation coefficient is calculated as a function of window size. Figure 6-4a indicates the optimal window size lies between 9 s - 11 s. Figure 6-4b shows the absolute high-frequency content of the aerodynamic OOPBM magnitude and three effectively filtered high-pass filtered signals at 3 s, 6 s and 9 s. A window size of 9 s is chosen as, Figure 6-4b shows a window size of 9 s filters most the high-frequency content, compared to the other window sizes, and produces a signal which best captures the modulation of the high-frequency content.

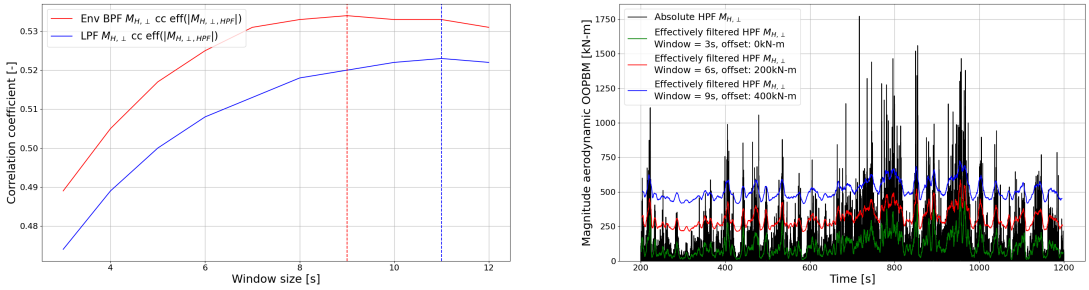

(a) (b)

Figure 6-4: (a) correlation coefficient between (red) envelope of the 3P frequency OOPBM and effectively filtered high frequency OOPBM, (blue) low frequency content of the OOPBM and effectively filtered high frequency OOPBM as a function of window size. (b) The black curves is the absolute high-frequency OOPBM and three effectively filtered high-frequency out-of-plane bending moment signals offset.

Figure 6-5 shows the low-frequency content, the envelope of the 3P-frequency content, and effectively filtered high-pass filtered, at 9 s, aerodynamic OOPBM magnitude. The correlation coefficient between the low-frequency content of the OOPBM, envelope of

the 3P-frequency, and effectively filtered high-pass filtered OOPBM magnitude, are between 0.52-0.53. The correlation coefficients suggests some level of interrelationships between the three frequency ranges, but the relationships are not as strong and originally thought to be. The correlation coefficients may also indicate differences in the mechanisms which drive the time variations in the three frequencies.

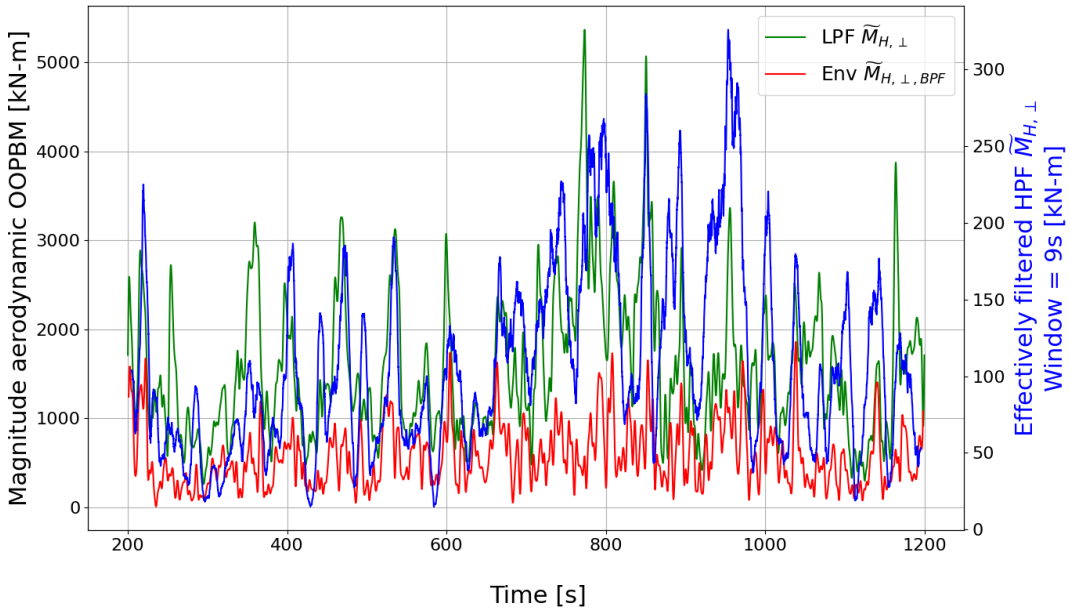

Figure 6-5: Low-frequency content, envelope of the 3P-frequency content, and effectively filtered high-pass filtered at 9 s, aerodynamic out-of-plane bending moment magnitude.

In the following analysis, the bursting periods in the three frequencies are defined, and the level at which these bursting periods overlap between signals is quantified. A bursting period is defined as a time period where the signal exceeds a specified threshold, where signal can refer to the low-frequency OOPBM, the envelope of the 3P frequency of the OOPBM, or effectively filtered high-pass filtered OOPBM magnitude. The bursting periods in the three frequency ranges in the OOPBM magnitude, can be defined for a range of threshold values, to investigate whether our conclusions depend on our choice of threshold. As the signal exceeds the threshold for the first time, this defines the start of a bursting period. The next time the signal drops below the threshold this

defines the end of the bursting period. Figure 6-6 shows the low-frequency OOPBM magnitude, and the effectively filtered, at 9 s, high-frequency OOPBM magnitude. The highlighted regions show the bursting periods for a threshold equal to the average plus one standard deviation for their respective signals.

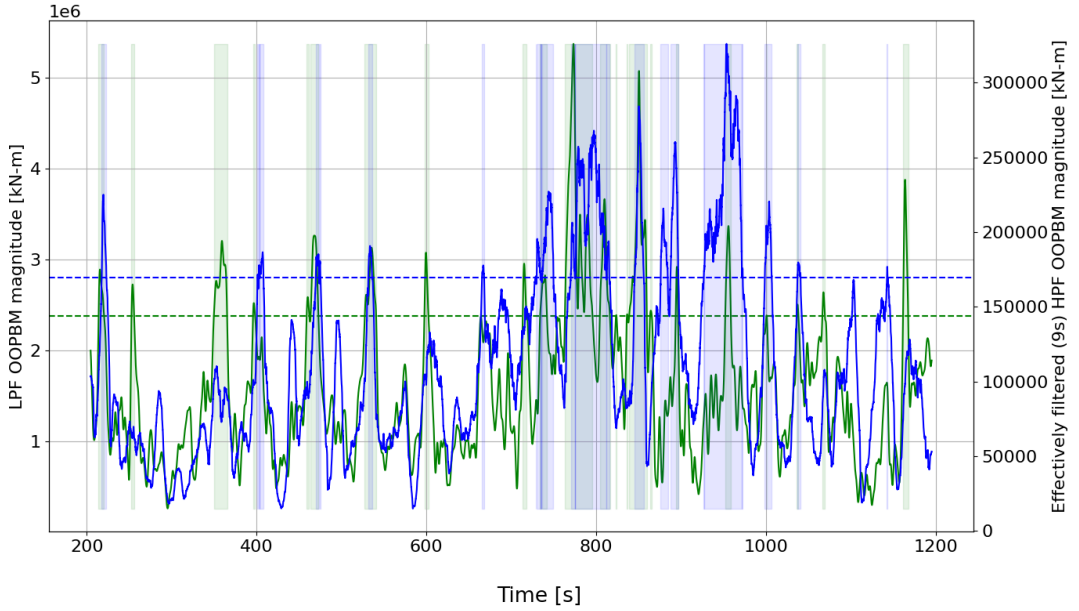

Figure 6-6: The green curve is the low frequency OOPBM magnitude, green dashed line indicates the threshold used to define the bursting periods in the low frequency OOPBM magnitude, and the green boxes indicate the bursting periods for the low frequency OOPBM magnitude. The blue curve is the effectively filtered, at 9 s, high frequency OOPBM magnitude, the blue dashed line indicates the threshold used to define the bursting periods in the effectively filtered high frequency OOPBM magnitude, and the blue boxes indicate the bursting periods of the effectively filtered high frequency OOPBM magnitude.

The interrelationships between the low frequency, 3P frequency and high-frequency signals are quantified by calculating the percentage overlap between the bursting periods, defined as

$$Overlap = \frac{\sum t_B}{\sum T_B} \times 100, \tag{6.1}$$

where t_B is the amount of time the bursting periods between two signals are overlapped,

and T_B is the summation of the bursting periods for a signal. Figure 6-7 illustrates the four possible combinations the bursting periods between two signals can overlap.

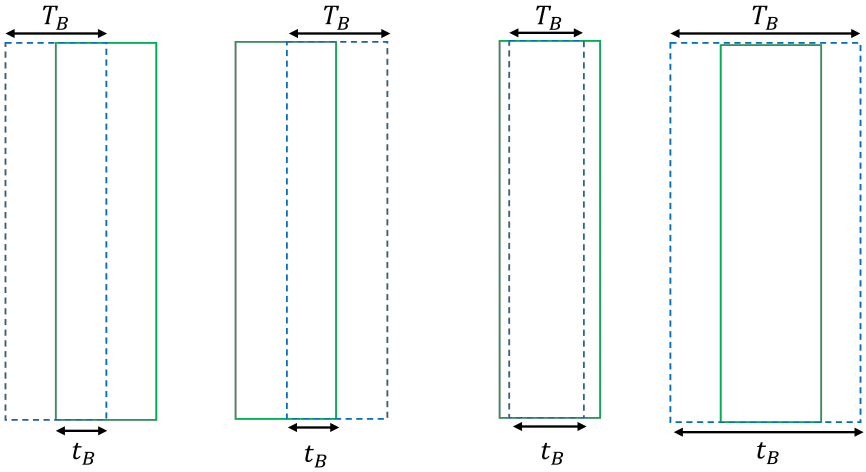

Figure 6-7: Illustration of potential overlap combinations between bursting periods, between two signals.

The threshold is varied between the average of the signal to the average plus one standard deviation of the signal. A general form for the threshold is: $T = \bar{x} + t\sigma\,(x)$, where $\bar{x}$ is the time average of the signal, $\sigma\,(x)$ is the standard deviation of the signal x, and t is systematically varied between $0 - 1.0$.

Figure 6-8 shows the six combinations of overlap possible between the bursting periods of two signals. Figure 6-8 shows the percentage overlaps calculated between the aerodynamic OOPBM magnitude filtered over the three characteristic frequencies. Figure 6-8 shows the percentage overlap decreases roughly linearly between 66-33%, indicating significant variability in the choice of threshold. Figure 6-8 shows when the time average is chosen as our choice of threshold, $t = 0.0$, the percentage overlaps calculated for the three frequencies, are concentrated between 59-66%. However for our largest choice of threshold, $t = 1.0$, the percentage overlaps calculated are spread over a wider range 33-47%, compared to $t = 0.0$. Indicating the interrelationships between the three frequencies deteriorate as the threshold, which defines the bursting periods, increases.

The results presented indicates there are strong interrelationships between the three

frequencies, likely connected to the interactions between the rotor and the ABL turbulence. However, Figure 6-8 shows the "strongest" bursting periods in each of the three frequencies do not strongly overlap, where strongest refers to the bursting periods with the largest peak-to-peak variations ($t = 1.0$). Which may suggest there are differences in the mechanisms driving the time variations in the three frequencies.

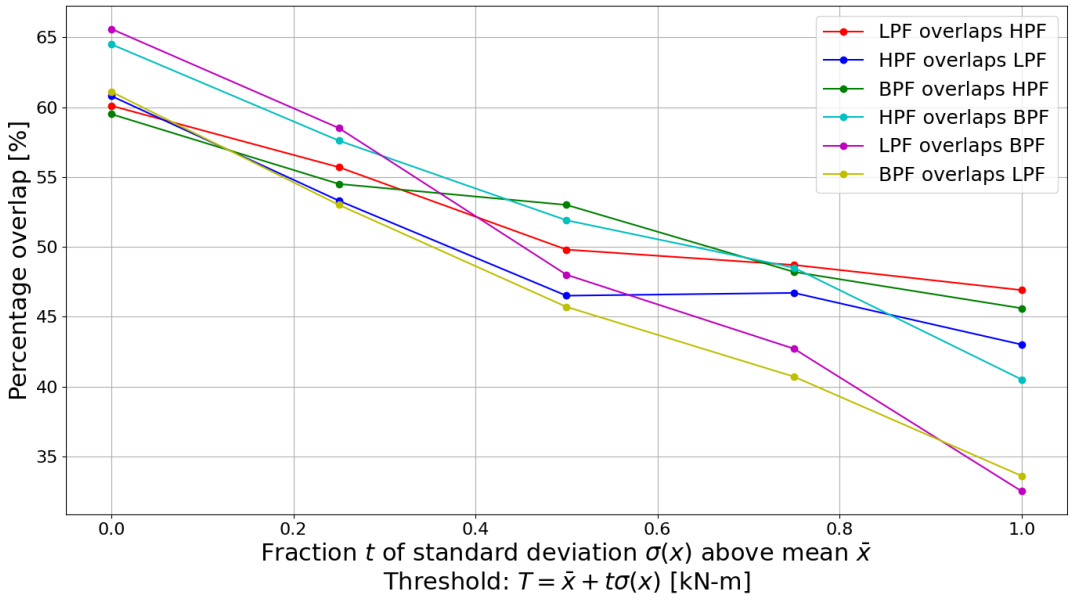

Figure 6-8: Percentage overlap calculated as a function of threshold for the three frequency ranges. Where LPF is low-frequency content of the OOPBM magnitude, BPF is envelope of the 3P frequency, and HPF is the effectively filtered, at 9 s, high-frequency OOPBM magnitude.

A previous analysis showed that turbulence generated asymmetry is strongly correlated with the low-frequency OOPBM signal, the interrelationship between the three frequencies suggests that asymmetry may be the primary mechanism driving the time variations in all three frequency ranges. However, the bursting periods across the three frequencies defined using a range of thresholds, show significant variability in the amount of overlap over the 1000 s period, which may indicate differences in the mechanisms driving the time variations in the three frequency ranges.

6.3 Passage of Atmospheric Eddies Creation of Asymmetrical Velocity Distributions on the Time Variations in the Three Frequencies

In the atmospheric boundary layer the most energetic coherent eddies within the fluctuating velocity field of the daytime ABL are well-known to be highly elongated in the direction of the mean velocity, due to the impact of strong shear near the ground. These coherent structures are often categorized by their fluctuating velocities. Low-speed streaks (LSS), in our analysis are defined as –0.61 m/s below the average velocity, and high-speed regions (HSR) are defined as +0.76 m/s above the average velocity. The passage of these highly energetic coherent eddies through the rotor disk creates asymmetrical velocity distributions over the rotor disk (Figure 6-9). As the blades rotate through the velocity field, they respond to the time variations in asymmetry across the rotor disk, causing time changes of various time scales, in the OOPBM and MB force vector.

In Section 5.4 the time variations in the asymmetrical velocity distribution over the rotor disk were shown to be strongly correlated with the time variations in the aerodynamic OOPBM vector. However, the conclusions were limited to the low-frequency content (0.3 Hz), as the frequency at which the velocity vector field was output, on planes of data, was limited to 2.5 Hz, due to practical reasons. Therefore, to expand the analysis a new asymmetry metric was developed to be able to correlate with the OOPBM vector at all frequencies. The new asymmetry metric utilises the velocity output at each actuator point on the three blades. The new asymmetry metric is denoted the blade asymmetry vector, and has a similar derivation to the asymmetry vector. The asymmetry vector is integrated over every grid point within the rotor disk, whereas, the blade asymmetry is integrated over the blades individually, then summed over the three blades, shown in Eq. 3.10. A detailed derivation and explanation of the blade

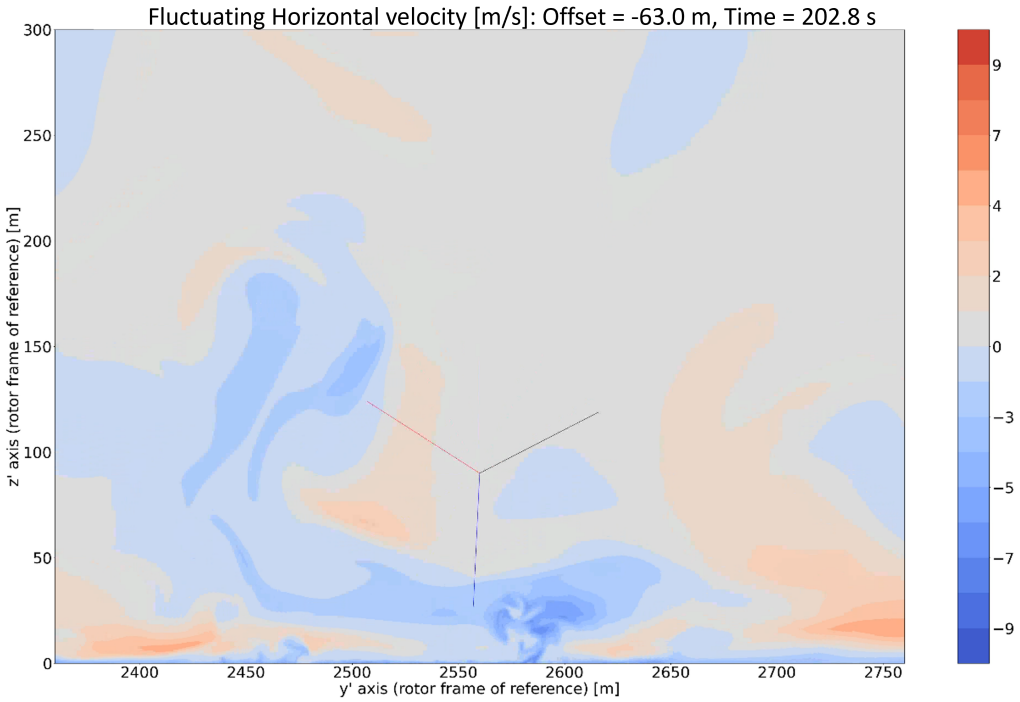

Figure 6-9: Isocontour of the fluctuating x component of the horizontal mean velocity vector $u'_{x'}$ on a plane normal to the rotor plane offset -63.0 m in front of the rotor disk.

asymmetry is given in Section 3.7 and shows the relationship between blade asymmetry and the asymmetry parameter.

Figure 6-10 shows the correlation coefficients, between the blade asymmetry vector (magnitude and direction) and aerodynamic out-of-plane bending moment vector, are consistent with the correlations between the asymmetry vector and out-of-plane bending moment vector. Furthermore, Figure 6-10 shows the time variations correlate very well across all three frequency ranges. Which implies the primary mechanism driving the time variations in the aerodynamic OOPBM vector is the time changes in the asymmetry due to the distribution of the streamwise velocity $u_{x'}$ over the rotor disk, due to the passage of atmospheric eddies.

However, analysis of the interrelationships between the modulation of the low-frequency,

3P-frequency and high-frequency content, due to the passage of eddies through the rotor disk, which appear as groups of high activity in the signals, showed the "strongest" regions of the high activity periods in each of the three frequencies do not strongly overlap, where strongest refers to the regions of high actively with the largest peak-to-peak variations. Which suggests there are differences in the asymmetry mechanism which drives the time variations in the three frequencies.

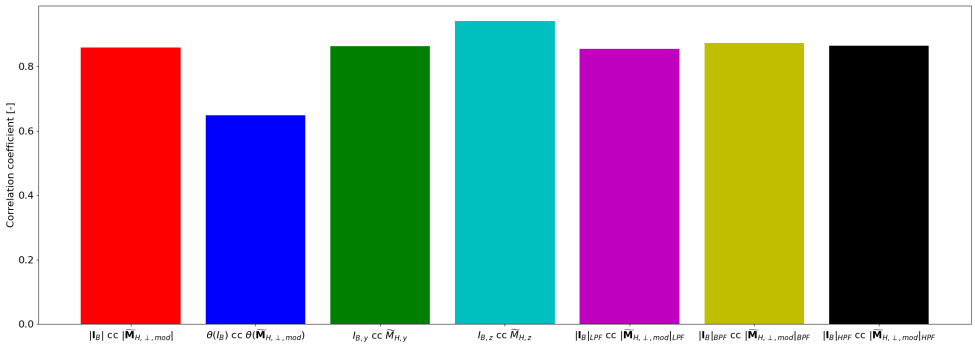

Figure 6-10: Summary of correlation coefficients between the blade asymmetry vector and aerodynamic out-of-plane bending moment vector, including correlation coefficients between components and filtered $\mathbf{I}_B$ and $\widetilde{\mathbf{M}}_{H,\perp,mod}$.

Figure 6-11 illustrates the strength of the relationship between asymmetry and the time variations in the OOPBM vector. Which indicates while there may be differences in the mechanisms that drives the time variations in the three frequencies, the mechanisms are all related to asymmetry. The following analysis aims to answer the question: how does the passage of atmospheric eddies create time variations in the asymmetrical distribution of the velocity field over the rotor disk which drives the time variations in the three frequencies?

The results have shown that the time variations in the low-pass filtered (LPF) aerodynamic OOPBM correlates very well with the LPF blade asymmetry, LPF asymmetry vector, and LPF asymmetry parameter. Indicating that all measures of asymmetry give the same time variations at the low-frequencies. The LPF signals are associated with the passage of atmospheric eddies, calculated between 19 s - 71 s. During an

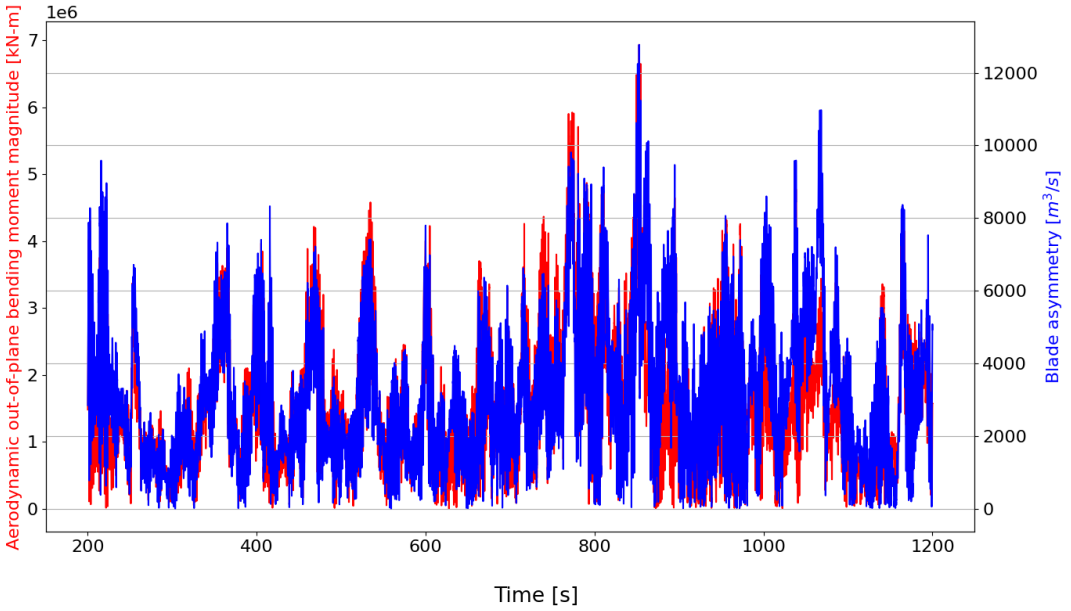

(a)

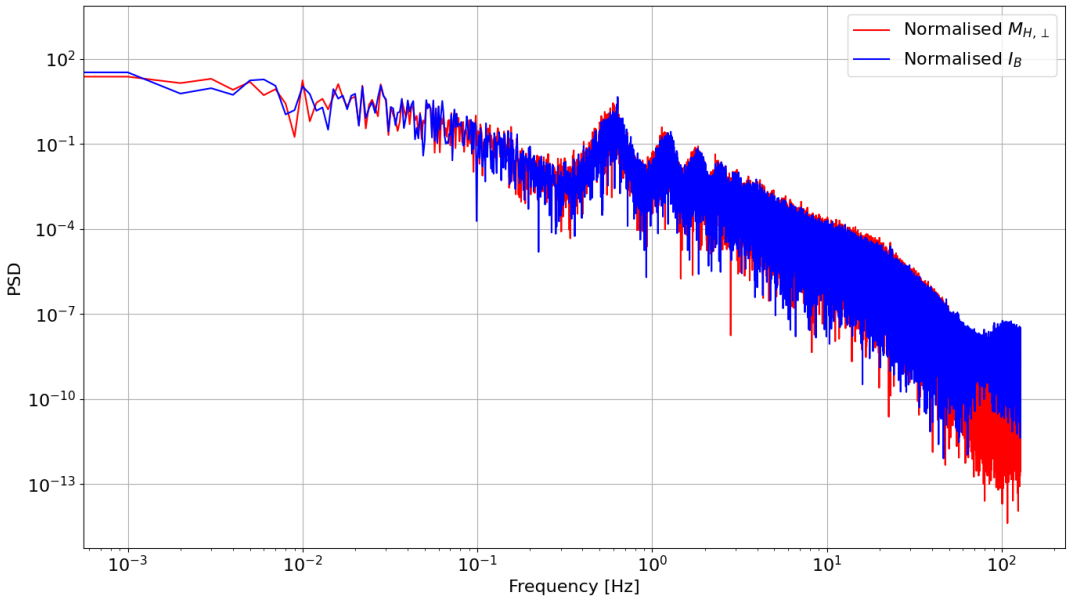

(b)

Figure 6-11: Aerodynamic out-of-plane bending moment and blade asymmetry magnitude normalised on the average of the magnitude. (a) plotted against time, (b) spectra.

eddy passage the three blades will make approximately 5-15 full rotations. So, from the point of view of the blades which make multiple rotations per eddy passage, the

eddy appears frozen. Essentially infinite blades are sampling the velocity field over the rotor disk at the lower frequency, which is the same description as the asymmetry vector and asymmetry parameter. The results demonstrate the low-frequency content is responding to the time variations in the average asymmetry generated over the rotor disk, due to the passage of eddies through the rotor disk.

The HPF frequency content is associated with the blades interacting with the strongest internal variations within the eddy structures [Nandi et al., 2017]. It is hypothesised that, as the blades rotate through the eddy structure, a blade could experience a sudden increase or decrease in velocity, creating a rapid change in the asymmetry, and therefore the OOPBM vector. To test the hypothesis a new measure is developed to capture the changes in the streamwise velocity, the blades experience as they rotate through the velocity field. Several assumptions are made in the development of the metric used to correlate the change in the streamwise velocity, to the change in the high-frequency OOPBM magnitude. Firstly, the velocity on each blade at only the 75% span location are used in the calculation, as it is assumed the time variations in asymmetry can be represented by the contribution from the actuator point at the 75% span location given in the expression below

$$\mathbf{I}_{B,75\%} = \left(I_{B,75\%}, \theta_{I_{B,75\%}}\right) = \sum_{j=1}^{3} u_{x',75\%,j}\mathbf{r}_{75\%,j}\, dr, \tag{6.2}$$

where 75% indicates the actuator point at 75% span location, j indicates blade 1-3 and $|\mathbf{I}_{B,75\%}| = I_{B,75\%}$.

Figure 6-12 shows the correlation between the blade asymmetry vector magnitude integrating along the entire span of the blade Eq. 3.10 with the blade asymmetry vector magnitude calculated only using the actuator point at the 75% span location Eq. 6.2, the strong correlation suggests the assumption is acceptable. The 75% span location was chosen rather than another actuator point, because the 75% span location

is the peak in the airfoil forces as a function of span, and after being multiplied by the moment arm strongly contributes to the hub moments.

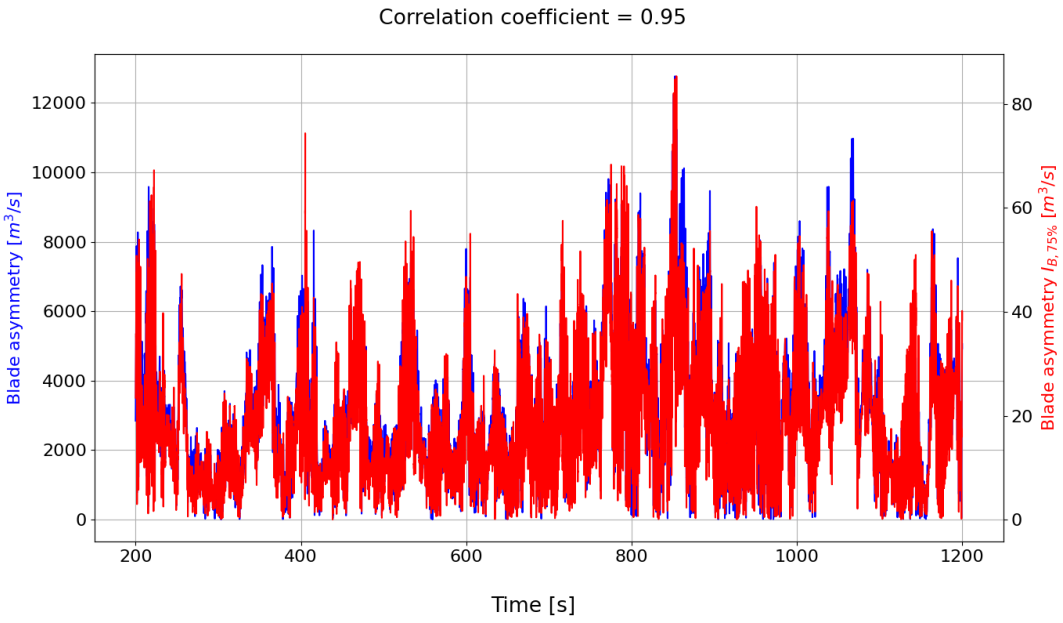

Figure 6-12: Correlation between blade asymmetry magnitude and blade asymmetry magnitude calculated only using the actuator point at the 75% span location Eq. (6.2).

The streamwise velocity at the 75% on each blade $u_{x',75\%,j}$, where j is the blade index, is used to calculate the change in velocity between two points in time. It is assumed the largest change in velocity on one blade is the primary driver of the time variations in blade asymmetry. Therefore, the maximum absolute change in the streamwise velocity between the three blades $max[|du_{x',75\%,j}|]\,(t)$ is correlated in time with the absolute change in the high-frequency content (HPF 1.5 Hz - 40 Hz) in the out-of-plane bending moment magnitude, $|dM_{H,\perp,HPF}|\,(t)$.

Figure 6-13 shows the correlation between $max[|du_{x',75\%,j}|]\,(t)$ and $|dM_{H,\perp,HPF}|\,(t)$ is 0.66. The correlation between the HPF blade asymmetry and HPF OOPBM magnitude is 0.86, indicating the maximum change in the streamwise velocity at the 75% span location, between the three blades, is a strong contributor to the time variations in the HPF OOPBM magnitude, however, may not be the entire reason for the rapid changes

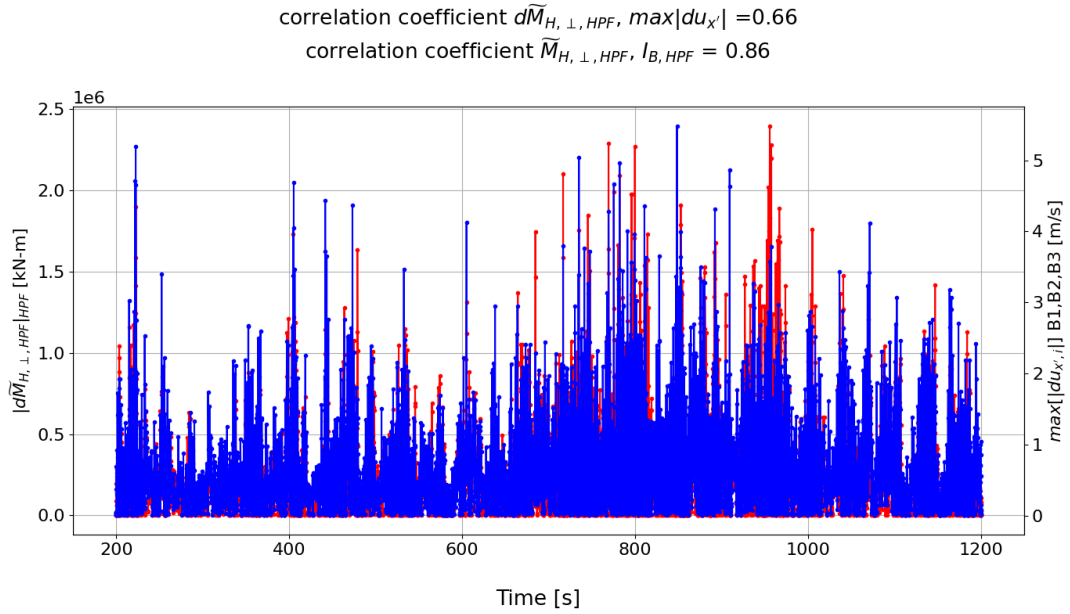

Figure 6-13: Correlation between $max|d_{u_{x',75\%,j}}|$ and $|d\widetilde{M}_{H,\perp,HPF}|$.

in asymmetry driving the time variations in the high-frequency OOPBM magnitude. It is also likely the assumptions are oversimplifying the metric used to correlate the changes in the streamwise velocity to the time changes in the HPF OOPBM magnitude, thus may cause some of the difference between the correlations.

The 3P frequency content of the OOPBM is associated with the periodic rotation of three blades through the turbulent non-uniform inflow. It has been shown the 3P-frequency content is modulated by the passage of atmospheric eddies, which increases the variability of the 3P-frequency over a wide range of frequencies (0.3 Hz - 0.9 Hz). In a steady-shear inflow, where the inflow profile is that of a mean shear profile, Figure 6-14a shows as the shear exponent (α_s) increases, the time average and peak-to-peak variation increase. Suggesting the 3P-frequency content of the OOPBM magnitude is modulated by the eddy passage, which is varying the average gradient over the rotor disk.

The average gradient magnitude over the rotor is calculated using the planar data at 63.0 m in front of the rotor disk. After linearly shifting the average gradient magnitude

in time to account for the advection time to the rotor disk (see section 3.8), Figure 6-14b shows poor correlation with the envelope of the 3P-frequency content of the aerodynamic OOPBM magnitude, which represents the modulation of the 3P-frequency content. However, qualitatively there are periods of time where the two signals display similar time variations. Which implies the average gradient is part of the mechanism, but while the average velocity gradient over the rotor disk is the primary mechanism that drives the time variations in the OOPBM for a steady shear inflow, this does not translate well when applied to the LES-turbine simulation. Possibly due to the structure of the true ABL being highly complex compared to the simple shear inflow.

The results indicate the primary mechanism driving the time variations in the 3P-frequency content of the OOPBM is much more complex, than simply the average velocity gradient magnitude over the rotor disk. Studying the isocontour of the rotor plane, the velocity field is highly complex and furthermore, the 3P-frequency content lies between the low-frequency and high-frequency content, which are driven by the average asymmetry, and the instantaneous changes in asymmetry respectively. Suggesting the 3P frequencies may be driven by a combination of average asymmetry and instantaneous asymmetry.

To summarise, as the blades rotate through the velocity field all frequencies of the aerodynamic out-of-plane bending moment vector are forced by the asymmetry in the velocity over the blades. However, there are subtle differences in the way asymmetry drives the time variations across the three frequencies. The low-frequency content (0.3 Hz) is forced by the average asymmetry, while the high-frequency content is forced by the blades rotating through the internal eddy structures. As the blades rotate through the velocity field the blades respond to the largest velocity gradients causing instantaneous changes in asymmetry. The 3P-frequency mechanism is complicated, the average gradient magnitude is not strongly correlated with the envelope of 3P-frequency OOPBM magnitude, indicating the modulation of the 3P frequency content

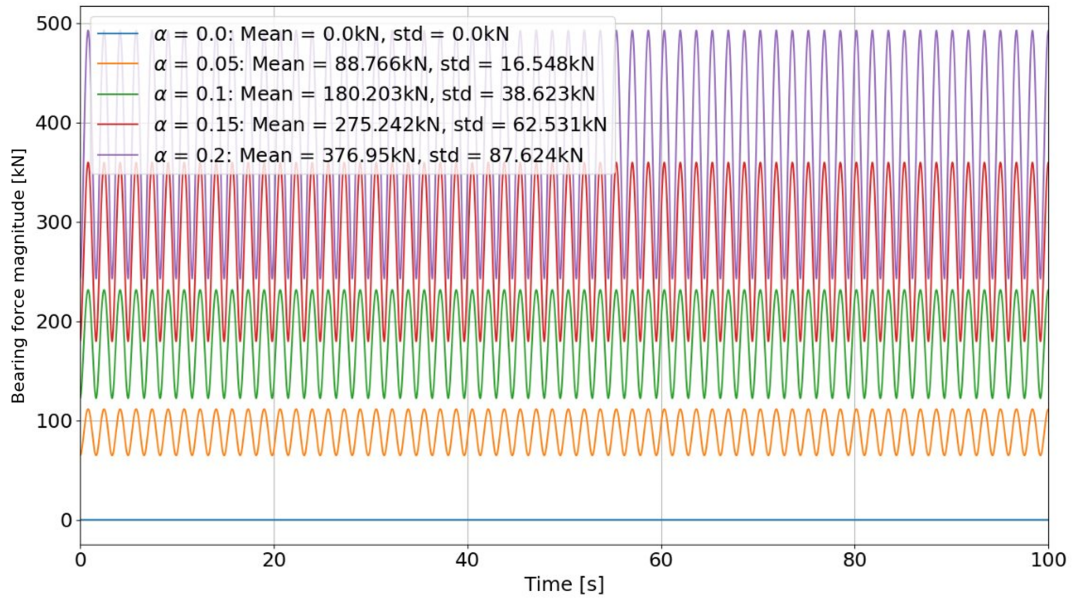

(a)

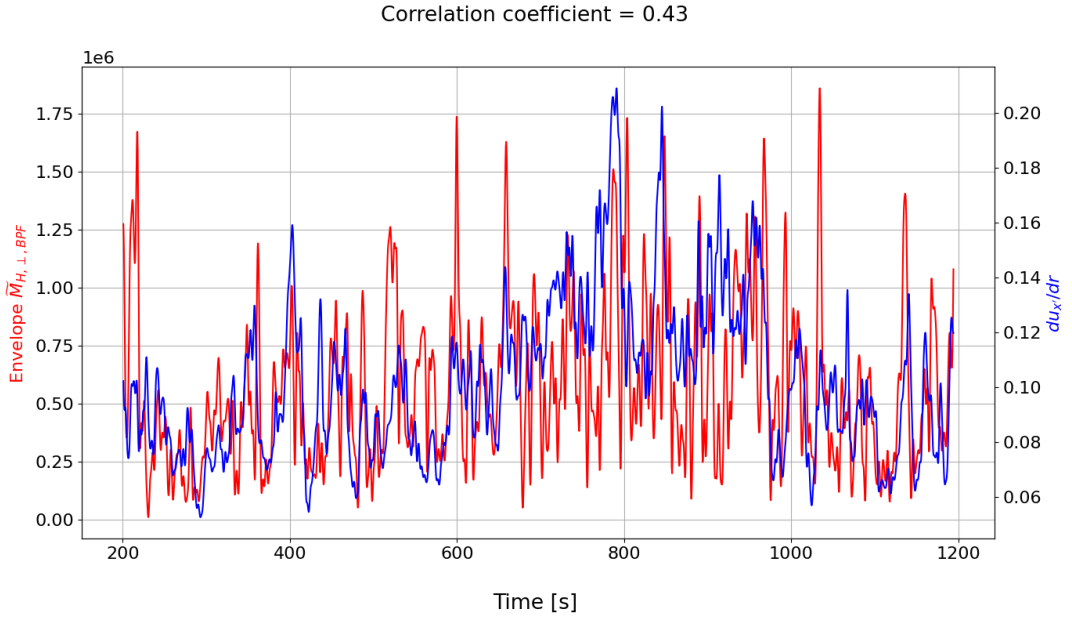

(b)

Figure 6-14: (a) Systematic variation of shear exponent plotting the resultant bearing force magnitude over a 100s period. (b) Correlation between the envelope of the 3P content in the out-of-plane bending moment and average of the magnitude of the velocity gradient over the rotor disk $du_{x'}/dr$.

is too complicated to be described with a simple metric.

6.3.1 Relating the Responses of the Time Variations in the Out-of-plane Bending Moment at each of the Three Frequency Ranges with Specific Classes of Energy-containing Atmospheric Turbulence Eddies

Previous analysis showed the overall asymmetry over the rotor disk drives the low-frequency content in the MB radial force. By calculating the asymmetry vector components (Eq. 3.8 & Eq. 3.9), segregated for high, low and intermediate-speed fluid, the contributions from the specific classes of energy-containing eddies can be analysed. The reason the components are analysed, rather than the asymmetry vector magnitude is because the non-linear operation creates cross product components between the contributions making it much more complicated to analyse the contributions from the classes of eddies. It can be shown the summation of the asymmetry vector component from the classes of eddies is equivalent to the asymmetry vector component. $\mathbf{I} = \iint_A u_{x',HSR}\mathbf{r}dA + \iint_A u_{x',LSS}\mathbf{r}dA + \iint_A u_{x',Int}\mathbf{r}dA$, where subscript HSR,LSS,Int indicates the velocity is associated with a HSR, LSS or intermediate fluid respectively.

Figure 6-15 shows the contributions from HSRs, LSSs and intermediate velocities to the asymmetry vector components. The probability distributions of the contributions to the asymmetry vector components shows the probability of contributions from LSSs are on average higher compared with HSRs. Furthermore, the average of the contribution to I_y and I_z from LSSs are calculated as $40000\,\mathrm{m}^4/\mathrm{s}$ and $194000\,\mathrm{m}^4/\mathrm{s}$ respectively, which are approximately 2.5 times and 3 times larger than the average of the contribution from HSRs ($17000\,\mathrm{m}^4/\mathrm{s}$ and $-62000\,\mathrm{m}^4/\mathrm{s}$). The tails of the PDFs indicates HSRs play a larger role in the generation of the largest asymmetries, compared with LSSs as the tails of the PDF for LSS ends at a lower value. However, since the occurrence of the most extreme events is very low, it is still fair to conclude the contributions to asymmetry from low-speed streaks are on average higher compared with those from

high-speed regions. The intermediate velocities do play a role in the time variations in the asymmetry vector, however regions of intermediate velocity are not classed as a type of eddy, therefore, are not of interest in the analysis.

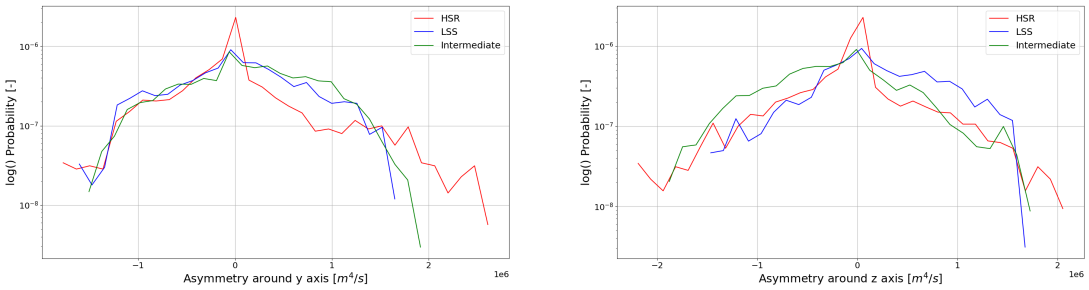

(a) (b)

Figure 6-15: Probability density distribution of (a) Asymmetry around y axis, (b) asymmetry around z axis calculated for high-speed regions, low-speed streaks and intermediate regions.

Qualitative analysis of the line plots of the streamwise velocity at 75% span location at each blade $u_{x',75\%,j}\,(t)$ (Figure 6-16), the isocontour movies of the streamwise velocity field $u_{x'}$ and the high-frequency MB radial force magnitude, indicate a significant number of the largest "jumps" in the high-frequency MB radial force magnitude may be occurring when a blade is entering or leaving a low-speed streak. Where jump refers to the peak-to-peak change in the magnitude of the signal (See section 3.9).

To quantify the fraction of the largest "jumps" in the high-frequency MB radial force magnitude (denoted 2σ events), that occur due to a particular type of eddy: firstly the largest jumps are defined as the peak-to-peak changes in the high-frequency MB radial force magnitude that are two standard deviations greater than or less than the average (See Figure 6-16). Next, the change in the streamwise velocity at the 75% span locations of each of the three blades are output during the 2σ events, and the maximum absolute change in the velocity is identified, as Section 6.3 showed the high-frequency OOPBM responds strongly to the maximum change in the velocity at 75% span across the three blades.

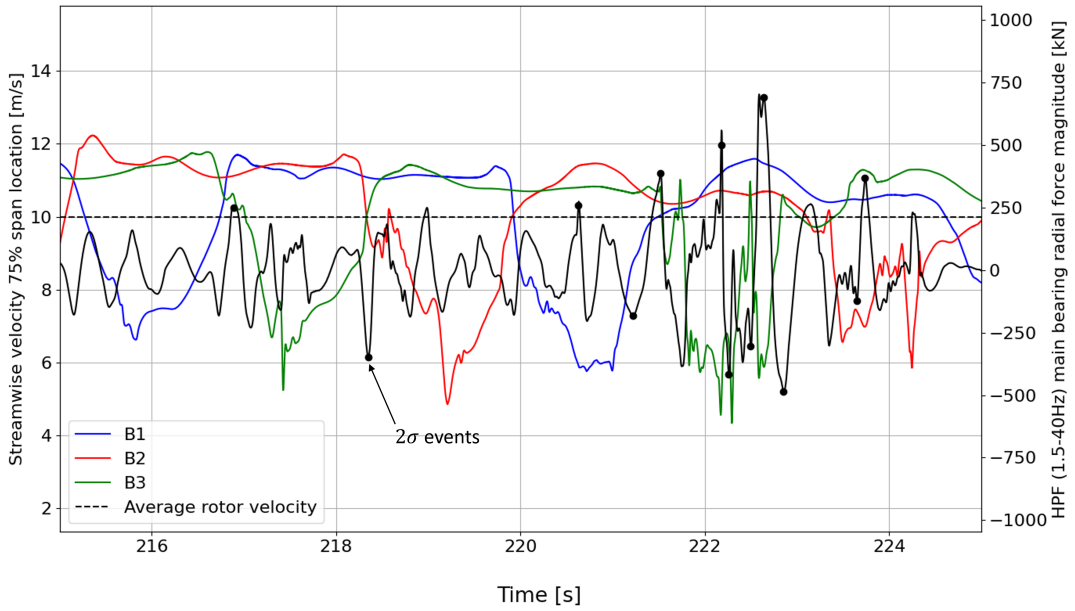

Figure 6-16: Left axis streamwise velocity at 75% span location for all three blades $u_{x',75\%,j}$, where the dashed line is the time averaged velocity averaged over the rotor disk. Right axis high-frequency out-of-plane main bearing force magnitude, where the black dots indicate the initial time in the 2σ event.

While the analysis in Section 6.3 only used the maximum change in the streamwise velocity over the three blades, to potentially account for the changes in the streamwise velocity of the other two blades, a set of conditions are set forth. If the change in the velocity of a blade at the 75% span location is within a 0.5 times the maximum absolute change in the velocity, the blade is included in the subsequent calculation. The threshold is varied from 0.5-1.0, to examine the effect of our choice of threshold. 0.5 was chosen as the lowest threshold accepted, because it was decided that if the change in velocity is less than a factor of 2, compared with the maximum absolute change, it will likely not produce a significant contribution to the change in asymmetry.

After the blades have been checked whether they meet the conditions described above, the type of eddies the blades are interacting with needs to be determined for the blades that met the criteria. This is done by checking the initial and final velocities over the 2σ jump in the high-frequency MB radial force magnitude. The conditional

statements to decide the type of eddy are: if the initial and final streamwise velocity on the blade are below the rotor averaged streamwise velocity, then the blades are only interacting with LSSs. If the initial and final streamwise velocity on the blade are above the rotor averaged streamwise velocity, then the blades are only interacting with HSRs. Otherwise, the blades are interacting with both HSRs and LSSs, the conditional statements are given in Table 6.1.

$u_{x',75\%,j,i}$	$u_{x',75\%,j,i+1}$	eddy type
$\leq \langle u_{x'} \rangle_{A,t}$	$\leq \langle u_{x'} \rangle_{A,t}$	LSS only
$\leq \langle u_{x'} \rangle_{A,t}$	$\geq \langle u_{x'} \rangle_{A,t}$	LSS and HSR
$\geq \langle u_{x'} \rangle_{A,t}$	$\leq \langle u_{x'} \rangle_{A,t}$	LSS and HSR
$> \langle u_{x'} \rangle_{A,t}$	$> \langle u_{x'} \rangle_{A,t}$	HSR only

Table 6.1: Conditional statements used to decide the type of eddy a blade is interacting with, where i is the initial time and $i + 1$ is the final time.

The fraction of the 452 2σ events over the 1000 s corresponding to different types of eddies, using the algorithm detailed above is plotted against the threshold used to decide whether or not to include the change in velocity from each of the blades. If the threshold is 1.0, meaning the change in the blade velocity must be equal to the maximum change in the velocity over the three blades to be included in the subsequent calculation, the fraction of 2σ events likely caused by low-speed streaks is 71%, while HSR only accounts for 7%, and 22% from both LSS and HSRs. If the threshold is 0.5, meaning the change in the blade velocity must be within a factor of 2 of the maximum change in the velocity over the three blades to be included in the subsequent calculation, the fraction of 2σ events likely caused by low-speed streaks is 54%, while HSR only accounts for 4%, and 42% from both LSS and HSRs.

The results indicate low-speed streaks are the dominant eddy type, which generates the largest changes in the MB radial force magnitude, in the high-frequency content, as the blade interacts with the internal gradients within the eddy. Low-speed streaks are likely

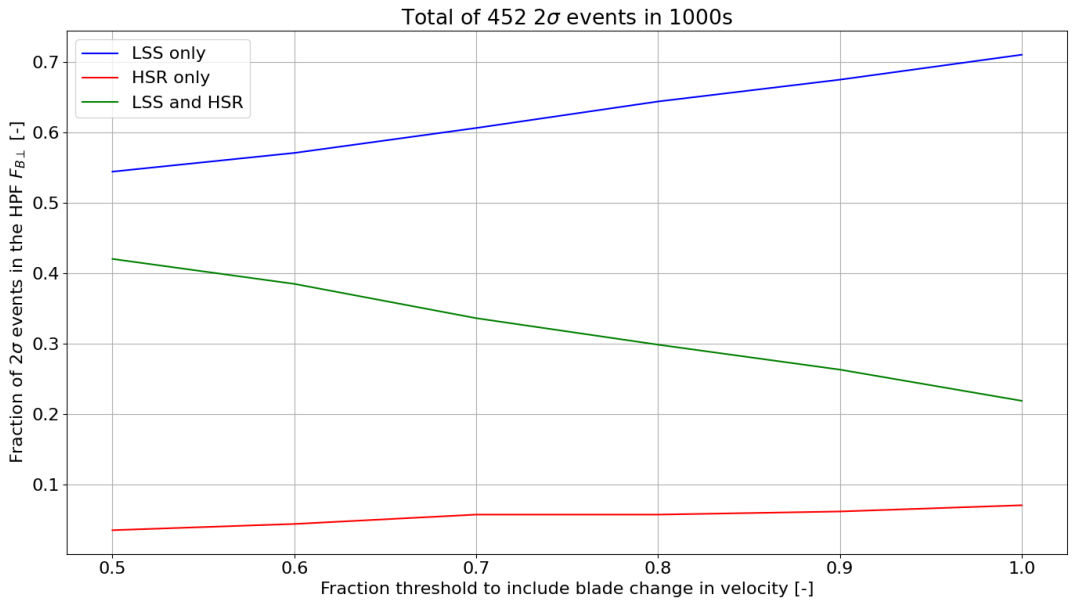

Figure 6-17: Fraction of 2σ events in the high-frequency out-of-plane main bearing force magnitude due to the different types of eddies plotted as a function of threshold.

the dominant eddy type because they are known to be much more coherent, and tend to have higher internal gradients, and high-speed regions are known to be less coherent, thus the gradients are on average lower compared to low-speed streaks. Figure 6-18 shows the gradient magnitude averaged for low-speed streaks and high-speed regions, which confirms on average LSSs have higher internal gradients compared to HSRs. The results suggest LSS may be potentially more detrimental to WTs as they are responsible for most of the largest peak-to-peak variations in the high-frequency content.

The analysis above suggests LSSs are the primary cause of the largest peak-to-peak variations in the high frequency content of the MB radial force magnitude. In the 1000 s calculation there is a 100 s period where an especially large and coherent low-speed streak covers the entire rotor disk, and a 60 s period where an especially large high-speed region covers the rotor disk. The time periods are determined by examining the rotor averaged velocity (Figure 6-19a), the area of rotor covered by a class of eddy as a fraction of rotor area (Figure 6-19b), and qualitatively studying the isocontours of the

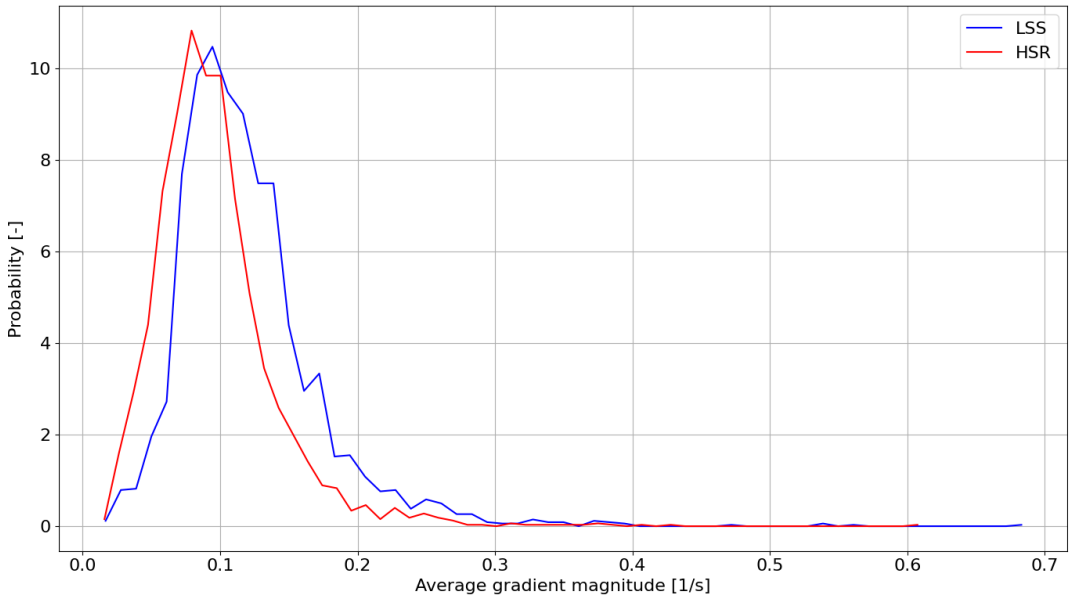

Figure 6-18: Average velocity gradient magnitude threshold on types of eddy defined on the fluctuating velocity.

fluctuating velocity, on planes normal to the rotor disk (Figure 6-19c-6-19d). The time periods are selected so the rotor average velocity is above or below the average, and the rotor area is covered primarily by low-speed fluid or high-speed fluid. To investigate the high-frequency response due to HSR and LSS further, the standard deviation of the high frequency content in the aerodynamic OOPBM magnitude is calculated over the entire 1000 s, the 700 s - 800 s period and the 850 s - 910 s period to compare. The standard deviations are calculated as: 80.2 kN, 114.2 kN and 97.2 kN respectively. The standard deviation is 17% larger over the period of time where the LSS dominated the rotor disk area, compared to the period of time where the HSR dominates the rotor disk. Indicating that LSS on average generate larger peak-to-peak variations at the high-frequencies, consistent with the previous results. In addition, the average of the of the MB radial force magnitude is 1133.6 kN, significantly larger than the average over the total 1000 s and the 815 s - 915 s (during the HSR), which are: 926.4 kN and 751.8 kN respectively. Which indicates LSS are also contributing more to the overall/average asymmetry over the rotor disk compared to HSR.

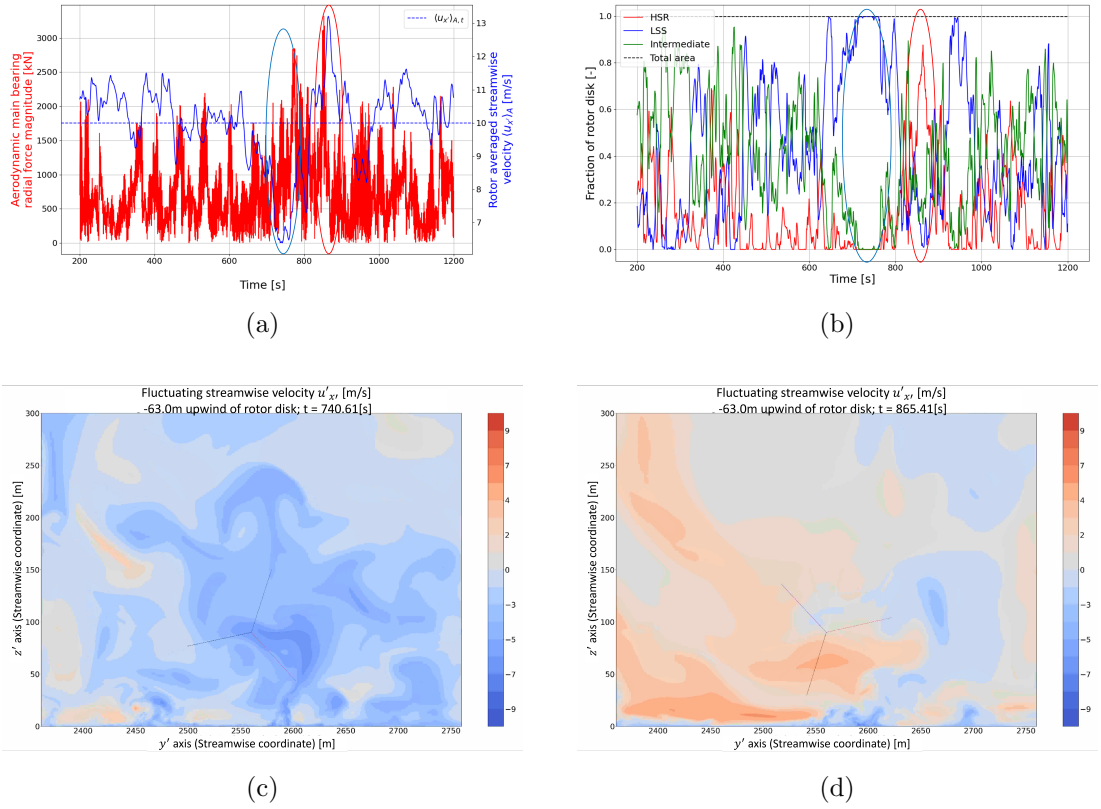

Figure 6-19: (a) Area of rotor covered by a class of eddy as a fraction of rotor area, the blue circle indicates 700 - 800 s, and the red circle indicates 850 - 910 s. (b) Main bearing radial force magnitude (left axis), rotor averaged streamwise velocity (right axis) rotor-averaged streamwise velocity is indicated by the dashed line, the blue circle indicates 700 - 800 s, and the red circle indicates 850 - 910 s. (b) Isocontour of the fluctuating streamwise velocity on a plane normal to rotor disk, -63 m in front of rotor disk, at t=740.61 s, (c) Isocontour of the fluctuating streamwise velocity on a plane normal to rotor disk, -63 m in front of rotor disk, at t=865.41 s.

The analysis of the specific classes of energy-containing atmospheric turbulence eddies highlights the importance of the accurately representing the classes of eddies, in the nonsteady response of the WT to the passage of atmospheric eddies. The coherence and magnitude of the internal gradients present in the eddies has been shown to be of great importance, as the difference in the coherence and magnitude of the internal gradients of LSSs and HSRs is shown to result in significant differences in the high-frequency response of the MB radial force magnitude. The structure of the daytime atmospheric boundary layer and key characteristics of the LSS and HSR are captured

well by the LES-ABL model developed in this study. Kinematic turbulence models are the industry standard to perform design load calculations, when designing WTs [International Electrotechnical Commission, 2019]. However, kinematic turbulence models are likely unable to accurately capture the true structure of the ABL, coherence and magnitude of the internal gradients within the eddy structures. Therefore, the nonsteady response calculated from a WT simulation using kinematic turbulence will likely not be representative of the nonsteady response due to true atmospheric turbulence.

6.3.2 Surges of Low-speed Fluid from the Surface into the Rotor Disk

Studying isocontours of the fluctuating streamwise velocity ($u'_{x'}$) on planes normal to the rotor disk, surges of low-speed fluid were observed advecting vertically into the rotor disk, originating from the surface layer (Figure 6-20). It was hypothesised that low-speed fluid is pushed off the surface and carried vertically into the rotor disk by the vertical velocity component, and could potentially have a significant contribution to the time variations in asymmetry.

These coherent regions are referred to as "surges" of low-speed fluid, and are defined as coherent regions of low-speed fluid directly connected to the surface. An algorithm is developed to identify surges of low-speed fluid, using planar data, normal to the rotor disk, of the fluctuating streamwise velocity $u'_{x'}$ between -1.4 m/s - -4.5 m/s. -1.4 m/s below the rotor-averaged velocity was chosen as the upper limit, to define a surge of low-speed fluid, because when -0.61 m/s (definition of a LSS) was used, the algorithm began identifying horizontally advecting LSS close to the surface as surges. -4.5 m/s below the rotor-averaged velocity was chosen as the lower limit, because between -4.0 m/s and -4.5 m/s the algorithm did not find any surges in the 1000 s. The algorithm outputs the (y', z') coordinates on the rotor-normal plane, where it determines a surge. The algorithm starts with the coordinate in the lower left corner, the fluctuating velocity at that coordinate is compared against the threshold velocity. If the fluctuating velocity at that coordinate is greater than the threshold velocity, the

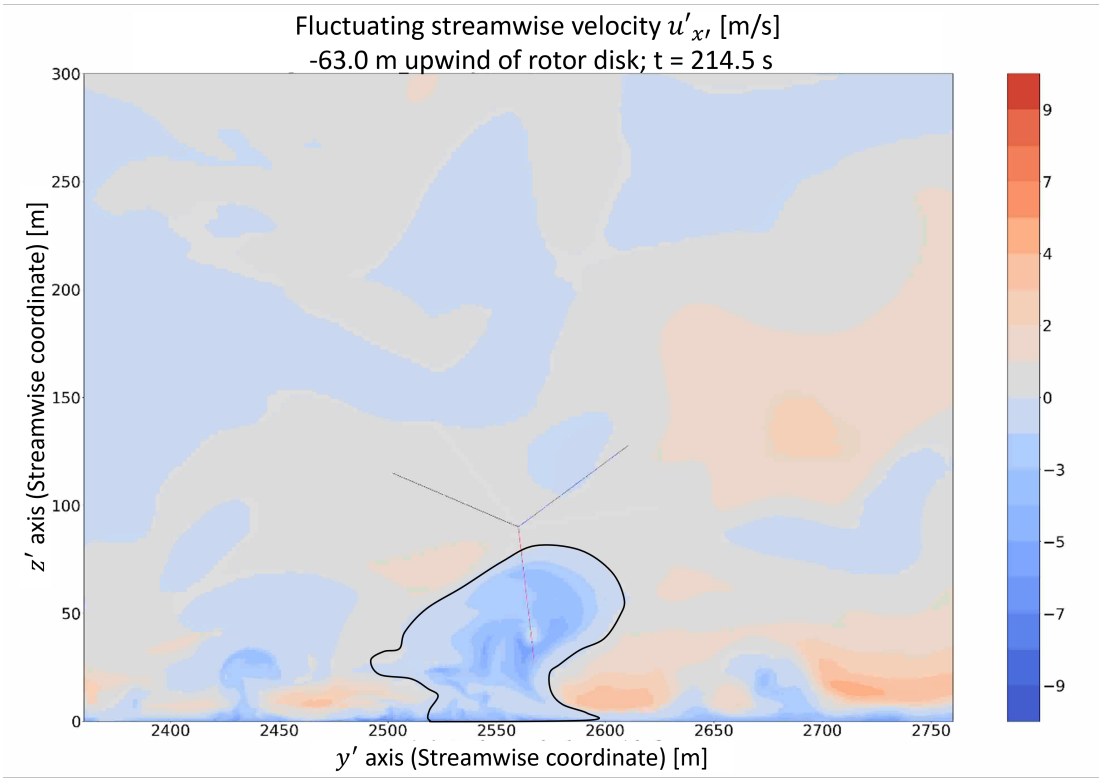

Figure 6-20: Isocontour of the fluctuating streamwise velocity, on a plane normal to rotor disk -63 m in front of rotor disk, at t=214.5 s. The black curve illustrates a "surge" of low-speed fluid from the surface.

fluctuating streamwise velocity at the coordinate above is checked. This continues until the fluctuating streamwise velocity at coordinate (y'_i, z'_{j+m}) is less than the threshold velocity, the coordinate (y'_i, z'_{j+m}) is then stored in an array. The height from the surface, z' coordinate, is determined for all y' coordinates, which defines the surges of low-speed fluid; the algorithm is repeated for all time steps. The algorithm ensures the surge conforms to the definition of a surge, "coherent region of low-speed fluid directly connected to the surface", which is important to maintain.

To study the surges of low-speed fluid the percentage of time a surge is inside the rotor disk and the contribution to asymmetry from these surges is calculated for decreasing fluctuating velocity. Using the coordinate data the percentage of time the surges are inside the rotor disk and the contributions from the surges to the asymmetry vector

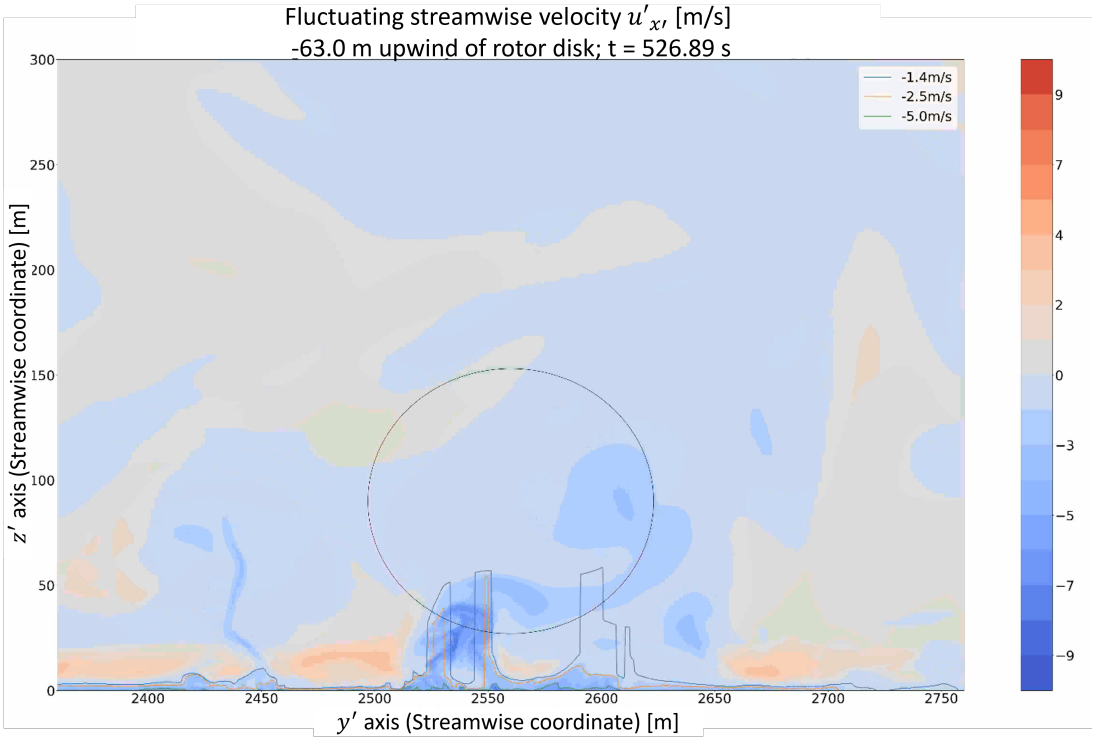

Figure 6-21: Isocontour fluctuating streamwise velocity on plane normal to rotor disk -63 m in front of rotor disk t=526.89 s black, orange and green curves illustrating surge identification algorithm for a fluctuating velocity thresholds of -1.4 m/s, -2.5 m/s and -5.0 m/s illustrating the height of surge as a function of y' coordinate.

can be calculated as a function of velocity threshold. Table 6.2 shows the surges will contribute to the asymmetry vector up to 33.8% of the 1000 s. Figure 6-22 shows the magnitude of the asymmetry vector (black), and shows the contributions to the asymmetry vector magnitude from the low-speed surges, which are not insignificant. As the surges first impact the bottom of the rotor disk, the radial distance between the low-speed surge (bottom of the of the rotor disk) and the centre of the rotor disk is at its largest, thus the low-speed surges can generate large asymmetries. These surges of low-speed fluid could potentially be driven by vertical velocity fluctuations, thus would only be present in MCBLs, where LSSs are strongly correlated spatially with updrafts. In an offshore environment, where the ABL is stably stratified, surges of low-speed fluid originating from the surface are likely not appear as a mechanism driving asymmetry

over the rotor disk.

Table 6.2: Percentage of 1000 s surge with specific threshold below the average, is inside rotor disk.

velocity threshold [m/s]	-1.4	-2.0	-2.5	-3.0	-3.5	-4.0	-4.5
Percentage of 1000 s [%]	33.8	20.1	11.8	7.29	3.35	0.70	0.0

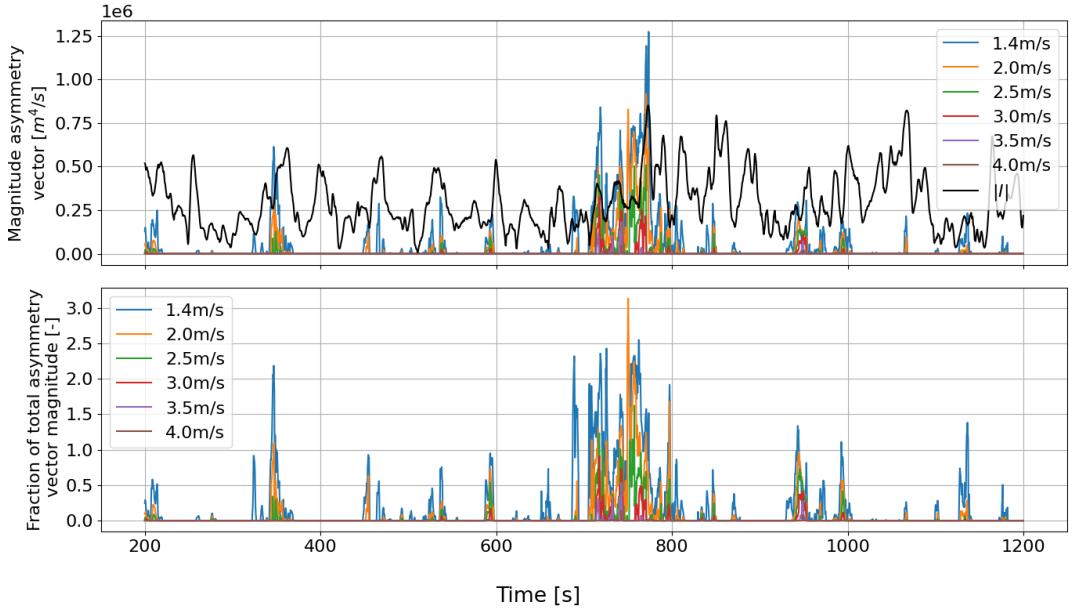

Figure 6-22: Contributions to the magnitude of the asymmetry vector from low-speed surges plotted as a function of velocity threshold. (upper) magnitude asymmetry vector, (lower) fraction of total asymmetry vector magnitude.

The algorithm developed for the above analysis is likely not able to distinguish between a surge and a horizontally advecting low-speed streak which is close to the ground. Therefore, there is a good chance some of the surges found in the above analysis are horizontally advecting eddies close to the ground, but the algorithm developed classified them as surges. Therefore, to determine the mechanism generating the low-speed surges, a better definition of what a surge is, is required. The aim was to develop a more rigorous physics based approach to define the low-speed surges, compared to the approach used so far.

With the data available the origins of the surges are hard to identify. Full three-

dimensional datasets of the velocity field are be required to trace the origins of these surges to establish, whether or not they are due to low speed fluid being pushed off the surface, and then advect into the rotor disk. Or whether these regions of low speed fluid are actually low speed streaks but coincidently close to the ground. Due to practical reasons full three-dimensional datasets of the velocity field in time were not output, therefore, further analysis into the low-speed surges was not practical.

6.4 Contributions of the Three Frequencies to the Main Bearing Radial Force Magnitude

The aim of this section is to analyse the contributions from the three frequency ranges to the time variations in the MB radial force magnitude. The time variations in the MB radial force magnitude and MB radial force magnitude over the three frequency ranges are quantified by the changes in the magnitude and the corresponding time over the change. These changes are referred to as "jumps", and are calculated using the method detailed in Section 3.9. The method calculates the jumps from a peak to the next trough in the signal, then from the trough to the next peak and so on.

The method is used in conjunction with the filtering method to quantify the jumps in the filtered signals. Figure 6-23 plots the "jumps" in the main bearing force magnitude against the corresponding change in time for the three filtered signals, and highlights the filter frequency with vertical lines. Any points to the left, or in the case of Figure 6-23b the left and right, of the vertical lines indicates a jump that the filtering process has failed to remove. It should be noted that Δt is calculated from a peak to the next trough, which is only half a period, so the filter frequency is divided by 2.

Figure 6-23 shows there are data points across all three filters that lie outside the cutoff frequency. The scatter plots indicates these points occur at the smallest ΔF. These points may be being picked up since they occur at such small ΔF, also they may be

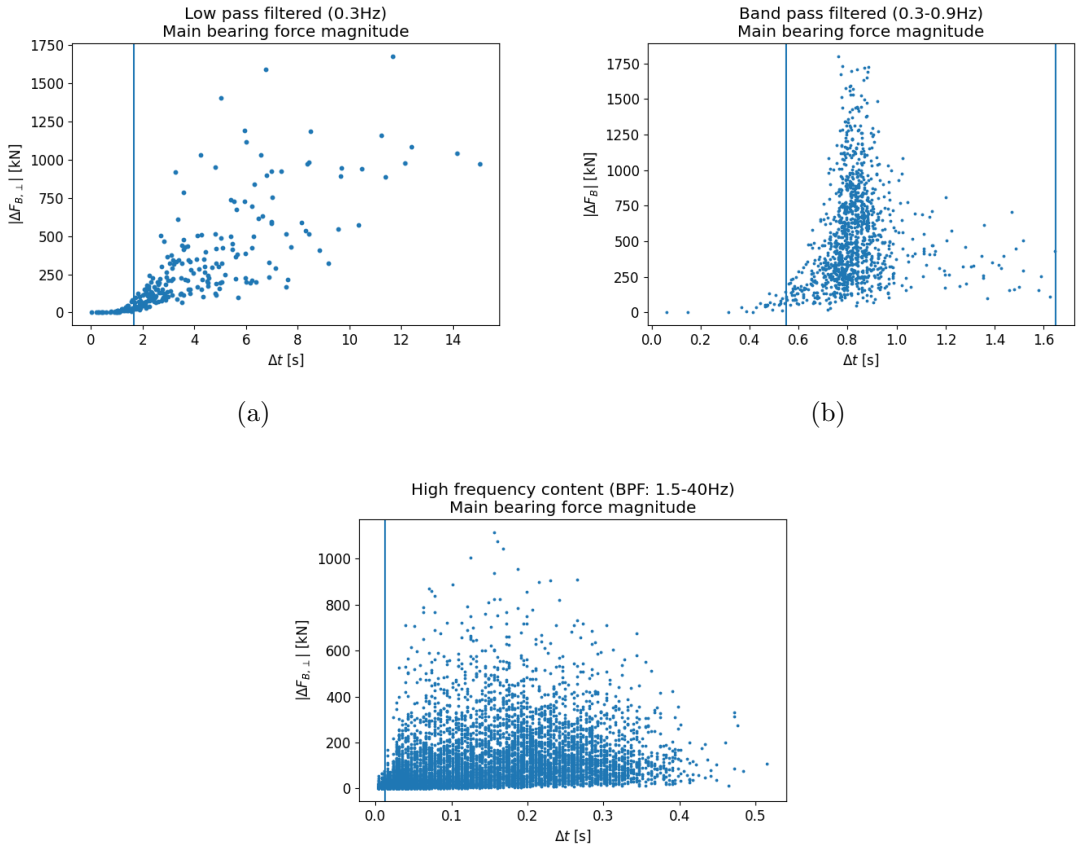

Figure 6-23: Scatter plot of $|\Delta F|$ against the corresponding Δt for the jumps in the filtered main bearing force magnitude signal. The vertical line indicates the inverse of the filter frequency. (a) Low pass filtered (0.3 Hz). (b) Band pass filtered (0.3-0.9 Hz). (c) High frequency content (Band pass filter (1.5-40 Hz).

due to artifacts in the signal. Either way all data points calculated from the filtered signals are included in the analyses.

To analyse the magnitude of the jumps, the absolute change in the magnitude is calculated, as the sign is not of importance to the analysis. The absolute change in the magnitude is normalised on the rotor weight at the MB ($W_R\,(L/L_2)$), to put the change in the magnitude into perspective. Furthermore, the corresponding time over the jump is calculated for half a period, therefore to estimate the period, one can multiply the calculated Δt by a factor of 2.

$\Delta F_{B,\perp}/W_R\,(L/L_2)\,[-]$				
	Total	LPF	BPF	HPF
Mode X_{max}	0.012	0.015	0.15	0.0065
average μ_1	0.063	0.134	0.261	0.05
Standard deviation μ_2	0.122	0.152	0.167	0.065
Skewness μ_3	2.92	1.77	0.96	2.38
Kurtosis μ_4	13.2	6.04	3.67	10.77

Table 6.3: Summary of statistics of the absolute change in the main bearing radial force magnitude peak-to-peak variations normalized on the rotor weight contribution at the main bearing.

$\Delta t[s]$				
	Total	LPF	BPF	HPF
Mode X_{max}	0.021	2.38	0.79	0.014
average μ_1	0.11	3.76	0.82	0.12
Standard deviation μ_2	0.18	2.61	0.14	0.10
Skewness μ_3	2.40	1.44	1.34	0.73
Kurtosis μ_4	9.19	5.40	11.16	2.49

Table 6.4: Summary of statistics corresponding change in time in the main bearing radial force magnitude peak-to-peak variations.

The jumps are calculated for the MB radial force magnitude, low-frequency, 3P frequency and high-frequency content in the MB radial force magnitude, and statistics for the jumps are compared to investigate the contributions from the three frequency ranges to the MB radial force magnitude. The statistics for the jumps in the MB radial force magnitude are summarised in Table 6.3 and the corresponding time over the jumps are summarised in Table 6.4. Table 6.3 shows a large proportion of the jumps in the MB radial force magnitude are between $0.012W_R\,(L/L_2)$ and $0.185W_R\,(L/L_2)$, between the most probable value and the average plus one standard deviation. Which means in the 1000 s period a significant proportion of the jumps in the magnitude are

less than 20% of the rotor weight. Table 6.4 indicates a large proportion of the time changes are between 0.021 s - 0.29 s, which is in the sub-second/high-frequency region. The skewness of the jumps does not hold any significance since the absolute value of the jump in the magnitude is used.

The flatness of the changes in magnitude is calculated as 13.2, which indicates while a large proportion of the data lies around the peak in the probability distribution, there are some especially large jumps in the magnitude which reside in the tails. Even if only a couple of these especially large jumps occur over the 1000 s, over a full 12 hour day (daytime), a significant number could occur which may have the potential to cause damage to the MB. The flatness of the corresponding changes in time is calculated as 9.19, which highlights that the time response of the MB radial force is spread over a wide range of time scales, which is due to the interaction with atmospheric turbulence which forces the WT at a wide range of time scales.

Comparing the statistics of the jumps in the total MB radial force magnitude the jumps in the three frequency ranges, Table 6.3 suggests all three frequencies play a role in changes in the magnitude, as it is hard to identify one frequency range in particular, where the statistics match the statistics of the total MB radial force magnitude the closest. However, the distributions of the jumps in the magnitude of the total MB radial force magnitude (Figure 6-24a) and the jumps in the magnitude of the high-frequency content in the OOPBM magnitude qualitatively have very similar distributions. Indicating the high-frequency content may be contributing significantly the time variations in the MB radial force vector. Figure 6-25a and Figure 6-26a show the distribution of the jumps in the magnitude over the low-frequency and 3P-frequency content in the OOPBM magnitude. The tails of the distributions suggests these two signals contribute to some of the largest jumps in the total MB radial force magnitude.

Comparing the statistics of the corresponding time changes over the jumps in the total MB radial force magnitude, with the MB radial force magnitude filtered over the three

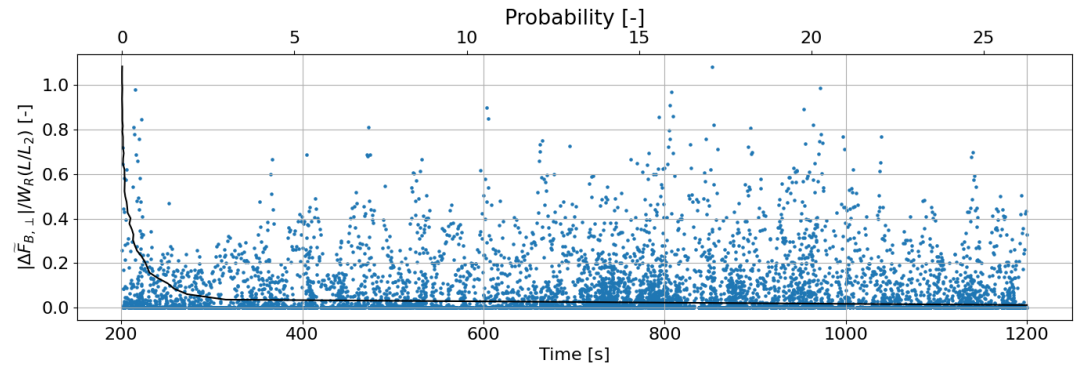

(a)

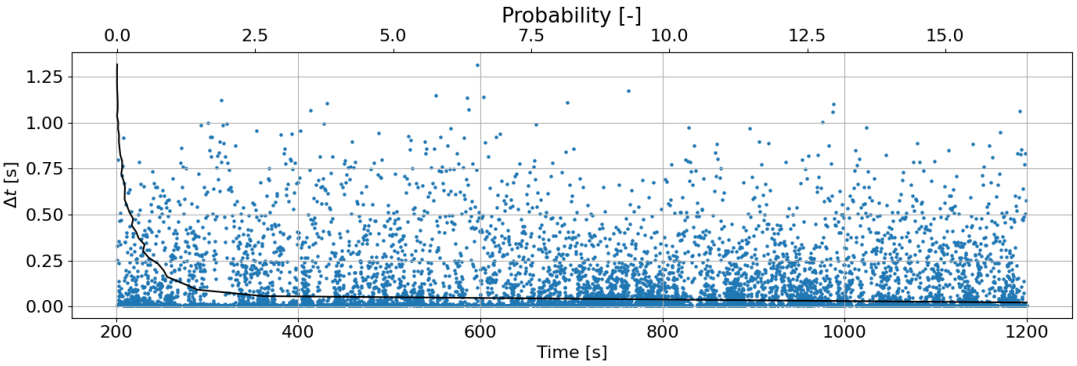

(b)

Figure 6-24: (a) Absolute changes in total main bearing radial force magnitude peak-to-peak variations normalized on the rotor weight contribution at the main bearing and (b) corresponding change in time, where the blue dots are the locations of the jumps in time and the black line indicates the probability of a jump over the 1000 s.

frequency ranges, Table 6.4 indicates the high-frequency content is primarily responsible for the time variations in the MB radial force magnitude. As the statistics calculated in Table 6.4, for the high-frequency content in the MB radial force magnitude, most closely match those from the total MB radial force magnitude. However, qualitatively the 3P-frequency content, which drives the periodic variations in the MB radial force magnitude, contributes significantly to the time variations. Table 6.4 shows the time changes from low-frequency content in the MB radial force magnitude are an order of magnitude longer compared with the 3P-frequency content, which is likely why the low-frequency content does not contribute significantly to the time variations of the

MB radial force magnitude, compared with the 3P- and high-frequency content.

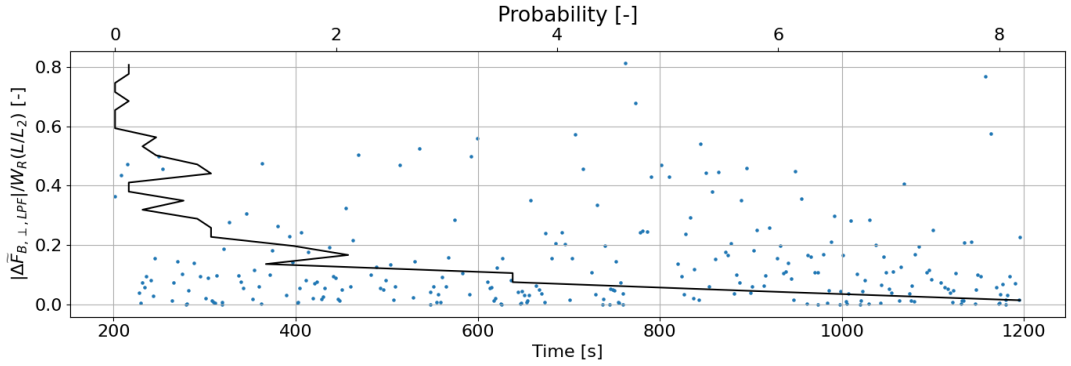

(a)

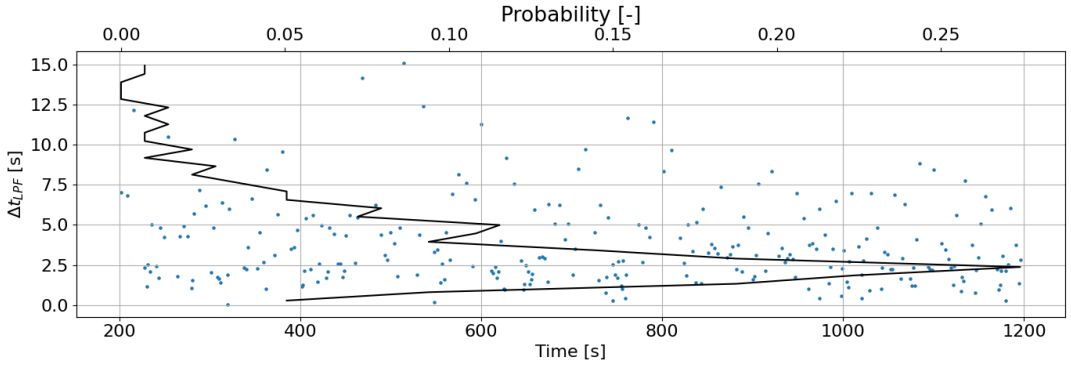

(b)

Figure 6-25: (a) Absolute changes in low-pass filtered (0.3 Hz) main bearing radial force magnitude peak-to-peak variations normalized on the rotor weight contribution at the main bearing and (b) corresponding change in time, where the blue dots are the locations of the jumps in time and the black line indicates the probability of a jump over the 1000 s.

It is important to note that the aforementioned results arise from the interaction between daytime atmospheric turbulence and a utility-scale wind turbine operating at a fixed rotor speed and constant pitch angle, under an average wind speed of 12.75 m/s. As such, these findings may not be directly applicable to other operating regimes. As the average wind speed decreases—transitioning from 12.75 m/s into Region 2, one would expect the peak-to-peak variations in the main bearing force magnitude, relative to the rotor weight contribution, to diminish. This is due to reduced turbulence

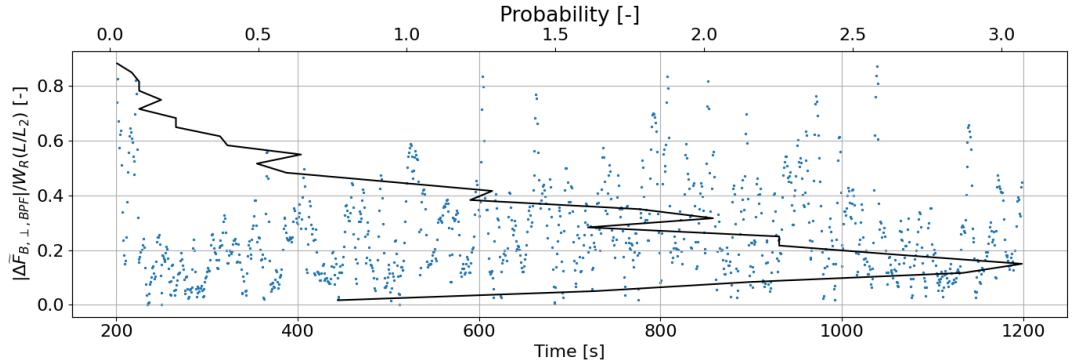

(a)

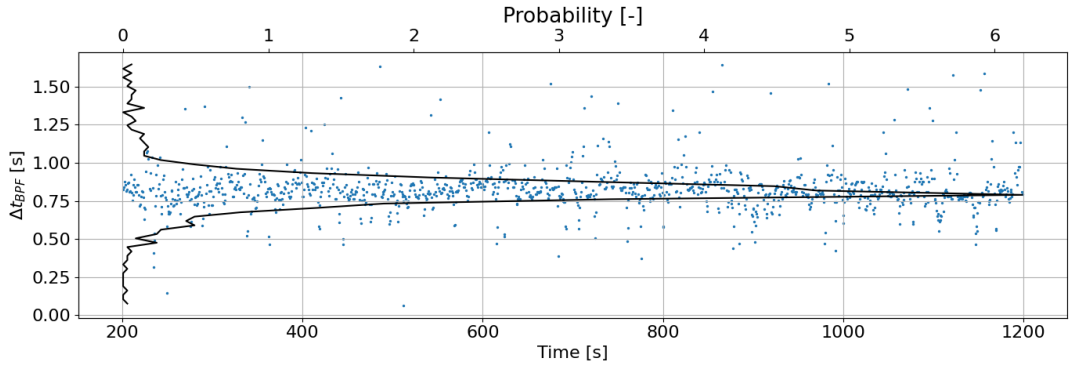

(b)

Figure 6-26: (a) Absolute changes in band-pass filtered (0.3-0.9 Hz) main bearing radial force magnitude peak-to-peak variations normalized on the rotor weight contribution at the main bearing and (b) corresponding change in time, where the blue dots are the locations of the jumps in time and the black line indicates the probability of a jump over the 1000 s.

production from lower shear rates and potentially more stable atmospheric conditions. Additionally, the lower wind speed results in slower advection of turbulent eddies. However, because the shear-rate also decreases with wind speed, the integral length scale correspondingly reduces [Emes et al., 2016]. Therefore, it is not immediately clear whether the eddy passage time, and thus the low-frequency content of the load fluctuations, will be significantly affected by a reduction in wind speed.

In region 2 as wind speed varies, to maximise power production the controller varies the rotor speed. If different operating points in region 2 of the NREL 5 MW WT

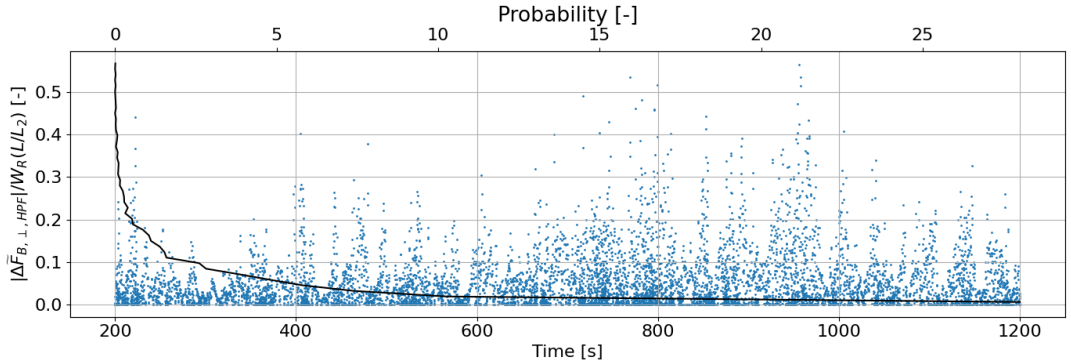

(a)

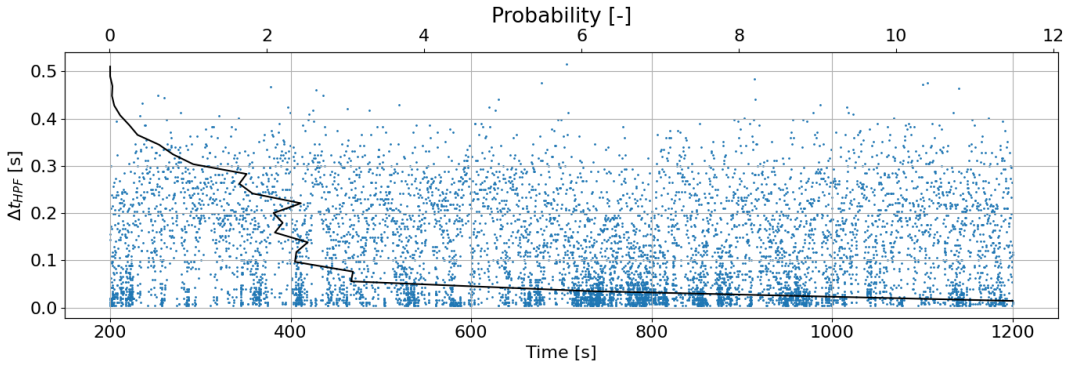

(b)

Figure 6-27: (a) Absolute changes in high-frequency content of the (BPF 1.5-40 Hz) main bearing radial force magnitude peak-to-peak variations normalized on the rotor weight contribution at the main bearing and (b) corresponding change in time, where the blue dots are the locations of the jumps in time and the black line indicates the probability of a jump over the 1000 s.

control strategy curve (see Figure 9-1 [Jonkman et al., 2009]) are considered, lower rotor speeds at lower average wind speeds would result in a higher 3P frequency (7.5 rpm = 8 Hz) and blade tip speed of 49.5 m/s. The higher 3P and lower blade tip speed resulting from a lower average wind speed in region 2 will likely affect the high-frequency content as the blades are interacting with the internal eddy structure at a much slower rate. At lower rotor speeds a blade may be forced by a persistent LSS for longer durations leading to larger asymmetries and peak-to-peak variations but shifted to lower-frequencies.

Considering the opposite as the average wind speed increases into region 3, the controller varies the blade pitch to reduce aerodynamic loads and maintain rated power, while rotor speed is held constant at rated. The collective blade pitch leads to a reduction in total blade loading, and hence in the peak-to-peak variations in aerodynamic OOPBM. The relative asymmetry in the velocity over the rotor disk does not change, but the overall OOPBM reduces.

To further investigate the relative contributions of the 3P- and high-frequency content to the total MB radial force magnitude, the zero crossings in the MB radial force magnitude, (see Section 3.9), are used to calculate the jumps in the magnitude of the total and low- plus 3P-frequency content signals. The difference in the absolute ΔF between the total and LPF+BPF signals is calculated, as this represents the contribution to the total signal from the high-frequency content. Figure 6-28a shows a 20 s period of the total signal and the LPF+BPF signal, highlighting the difference between the two signals as this is the contribution from the high-frequency content.

Figure 6-28b shows the contribution from the high-frequency content to the peak-to-peak time variations in the MB radial force magnitude. The statistics are summarised and indicates a large proportion of the contribution from the high-frequency content is between +/- 62.25 kN which is small relative to the rotor weight contribution. However, the large positive skewness, and quantitively examining Figure 6-28b, shows a significant number of the data points lie on the positive side of the distribution, which indicates the high-frequency content is on average increasing the jumps in the magnitude when added to the low- and 3P-frequency content. Lastly, the flatness implies long tails, and Figure 6-28b shows the largest contribution from the high-frequency content is approximately 1500 kN or $\sim$ 70% of the rotor weight contribution at the MB. The evidence demonstrates the importance of the high-frequency content to the time variations in the MB radial force magnitude.

The tails of the distributions of the jumps in the magnitude are of interest as this is

where the largest changes in magnitude lie, and are likely contributors to potential damage and premature failures of MBs. The jumps in the magnitude of the total MB radial force are threshold at the average plus two standard deviations to isolate the largest jumps in magnitude and the corresponding time over the jump, these jumps are denoted 2σ event/jumps. Figure 6-29 shows the 2σ events over the 1000 s, the largest jumps are shown to be of order the rotor weight. Interestingly, a significant number of the 2σ events are in the sub-second region, which suggest the high-frequency content is responsible for some of the largest changes in magnitude. Likely, the superposition between the 3P- and high-frequency content is what is creating these especially large jumps. The number of 2σ events over the 1000 s simulation is calculated as 543.

If the 1000 s is extrapolated to represent the WT operating over a 12 hour daytime, acknowledging that the WT is modelled as rigid, constant rotor speed and simulated at 12.75 m/s which will change the following result, it is estimated that the MB could experience approximately 23000 2σ jumps. This estimate assumes continuous operation under similar conditions, specifically, rigid, constant rotor speed, and operating with an average wind speed of 12.75 m/s, therefore, should be interpreted with those caveats in mind.

6.5 Summary

This chapter examined the frequency response of the OOPBM to the passage of atmospheric turbulence eddies, with the objective to understand the role atmospheric turbulence is playing in the generation of the time variations in the aerodynamic out-of-plane bending moment, which is responsible for driving the time variations in the MB force vector. The analysis distinguished three frequency ranges: low-, 3P-, and high-frequency, and linked each to distinct characteristics of the atmospheric boundary layer (ABL) and its interaction with the wind turbine rotor.

Comparing the OOPBM spectra from ABL turbulence against that from a steady shear

inflow showed atmospheric turbulence generates high levels of fluctuations at the low and high frequency content, and modulates the time variations in the 3P frequency content.

The low-frequency content in the OOPBM, described as the trend of the OOPBM signal, is shown to be driven by the passage of the most energy-dominant coherent atmospheric eddies with time scales on the order of 30 s – 90 s. These eddies cause changes in the average/overall asymmetry over the rotor disk, which modulates the operating point of the MB. It is likely that the low-frequency content is a significant contributor to the rating life, as it moves the signal to higher and lower operating points. Which subsequently implies, higher levels of asymmetry in the ABL on average is potentially detrimental to the MB.

In contrast, the 3P and high-frequency content were shown to dominate the fluctuations in MB force. The 3P response is due to the periodic rotation of the three blades through the non-uniform inflow, while the high-frequency content is driven by the blades rotating through the internal eddy structures. As the blades rotate through the velocity field the blades respond to the largest velocity gradients causing sub-second changes in asymmetry The high-frequency content is shown to result in changes in the MB force magnitude on the order of 50% of the rotor weight, the high-frequency content qualitatively sit atop of the periodic 3P frequency peak-to-peak variations. It was shown the addition of the high-frequency content to the 3P-frequency content increases the time derivatives of the total (resultant) signal, and the resultant changes in the magnitude are shown to be of order the rotor weight, and can occur over a 10th of a second.

The asymmetry generated by the passage of eddies through the rotor disk is potentially important to premature failures in MBs, because asymmetry is the primary mechanism driving the three characteristic frequency ranges, which are all likely to contribute to failure mechanisms of MBs. The atmospheric boundary layer forms distinct elongated

coherent patterns near the surface aligned with the average streamwise velocity. The coherent eddy structures are referred to as low-speed streaks and high-speed regions. Analysis of the contributions of these coherent regions of low-speed and high-speed fluid showed low-speed streaks are the dominant eddy type which generates the largest changes in the out-of-plane bending moment and thus MB force, due to LSS being much more coherent and having on average higher internal gradients. Furthermore, surges of low-speed fluid from the surface vertically advecting into the rotor disk have been identified as another potential mechanism for generating asymmetry across the rotor disk. The evidence suggests low-speed streaks on average contribute more to the asymmetry over the rotor disk and to the largest time changes in the MB force, compared to high-speed regions. Therefore, low-speed streaks are identified as potentially important in the premature failures of MBs.

The nonsteady time variations in the MB force, dominated by the time changes in the 3P- and high-frequency content, can cause sudden unloading and then loadings of the MB of the order of the rotor weight in a fraction of a second. Rollers in the unloaded regions of the bearing naturally become skewed, a sudden "extreme" change in direction of the load could cause the skewed roller to be loaded in a way which creates an off design load case such as: edge loading, flange impact, large-scale deformations and possibly even through-cracking, due to sudden extreme load changes.

In this context "extreme" load changes refer to the tails of the PDFs calculated from the 1000 s of data collected in this study. Which is representative of typical operating conditions during power production, rather than the extreme load cases due to storms/hurricanes or the highest wind speed recorded in 50 years [International Electrotechnical Commission, 2019]. Extreme load changes in the MB force are shown to occur 543 times in the 1000 s, therefore, could occur ~ 23000 times over a 12 hour day (sun up to sun down). Indicating the extreme time variations in the MB force could be playing a significant role in the premature failures of MBs.

Extreme changes in the load could also initiate surface fatigue, adhesive wear, which may present as micro-pitting and/or spalling [Hart et al., 2020]. [Hart et al., 2023] found spalling, micro-pitting and other surface initiated damage mechanisms to account for a significant proportion of the replacements. Surface initiated damage mechanisms are an indicator of poor lubrication conditions.

Lubrication condition is affected by surface roughness, contaminants, temperature and also some nonsteady applied loads. The minimum film thickness can be affected when there are rapid changes in the loads which can lead to asperity contact. The literature argues the rapid changes in the loads only become important when the changes in the load occurs at times faster than the time it takes a particle of lubricant to pass through the contact area t_c [Hart et al., 2022a] [Venner and Wijnant, 2005]. [Venner and Wijnant, 2005] calculated t_c to be between 14 ms - 36 ms. However, this is dependent on the bearing geometry, the angular velocity of the bearing and the size of the contact patch. The evidence suggests the largest changes in the 3P- and high-frequency content which occur over the smallest Δt could potentially cause a reduction in the lubrication film thickness, which could lead to asperity contact.

Overall, the chapter demonstrates the importance of true atmospheric turbulence interactions, in particularly at high frequencies, for understanding the MB force response. The results indicates a potential limitation in current fatigue design practices that rely on kinematic turbulence and average loading metrics, which may underestimate the damage of the high magnitude, sub-second variations present in true atmospheric conditions.

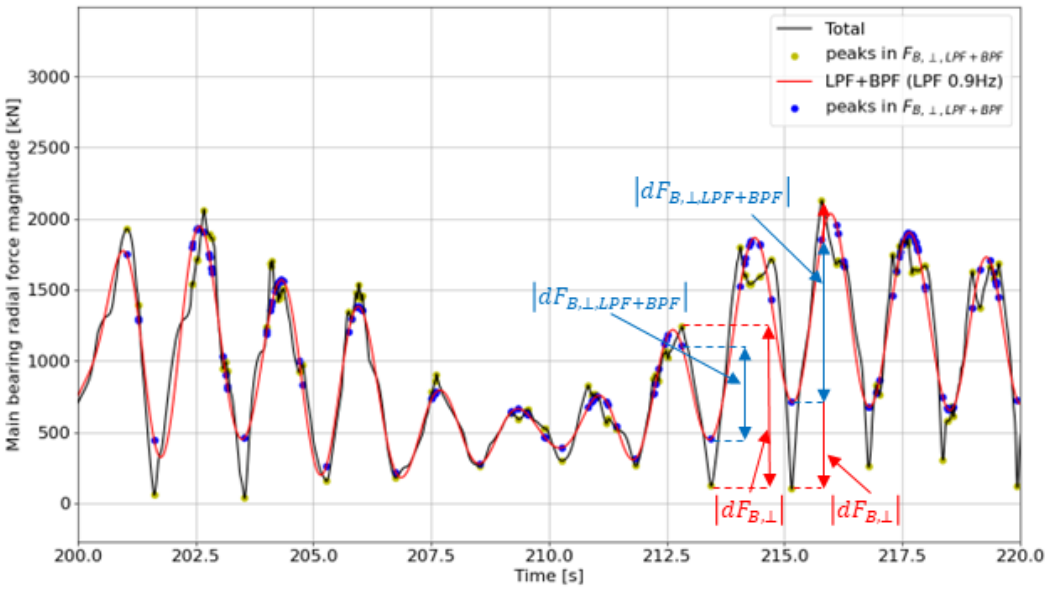

(a)

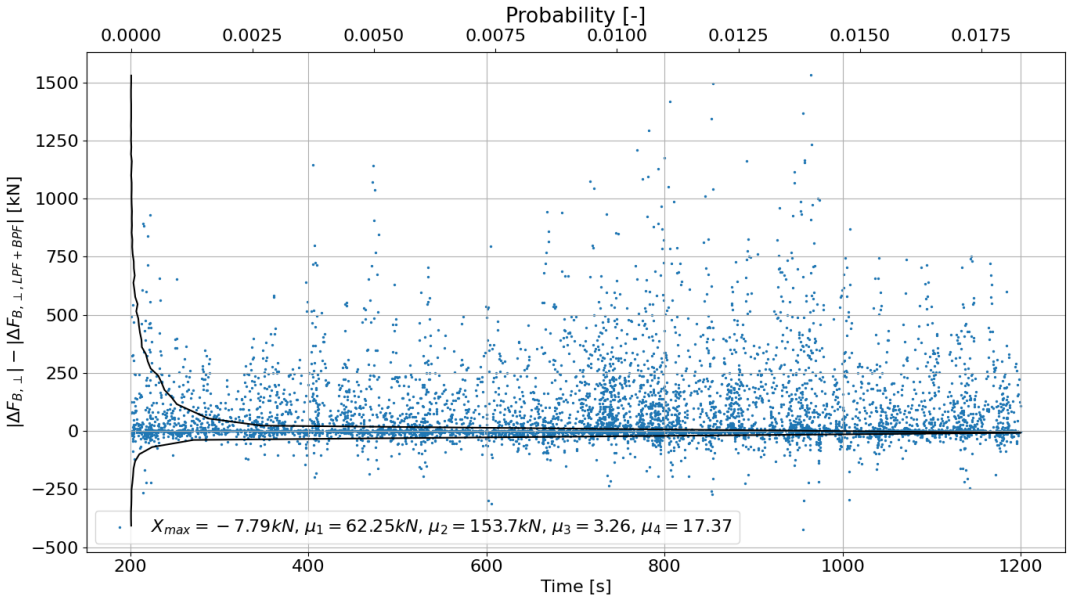

(b)

Figure 6-28: (a) Main bearing radial force magnitude and low-frequency+3P frequency (LPF 0.9 Hz) main bearing radial force magnitude plotted over 20 s period. (b) Contributions from the high-frequency content to the peak-to-peak variations in the main bearing radial force magnitude where the blue dots are the locations of the jumps in time and the black line indicates the probability of a jump over the 1000 s.

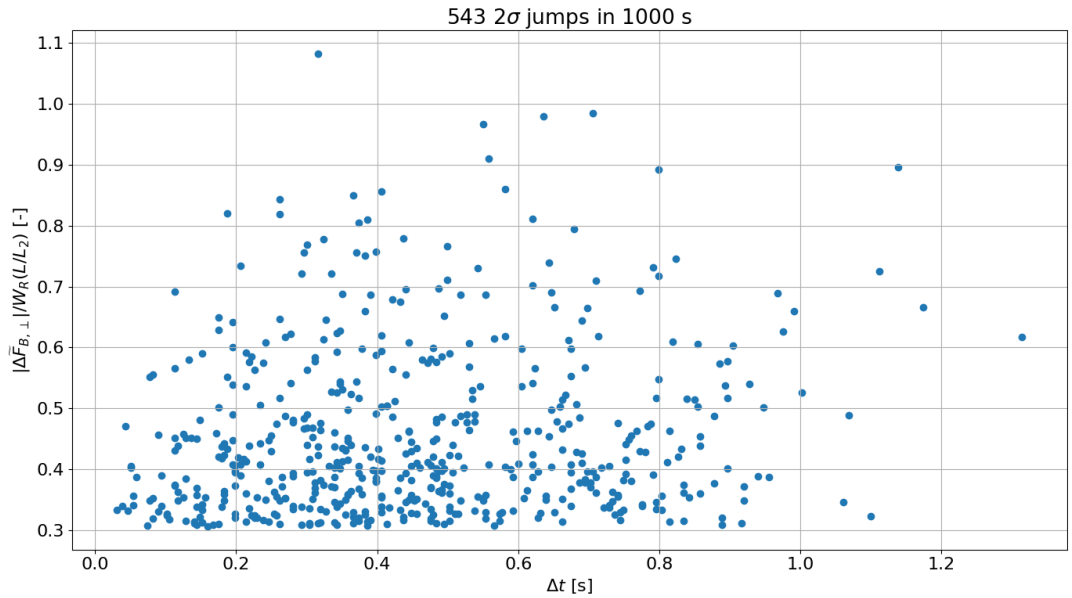

Figure 6-29: Scatter plot of the largest (2σ) jumps in the total main bearing radial force magnitude over the 1000 s, normalised on rotor weight contribution at the main bearing plotted against the corresponding time over the jump.

Chapter 7

Aeroelastic Response of a Deformable Wind Turbine to the Passage of Atmospheric Turbulence Eddies

Chapters 5 and 6 analysed the time variations in the main bearing force vector from the passage of atmospheric turbulence eddies, in a rigid configuration (see Section 3.4), to isolate the contributions of atmospheric turbulence to the aerodynamic response of the WT response. The aim of this chapter is to analyse the aeroelastic WT response to the passage of atmospheric eddies, to investigate the relative contribution of the blade deformations to the time variations in the MB force vector. To answer the question, to what extent are the conclusions drawn from the rigid rotor analysis applicable for a deformable rotor. Furthermore, the analysis of the deformable rotor aims to study the impacts of blade deformations on the characteristic frequency responses of the MB force.

7.1 Blade Deformations to the Passage of Atmospheric Turbulence

At the initial time step the blades are initialized with a coning angle of $-2.5°$ then after are allowed to deform, and there will be a transient associated with the blade deformation. Figure 7-1 shows the displacement of the blade tip relative to the rigid blade, in the $\widehat{x}$ direction in the rotating hub coordinate system, which indicates the transients associated with the blade deformations are approximately 5 s. Before starting any calculation the first 200 s of the simulation data is removed, to allow time for the wake to develop and reach a new quasi-stationary state. Therefore, the transients associated with the blade deformations are much shorter compared to the 200 s removed to allow for the wake development.

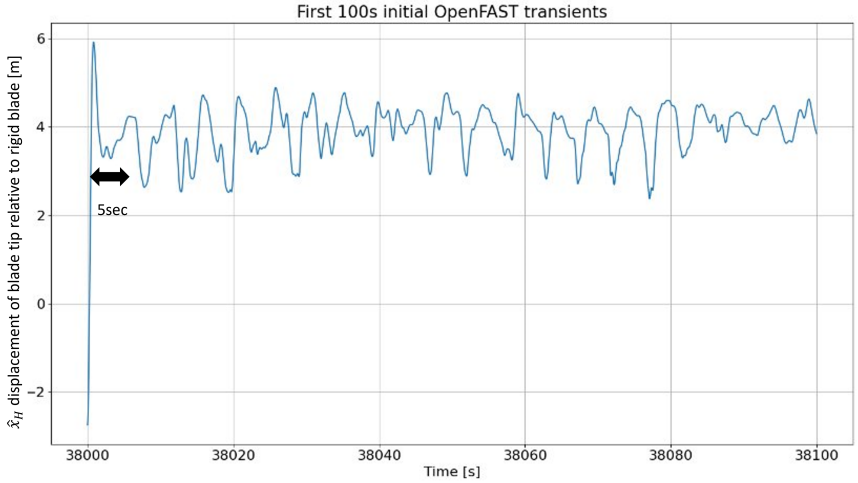

Figure 7-1: Relative displacement of the blade tip relative to the rigid blade in the x direction in the hub coordinate system.

Figure 7-2 shows the average blade position of the rigid blade and deforming blade, as if one was observing the rotor side-on in the rotating hub frame of reference. The left Figure shows the deformation in the $x_{\widehat{H}}$ direction, (in and out of the rotor plane), along the span. The blade is coned $-2.5°$ and since the root is especially stiff compared to the tip of the blade, the first $\sim 50\,\text{m}$ of the blade deflects in the negative θ direction, the

blade then bends backwards in the positive θ direction, and the average tip deflection in the $x_{\widehat{H}}$ direction is 3.40 m.

Figure 7-2 also shows the average blade position of the rigid and deforming blades, as if one was observing the rotor in the y', z' plane rotating hub frame of reference. The right Figure shows the deformation in the $y_{\widehat{H}}$ direction (deformation in the plane of the rotor). The average deflection is shown to increase with span due to a reduction in stiffness with increasing distance from the hub, and the average tip deflection in the $y_{\widehat{H}}$ direction is calculated as -0.71 m, which corresponds to a higher stiffness in the edgewise direction.

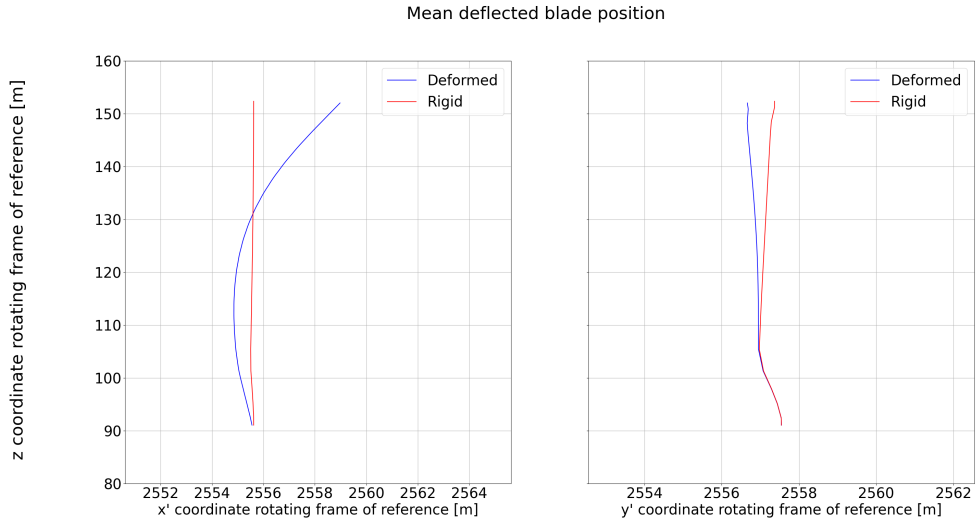

Figure 7-2: Time averaged rigid and deforming blade. Average position in the (left) $(x_{\widehat{H}}, z_{\widehat{H}})$ and (right) $(y_{\widehat{H}}, z_{\widehat{H}})$.

Figure 7-3a shows the displacement of the blade tip is calculated relative to the rigid blade tip in the rotating hub frame of reference, in the $x_{\widehat{H}}$ direction. The tip displacement is qualitatively similar to thrust, and the correlation coefficient between thrust and tip displacement in the $x_{\widehat{H}}$ direction was calculated as 0.69. Which indicates the time variations in the blade deformation is driven in part by the rotor-averaged streamwise velocity $u_{x'}$. The correlation between tip displacement and thrust is lower compared to the correlation between the streamwise velocity and thrust, (Figure 7-10),

suggesting the dynamics of the deforming blade creates correlations that do not exist in the rigid case. The standard deviation of the tip displacement in the $x_{\widehat{H}}$ direction is 0.71 m, and the minimum and maximum tip displacement are 0.61 m and 5.44 m, which is a range of 4.83 m.

Figure 7-3b shows the tip deflections in the $y_{\widehat{H}}$ direction are much more consistent compared with the tip displacement in the $x_{\widehat{H}}$ direction. The standard deviation is 0.38 m, and the range is calculated as 1.76 m. The period the peak-to-peak variations in the tip displacement occur every 5 s (1P), where the weight of the blade likely plays a significant role in the 1P variations of the tip displacements in the $y_{\widehat{H}}$ direction. Figure 7-3b shows the highly periodic tip displacements in the $y_{\widehat{H}}$ direction are modulated, similar to the 3P frequency OOPBM magnitude, indicating the aerodynamic contribution, from the passage of atmospheric eddies also contributes to the time variations.

The deformations of the blade introduces new physics to the dynamical response of the turbine, due to the blade response to the passage of atmospheric eddies. Furthermore, the position of the blade changes relative to the rigid blade, meaning the actuator points will see a slightly different velocity field. However, the average eddy size is between 200 m - 400 m which is 2 orders of magnitude larger than the maximum tip displacements. Therefore the change in the velocity, due to the displacement relative to the rigid blade, will likely not lead to significant changes in the velocity, and the forces and moments on the blades .

Figure 7-4 shows the frequency response due to the time variations in the deformation relative to the rigid blade, at the blade tip, midspan of the blade, and inboard regions of the blade, in the $x_{\widehat{H}}$ and $y_{\widehat{H}}$ directions. Figure 7-4 shows a decrease in the variability in displacement with decreasing distance from the root, consistent with the increasing stiffness towards the root.

Interestingly, Figure 7-4 shows the variability, at all locations, at approximately 3 Hz diminish, which suggests a reduction in the variance in the hub forces and moments at

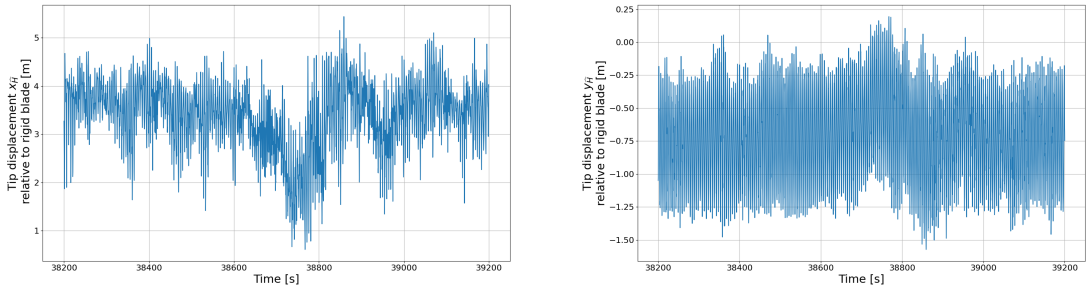

(a) (b)

Figure 7-3: Displacement of the blade tip in the rotating hub frame of reference relative to the rigid blade in the (a) $x_{\widehat{H}}$ and (b) $y_{\widehat{H}}$ directions.

the higher frequencies. The variability in the spectra diminishing at 3 Hz may be due to the fact that the ElastoDyn structural model only considers the lowest structural bending modes up to about 3 Hz, neglecting higher natural frequencies. The behaviour of the spectra at the high-frequencies are therefore attributed to the structural model and blade structural properties such as stiffness and damping.

Comparing with known frequencies from the aerodynamic response, Figure 7-4a displays a potentially new frequency at approximately 2.05 Hz. The black box surrounding frequencies between 0.32 Hz - 2.94 Hz indicates the natural frequencies of the NREL 5 MW WT [Jonkman et al., 2009], therefore, the new frequency, identified at approximately 2.05 Hz, may be a result of a blade natural frequency. The peak in the frequency is at 2.05 Hz is not a well defined peak compared to the 3P frequency, suggesting the new frequency, at 2.05 Hz, will not contribute to the frequency response of the hub forces and moments. Figure 7-4b displays a potential new frequency at approximately 1.3 Hz, which falls in the range of natural frequencies. However, it is likely associated with the time variations in the edgewise displacements. The potential new frequency, at 1.3 Hz, is a well defined peak in the frequency spectra, therefore, may contribute to a new frequency in the MB force magnitude.

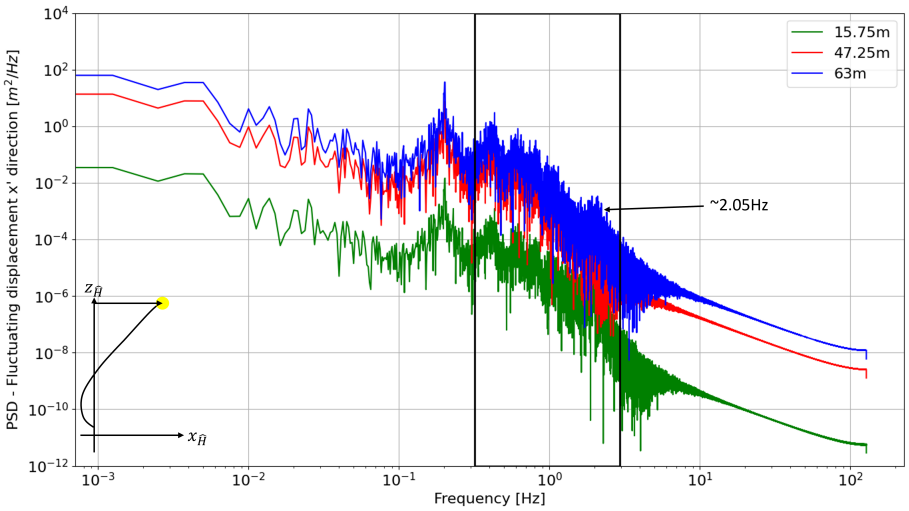

(a)

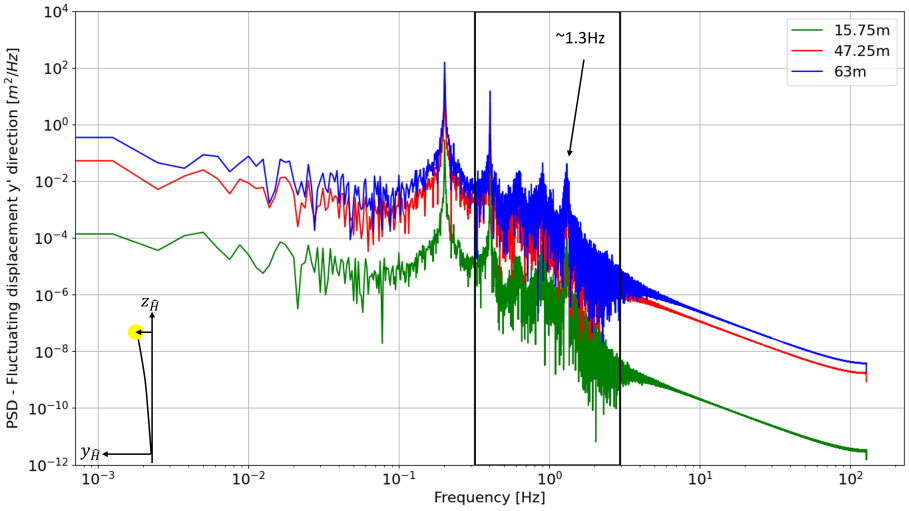

(b)

Figure 7-4: PSD frequency spectra of the displacement relative to the rigid blade at three locations along the blade in the (a) $x_{\widehat{H}}$ and (b) $y_{\widehat{H}}$ direction. Where the box indicates range of natural frequencies of the NREL 5 MW wind turbine [Jonkman et al., 2009].

7.2 Impact of Blade Deformations on the Aerodynamic Response of the Main Bearing

This section aims to analyse the aeroelastic WT response to the passage of atmospheric eddies, to answer the question, to what extent are the conclusions drawn from the rigid rotor analysis applicable for a deformable rotor.

7.2.1 Impact of Blade Deformations on the Roles of the Constituent Terms in the Bearing Force Equation to the Time Variations in the Main Bearing Force Vector

In section 5.1 the time changes in the aerodynamic MB radial force vector were shown to be dominated by the time changes in the aerodynamic out-of-plane bending hub moment vector, due to an order of magnitude difference in the standard deviation compared to the aerodynamic out-of-plane hub force magnitude. Table 7.1 summarizes the key statistics over the 1000 s of the aerodynamic MB radial force, aerodynamic OOPBM and aerodynamic OOP hub force vector magnitudes, directions and components. The observations made, using the statistics in Table 5.1, for a rigid rotor, are consistent with Table 7.1. To summarize, the time variations in the MB radial force vector are driven by the OOPBM vector, as although the correlation between the OOP hub force vector magnitude is 0.86, the standard deviation is an order of magnitude smaller compared to the OOPBM vector magnitude. Suggesting the addition of blade deformations does not alter the relationship between the aerodynamic OOPBM and the aerodynamic MB radial force, with a rigid rotor.

Figure 7-5 shows the average (bars) and +/- 1 standard deviation (error bars) for MB and hub forces and moments. Comparing the rigid case (red bars, subscript R) with the deformable rotor case (blue bars, subscript E), and also comparing aerodynamic (AeroDyn) variables with aerodynamic+blade deformations (ElastoDyn) variables. Qualitatively the summary indicates there isn't a significant difference between the rigid and

Table 7.1: Statistical analysis of main bearing force constituent components with blade deformation.

	average [kN]	Standard deviation [kN]	CC with ...
$\lvert\widetilde{\mathbf{F}}_{H,\perp}\rvert\,(L/L_2)$	24.13	16.12	$\widetilde{F}_{B,\perp}$: 0.86
$\lvert\widetilde{\mathbf{M}}_{H,\perp,mod}\rvert\,(1/L_2)$	645.94	389.33	$\widetilde{F}_{B,\perp}$: 1.0
$\theta\left(\widetilde{\mathbf{F}}_{H,\perp}\right)$	239.60	69.18	$\widetilde{F}_{B,\perp}$: 0.09
$\theta\left(\widetilde{\mathbf{M}}_{H,\perp,mod}\right)$	129.57	74.33	$\widetilde{F}_{B,\perp}$: 0.98
$\widetilde{F}_{B,y}$	-184.65	495.06	$\widetilde{F}_{B,z}$: -0.05
$\widetilde{F}_{B,z}$	314.06	402.37	$\widetilde{F}_{B,y}$: -0.05
$-\frac{1}{L_2}\widetilde{M}_{H,z}$	-180.10	507.51	$\widetilde{F}_{B,y}$: 1.0
$\frac{L}{L_2}\widetilde{F}_{H,y}$	-4.55	21.08	$\widetilde{F}_{B,y}$: -0.58
$\frac{1}{L_2}\widetilde{M}_{H,y}$	331.00	411.42	$\widetilde{F}_{B,z}$: 1.0
$\frac{L}{L_2}\widetilde{F}_{H,z}$	-16.92	18.89	$\widetilde{F}_{B,z}$: -0.46

deformable cases.

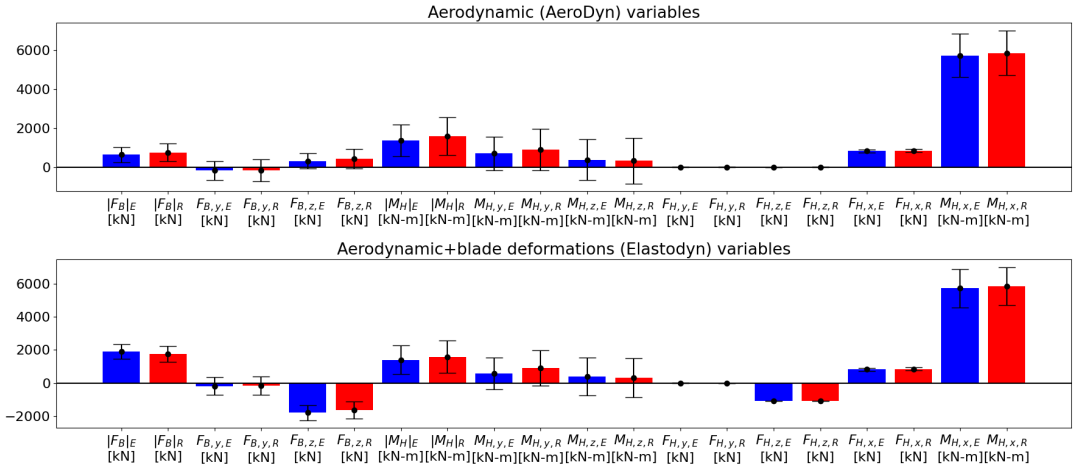

Figure 7-5: Summary of the average (bar) and standard deviation (error bars +/- 1 standard deviation). Comparing rigid rotor (subscript R, red bars) and deformable rotor (subscript E, blue bars) for aerodynamic (AeroDyn) and aerodynamic+blade deformations (ElastoDyn) main bearing and hub forces and moments.

The percentage change in the average between the deformable and rigid WT simulations

is calculated for the variables in Figure 7-5, and is summarised in Figure 7-6. The dashed lines indicate a percentage change of +/-10%, as a reference point. The hub force y and z components percentage change in the average are set to 0.0, because the percentage change was calculated as 60%. The significantly larger percentage change from the hub force y and z components skewed the y axis scale, making it difficult to examine the other percent changes. The change in the average hub force y and z components are -4.17 kN and 6.39 kN, which is small relative to the changes in the hub moments, and bearing forces (see Figure 7-7). Thus, it was decided to set the hub force percent changes to 0.0 and focus on the other variables.

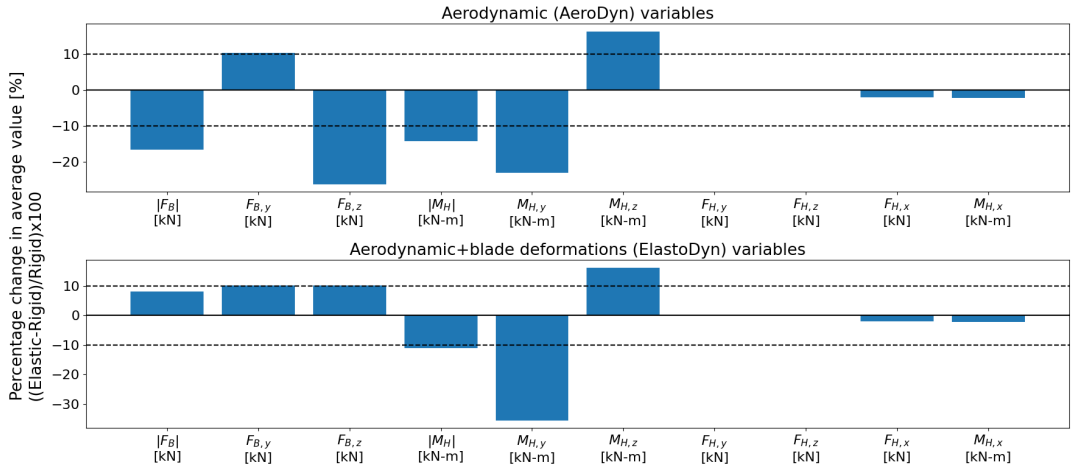

Figure 7-6: Summary of the percentage change in the average between rigid and deformable cases for aerodynamic (AeroDyn) and aerodynamic+blade deformations (ElastoDyn) variables.

Figure 7-6 shows, the percentage change in the average for the ElastoDyn MB force magnitude and components are less than 10%, while the percentage change in the average for the aerodynamic (AeroDyn) MB force magnitude and components are between -26 - 10%. Additionally there is a change in sign in $F_{B,z}$ between AeroDyn and ElastoDyn. The reduction in the percentage change and change in sign is due to the introduction of weight into the equations for the forces and moments at the hub.

Figure 7-6 indicates most of the percentage change in the bearing force is due to the

percentage changes from the hub moments. The percentage change in the average for hub moment around the z axis, from both AeroDyn and ElastoDyn, is 16%. Indicating the addition of the weight and acceleration terms, in Eq. 3.4, does not affect the change in the average in $M_{H,z}$. The percentage change in the aerodynamic $\widetilde{M}_{H,z}$ is attributed to the blade deformation rotating and twisting the airfoil sections relative to the rigid blade, changing the contributions of the lift and drag forces to the hub moments. Furthermore, the rotation and twisting of the airfoil sections relative to the rigid blade, changes the relative velocity vector projected onto the airfoil coordinate system, which is used to calculate the lift and drag forces. The change in the relative orientation of the airfoil is the most likely cause of the 16% change in the hub moment around the z axis.

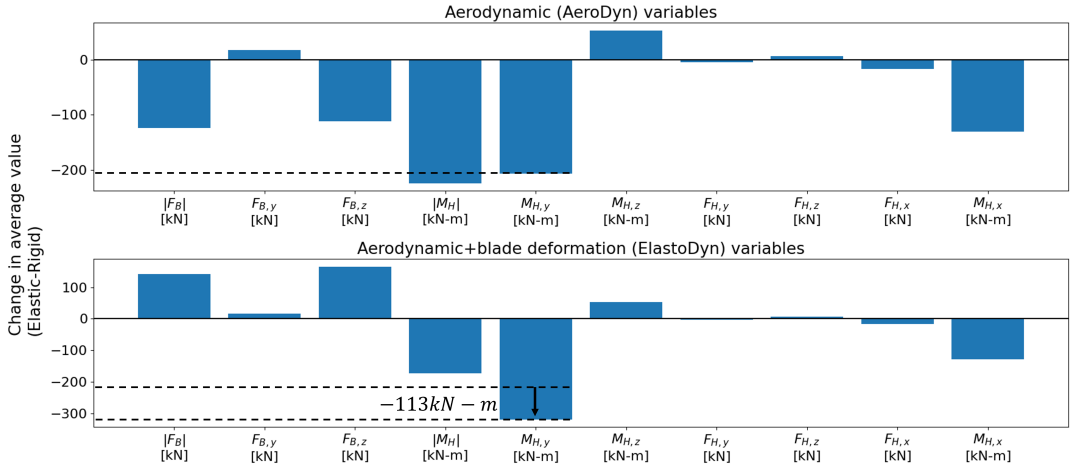

Figure 7-7: Summary of the change in the average between rigid and deformable cases for aerodynamic (AeroDyn) and aerodynamic+blade deformations (ElastoDyn) variables.

The percentage change in the average in torque and thrust, from AeroDyn and ElastoDyn, are both -2% which is small compared with the OOPBM. Figure 7-7 shows the change in the average in thrust and torque are -17 kN and -130 kN respectively. Indicating deformation has a relatively larger affect on the out-of-plane bending moment compared to torque and thrust.

Lastly, Figure 7-6 shows there is a -26% change in the average in the aerodynamic hub moment around the y axis, due to the changes in airfoil orientation relative to the rigid blade. However, unlike the z hub moment, which showed no change in the percentage change between AeroDyn and ElastoDyn, there is an additional -9% change in average percent change for $M_{H,y}$, comparing between AeroDyn and ElastoDyn. This is discussed further in Section 7.2.2.

7.2.2 Impact of Blade Deformations on the Role of Rotor Weight to the Time Variations in the Main Bearing Force Vector

The additional -9% change in $M_{H,y}$ between AeroDyn (Aerodynamic) and ElastoDyn (Aerodynamic+weight+acceleration), which is -113 kN-m (Figure 7-7), suggests rotor weight and acceleration contributes to the differences in $M_{H,y}$. In the rigid configuration the weight of the rotor only contributes to $F_{B,z}$, and Section 5.3 showed in the rigid configuration the weight does not contribute the time variations in the MB force vector.

However, in the deformable configuration the weight of the blades can also contribute to the $M_{H,y}$, as there is moment arm between to hub centre and the blade (Figure 7-8). Furthermore, as the blade deforms in time there will be a change in moment arm thus, the weight of the blade generates a contribution to the time variations in $M_{H,y}$. Figure 7-8 shows the mass density is largest at the root of the blade where the moment arm is the smallest. Therefore, it is expected that the contributions, to the time variation in $M_{H,y}$, from the weight will be small relative to the contributions from the aerodynamic forces.

Figure 7-9 shows an estimation for the time variations to $M_{H,y}$, from the weight, with deforming rotor blades. The average is estimated as -136.93 kN-m, which is in good agreement with the -113 kN-m increase in the average of $M_{H,y}$, between AeroDyn and ElastoDyn (Figure 7-7). Furthermore, the standard deviation of the contribution of rotor weight to $M_{H,y}$, from the time variations in the blade deformation, is estimated

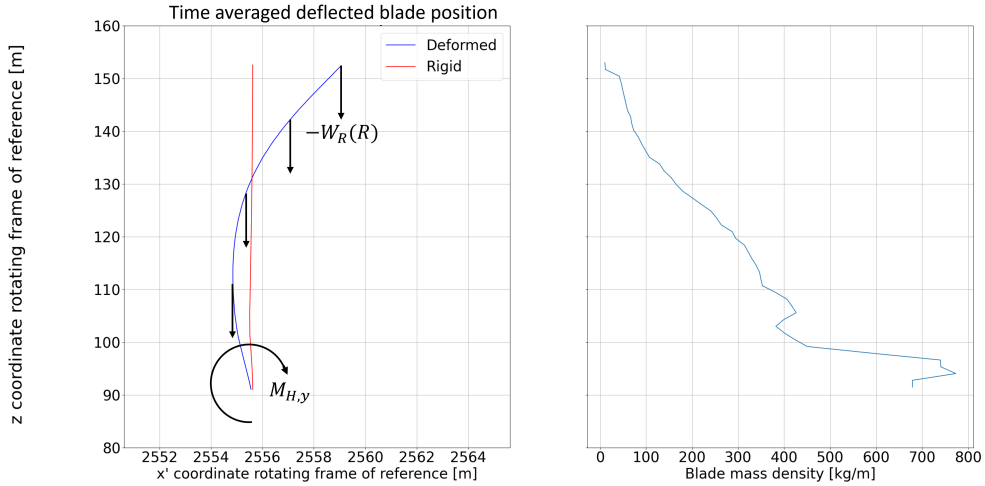

Figure 7-8: Left - Illustration of the contribution to $M_{H,y}$ due blade weight. Right - NREL 5 MW blade blade mass density.

as 30.46 kN-m, which is 3.5% of the standard deviation of the time variations from $M_{H,y}$. Indicating the time variations due to the weight of the blades, because of blade deformation, does not contribute significantly to the time variations in $M_{H,y}$.

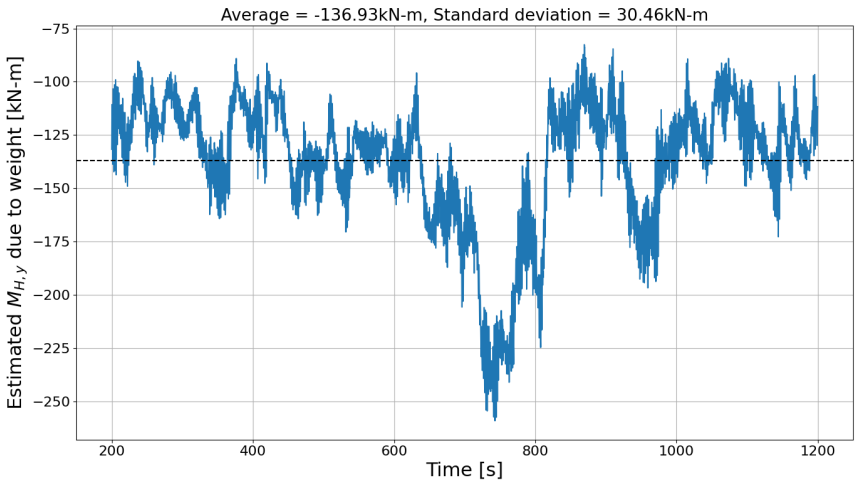

Figure 7-9: Estimation of time variations to $M_{H,y}$ due to rotor weight.

7.2.3 Impact of Blade Deformations on the Time Variations in the Wind Turbine Response

Section 5.4 summarises key correlations between the asymmetry parameter, out-of-plane bending moment, rotor-averaged streamwise velocity ($\langle u_{x'} \rangle_A$), torque and thrust for a rigid rotor. The aim of this section is to investigate the impact, on the time variations and the subsequent the correlations, from blade deformations.

Figure 7-10 summarises key correlations between rotor-averaged streamwise velocity, asymmetry parameter, torque, thrust, and out-of-plane bending moment, for the deformable rotor simulation. Figure 7-10 shows the correlations between torque, thrust and rotor averaged streamwise velocity are equally strong compared with correlations from the rigid rotor simulation. The asymmetry parameter is strongly correlated with the OOPBM, however, there is a very slight reduction in the correlation compared with the rigid case. Lastly, the OOPBM and torque are poorly correlated, and also shows a similar change to the correlation compared with the rigid rotor analysis. The minor changes to the correlations may be due to the addition of the dynamic response of the blade deformation to turbulence.

To investigate the differences in the time variations due to the dynamic response of the blade deformations, the percentage change in the standard deviation between the deformable and rigid cases calculated for the variables in Figure 7-5. Figure 7-11 summarises the percentage change in the standard deviations between variables calculated from the deformable and rigid cases. The dashed lines indicates a percentage change of -10%, as a reference point. Figure 7-11 shows the time variations in the AeroDyn (aerodynamic) variables are reduced by -21% - -3.86%. However, comparing with the percentage change in the standard deviations from ElastoDyn variables, the percentage change reduces by approximately 50%, likely due to the addition of the dynamics response of blade deformations.

The reduction in the standard deviations indicates the variance has been reduced by the

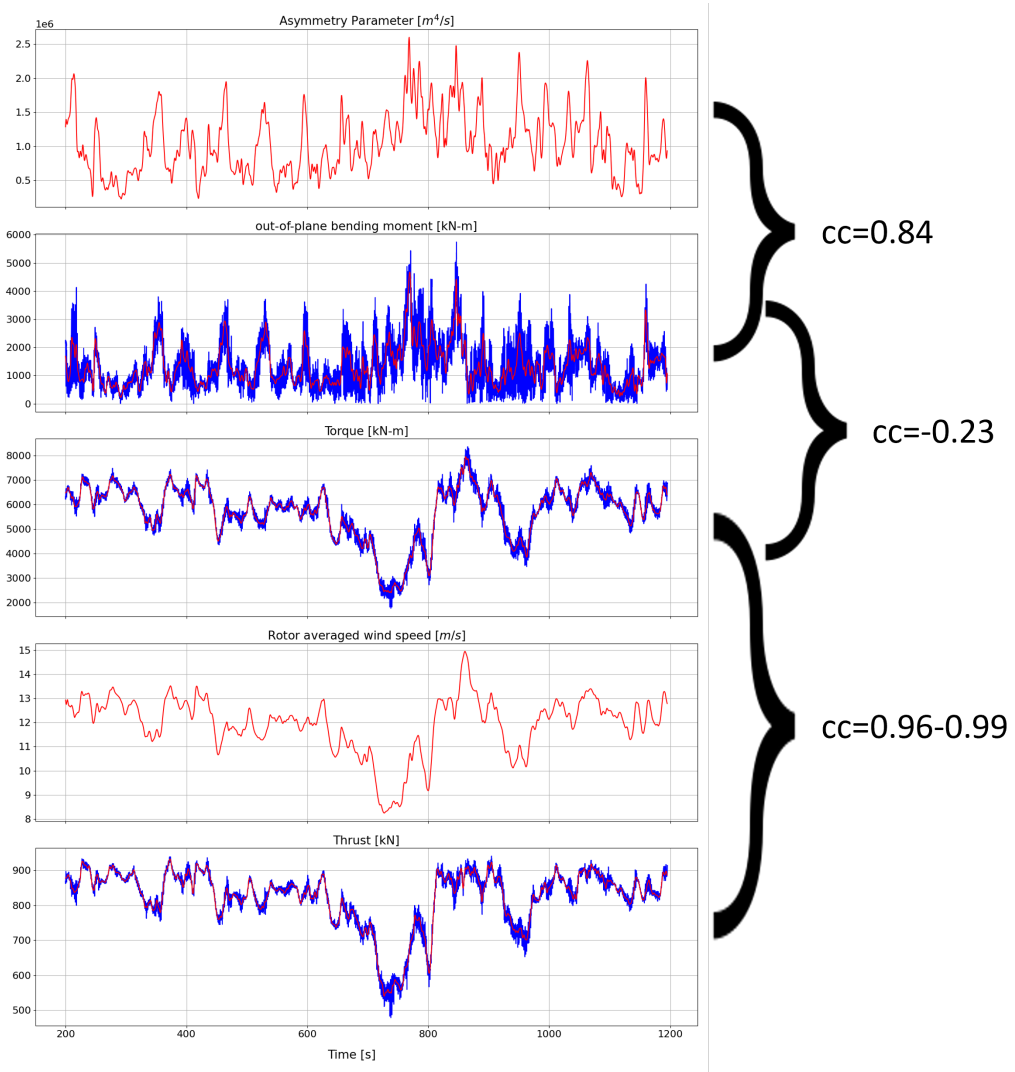

Figure 7-10: Summary of the correlation coefficients for a deformable rotor analysis. Blue lines show total signals, red lines show low pass filtered signals below 3P (0.3 Hz), curly brackets indicate which variables are being correlated.

dynamic response of the blade deformations. Figure 7-12 shows the spectra of the MB radial force magnitude, which shows a reduction in the variance at the high frequency range (1.5 Hz - 40 Hz). This suggests the reduction in the peak-to-peak time variations may be confined to the high-frequencies. A detailed spectral analysis is performed in Section 7.2.4, and the time variations in the three frequencies are investigated in Section 7.3.

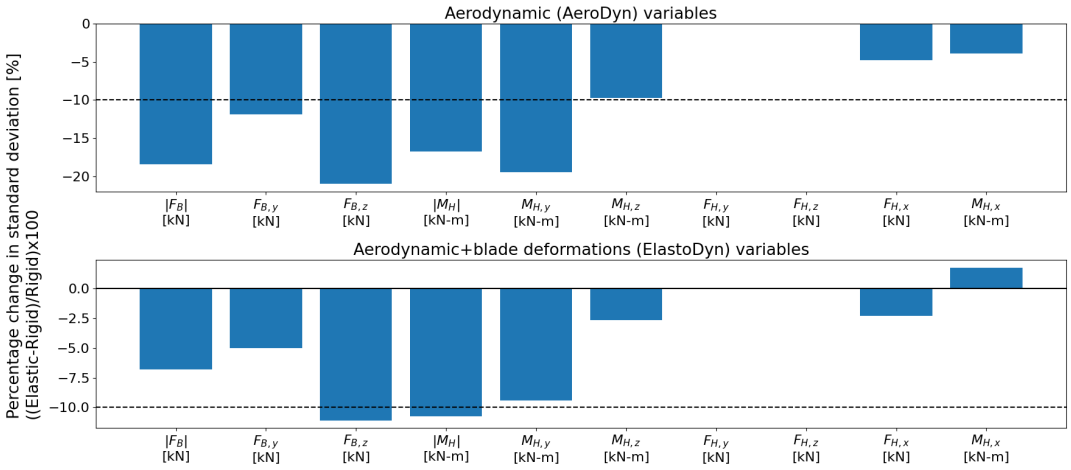

Figure 7-11: Summary of the percentage change in the standard deviations between rigid and deformable cases for aerodynamic (AeroDyn) and aerodynamic+blade deformations (ElastoDyn) variables.

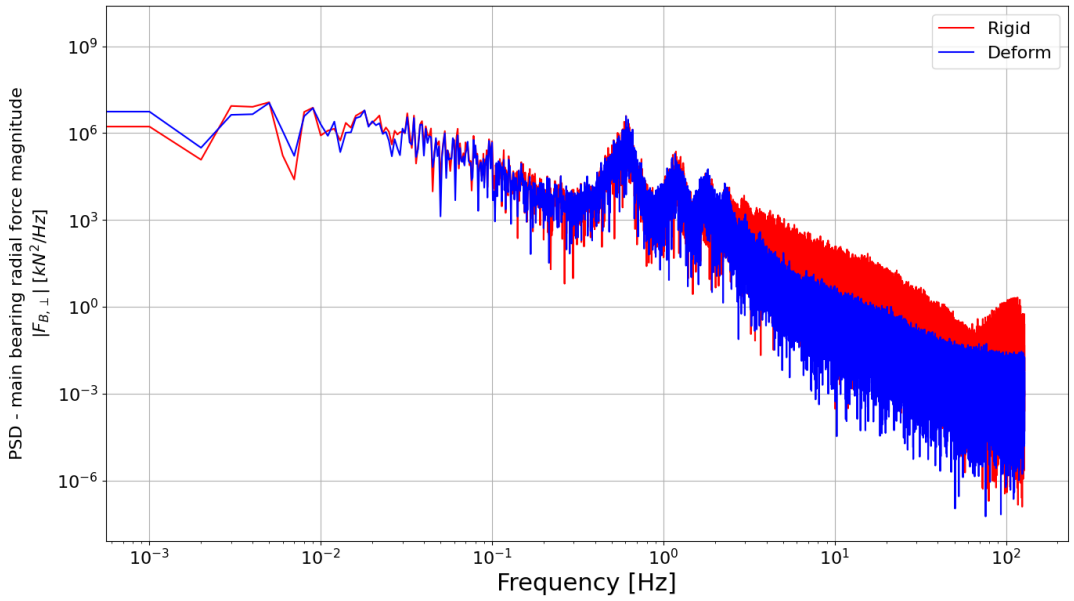

Figure 7-12: PSD frequency spectra, comparing rigid and deformable rotor simulations, for out-of-plane main bearing force magnitude.

7.2.4 Spectral Analysis of the Impacts of Blade Deformations to the Time Variations in the Wind Turbine Response

In section 7.2.3 a reduction in the variability in the MB radial force magnitude was observed. The following analysis undertakes a spectral analysis to investigate the frequency response of the WT with a deformable rotor. To compare with the response from a WT with a rigid rotor, and investigates the reduction in the variability in the MB radial force magnitude. Eq. 5.2 shows the OOPBM vector and OOP force vector contribute to the time variations in the MB radial vector. However, analysis of the contributions of the constituent terms to the time variations in the MB radial force vector, showed the the OOPBM drives the time variations in the MB radial vector, while the OOP force vector can be neglected. Comparing Figure 7-13a and Figure 7-13b the spectra of the OOPBM magnitude is between 1-3 orders of magnitude above the spectra of the OOP hub force magnitude. Indicating, as with the rigid rotor simulation, the MB radial force vector time variations are primarily driven by the OOPBM vector.

Figure 7-13a shows the OOPBM magnitude displays the reduction in the variability at high-frequencies, seen in the MB radial force magnitude. However, Figure 7-13a shows the OOP hub force magnitude does not exhibit a reduction in the variability. It is interesting why only the OOPBM shows a reduction in the variance at the high-frequencies. In Section 7.1 a similar reduction in the variability in the frequency spectra of the blade displacement relative to the rigid blade was discovered. The reduction in the variability of the blade displacement was located at 3 Hz and higher frequencies, the behaviour was attributed to the structural model and blade structural properties. The evidence suggests the reduction in the variability in the OOPBM spectra may also due to the structural model and blade structural properties. Which may indicate structural damping and stiffness reduces the peak-to-peak variations at the high-frequencies.

Figure 7-4 shows two potentially new frequencies at: 2.05 Hz in displacement in the

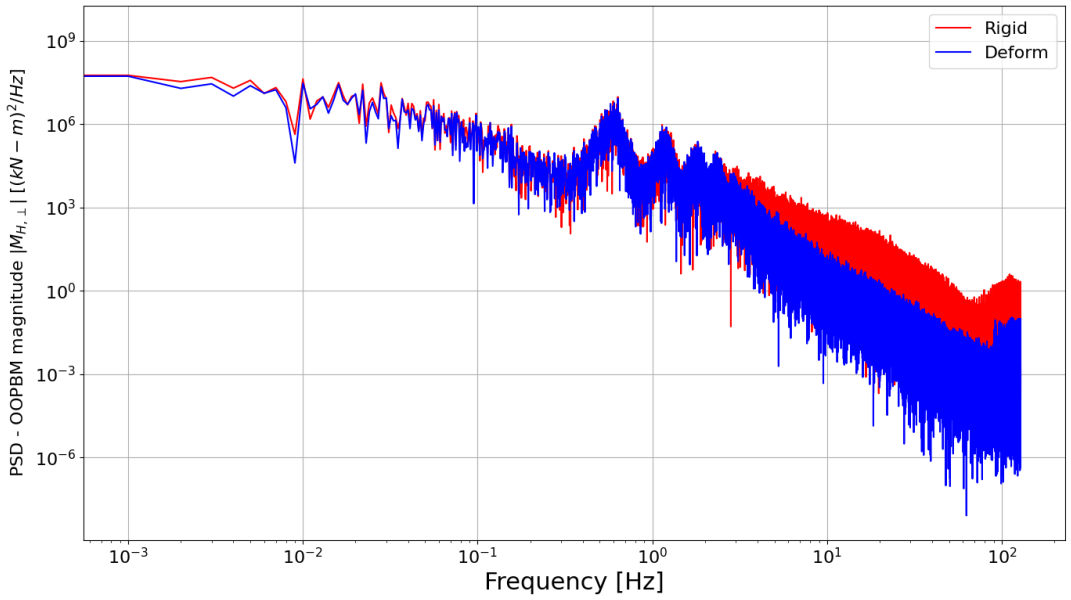

(a)

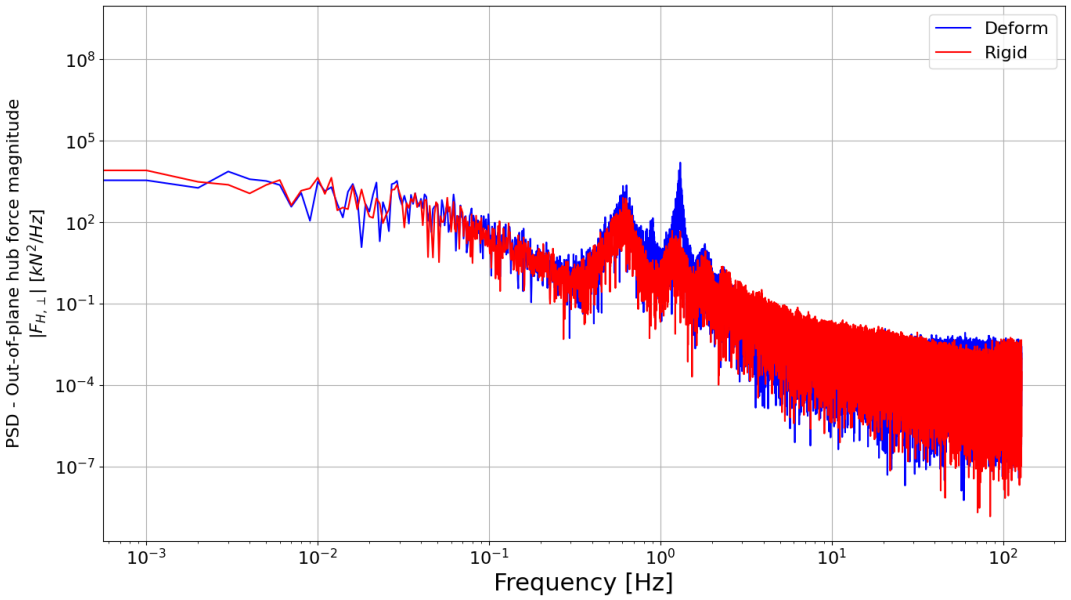

(b)

Figure 7-13: PSD frequency spectra comparing the rigid and deformable rotor simulations, (a) out-of-plane bending moment magnitude, (b) out-of-plane hub force magnitude.

$x_{\widehat{H}}$ direction, and 1.3 Hz in the displacement in the $y_{\widehat{H}}$ direction. If the blade deformations are affecting on the hub force and moment responses, one may expect the new frequencies to appear in the appropriate force and moment spectra. The blade deflection in the $x_{\widehat{H}}$ direction is likely to contribute to the OOPBM response, however, a peak at 2.05 Hz does not appear in Figure 7-13a. This may be because the 2.05 Hz frequency in the displacement in the $x_{\widehat{H}}$ direction was not a well defined peak, and thus, is enveloped by other frequencies. The deflection in the $y_{\widehat{H}}$ direction is likely to contribute to the OOP force magnitude, and as predicted Figure 7-13b shows a distinct peak at $\sim$ 1.3 Hz. However, Figure 7-12 is absent of any additional frequencies. This is likely a result of the 1-3 order of magnitude difference in the OOPBM and OOP hub force spectra. Therefore, the strong spike in the OOP hub force spectra is swamped by the 6P frequency in the OOPBM.

7.3 Impact of Blade Deformations on the Three Characteristic Frequency Responses of the Wind Turbine Main Bearing to the Passage of Atmospheric Turbulence through the Rotor.

In section 6.4 the contributions from the three characteristic frequency ranges to the time variations in the MB radial force were investigated. The analysis highlighted the contributions from the high-frequency content to the MB force vector are significant compared with the low- and 3P-frequency content. This section aims to compare the frequency responses, over the characteristic frequency ranges identified in Chapter 6, of the MB to the passage of atmospheric turbulence with and without blade deformations.

Figure 7-14 shows the out-of-plane bending moment over short 100 s periods, and the OOPBM filtered over the three characteristic frequency ranges. Qualitatively the characteristics of the three frequency ranges do not show any significant differences,

compared to the aerodynamic (rigid blades) response, in the OOPBM filtered over the three frequency ranges. The low-frequency content is shown to drive the "trend" in the OOPBM, the 3P-frequency content is highly periodic and the peak-to-peak variations are modulated, at a time scale on the order of the eddy passage time, the high-frequency content is highly chaotic (turbulent), and the peak-to-peak variations also, appear to be modulated in time. The modulation of the 3P- and high-frequency content are qualitatively correlated and appear to be modulated by the low-frequency content which has been shown to be driven by the passage of eddies through the rotor disk.

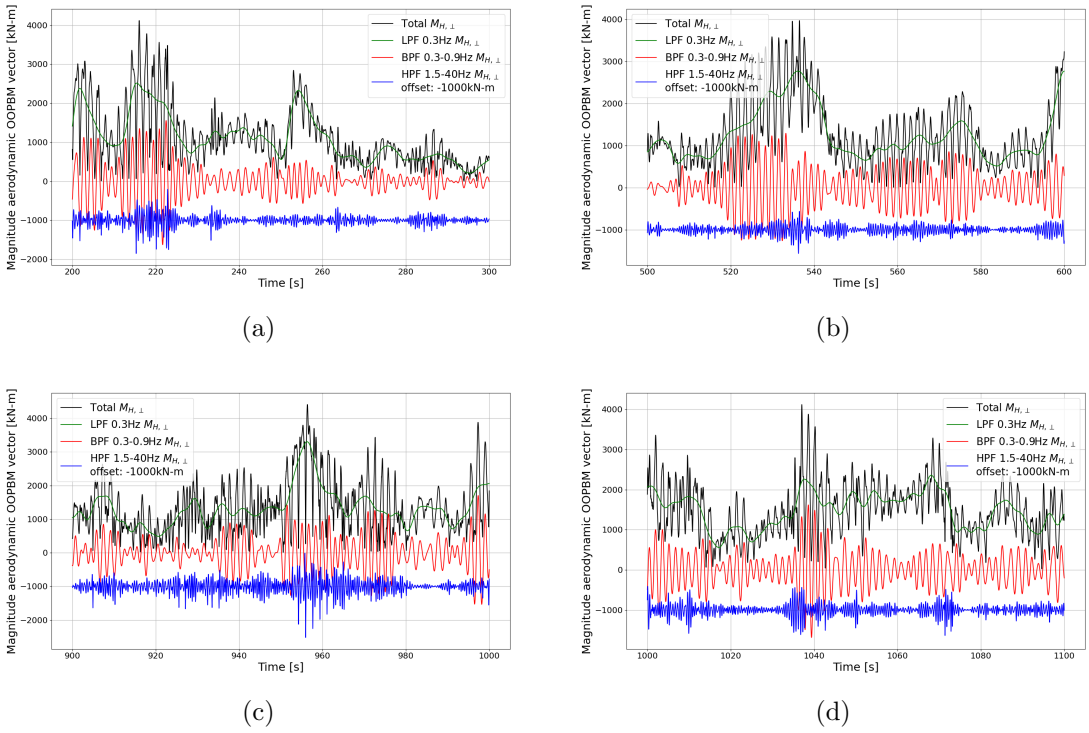

Figure 7-14: Out-of-plane bending moment magnitude, including blade deformations, over 100 s periods, where the black curve is the total OOPBM magnitude, the green curve is the low-frequency (LPF 0.3 Hz) content of the OOPBM magnitude, the red curve is the 3P-frequency (BPF 0.3-0.9 Hz) content of the OOPBM magnitude, and the blue curve is the high-frequency (BPF 1.5-40 Hz) content of the OOPBM magnitude offset -1000 kN-m. (a) 200-300 s, (b) 500-600 s, (c) 900-1000 s, (d) 1000-1100 s.

To compare the time variations in the three frequency ranges between the rigid and deformable rotor analyses, the change in the magnitude and corresponding change

in the time is calculated for the MB radial force magnitude, using the methodology described in Section 3.9. The absolute change in the magnitude normalised by the contribution from the rotor weight at the MB and the corresponding change in time are compared between the rigid rotor and deformable rotor. Figure 7-15 shows the probability distribution of the "jumps" in magnitude and corresponding time over the jumps, comparing the total MB radial force magnitude and the MB radial force magnitude filtered over the three frequency ranges; key statistics are summarised and shown above the corresponding plots. Figure 7-15a shows on average the jumps in magnitude calculated from the deforming blade analysis are smaller compared to the rigid rotor analysis. The average and standard deviation of the jumps from the deforming blade analysis are shown to be marginally smaller and the probability of the largest jumps in magnitude are lower, consistent with the analysis in Section 7.2.

The analysis in Section 7.2.3 and Section 7.2.4 indicated a reduction in the variance of the MB force magnitude located over the high-frequency range. However, Figure 7-15b - 7-15d suggests the reduction in the variance may be present at all frequency ranges, to some degree. Similar to the jumps in the rigid rotor analysis (see Section 6.4, the statistics suggest the high-frequency content contributes significantly to the time variations in the MB radial force, which may explain why qualitatively the spectra only displays a reduction at the high-frequency range.

The contributions from the high-frequency content in the MB radial force magnitude, to the peak-to-peak variations in the total MB radial force magnitude, with and without blade deformations, using the same approach in Section 6.4, are compared. Figure 7-16 shows the contributions from the high-frequency content, from the deformable rotor analysis has reduced, compared to the contributions from the rigid rotor analysis. Figure 7-16 also shows the largest contributions from the high-frequency content, in MB radial force magnitude calculated from the deformable rotor, are smaller compared to those from the rigid rotor analysis. Finally, the number of especially large jumps,

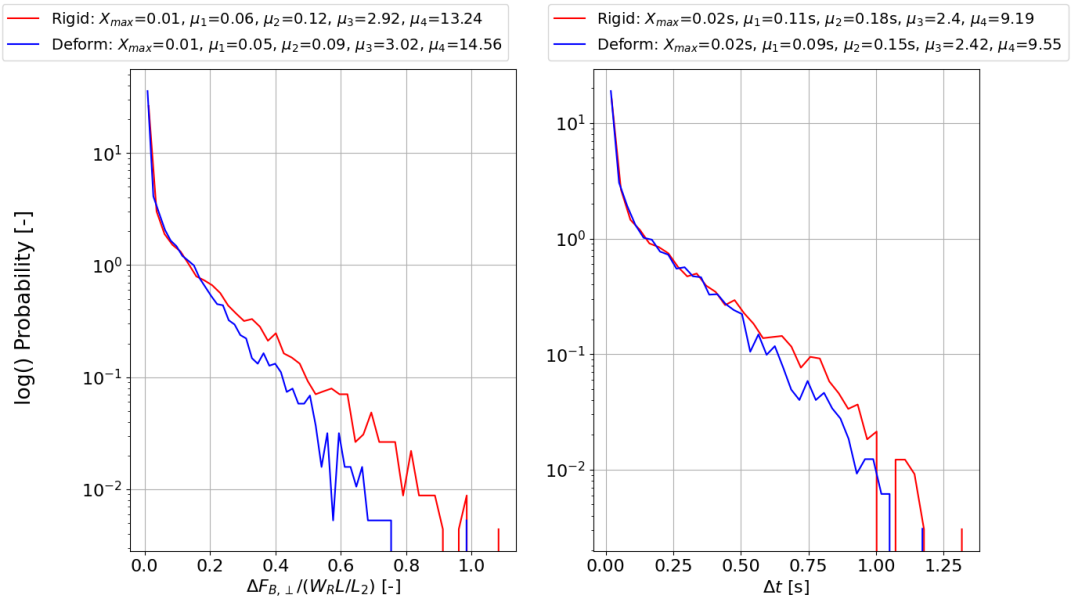

(a)

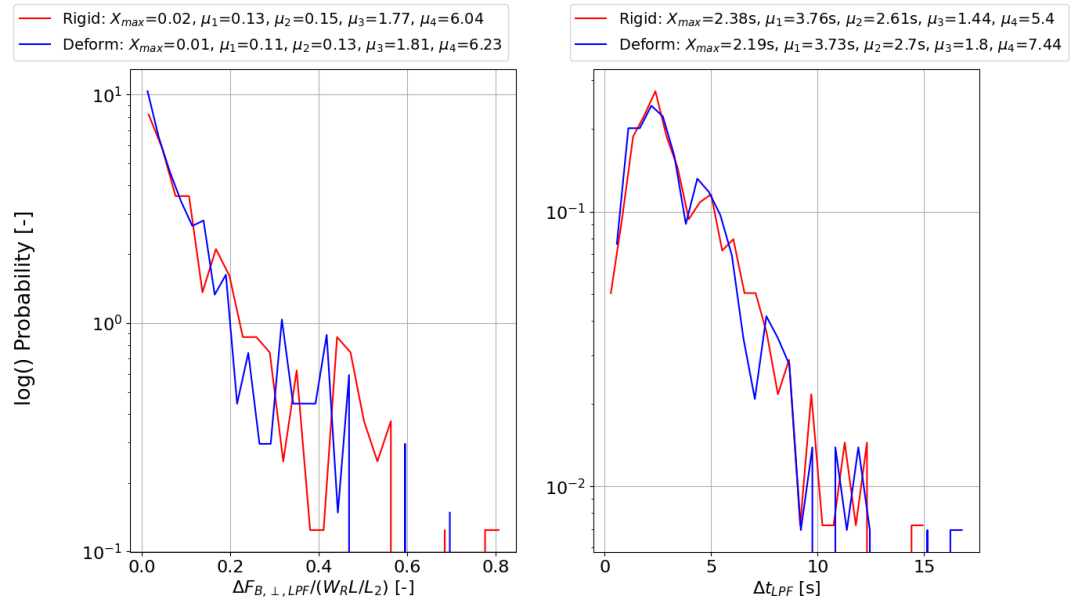

(b)

average plus two standard deviations denoted 2σ events/jumps, was found to be 543 for the rigid rotor analysis. Using the threshold from the rigid rotor analysis to compare the number of 2σ events in the MB radial force magnitude in the deformable rotor

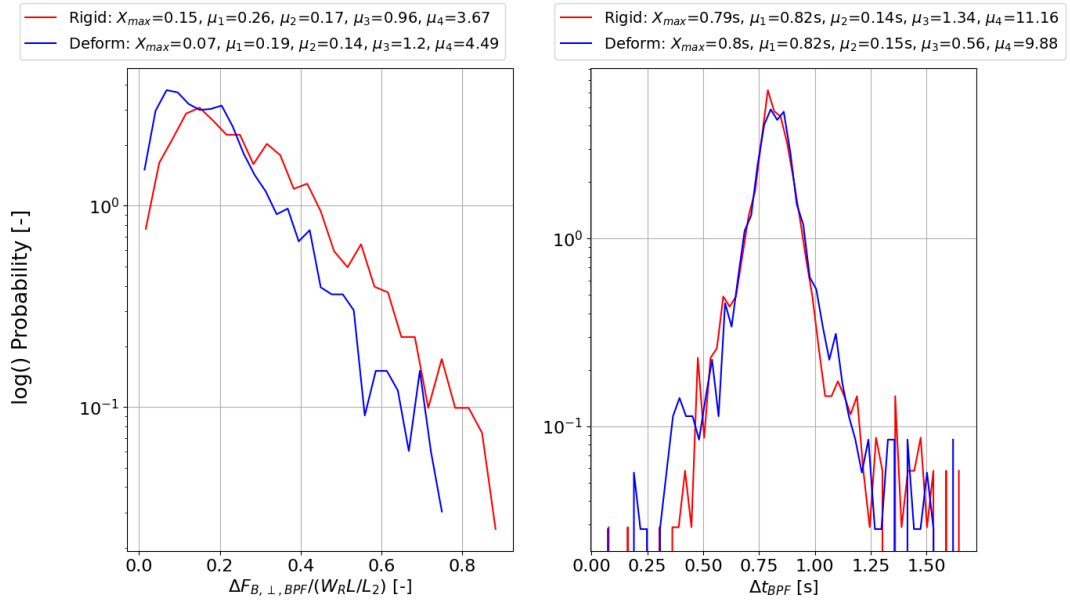

(c)

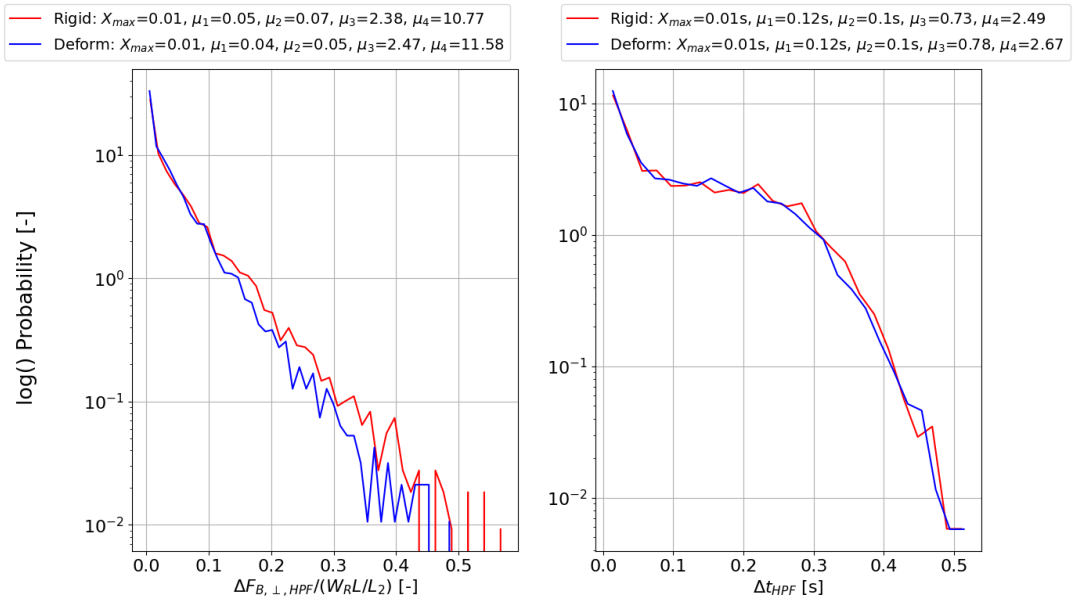

(d)

Figure 7-15: Probability distribution of the absolute change in the main bearing radial force magnitude normalised on the contribution for the rotor weight at the main bearing (left), and the corresponding time over the change in magnitude (right), plotted on a log scale (a) magnitude main bearing radial force magnitude normalised on rotor weight at main bearing (b) low-frequency content (LPF 0.3 Hz) (c) 3P-frequency content (BPF 0.3-0.9 Hz) (d) high-frequency content (HPF 1.5-40 Hz).

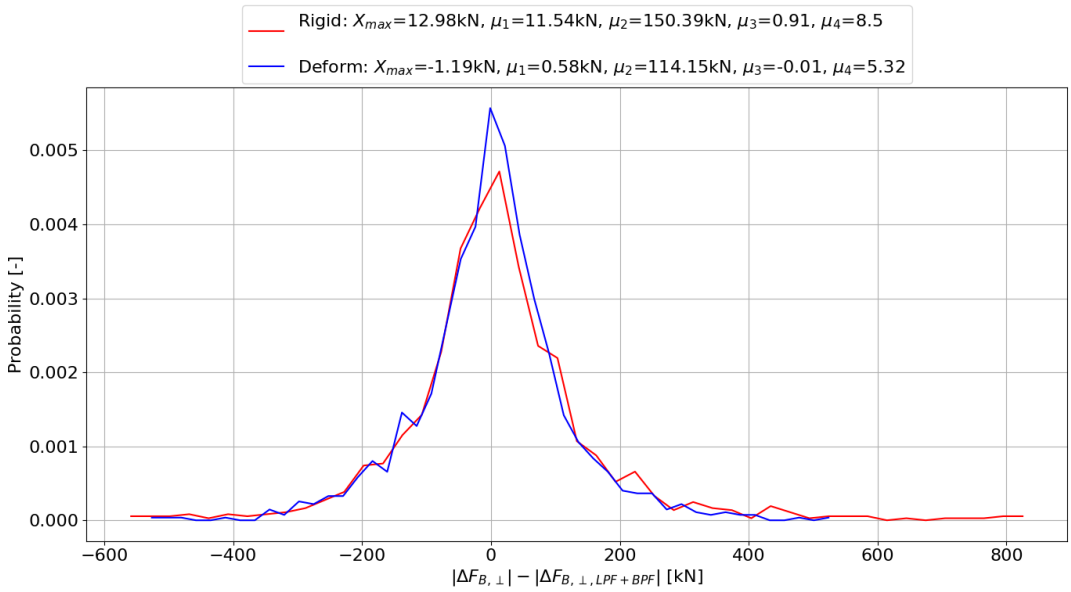

Figure 7-16: Comparing the contributions from the high-frequency content to the peak-to-peak variations in the main bearing radial force magnitude probability with and without blade deformations.

analysis, the number of 2σ events in the deformable rotor analysis was calculated as 283, approximately 50% less compared to the rigid rotor. The reduction in the number of 2σ events between the rigid and deformable rotor analyses is consistent with the reduction of some of the largest jumps observed, likely due to the reduction in the peak-to-peak variations, primarily in the high-frequency content in the deformable rotor analysis.

In summary the evidence presented in Chapter 7 has shown the conclusions from the rigid rotor analysis are directly applicable to a deformable rotor analysis, as the contribution to the time variations from blade deformations is small relative to the aerodynamic contributions. However, a comparison of the contributions to the time variations in the MB radial force magnitude, from the three frequency ranges, between the rigid and deformable rotor analyses, showed there are differences in the time variations. Which led to a reduction in the magnitude of peak-to-peak variations of the MB radial force magnitude. It was identified the reduction is primarily due to a reduction in

peak-to-peak variations in the high-frequency content. Since the high-frequency content is driven by the high-frequency changes in asymmetry due to the blades rotating through the internal eddy structures of the velocity field, which is a direct result of the atmospheric turbulence; for certain analyses it may be necessary to perform the analysis with blade deformations enabled to accurately represent the turbine response.

7.4 Summary

Chapter 7 investigated how blade flexibility influences the wind turbine's aeroelastic response to atmospheric turbulence eddies and the resulting main bearing (MB) load response. By comparing simulations of a rigid and a deformable rotor, it was shown that the overall MB load response changes by less than 10% and the correlations established in Section 5-8 remain largely unchanged. Furthermore, the high-frequency MB force fluctuations, previously linked to atmospheric turbulence, persists even with blade deformation, indicating that these fluctuations are not suppressed by blade flexibility. Consequently, the additional dynamics of the blade deformation due to turbulence is a second order effect compared with the time variations due to the aerodynamic contribution, therefore the key conclusions from earlier chapters remain valid.

Chapter 8

Conclusions and Future Work

8.1 Summary of Key Results

The aim of this research was to characterise the role and quantify the impacts of the continual passage of energetic daytime atmospheric turbulence eddies through the WT rotor on the nonsteady forcing of WT MBs using high-fidelity computer models and simulations.

In order to answer the research questions (R1, R2 & R3 see Section 1.2), AMR-Wind [ExaWind Project, 2025] was used to develop several high-resolution large-eddy simulations of the atmospheric boundary layer. A neutral atmospheric boundary layer was used to study the effect of aspect ratio and numerical dissipation on deviations from the law of the wall, a known issue of large-eddy simulations of the ABL [Brasseur and Wei, 2010]. The analysis concluded that attempts to completely remove the deviations from the law of the wall, which present themselves as an overshoot in the surface layer, were ultimately unsuccessful. The relative contribution of numerical dissipation and dispersion, that arises from the algorithms implemented in AMR-Wind, in-addition to model dissipation from the sub-filter stress model are not fully understood, and it was outside of the scope of this research to undertake an in-depth investigation.

Several precursor moderately convective boundary layers (MCBLs) were simulated to produce a boundary layer where the conditions are representative of the daytime ABL. To ensure accuracy the optimised grid spacing, advective scheme and one-equation model constant, used to limit the influence of the overshoot in the simulations of the neutral ABL but could not be completely removed in the boundary layer, were applied in the development of the precursor MCBL. Statistics and the instantaneous structure of the MCBL were characterised and then verified against the existing literature [Moeng and Sullivan, 1994] [Moeng, 1984] [Khanna and Brasseur, 1998] [Jayaraman and Brasseur, 2021] [Deardorff, 1974]. Lastly, the eddy advection time, ensemble averaged time associated with the time taken for eddies to advect past the WT, was characterised for the energy-containing eddies at hub height, and was calculated to be between 19 s - 71 s (Figure 3-23), consistent with the existing literature [Lavely, 2017] [Vijayakumar, 2015].

The interactions between the atmospheric turbulence and the NREL 5 MW WT [Jonkman et al., 2009] is modelled using the two-way coupled actuator line model (ALM) embedded in AMR-Wind, and the nonsteady response of the WT is calculated using OpenFAST [National Renewable Energy Laboratory, 2023]. The precursor MCBL was applied as a Dirichlet inflow condition to the two-way coupled LES-ABL-turbine calculation of the NREL 5 MW turbine. The precursor was restarted at 38000 s, during a period of quasi-stationarity, and run for 1200 s. A state-of-the art two-way coupled LES-ABL WT simulation was developed using the actuator line model (ALM) embedded in AMR-Wind, including the filtered-lifting-line correction (FLLC) [Martínez-Tossas and Meneveau, 2019], an advancement to the classical ALM. The FLLC implementation was verified by comparing with the existing literature [Martínez-Tossas and Meneveau, 2019] [Stanly et al., 2022]. The accuracy of the ALM with FLLC was compared against the classical ALM and concluded the addition of the FLLC gave a more accurate representation of the blade distributed loads (Figure 4-8) and therefore, the integrated loads. Classical ALM can achieve similar accuracy but with significantly

higher computational cost compared with FLLC.

The computational platform was used to contrast the MB response with rigid and deformable blades, to answer the research question R3: to what extent does blade deformations influence the time variations in main bearing loads. Although, two additional frequencies in the displacement of the deforming blades were identified as potential new frequencies, due to the deformation of the blades, it was concluded the additional dynamics created by the deforming blades does not change the conclusions drawn using the rigid rotor. In conclusion the effect of blade deformations on the time variations on the main bearing force are found to be of lower order compared to the aerodynamic contributions.

In response to R1 and R2, the computational platform was used to investigate the role of turbulence in the energetic daytime atmospheric turbulence eddies in the generation of the time variations in the loads on wind turbine main bearings. A simple static force balance model was used to derive an equation for the MB force vector. In the equation for the MB force vector $\mathbf{F}_B$ there are four terms contributing to the time variations: thrust $F_{H,x}$, out-of-plane bending moment vector $\mathbf{M}_{H,\perp}$, out-of-plane hub force vector $\mathbf{F}_{H,\perp}$ and rotor weight vector $\mathbf{W}_R$. The analysis established the time changes in the MB force vector are primarily driven by the time changes in the out-of-plane bending moment vector at the rotor hub.

The primary role of the contributions from rotor weight to the MB force is shown to be a contribution to the average MB force vector, as rotor weight does not contribute to the time variations in the MB force vector in the rigid rotor configuration (Figure 5-7). Furthermore, when blade deformations are introduced into the calculation, it was concluded the contribution to the MB time variations from time variations due to the weight of the blades due to deformations were negligible compared to the aerodynamic contribution.

Analysis showed that rotor thrust does not contribute significantly to the time varia-

tions in the MB force vector (Figure 5-12). However, in the context of rolling contact fatigue, following the methodology in [International Organization for Standardization, 2007], the analysis suggests when internal geometry is being accounted for, the time variations in rotor thrust modified by the dynamic load factor are comparable to the out-of-plane bending moment modified by the dynamic load factor.

In addressing R2, several analyses were undertaken to characterise the main bearing response to spatially and temporally varying coherent structures within the daytime atmospheric boundary layer turbulence. A comparison of atmospheric turbulence and a steady shear inflow demonstrated the structure of the atmospheric turbulence significantly affects the characteristics of the main bearing response. The atmospheric turbulence dramatically increases the level of fluctuations in the out-of-plane bending moment vector and therefore, the MB force vector outside the 3P frequency range. In-addition, atmospheric turbulence dramatically modulates the time variations in the out-of-plane bending moment vector and therefore, the MB force vector within the 3P frequency range (Figure 6-1). The three frequency ranges in the time variations in the out-of-plane bending moment have fundamentally different characteristics (Figure 6-2), however, analysis of the mechanisms driving the time variations in the OOPBM concluded, at all frequencies the time changes in OOPBM thus, main bearing force vector are driven by the asymmetry generated by the spatially and temporally varying structure of the atmospheric boundary layer (Figure 6-11).

The MB force vector driven by the time variations in the OOPBM vector which is shown to be driven by the time variations in the asymmetry in the velocity field generated by the passage of atmospheric turbulence eddies through the rotor disk. Consequently as WTs increase in size, there is the potential for an increase in the level of asymmetry, due to an increase in the rotor disk size, and also due to capturing larger variations in the velocity field. Furthermore, blades capturing larger variations in the eddy structures, could lead to larger time variations, higher frequencies and higher variability in

asymmetry, and therefore, deviations from the average in the MB force vector.

As the blades rotate through the velocity field all frequencies of the out-of-plane bending moment are forced by the asymmetry in the velocity over the blades. However, an analysis of the mechanisms driving the time variations in the three frequency ranges showed there are subtle differences in the way asymmetry drives the time variations across the three frequencies. The low-frequency content 0.3 Hz is driven by average/overall asymmetry over the rotor disk (Figure 5-10). The 3P is associated with the periodic rotation of three blades through a non-uniform inflow which always creates a well-defined peak at the 3P frequency. Due to the interaction with the turbulent daytime atmospheric boundary layer which contains eddies with a wide range of length and time scales the variability of the 3P-frequency increases over a wide range of time scales (Figure 6-1). Analysis showed a systematic increase in the average gradient, in a steady shear inflow, resulting in a systematic increase in the peak-to-peak variations of the 3P signal (Figure 6-14a). However, the average gradient magnitude calculated from planes of 2D velocity data, over the 1000 s LES-turbine simulation, was not strongly correlated with the modulation of 3P-frequency content of the OOPBM (Figure 6-14b). Indicating the modulation of the 3P frequency content is too complicated to be described with a simple metric. Lastly, the time changes in the high-frequency content (sub-second) is forced by the blades rotating through the internal eddy structures. As the blades rotate through the velocity field the blades respond to the largest velocity gradients causing sub-second changes in asymmetry (Figure 6-13).

The interactions between the three frequency ranges are shown to create time variations in the MB force of order the rotor weight, at sub-second time scale (Figure 6-24), that may underlie the premature failures of MBs. Furthermore, analysis shows the importance of the high-frequency content to the total MB force (Figure 6-28).

Analysis of the specific classes of energy-containing atmospheric turbulence eddies concluded the structure of the ABL is important to the nonsteady response of the WT.

Analysis showed low-speed streaks are the dominant eddy type which generates some of the largest changes in the out-of-plane bending moment and MB force (Figure 6-17), due to LSS being much more coherent and having on average higher internal gradients (Figure 6-18). The importance of accurately representing the structure of the ABL to capture the time response of WTs implies, as kinematic turbulence does not capture the structure of the ABL, the nonsteady response calculated from a WT simulation using kinematic turbulence will likely not be representative of the nonsteady response due to true atmospheric turbulence.

8.2 Future Work

This research has focused on analysis of the time variations in the main bearing reaction force vector to the passage of atmospheric eddies. Using models of the main bearing, the internal system response to the nonsteady loads from atmospheric turbulence can be calculated such as: loads, stresses and deformations of the rollers and inner and outer rings, and lubrication film thickness can be studied, and compared with existing studies. There is also a need for advancements in main bearing models that are publicly available to study the impact of non-steadiness on main bearing failures.

This research has undertaken an in-depth analysis of the nonsteady response of the NREL 5 MW wind turbine to the passage of daytime atmospheric turbulence eddies, comparing the response using rigid and deforming blades. In both configurations of the NREL 5 MW wind turbine the rotor speed and blade pitch angle were fixed to isolate the aerodynamic response. An obvious extension of this current work would be to repeat the calculation using the rigid configuration, restarting at 38000 s in the precursor, to directly compare the time variations in the hub forces and moments to the same inflow with and without controller influence. Using the rigid configuration allows one to more easily isolate the effects of the controller to the time variations. One objective that should be high in priority would be to identify then quantify how

the influence of the controller changes the relationship between asymmetry and the out-of-plane bending moment in the different regions of operation.

While the conclusions drawn from this study, particularly the strong influence of energetic daytime ABL eddies on the nonsteady loading of the main bearing, are valid for turbines operating in region 3 within moderately convective conditions. Therefore, caution must be exercised in generalising the key findings to other operating regimes or atmospheric conditions. Future work should include a broader range of inflow conditions, including offshore (stable) ABLs, different operating points across regions 1 to 3, to investigate the effect of stability state and operating point on atmospheric turbulence and the main bearing response. Additionally, future studies should investigate the influence of upstream turbine wakes on main bearing loading, as these interactions are expected to modify the frequency content and magnitude of nonsteady loads. The nonsteady response from the combination of a turbine's wake plus atmospheric turbulence introduces additional complexity, which can be addressed using the methodologies developed in this study. Arguably the research conducted in this thesis has studied the impacts of daytime atmospheric turbulence on the nonsteady response of WTs in much greater detail than has been previously studied. Therefore, this research serves as an excellent platform to extend the current work to the offshore boundary layer and wake effects.

Aeroelastic simulations use kinematic turbulence models to generate turbulent wind fields to simulate several load cases [International Electrotechnical Commission, 2019]. The reliability of the aeroelastic simulations is important to the design of WTs as designers rely on the loads output to accurately calculate the fatigue life of components, as well as inform other design choices. The results of this research highlighted the importance of the structure of the ABL to the nonsteady response of the WT drivetrain, although it is likely this extends to the entire WT. The importance of accurately representing the structure of the ABL to capture the time response of WTs implies,

as kinematic turbulence is unable to capture the structure of the ABL, the nonsteady response calculated from a WT simulation using kinematic turbulence will likely not be representative of the nonsteady response due to true atmospheric turbulence. Using a kinematic turbulence wind field generator, a wind field with the same average wind parameters as the LES wind field can be generated, and the loads can be calculated for the NREL 5MW WT using kinematic turbulence models. In the LES-ABL calculation ALM was used to two-way couple to the WT to calculate the response of the wind turbine. However, two-way coupling a wind turbine to kinematic turbulence calculation using ALM does not make sense as ALM requires the Navier-Stokes equations to be solving the evolution of the flow, which makes kinematic turbulence redundant. A one-way blade element momentum theory model can be implemented in both LES-ABL and kinematic turbulence simulations, however, it becomes difficult to quantify the relative contribution of the differences from the different models (kinematic, LES, ALM, BEM). The aim of the research would be to compare the nonsteady loads from the kinematic and LES simulations, with the objective to compare the differences in the time responses and quantify the relative contribution of the differences from the different models. However, careful consideration should be placed on the models used to calculate the aerodynamic loads.

Bibliography

[Ai, 2001] Ai, X. (2001). Effect of Debris Contamination on the Fatigue Life of Roller Bearings. *Proceedings of the Institution of Mechanical Engineers, Part J: Journal of Engineering Tribology*, 215(6):563–575.

[Allaerts and Meyers, 2018] Allaerts, D. and Meyers, J. (2018). Gravity Waves and Wind-Farm Efficiency in Neutral and Stable Conditions. *Boundary-Layer Meteorology*, 166(2):269–299.

[Almgren et al., 1998] Almgren, A. S., Bell, J. B., Colella, P., Howell, L. H., and Welcome, M. L. (1998). A Conservative Adaptive Projection Method for the Variable Density Incompressible Navier–Stokes Equations. *Journal of Computational Physics*, 142(1):1–46.

[Bergua Archeli et al., 2021] Bergua Archeli, R., Keller, J., Bankestrom, O., Dunn, M., Guo, Y., Key, A., and Young, E. (2021). Up-Tower Investigation of Main Bearing Cage Slip and Loads. Technical report, National Renewable Energy Laboratory (NREL), Golden, CO (United States).

[Brasseur et al., 2024] Brasseur, J. G., Morris, J., Hart, E., Amiri, A. K., Guo, Y., and Keller, J. (2024). Nonsteady Load Responses of Wind Turbine Atmospheric and Mountain-Generated Turbulence Eddies, With Impacts on the Main Bearing: A Validation Study. Technical report, National Renewable Energy Laboratory (NREL), Golden, CO (United States).

[Brasseur and Wei, 2010] Brasseur, J. G. and Wei, T. (2010). Designing Large-Eddy Simulation of the Turbulent Boundary Layer to Capture Law-of-the-Wall Scaling. *Physics of Fluids*, 22(2):021303.

[Burton et al., 2011] Burton, T., Jenkins, N., Sharpe, D., and Bossanyi, E. (2011). *Wind Energy Handbook*. John Wiley & Sons.

[Cardaun et al., 2019] Cardaun, M., Roscher, B., Schelenz, R., and Jacobs, G. (2019). Analysis of Wind-Turbine Main Bearing Loads Due to Constant Yaw Misalignments over a 20 Years Timespan. *Energies*, 12(9):1768.

[Chattot and Hafez, 2015] Chattot, J.-J. and Hafez, M. (2015). *Theoretical and Applied Aerodynamics*. Springer.

[Chaviaropoulos, 2001] Chaviaropoulos, P. (2001). Flap/Lead–Lag Aeroelastic Stability of Wind Turbine Blades. *Wind Energy: An International Journal for Progress and Applications in Wind Power Conversion Technology*, 4(4):183–200.

[Chovan, 2018] Chovan, C. (2018). Tdi Mainshaft Bearing Field Test Results. In *AWEA Wind Project O&M and Safety Conference AWEA*.

[Chovan, 2019] Chovan, C. (2019). Seven Years of Solid Results. *Wind Systems*, page 17.

[Churchfield et al., 2012a] Churchfield, M., Lee, S., Moriarty, P., Martinez, L., Leonardi, S., Vijayakumar, G., and Brasseur, J. (2012a). A Large-Eddy Simulation of Wind-plant Aerodynamics. In *50th AIAA aerospace sciences meeting including the new horizons forum and aerospace exposition*, page 537.

[Churchfield et al., 2012b] Churchfield, M. J., Lee, S., Michalakes, J., and Moriarty, P. J. (2012b). A Numerical Study of the Effects of Atmospheric and Wake Turbulence on Wind Turbine Dynamics. *Journal of Turbulence*, 13:N14.

[Churchfield et al., 2015] Churchfield, M. J., Lee, S., Schmitz, S., and Wang, Z. (2015). Modeling Wind Turbine Tower and Nacelle Effects within an Actuator Line Model. In *33rd Wind Energy Symposium*, page 0214.

[Churchfield et al., 2017] Churchfield, M. J., Schreck, S. J., Martinez, L. A., Meneveau, C., and Spalart, P. R. (2017). An Advanced Actuator Line Method for Wind Energy Applications and Beyond. In *35th Wind Energy Symposium*, page 1998.

[Churchfield et al., 2010] Churchfield, M. J., Vijayakumar, G., Brasseur, J. G., and Moriarty, P. J. (2010). Wind Energy-Related Atmospheric Boundary Layer Large-Eddy Simulation Using OpenFOAM. Technical report, National Renewable Energy Lab.(NREL), Golden, CO (United States).

[de Mello et al., 2021] de Mello, E., Kampolis, G., Hart, E., Hickey, D., Dinwoodie, I., Carroll, J., Dwyer-Joyce, R., and Boateng, A. (2021). Data Driven Case Study of a Wind Turbine Main-Bearing Failure. In *Journal of Physics: Conference Series*, volume 2018, page 012011. IOP Publishing.

[Deardorff, 1979] Deardorff, J. (1979). Prediction of Convective Mixed-Layer Entrainment for Realistic Capping Inversion Structure. *Journal of Atmospheric Sciences*, 36(3):424–436.

[Deardorff, 1972] Deardorff, J. W. (1972). Numerical Investigation of Neutral and Unstable Planetary Boundary Layers. *Journal of Atmospheric Sciences*, 29(1):91–115.

[Deardorff, 1974] Deardorff, J. W. (1974). Three-Dimensional Numerical Study of the Height and Mean Structure of a Heated Planetary Boundary Layer. *Boundary-Layer Meteorology*, 7(1):81–106.

[Deardorff, 1980] Deardorff, J. W. (1980). Stratocumulus-Capped Mixed Layers Derived from a Three-Dimensional Model. *Boundary-Layer Meteorology*, 18(4):495–527.

[Dose et al., 2018] Dose, B., Rahimi, H., Herráez, I., Stoevesandt, B., and Peinke, J. (2018). Fluid-Structure Coupled Computations of the NREL 5 MW Wind Turbine by Means of CFD. *Renewable Energy*, 129:591–605.

[Dwyer-Joyce, 1993] Dwyer-Joyce, R. S. (1993). *The Effects of Lubricant Contamination on Rolling Bearing Performance*. PhD thesis, Imperial College London (University of London).

[Ekaterinaris and Menter, 1994] Ekaterinaris, J. and Menter, F. (1994). Computation of Oscillating Airfoil Flows with One-and Two-equation Turbulence Models. *AIAA Journal*, 32(12):2359–2365.

[El Laithy et al., 2019] El Laithy, M., Wang, L., Harvey, T. J., Vierneusel, B., Correns, M., and Blass, T. (2019). Further Understanding of Rolling Contact Fatigue in Rolling Element Bearings - A Review. *Tribology International*, 140:105849.

[El-Thalji and Jantunen, 2014] El-Thalji, I. and Jantunen, E. (2014). A Descriptive Model of Wear Evolution in Rolling Bearings. *Engineering Failure Analysis*, 45:204–224.

[Emes et al., 2016] Emes, M., Arjomandi, M., Kelso, R., and Ghanadi, F. (2016). Integral Length Scales in a Low-Roughness Atmospheric Boundary Layer. Technical Report AWES–2.06, Australasian Wind Engineering Society (AWES), Australia.

[ExaWind Project, 2025] ExaWind Project (2025). AMR-Wind: AMReX-based structured wind solver. Accessed: 2025-05-20.

[Fedorovich and Mironov, 1995] Fedorovich, E. and Mironov, D. (1995). A Model for a Shear-Free Convective Boundary Layer with Parameterized Capping Inversion Structure. *Journal of Atmospheric Sciences*, 52(1):83–96.

[Gadde and Stevens, 2021] Gadde, S. N. and Stevens, R. J. (2021). Effect of Low-Level Jet Height on Wind Farm Performance. *Journal of Renewable and Sustainable*

Energy, 13(1).

[Gao et al., 1999] Gao, N., Dwyer-Joyce, R., and Beynon, J. (1999). Effects of Surface Defects on Rolling Contact Fatigue of 60/40 Brass. *Wear*, 225:983–994.

[Ghosal, 1996] Ghosal, S. (1996). An Analysis of Numerical Errors in Large-Eddy Simulations of Turbulence. *Journal of Computational Physics*, 125(1):187–206.

[Giacomini and Giometto, 2021] Giacomini, B. and Giometto, M. G. (2021). On the Suitability of Second-Order Accurate Finite-Volume Solvers for the Simulation of Atmospheric Boundary Layer Flow. *Geoscientific Model Development*, 14(3):1409–1426.

[Guo et al., 2021] Guo, Y., Bankestrom, O., Bergua, R., Keller, J., and Dunn, M. (2021). Investigation of Main Bearing Operating Conditions in a Three-Point Mount Wind Turbine Drivetrain. *Forschung im Ingenieurwesen*, 85(2):405–415.

[Gutierrez et al., 2016] Gutierrez, W., Araya, G., Kiliyanpilakkil, P., Ruiz-Columbie, A., Tutkun, M., and Castillo, L. (2016). Structural Impact Assessment of Low Level Jets over Wind Turbines. *Journal of Renewable and Sustainable Energy*, 8(2).

[Gutierrez et al., 2017] Gutierrez, W., Ruiz-Columbie, A., Tutkun, M., and Castillo, L. (2017). Impacts of the Low-Level Jet's Negative Wind Shear on the Wind Turbine. *Wind Energy Science*, 2(2):533–545.

[Halme and Andersson, 2010] Halme, J. and Andersson, P. (2010). Rolling Contact Fatigue and Wear Fundamentals for Rolling Bearing Diagnostics-State of the Art. *Proceedings of the Institution of Mechanical Engineers, Part J: Journal of Engineering Tribology*, 224(4):377–393.

[Hansen et al., 2006] Hansen, M. O. L., Sørensen, J. N., Voutsinas, S., Sørensen, N., and Madsen, H. A. (2006). State of the Art in Wind Turbine Aerodynamics and Aeroelasticity. *Progress in Aerospace Sciences*, 42(4):285–330.

[Harris, 2001] Harris, T. A. (2001). *Rolling Bearing Analysis*. John Wiley & Sons.

[Hart, 2020] Hart, E. (2020). Developing a Systematic Approach to the Analysis of Time-Varying Main Bearing Loads for Wind Turbines. *Wind Energy*, 23(12):2150–2165.

[Hart et al., 2020] Hart, E., Clarke, B., Nicholas, G., Kazemi Amiri, A., Stirling, J., Carroll, J., Dwyer-Joyce, R., McDonald, A., and Long, H. (2020). A Review of Wind Turbine Main Bearings: Design, Operation, Modelling, Damage Mechanisms and Fault Detection. *Wind Energy Science*, 5(1):105–124.

[Hart et al., 2022a] Hart, E., de Mello, E., and Dwyer-Joyce, R. (2022a). Wind Turbine Main-Bearing Lubrication–Part 1: An Introductory Review of Elastohydrodynamic Lubrication Theory. *Wind Energy Science*, 7(3):1021–1042.

[Hart et al., 2022b] Hart, E., De Mello, E., and Dwyer-Joyce, R. (2022b). Wind Turbine Main-Bearing Lubrication–Part 2: Simulation-Based Results for a Double-Row Spherical Roller Main Bearing in a 1.5 MW Wind Turbine. *Wind Energy Science*, 7(4):1533–1550.

[Hart et al., 2023] Hart, E., Raby, K., Keller, J., Sheng, S., Long, H., Carroll, J., Brasseur, J., and Tough, F. (2023). Main Bearing Replacement and Damage: A Field Data Study on 15 Gigawatts of Wind Energy Capacity. Technical Report NREL/TP-5000-86228, National Renewable Energy Laboratory (NREL), Golden, CO, USA.

[Hart et al., 2022c] Hart, E., Stock, A., Elderfield, G., Elliott, R., Brasseur, J., Keller, J., Guo, Y., and Song, W. (2022c). Impacts of Wind Field Characteristics and Non-Steady Deterministic Wind Events on Time-Varying Main-Bearing Loads. *Wind Energy Science*, 7(3):1209–1226.

[Hart et al., 2019] Hart, E., Turnbull, A., Feuchtwang, J., McMillan, D., Golysheva,

E., and Elliott, R. (2019). Wind Turbine Main-Bearing Loading and Wind Field Characteristics. *Wind Energy*, 22(11):1534–1547.

[Hooke, 2003] Hooke, C. (2003). Dynamic Effects in EHL Contacts. In *Tribology Series*, volume 41, pages 69–78. Elsevier.

[International Electrotechnical Commission, 2019] International Electrotechnical Commission (2019). IEC 61400-1:2019(E). Wind Energy Generation Systems - Part 1: Design Requirements. Standard, International Electrotechnical Commission, Geneva, CH.

[International Organization for Standardization, 2007] International Organization for Standardization (2007). ISO 281:2007(E). Rolling Bearings — Dynamic Load Ratings and Rating Life. Standard, International Organization for Standardization, Geneva, CH.

[Jayaraman and Brasseur, 2021] Jayaraman, B. and Brasseur, J. G. (2021). Transition in Atmospheric Boundary Layer Turbulence Structure from Neutral to Convective, and Large-Scale Rolls. *Journal of Fluid Mechanics*, 913.

[Jha et al., 2013] Jha, P., Churchfield, M., Moriarty, P., and Schmitz, S. (2013). Accuracy of State-of-the-Art Actuator-Line Modeling for Wind Turbine Wakes. In *51st AIAA Aerospace Sciences Meeting including the New Horizons Forum and Aerospace Exposition*, page 608.

[Jha et al., 2014] Jha, P. K., Churchfield, M. J., Moriarty, P. J., and Schmitz, S. (2014). Guidelines for Volume Force Distributions Within Actuator Line Modeling of Wind Turbines on Large-Eddy Simulation-Type Grids. *Journal of Solar Energy Engineering*, 136(3).

[Jonkman et al., 2009] Jonkman, J., Butterfield, S., Musial, W., and Scott, G. (2009). Definition of a 5-MW Reference Wind Turbine for Offshore System Development.

Technical report, National Renewable Energy Lab.(NREL), Golden, CO (United States).

[Jonkman et al., 2005] Jonkman, J. M., Buhl, M. L., et al. (2005). *FAST User's Guide*, volume 365. National Renewable Energy Laboratory Golden, CO, USA.

[Joustra et al., 2021] Joustra, J., Flipsen, B., and Balkenende, R. (2021). Structural Reuse of Wind Turbine Blades through Segmentation. *Composites Part C: Open Access*, 5:100137.

[Kallesøe and Hansen, 2009] Kallesøe, B. and Hansen, M. (2009). Some Effect of Large Blade Deflections on Aeroelastic Stability. In *47th AIAA Aerospace Sciences Meeting including The New Horizons Forum and Aerospace Exposition*, page 839.

[Kallesøe, 2011] Kallesøe, B. S. (2011). Effect of Steady Deflections on the Aeroelastic Stability of a Turbine Blade. *Wind Energy*, 14(2):209–224.

[Kenworthy et al., 2024] Kenworthy, J., Hart, E., Stirling, J., Stock, A., Keller, J., Guo, Y., Brasseur, J., and Evans, R. (2024). Wind Turbine Main Bearing Rating Lives as Determined by IEC 61400-1 and ISO 281: A Critical Review and Exploratory Case Study. *Wind Energy*, 27(2):179–197.

[Khanna, 1995] Khanna, S. (1995). *Structure of the Atmospheric Boundary Layer from Large Eddy Simulation*. The Pennsylvania State University.

[Khanna and Brasseur, 1998] Khanna, S. and Brasseur, J. G. (1998). Three-Dimensional Buoyancy-and Shear-Induced Local Structure of the Atmospheric Boundary Layer. *Journal of the Atmospheric Sciences*, 55(5):710–743.

[Kravchenko and Moin, 1997] Kravchenko, A. and Moin, P. (1997). On the Effect of Numerical Errors in Large Eddy Simulations of Turbulent Flows. *Journal of Computational Physics*, 131(2):310–322.

[Langtry et al., 2006] Langtry, R., Gola, J., and Menter, F. (2006). Predicting 2D Airfoil and 3D Wind Turbine Rotor Performance Using a Transition Model for General CFD Codes. In *44th AIAA Aerospace Sciences Meeting and Exhibit*, page 395.

[Larsen et al., 2004] Larsen, T. J., Hansen, A. M., and Buhl, T. (2004). Aeroelastic Effects of Large Blade Deflections for Wind Turbines. *Proceedings of The Science of Making Torque from Wind*, pages 238–246.

[Laursen et al., 2007] Laursen, J., Enevoldsen, P., and Hjort, S. (2007). 3D CFD Quantification of the Performance of a Multi-Megawatt Wind Turbine. In *Journal of Physics: Conference Series*, volume 75, page 012007. IOP Publishing.

[Lavely et al., 2011] Lavely, A., Vijayakumar, G., Kinzel, M., Brasseur, J., and Paterson, E. (2011). Space-Time Loadings on Wind Turbine Blades Driven by Atmospheric Boundary Layer Turbulence. In *49th AIAA Aerospace Sciences Meeting Including the New Horizons Forum and Aerospace Exposition*, page 635.

[Lavely, 2017] Lavely, A. W. (2017). *Effects of Daytime Atmospheric Boundary Layer Turbulence on the Generation of Nonsteady Wind Turbine Loadings and Predictive Accuracy of Lower Order Models*. PhD dissertation, The Pennsylvania State University, University Park, PA. (accessed: 23.12.2024).

[Lavely et al., 2014] Lavely, A. W., Vijayakumar, G., Craven, B., Jayaraman, B., Paterson, E. G., Nandi, T. N., and Brasseur, J. (2014). Towards a Blade-Resolved Hybrid URANS-LES of the NREL 5-MW Wind Turbine Rotor within Large Eddy Simulation of the Atmospheric Boundary Layer. In *32nd ASME Wind Energy Symposium*, page 0869.

[Lee et al., 2017] Lee, K., Huque, Z., Kommalapati, R., and Han, S.-E. (2017). Fluid-Structure Interaction Analysis of NREL Phase VI Wind Turbine: Aerodynamic Force Evaluation and Structural Analysis Using FSI Analysis. *Renewable Energy*, 113:512–531.

[Leishman, 2002] Leishman, J. G. (2002). Challenges in Modelling the Unsteady Aerodynamics of Wind Turbines. *Wind Energy: An International Journal for Progress and Applications in Wind Power Conversion Technology*, 5(2-3):85–132.

[Lemone, 1973] Lemone, M. A. (1973). The Structure and Dynamics of Horizontal Roll Vortices in the Planetary Boundary Layer. *Journal of Atmospheric Sciences*, 30(6):1077–1091.

[Liang et al., 2013] Liang, Y., An, Z., and Liu, B. (2013). Fatigue Life Prediction for Wind Turbine Main Shaft Bearings. In *2013 International Conference on Quality, Reliability, Risk, Maintenance, and Safety Engineering (QR2MSE)*, pages 888–893. IEEE.

[Lilly, 1968] Lilly, D. K. (1968). Models of Cloud-Topped Mixed Layers Under a Strong Inversion. *Quarterly Journal of the Royal Meteorological Society*, 94(401):292–309.

[Lindenburg and Snel, 2003] Lindenburg, C. and Snel, H. (2003). Aero-Elastic Stability Analysis Tools for Large Wind Turbine Rotor Blades. In *Proceedings of the 2003 European Wind Energy Conference and Exhibition*, volume 6. European Wind Energy Association Madrid, Spain.

[Loriemi et al., 2021] Loriemi, A., Jacobs, G., Reisch, S., Bosse, D., and Schröder, T. (2021). Experimental and Simulation-Based Analysis of Asymmetrical Spherical Roller Bearings as Main Bearings for Wind Turbines. *Forschung im Ingenieurwesen*, 85(2):189–197.

[Martinez et al., 2012] Martinez, L., Leonardi, S., Churchfield, M., and Moriarty, P. (2012). A Comparison of Actuator Disk and Actuator Line Wind Turbine Models and Best Practices for Their Use. In *50th AIAA Aerospace Sciences Meeting including the New Horizons Forum and Aerospace Exposition*, page 900.

[Martínez-Tossas et al., 2016] Martínez-Tossas, L. A., Churchfield, M. J., and Mene-

veau, C. (2016). A Highly Resolved Large-Eddy Simulation of a Wind Turbine Using an Actuator Line Model with Optimal Body Force Projection. In *Journal of Physics: Conference Series*, volume 753, page 082014. IOP Publishing.

[Martínez-Tossas et al., 2017] Martínez-Tossas, L. A., Churchfield, M. J., and Meneveau, C. (2017). Optimal Smoothing Length Scale for Actuator Line Models of Wind Turbine Blades Based on Gaussian Body Force Distribution. *Wind Energy*, 20(6):1083–1096.

[Martínez-Tossas and Meneveau, 2019] Martínez-Tossas, L. A. and Meneveau, C. (2019). Filtered Lifting Line Theory and Application to the Actuator Line Model. *Journal of Fluid Mechanics*, 863:269–292.

[Mason and Thomson, 1992] Mason, P. J. and Thomson, D. J. (1992). Stochastic Backscatter in Large-Eddy Simulations of Boundary Layers. *Journal of Fluid Mechanics*, 242:51–78.

[McKenna et al., 2016] McKenna, R., vd Leye, P. O., and Fichtner, W. (2016). Key Challenges and Prospects for Large Wind Turbines. *Renewable and Sustainable Energy Reviews*, 53:1212–1221.

[Mo et al., 2015] Mo, W., Li, D., Wang, X., and Zhong, C. (2015). Aeroelastic Coupling Analysis of the Flexible Blade of a Wind Turbine. *Energy*, 89:1001–1009.

[Moeng, 1984] Moeng, C.-H. (1984). A Large-Eddy-Simulation Model for the Study of Planetary Boundary-Layer Turbulence. *Journal of the Atmospheric Sciences*, 41(13):2052–2062.

[Moeng and Sullivan, 1994] Moeng, C.-H. and Sullivan, P. P. (1994). A Comparison of Shear-and Buoyancy-Driven Planetary Boundary Layer Flows. *Journal of Atmospheric Sciences*, 51(7):999–1022.

[Moriarty and Hansen, 2005] Moriarty, P. J. and Hansen, A. C. (2005). AeroDyn Theory Manual. Technical report, National Renewable Energy Lab., Golden, CO (US).

[Muñoz-Simón et al., 2020] Muñoz-Simón, A., Wynn, A., and Palacios, R. (2020). Unsteady and Three-Dimensional Aerodynamic Effects on Wind Turbine Rotor Loads. In *AIAA Scitech 2020 Forum*, page 0991.

[Nandi et al., 2016] Nandi, T. N., Brasseur, J. G., and Vijayakumar, G. (2016). Prediction and Analysis of the Nonsteady Transition and Separation Processes on an Oscillating Wind Turbine Airfoil Using the $\gamma - Re_\theta$ Transition Model. Technical report, Penn State University.

[Nandi et al., 2017] Nandi, T. N., Herrig, A., and Brasseur, J. G. (2017). Non-Steady Wind Turbine Response to Daytime Atmospheric Turbulence. *Philosophical Transactions of the Royal Society A: Mathematical, Physical and Engineering Sciences*, 375(2091):20160103.

[Nappo, 2012] Nappo, C. J. (2012). *Appendix A - The Hydrostatic Atmosphere*. International Geophysics.

[National Renewable Energy Laboratory, 2023] National Renewable Energy Laboratory (2023). OpenFAST: Open-Source Wind Turbine Simulation Tool (Version 3.4.1). Accessed: 2025-05-20.

[Ne´ lias and Ville, 2000] Ne´ lias, D. and Ville, F. (2000). Detrimental Effects of Debris Dents on Rolling Contact Fatigue. *Journal of Tribology*, 122(1):55–64.

[Nejad et al., 2022] Nejad, A. R., Keller, J., Guo, Y., Sheng, S., Polinder, H., Watson, S., Dong, J., Qin, Z., Ebrahimi, A., Schelenz, R., et al. (2022). Wind Turbine Drivetrains: State-of-the-Art Technologies and Future Development Trends. *Wind Energy Science*, 7(1):387–411.

[Oñate, 2013] Oñate, E. (2013). *Structural Analysis with the Finite Element Method. Linear Statics: Volume 2: Beams, Plates and Shells.* Springer Science & Business Media.

[Panteli et al., 2022] Panteli, A. N., Manolas, D. I., Riziotis, V. A., and Spiliopoulos, K. V. (2022). Comparative Study of Two Geometrically Non-Linear Beam Approaches for the Coupled Wind Turbine System. *Journal of Wind Engineering and Industrial Aerodynamics*, 231:105231.

[Patterson Jr and Orszag, 1971] Patterson Jr, G. and Orszag, S. A. (1971). Spectral Calculations of Isotropic Turbulence: Efficient Removal of Aliasing Interactions. *The Physics of Fluids*, 14(11):2538–2541.

[Pierce, 1996] Pierce, K. G. (1996). Wind Turbine Load Prediction Using the Beddoes-Leishman Model for Unsteady Aerodynamics and Dynamic Stall. Master's thesis, University of Utah, Salt Lake City, UT.

[Pulikollu et al., 2024] Pulikollu, R., Haus, L., Mclaughlin, J., and Sheng, S. (2024). "Wind Turbine Main Bearing Reliability Analysis, Operations, and Maintenance Considerations: Electric Power Research Institute (EPRI)".

[Salesky et al., 2017] Salesky, S. T., Chamecki, M., and Bou-Zeid, E. (2017). On the Nature of the Transition Between Roll and Cellular Organization in the Convective Boundary Layer. *Boundary-Layer Meteorology*, 163(1):41–68.

[Sethuraman et al., 2015] Sethuraman, L., Guo, Y., and Sheng, S. (2015). Main Bearing Dynamics in Three-Point Suspension Drivetrains for Wind Turbines; National Wind Technology Center (NWTC), NREL (National Renewable Energy Laboratory). Technical report, National Renewable Energy Lab.(NREL), Golden, CO (United States).

[Shen et al., 2005] Shen, W. Z., Sørensen, J. N., and Mikkelsen, R. (2005). Tip Loss

Correction for Actuator/Navier–Stokes Computations. *Journal of Solar Energy Engineering*, 127(2):209–213.

[Sheng et al., 2011] Sheng, S., Link, H., LaCava, W., van Dam, J., McNiff, B., Veers, P., Keller, J., Butterfield, S., and Oyague, F. (2011). Wind Turbine Drivetrain Condition Monitoring during GRC Phase 1 and Phase 2 Testing. Technical report, National Renewable Energy Lab.(NREL), Golden, CO (United States).

[Sheng et al., 2006] Sheng, W., Galbraith, R., Coton, F., and Gilmour, R. (2006). The Collected Data for Tests on an S809 Airfoil, Volume II: Pressure Data from Static and Oscillatory Tests. *GU Aero Report*, 607.

[Shimizu, 2009] Shimizu, S. (2009). Fatigue Limit Evaluation for JIS SUJ2/AISI 52100 Bearing Steel Using Alternating Torsion Life Test. *Research Reports School of Science and Technology Meiji University*, 41:1.

[Shives and Crawford, 2013] Shives, M. and Crawford, C. (2013). Mesh and load distribution requirements for actuator line CFD simulations. *Wind Energy*, 16(8):1183–1196.

[Simms et al., 2001] Simms, D., Schreck, S., Hand, M., and Fingersh, L. J. (2001). NREL Unsteady Aerodynamics Experiment in the NASA-Ames Wind Tunnel: A Comparison of Predictions to Measurements. Technical report, National Renewable Energy Lab.(NREL), Golden, CO (United States).

[Smith, 2010] Smith, R. B. (2010). Gravity Wave Effects on Wind Farm Efficiency. *Wind Energy*, 13(5):449–458.

[Sorensen and Shen, 2002] Sorensen, J. N. and Shen, W. Z. (2002). Numerical Modeling of Wind Turbine Wakes. *J. Fluids Eng.*, 124(2):393–399.

[Stanly et al., 2022] Stanly, R., Martínez-Tossas, L. A., Frankel, S. H., and Delorme, Y. (2022). Large-Eddy Simulation of a Wind Turbine Using a Filtered Actuator Line

Model. *Journal of Wind Engineering and Industrial Aerodynamics*, 222:104868.

[Stehly and Duffy, 2023] Stehly, T. and Duffy, P. (2023). 2021 Cost of Wind Energy Review [Slides]. Technical report, National Renewable Energy Laboratory (NREL), Golden, CO (United States).

[Stevens et al., 2018] Stevens, R. J., Martínez-Tossas, L. A., and Meneveau, C. (2018). Comparison of Wind Farm Large Eddy Simulations Using Actuator Disk and Actuator Line Models with Wind Tunnel Experiments. *Renewable Energy*, 116:470–478.

[Stirling et al., 2021] Stirling, J., Hart, E., and Kazemi Amiri, A. (2021). Constructing Fast and Representative Analytical Models of Wind Turbine Main Bearings. *Wind Energy Science*, 6(1):15–31.

[Stull, 2012] Stull, R. B. (2012). *An Introduction to Boundary Layer Meteorology*, volume 13. Springer Science & Business Media.

[Sullivan and Patton, 2008] Sullivan, P. P. and Patton, E. G. (2008). A Highly Parallel Algorithm for Turbulence Simulations in Planetary Boundary Layers: Results with Meshes up to 1024^3. In *Proceedings of the 18th Symposium on Boundary Layers and Turbulence*, Stockholm, Sweden. American Meteorological Society.

[Taschner et al., 2024] Taschner, E., Folkersma, M., A Martínez-Tossas, L., Verzijlbergh, R., and van Wingerden, J.-W. (2024). A New Coupling of a GPU-Resident Large-Eddy Simulation Code with a Multiphysics Wind Turbine Simulation Tool. *Wind Energy*, 27(11):1152–1172.

[Trigaux et al., 2022] Trigaux, F., Chatelain, P., and Winckelmans, G. (2022). A Flexible Actuator Curve Model for Aeroelastic Simulations of Wind Turbines in Atmospheric Boundary Layers. In *Journal of Physics: Conference Series*, volume 2265, page 022050. IOP Publishing.

[Troldborg, 2009] Troldborg, N. (2009). *Actuator Line Modeling of Wind Turbine Wakes*. PhD thesis, Technical University of Denmark, Lyngby, Denmark. (accessed: 23.12.2024).

[Tzimas and Prospathopoulos, 2016] Tzimas, M. and Prospathopoulos, J. (2016). Wind Turbine Rotor Simulation Using the Actuator Disk and Actuator Line Methods. In *Journal of Physics: conference series*, volume 753, page 032056. IOP Publishing.

[Van Der Tempel et al., 2011] Van Der Tempel, J., Diepeveen, N., De Vries, W., and Salzmann, D. C. (2011). Offshore Environmental Loads and Wind Turbine Design: Impact of Wind, Wave, Currents and Ice. In *Wind energy systems*, pages 463–478. Elsevier.

[Veers et al., 2023] Veers, P., Bottasso, C. L., Manuel, L., Naughton, J., Pao, L., Paquette, J., Robertson, A., Robinson, M., Ananthan, S., Barlas, T., et al. (2023). Grand Challenges in the Design, Manufacture, and Operation of Future Wind Turbine Systems. *Wind Energy Science*, 8(7):1071–1131.

[Venner and Wijnant, 2005] Venner, C. H. and Wijnant, Y. H. (2005). Validation of EHL Contact Predictions under Time Varying Load. *Proceedings of the Institution of Mechanical Engineers, Part J: Journal of Engineering Tribology*, 219(4):249–261.

[Vijayakumar, 2015] Vijayakumar, G. (2015). *Non-Steady Dynamics of Atmospheric Turbulence Interaction with Wind Turbine Loadings through Blade-Boundary-Layer-Resolved CFD*. PhD dissertation, The Pennsylvania State University, University Park, PA. (accessed: 23.12.2024).

[Vijayakumar et al., 2016] Vijayakumar, G., Brasseur, J., Lavely, A. W., Jayaraman, B., and Craven, B. (2016). Interaction of Atmospheric Turbulence with Blade Boundary Layer Dynamics on a 5 MW Wind Turbine Using Blade-Boundary-Layer-

Resolved CFD with Hybrid URANS-LES. In *34th Wind Energy Symposium*, page 0521.

[Vijayakumar and Brasseur, 2019] Vijayakumar, G. and Brasseur, J. G. (2019). Blade-Resolved Modeling with Fluid-Structure Interaction. Technical report, National Renewable Energy Lab.(NREL), Golden, CO (United States).

[Wang et al., 2016] Wang, L., Liu, X., and Kolios, A. (2016). State of the Art in the Aeroelasticity of Wind Turbine Blades: Aeroelastic Modelling. *Renewable and Sustainable Energy Reviews*, 64:195–210.

[Wang et al., 2014] Wang, L., Liu, X., Renevier, N., Stables, M., and Hall, G. M. (2014). Nonlinear Aeroelastic Modelling for Wind Turbine Blades Based on Blade Element Momentum Theory and Geometrically Exact Beam Theory. *Energy*, 76:487–501.

[Wang et al., 2017] Wang, Q., Sprague, M. A., Jonkman, J., Johnson, N., and Jonkman, B. (2017). BeamDyn: A High-Fidelity Wind Turbine Blade Solver in the FAST Modular Framework. *Wind Energy*, 20(8):1439–1462.

[Wang et al., 2010] Wang, S., Ingham, D. B., Ma, L., Pourkashanian, M., and Tao, Z. (2010). Numerical Investigations on Dynamic Stall of Low Reynolds Number Flow Around Oscillating Airfoils. *Computers & Fluids*, 39(9):1529–1541.

[WindEurope, 2024] WindEurope (2024). Wind Energy in Europe: 2023 Statistics and the Outlook for 2024–2030. `https://windeurope.org/intelligence-platform/product/wind-energy-in-europe-2023-statistics-and-the-outlook-for-2024-2030/`. (accessed: 23.12.2024).

[Wu, 2018] Wu, J. C. (2018). *Elements of Vorticity Aerodynamics*. Springer.

[Wu et al., 2023] Wu, M., Han, X., Tao, Y., and Pei, J. (2023). Lubrication Reliability Analysis of Wind Turbine Main Bearing in Random Wind Field. *Tribology International*, 179:108181.

[Wyngaard, 2010] Wyngaard, J. C. (2010). *Turbulence in the Atmosphere*. Cambridge University Press.

[Xie, 2021] Xie, S. (2021). An Actuator-Line Model with Lagrangian-Averaged Velocity Sampling and Piecewise Projection for Wind Turbine Simulations. *Wind Energy*, 24(10):1095–1106.

[Yang and Sotiropoulos, 2018] Yang, X. and Sotiropoulos, F. (2018). A New Class of Actuator Surface Models for Wind Turbines. *Wind Energy*, 21(5):285–302.

[Yucesan and Viana, 2019] Yucesan, Y. A. and Viana, F. (2019). Onshore Wind Turbine Main Bearing Reliability and its Implications in Fleet Management. In *AIAA Scitech 2019 Forum*, page 1225.

[Zaretsky, 2013] Zaretsky, E. V. (2013). Rolling Bearing Life Prediction, Theory, and Application. Technical Memorandum NASA/TM-2016-215163, NASA Glenn Research Center, Cleveland, OH.

[Zhang and Huang, 2011] Zhang, P. and Huang, S. (2011). Review of Aeroelasticity for Wind Turbine: Current Status, Research Focus and Future Perspectives. *Frontiers in Energy*, 5(4):419–434.

[Zheng et al., 2020] Zheng, J., Ji, J., Yin, S., and Tong, V.-C. (2020). Fatigue Life Analysis of Double-Row Tapered Roller Bearing in a Modern Wind Turbine under Oscillating External Load and Speed. *Proceedings of the Institution of Mechanical Engineers, Part C: Journal of Mechanical Engineering Science*, 234(15):3116–3130.